Crustal Structure, Tectonostratigraphy, and Hydrocarbon Potential of the Terranes Underlying the Caribbean Plate and the Camamu-Almada Rifted Passive Margin of Northeastern Brazil

by
Sean Romito

A dissertation submitted to the Department of Earth and Atmospheric Sciences,
College of Natural Sciences and Mathematics
in partial fulfillment of the requirements for the degree of

DOCTOR OF PHILOSOPHY

in Geology

Chair of Committee: Paul Mann

Committee Member: Dale E. Bird

Committee Member: Ana Krueger

Committee Member: Jonny Wu

University of Houston
December 2021

DEDICATION

To my partner, parents, brother, friends, and extended family, without whom this long journey would have been either considerably harder or downright impossible.

To the inherent stubbornness of humankind, also instrumental to this effort.

ACKNOWLEDGMENTS

I thank Dr. Paul Mann for his support and primary supervision throughout my research and doctoral dissertation, and to the Conjugate Basins, Tectonics, and Hydrocarbons (CBTH) consortium for funding my research. Special thanks to Dr. Dale E. Bird, Dr. Ana Krueger, and Dr. Jonny Wu for their service on my committee and for contributing their time and expertise to improve the ideas and data analysis in this dissertation.

Many thanks to those institutions and persons who helped me assemble and gain permissions for the regional geologic and geophysical databases that were used in this dissertation. For the Caribbean work in Chapter 2, I thank the previous PhD students, Javier Sanchez, Luis Carlos Carvajal and Bryan Ott, whose previous dissertation work for the CBTH project was integrated into my regional study; to Mike Saunders at Spectrum Geo (now TGS) for providing industry seismic reflection data; and to the Institute for Geophysics of the University of Texas at Austin for providing access to a regional grid of vintage seismic reflection data from the region.

For the Brazil studies in Chapters 3, 4, and 5, I thank Paulo de Tarso Silva Antunes and the team at the Brazilian Agência Nacional do Petróleo, Gás Natural e Biocombustíveis (ANP) for their assistance in obtaining gravity, magnetic, and seismic reflection data, and to James Deckelman and Kyle Reuber at ION Geophysical for providing me two deep-penetration seismic lines. I also thank Christiano Lopes and Igor Aquilino at Geopost for providing access to their web-based data platform for all Brazilian data. I thank Lei Sun and Nawaz Bugti from the CBTH project for their assistance with the CBTH database.

I would also like to thank the software providers to the Department of Earth and Atmospheric Sciences and the CBTH project including Schlumberger (Petrel and Petromod), Petex (Move), Seequent (Oasis Montage) and Bluware (Headwave and InteractivAI).

Finally, I express my heartfelt gratitude to my fellow students at CBTH (Marcus, Jack, Hualing, and others), industry professionals, and academic researchers for the countless conversations, jokes, difficult questions, and camaraderie. They turned what is an inherently lonely journey into much more.

ABSTRACT

This dissertation combines the results of two studies of the crustal structure and the Late Cretaceous-Cenozoic tectonostratigraphy of the 3,300,000 km^2 Caribbean plate and the 22,000 km^2 Camamu-Almada passive segment of northeastern Brazil.

In **Chapter 2**, the composite crustal structure of the Caribbean plate was described as including four terranes composed of island arc, continental, oceanic, and oceanic plateau crust. The terranes were characterized using seismic reflection, gravity, magnetics, and well data to demonstrate that the Late Cretaceous-Cenozoic basin size and depth were primarily controlled by the underlying terrane. Strongly flexed oceanic and oceanic plateau crust along zones at the edges of the Caribbean plate controlled the deepest sediment-filled basins. Areas of proven hydrocarbon source rocks are associated with continental and island arc crust, while organically-rich, Late Cretaceous source rocks may be widespread across the Caribbean plate interior.

In **Chapter 3**, the rifted-passive margin of the Camamu-Almada basin in northeastern Brazil was investigated through 2D and 3D gravity modeling and interpretation of two, deep-penetration seismic lines. Integration of these data suggested that the 40–110 km-wide transition zone between continental and oceanic crust is structurally complex and composed of three crustal blocks: a 10–40 km-wide zone of hyperextended continental crust, a 20 km-wide zone of exhumed mantle, and a 40–60 km-wide zone of incipient oceanic crust, characteristic of a magma-poor rifted margin.

In **Chapter 4**, two 200 km-long, seismic reflection profiles from the Camamu-Almada passive margin were structurally restored to understand Cretaceous-Cenozoic passive margin

uplift events previously proposed for this area. Structural restorations showed that original Aptian salt thickness ranged from 1750-3500 m but largely evacuated to the southeast. Passive margin uplift was quantified and compared to far field and mantle causes. Given this more complex passive margin history, 1D basin modeling predicted deep-water potential for oil-generation in preserved synrift lacustrine source rocks.

In **Chapter 5**, AI methods were applied to the structural interpretation of the Camamu rifted passive margin. Observations of evaporites, mini-basins, and salt detachments all supported an evaporitic influence on the post-salt evolution of the passive margin.

TABLE OF CONTENTS

LIST OF TABLES

LIST OF FIGURES

CHAPTER 1: INTRODUCTION TO THIS DISSERTATION

1.1 History and development of this dissertation

I was born in Livorno, Italy and spent my first eight years in the country before emigrating in 2001 to New Jersey, Quebec, and Texas. After arriving in Houston, Texas, in 2009, I obtained a Bachelor of Science degree in geology from the University of Texas at Dallas in 2015 and a Master of Science degree in subsurface geoscience from Rice University in 2017. As a MSc student at Rice, I was a 2017 summer intern in the Underground Injection Control Permits Department of the Texas Commission on Environmental Quality in Austin, Texas, where I was mentored by Lorrie Council and David Murry.

Following completion of my MS degree at Rice in December 2017, I worked as a lead wellsite geologist with Selman and Associates in the Permian basin, Texas, from January to June 2018. I applied and was accepted by Dr. Paul Mann as a graduate research assistant with the Conjugate Basins, Tectonics, and Hydrocarbons (CBTH) project at the University of Houston in May 2018. I also received supplementary salary support as a PhD student for two years (2018-2020) in the form of a University of Houston Presidential Fellowship.

I began my research with the CBTH project in July 2018 with a regional study of Caribbean basins and source rocks, which I presented at the Petroleum Geology of Mexico and the Northern Caribbean conference chaired by Jonathan Hull, Matthew Bowyer, and Ian Davison and convened in London on May 14–16, 2019. After attending the meeting and giving my oral presentation, I was invited to publish the study in a special publication of the Geological Society of London entitled *The Basins, Orogens, and Evolution of the Southern Gulf of Mexico and Northern Caribbean* that was edited by I. Davison, J.N.F. Hull, and J.

Pindell. I submitted my paper to this volume in December 2019, the paper was reviewed by K. Reuber, I. Neill, and J. Pindell, revised by me, and published in May 2020.

As CBTH began to increasingly focus on the Brazilian margin in 2019, I began my second research project concentrated on the Camamu-Almada segment of the northeastern Brazilian rifted-passive margin along with a second CBTH PhD student, Hualing Zhang, who had also entered the CBTH project in the fall of 2018. Hualing's study focused on the Sergipe-Alagoas located 250 km north of my study area. Hualing, Dr. Mann, and myself requested ION deeply-penetrating seismic lines from the Brazilian margin from James Deckelman and Kyle Reuber at ION Geophysical who provided me two, 200 km-long deep-penetration seismic reflection lines for the Camamu-Almada basin that were used in this study Hualing was provided two lines for the Sergipe-Alagoas basin which she used in her PhD study completed in August 2021.

CBTH was also approved as a recipient of data from the Brazilian Agência Nacional do Petróleo, Gás Natural e Biocombustíveis (ANP) to which I applied and received 19,000 line-km of seismic reflection data and 105 well log data for the Camamu-Almada basin. Through the efforts of Dr. Ana Krueger (Bluware and adjunct professor at UH), the Department of Earth and Atmospheric Sciences was approved for an academic donation of the Bluware AI-based software in March 2021. This AI-based software and data analysis became the basis for my study in Chapter 4 entitled: AI-assisted structural interpretation of complex faulting and salt on the shelf and slope of the Camamu basin northeastern Brazil.

In addition to my research, I was a summer intern at TGS in Houston for the summer of 2019 where I worked with James Keay on future investment opportunities in onshore Cretaceous US basins. In the following summer of 2020, my summer internship with

ConocoPhillips was postponed to the summer of 2021. At ConocoPhillips, I was mentored by Craig L. Schneider, Derik W. Kleibacker, and Daniel Favorito, and worked on the structural evolution or the Sarawak basin, offshore Malaysia. Following this internship, I was offered a fulltime position with ConocoPhillips in October 2021, to start in the Spring of 2021 in Midland, TX. At the University of Houston, I also served as the AAPG student chapter ("The Wildcatters") president for the period of September 2020 to May 2021. Under my leadership the student chapter sponsored eight visiting speakers, four workshops, and three social events for students, faculty, and staff.

Throughout my PhD research, I presented my work at local, national, and international Conferences. The personal and online interactions I experienced at these meetings were extremely useful to continuously challenge my conclusions and improve the quality of the research. I thank the CBTH project for providing the financial support for the registration and travel costs to attend these meetings.

Table 1.1 Conference and meeting presentations given throughout PhD

Event name	Title of presentation	Award	Year
CBTH Year-End Meeting	*Determining basement terrane boundaries in the modern Caribbean plate and their impact on regional hydrocarbon systems*		2018
HGS Sheriff Lecture	*Determining basement terrane boundaries in the modern Caribbean plate and their impact on regional hydrocarbon systems*		2018
HGS/EAGE Conference on Latin America: South & Central Petroleum Plays for the Third Millennium	*Caribbean basement terranes: boundaries, sedimentary thickness, subsidence histories, and regional controls on hydrocarbon source rocks, oil seeps, and shows*	2nd place poster	2019
Geological Society of London: Petroleum Potential of the Gulf of Mexico and the northern Caribbean	*Determining basement terrane boundaries in the modern Caribbean plate and their impact on regional hydrocarbon systems*		2019
HGS Sheriff Lecture	*Caribbean basement terranes: Boundaries, depth, and flexure effects on hydrocarbons*	2nd place poster	2019
AGU Fall Meeting	*Caribbean basement terranes: Boundaries, sedimentary thickness, and subsidence histories*		2019
UH Research Day	*Determining basement terrane boundaries in the modern Caribbean plate and their impact on regional hydrocarbon systems*	Scholarship for Outstanding Graduate Work in Geology	2019

CBTH Year-End Meeting	*Tectonic terranes underlying the present-day Caribbean plate: Their tectonic origin, sedimentary thickness, subsidence histories and regional controls on hydrocarbon resources*		2019
GEOGULF	*Cataloguing seven offshore basement terranes of the Caribbean Sea and their linkage history from integration of geophysical datasets, well logs, and dredged seafloor samples*		2019
AAPG South Atlantic Basins Virtual Research Symposium: Offshore Basins of Argentina, Brazil and Uruguay	*Structural restorations of the Camamu-Almada passive margin, northeastern Brazil: timing of movement, anomalous uplift, and thick sedimentation*		2020
HGS-PESGB Africa Conference	*Understanding the sub-salt rifting history of the South Gabon basin through interpretation and modeling of the directly conjugate Camamu and Almada margin, offshore northeastern Brazil*		2020
Southwest Caribbean Basins: Recent Studies and Advances in Understanding the Geology of Colombia, Panama and Venezuela	*Tectonic terranes underlying the present-day Caribbean Plate: their tectonic origin, sedimentary thickness, subsidence histories, and regional controls on hydrocarbon resources*		2020
HGS Sheriff Lecture	*Understanding the sub-salt rifting history of the South Gabon basin through interpretation and modeling of the directly conjugate Camamu and Almada margin, offshore northeastern Brazil*	Honorable mention	2020
CBTH Year-End Meeting	*Testing the composition of the hyper-extended Camamu-Almada basin, northeastern Brazil*		2020
1° Simposio de Geología y del Petróleo UIS	*Tectonic terranes underlying the present-day Caribbean plate: their tectonic origin, sedimentary thickness, subsidence histories and regional controls on hydrocarbon resources*		2020

AGU Fall Meeting	*Structural restoration of the ultrathin, Camamu-Almada rifted-passive margin, northeastern Brazil: Relations between crustal stretching, sedimentation, and uplift*		2020
AAPG/SEG IMAGE	*Cretaceous-Cenozoic structural and magmatic evolution of the Camamu-Almada rifted-passive margin, northeastern Brazil*		2021
UH Student Research Day	*Testing the composition of the hyper-extended Camamu-Almada basin, northeastern Brazil*		
HGS Sheriff Lecture	*AI-assisted structural interpretation of complex faulting and salt on the shelf and slope of the Camamu basin northeastern Brazil.*	3rd place poster	2021
CBTH Year-End Meeting	*Cretaceous-Cenozoic structural and magmatic evolution of the Camamu-Almada rifted-passive margin, northeastern Brazil*		2021
17th International Congress of the Brazilian Geophysical Society & Expogef	*AI-assisted structural interpretation of complex faulting and salt pillows on the shelf and slope of the Camamu basin, northeastern Brazil*		2021

1.2 Rationale, topics, and organization of this dissertation

The purpose of this dissertation was to improve understanding of the effects of large-scale plate movement on both basement morphology and overlying sedimentation. This dissertation includes one chapter in the Caribbean and three chapters offshore northeastern Brazil.

This dissertation addresses these main topics:

Chapter 2: Tectonic terranes underlying the present-day Caribbean plate: their tectonic origin, sedimentary thickness, subsidence histories and regional controls on hydrocarbon resources.

Chapter 3: Crustal structure of the Camamu-Almada margin along the northeastern rift segment of Brazil from an integration of deep-penetration seismic reflection profiles, refraction, and gravity modeling.

Chapter 4: Cretaceous-Cenozoic uplift and erosion events of the Camamu-Almada rifted-passive margin, northeastern Brazil: Their tectonic origin and impact on hydrocarbon potential.

Chapter 5: AI-assisted structural interpretation of complex faulting and salt on the shelf and slope of the Camamu basin, northeastern Brazil.

At the time of submission for this dissertation, Chapter 2 has been published as *Romito, S., and Mann, P., 2020, Tectonic terranes underlying the present-day Caribbean plate: Their tectonic origin, sedimentary thickness, subsidence histories, and regional controls on hydrocarbon resources, in Davison, I., Hull, J., and Pindell, J., eds., The Basins, Orogens, and Evolution of the Southern Gulf of Mexico and Northern Caribbean: Geological Society, Special Publications, London, UK, v. 504, p. 343-377.*

1.2.1 Summary of Chapter 2

Thick sedimentary cover (≤16 km), vintage seismic, and disparate crustal terranes have hindered understanding of the basement underlying the Caribbean plate. The plate formed by Early Cretaceous to Miocene amalgamation of four crustal types: the Caribbean Large Igneous Province oceanic plateau; the Chortis continental block; the related Great Arc of the Caribbean and Siuna/Mesquito Composite Oceanic Terranes island arc blocks; and the Colombian and Venezuelan basin oceanic crust. I characterized each terrane through interpretation of surface geology, 62,000 line-km of 2D seismic reflection data, 366 seismic refraction stations, 47 wells, 74 basement samples, 2D forward modeling, magnetic and gravity anomaly grids, and integration of other studies. Basins overlying island arc crust are small, fault-bounded, and deep, while on continental crust, they are broader and shallower. Strongly flexed oceanic and oceanic plateau crust along amagmatic subduction zones on the southern and northeastern edges of the Caribbean plate produce the largest and deepest sediment filled basins. Areas of proven hydrocarbon source rocks and mapped seeps are associated with continental and island arc terranes in the western Caribbean plate, while organically-rich, but immature, Late Cretaceous source rocks deposited across the more elevated areas of the central and eastern Caribbean plate interior.

1.2.2 Summary of Chapter 3

The Camamu-Almada segment of the northeastern Brazil rifted-passive margin covers an area of 22,000 km^2 and includes: 1) thin to ultra-thin metamorphic continental crust; 2) transitional crust of unknown composition; and 3) Albian and younger oceanic crust. Hypotheses for the disparate, sub-parallel belts or isolated blocks of crust within the 40–110 km-wide transitional zone included: 1) oceanic crust emplaced at a normal spreading ridge; 2) unroofing of lower continental crust along a low-angle detachment fault; 3) exhumation of mantle; and 4) igneous or incipient crust. I investigated the structural-magmatic evolution of the region by interpreting 19,000 line-km of 2D reflection seismic data including two long-offset PSDM transects, 105 offshore well logs, regional magnetic and gravity grids, and 15 seismic refraction stations. Interpretation of these data suggested that the 40–110 rifted zone is structurally complex and composed of at least three discrete crustal blocks: 1) a 10–40 km-wide and 4–6 km-thick zone of hyperextended continental and possibly unroofed lower continental crust with an average density of 2.88 g/cc that detached along a westward and shallowly-dipping (9º) normal fault; 2) 20 km-wide and 4–6 km-thick lenticular zones of exhumed mantle with an average density of 3.1 g/cc; and 3) 40–60 km-wide and 6–8 km-thick incipient oceanic crust that formed in situ. These blocks are comparable in thickness and composition to similar rifted zones described along its conjugate margin in Gabon, west Africa, and consistent with an analogous, magma-poor rifted margin in the western Mediterranean.

1.2.3 Summary of Chapter 4

The 22,000 km^2 Camamu-Almada segment of the 7 km-thick, sedimentary passive margin of northeastern South America underwent several uplift events that affected 113 million years following its rifting from west Africa during the Berriasian-Albian. Previous work based on apatite fission track thermochronology had shown three period of exhumation of this area of northeastern Brazil that began in the Late Cretaceous (80–75 Ma), late Eocene (48–45 Ma), and Miocene to Recent (18–15 Ma). The proposed tectonic mechanisms for these passive margin uplift and erosional events included: 1) episodic changes in the South Atlantic spreading rate; and 2) activity of the Andean orogeny on the western margin of South America. To better constrain the timing, magnitude, and origin of these passive margin uplift and erosion events, I quantitatively restored two, 200 km-long, deep-penetrating Kirchhoff PSDM seismic lines whose crustal structure and tectonic origins were described in Chapter 3 of this dissertation. The main results of this restoration include: 1) estimates of the initial deposition of evaporites up to 1750 m in the Camamu and 3500 m in the Almada. Salt tectonism remained active in the Camamu sub-basin until the Lower Eocene and in the Almada sub-basin until the Miocene, creating large salt-withdrawal mini-basins and laterally extensive salt welds; and 2) recognition of five major uplift periods throughout the late-rift and post-rift of the basin in the Early Cretaceous, Late Cretaceous, Eocene, Paleocene, and Miocene to Recent. Salt deflation was quickest during periods of intense uplift in the Cretaceous and Eocene, and salt exerted a first-order control on much of the overlying structures. A new potential mantle-induced cause is described for this anomalous uplift, as evidenced by the concurrent, and nearby, Poxoreu Igneous Province, Abrolhos Magmatic Province, and Trindade volcanic chain.

1.2.4 Summary of Chapter 5

As the Atlantic Ocean rifted from south to north during the Early Cretaceous, the Camamu sub-basin in northeastern Brazil underwent an oblique, northwest-to-southeast opening that led to a complex rifting history. The basin presently covers 12,000 km^2 and is bounded to the north by the Jacuípe and Recôncavo basins and to the south by the Almada sub-basin. The Camamu sub-basin preserved pre-rift, syn-rift, and post-rift sequences, and had been interpreted as the northern limit of Aptian salt. I mapped fault planes and salt bodies on the shelf and slope of the Camamu by applying supervised learning and AI-assisted interpretation methodologies to a 1,400 km^2 3D survey. My workflow included: 1) labeling key geologic features and interactively training an AI neural network; 2) fully interpreting select inlines and crosslines; and 3) creating a final 3D model of inferred fault planes and salt bodies. Results show that shallow, post-rift normal faults dip offshore, are listric, and sole out along two salt welds. Deeper faults within syn-rift, pre-rift, and basement rock are also listric normal faults but sole out across a mid-crustal detachment at a depth of 6.5 seconds two-way time. Today, salt occurs as isolated pillows, welds, and small diapirs, but I infer that the original Aptian evaporite body was much thicker following deposition and deflated under the shelf and slope through post-rift sedimentation, similar to the southern Almada sub-basin.

CHAPTER 2: TECTONIC TERRANES UNDERLYING THE PRESENT-DAY CARIBBEAN PLATE: THEIR TECTONIC ORIGIN, SEDIMENTARY THICKNESS, SUBSIDENCE HISTORIES AND REGIONAL CONTROLS ON HYDROCARBON RESOURCES

A version of the following chapter has been published in: *Romito, S., and Mann, P., 2020, Tectonic terranes underlying the present-day Caribbean plate: Their tectonic origin, sedimentary thickness, subsidence histories, and regional controls on hydrocarbon resources, in Davison, I., Hull, J., and Pindell, J., eds., The Basins, Orogens, and Evolution of the Southern Gulf of Mexico and Northern Caribbean, Geological Society, London, Special Publication 504, p. 343-377, doi:10.1144/SP504-2019-221*

2.1 Introduction

The present-day Caribbean plate is a complex region of contractional, strike-slip and extensional deformation that includes magmatic to amagmatic subduction along its plate margins, strike-slip motion along the northern and southern boundaries, and a 110 km-long spreading ridge, the Mid-Cayman Spreading Centre, embedded within its northern margin (Rosencrantz et al., 1988; Draper et al., 1994; Rogers et al., 2007a, 2007b). Major morphological features of the Caribbean plate boundaries and its interior were created by collision and subduction processes, which began in the Early Cretaceous with the collision and deformation of the northern Caribbean plate and the North American craton. The sole continental terrane within the Caribbean, the Precambrian/Paleozoic Chortis block, detached in the Late Cretaceous from the southern edge of what is present-day Mexico and later incorporated into the western part of the proto-Caribbean plate (Draper et al., 1994; Rogers et al., 2007a, 2007b; Pindell and Kennan, 2009). South of the Chortis block in the present-day plate, the Late Cretaceous Caribbean Large Igneous Province (CLIP) formed above a mantle plume in the eastern Pacific (Pindell and Kennan, 2009; Boschman et al., 2019). Multiple emplacement events created this 8–20 km-thick, relatively stable, central nucleus of the Caribbean plate (Edgar et al., 1971; Burke, 1988; Kerr et al., 1999; Pindell and Kennan, 2009; Escuder-Viruete et al., 2016; Dürkefälden et al., 2019a, 2019b) (Figure 2.1). As substrate to the CLIP and emerging within parts of the Colombian and Venezuelan basins, Early Cretaceous oceanic crust underlay thick sedimentation from the northern margin of South America (Ghosh, 1990; Diebold and Driscoll, 1999; Kroehler et al., 2011; Frost, 2018). Encircling the oceanic and oceanic plateau core, the Siuna/Mesquito Composite Oceanic Terranes (MCOT) and the Great Arc of the Caribbean (GAC) formed through Triassic to Recent intra-oceanic island arc collision and subduction-related accretion (Larue and Warner, 1991; Draper et al., 1994; Buchs et al., 2010; Escuder-Viruete et al., 2013; Flores et al., 2015; Lidiak and Anderson, 2015; Andjić et al., 2019b).

I applied the term ‘terrane’ to describe the four fundamentally different Caribbean basement areas that are covered by the 0–6 km-deep marine waters of the Caribbean Sea (Figure 2.1). I used the term ‘terrane’ according to the definition by Howell (1985, p. 119) as ‘a crustal block, not necessarily of uniform composition…whose history is distinct from the histories of adjoining terranes’.

Boundaries between these terranes are generally abrupt, steeply-dipping faults with an active strike-slip component (Carvajal-Arenas et al., 2015; Sanchez et al., 2019). These juxtaposed basement types of differing geological histories commonly contain coeval strata, making all terranes ‘suspect’ until their relationship to adjacent blocks was established in detail. It was, therefore, useful to classify each terrane according to their crustal type: continental, island arc, oceanic plateau and oceanic.

Researchers have attempted to determine the type and areal extent of the Caribbean basement terranes (Arden, 1975; Bowland and Rosencrantz, 1988; Rogers et al., 2007a; Baumgartner et al., 2008; Blanco et al., 2015; Andjić et al., 2019a; Gómez-García et al., 2019) along with characterization of the top basement surface, basement lithologies and ages, and origin of its intra-basement, seismic reflectors (Diebold et al., 1981; Bowland, 1993; Kroehler et al., 2011; Ott, 2015; Carvajal-Arenas, 2017; Sanchez et al., 2019). Most of these detailed geophysical and drilling studies were restricted to limited geographic areas of the Caribbean and did not reach the scope necessary for plate-scale interpretations.

In this study, I used both vintage and recent seismic reflection and refraction surveys (Figure 2.2) and regional magnetic and gravity anomaly grids (Figure 2.3 and 2.4) to characterize the mainly coeval, and largely submarine, Caribbean basement terranes (Figure 2.5). The assembled data grid covered large areas of the Caribbean plate margins and its more stable interior; in areas of sparse data coverage, I incorporated published interpretations (Figure 2.2). Where poor seismic reflection imaging, thick sedimentary successions, or both, hampered seismic interpretation, I created 2D gravity and magnetic forward models using key seismic reflection lines and seismic refraction control to constrain the top of the magnetic/crystalline basement.

Results of this study included more precise locations of Caribbean terrane boundaries, improved depth estimates to the top of the magnetic basement, and an improved plate-wide map of the total sedimentary thickness of basinal areas that overlie the various tectonic terranes. To explain the patterns of broadscale basement topography within the Caribbean plate interior, I characterized the importance of Cenozoic lithospheric flexure related to the south-dipping subduction of the Caribbean plate beneath the South Caribbean Deformed Belt (SCDB) and the north dipping subduction of the Caribbean plate beneath the Muertos trench and the eastern Greater Antilles. I also compiled industry and academic wells and compared long-term subsidence trends of the various terrane types. Finally, I correlated the plate-wide maps of terrane boundaries and total sedimentary thicknesses to areas of known hydrocarbon source rocks and seeps and identified areas of future exploration interest.

2.1.1 Current models for Caribbean plate evolution

An eastern Pacific origin and subsequent translation of the Caribbean plate into its present-day geographical position between South and North America (Pindell, 1990; Pindell et al., 2006) was supported by multiple datasets that included: 1) outcrop mapping (Gose, 1983; Gordon and Muehlberger, 1994; Hauff et al., 2000; Mitchell, 2003; Buchs et al., 2010); 2) palaeomagnetic data (Boschman et al., 2019; Molina-Garza et al., 2019); 3) 2D seismic reflection interpretation of offshore basins (Bowland, 1993; Driscoll and Diebold, 1998; Kroehler et al., 2011; Escalona and Mann, 2011); 4) recent analysis of deep-penetration 2D seismic reflection surveys (Sanchez et al., 2016; Carvajal-Arenas and Mann, 2018); and 5) academic, deep-sea drilling from the Deep Sea Drilling Project (DSDP) and Ocean Drilling Program (ODP) (Donnelly et al., 1973; Holcombe et al., 1990).

The Pacific origin model for the Caribbean began with three major tectonic stages: 1) Pangaea rifted apart from 210 to 140 Ma, initiating oceanic crust emplacement in the Northern Atlantic/Proto-Caribbean Seaway and separating the North American and South

American–African (Western Gondwana) plates (Mann et al., 2006; Pindell and Kennan, 2009); 2) Late Jurassic counterclockwise rotation of the Yucatan block accompanied formation of oceanic crust in the central Gulf of Mexico (Pindell and Kennan, 2009); and 3) seafloor spreading during Jurassic and Cretaceous times expanded the proto-Caribbean oceanic seaway between North and South America to allow the later entry of island arc and continental terranes (Pindell and Dewey, 1982; Mann et al. 2006; Pindell and Kennan, 2009) (Figure 2.1a).

Formation of the Siuna/MCOT/GAC terrane began approximately 140–90 Ma along multiple subduction zones that fringed the Farallon and proto-Caribbean plates (Escuder-Viruete et al., 2013; Andjić et al., 2019b) (Figure 2.1a). In the Late Cretaceous, the main body of the CLIP likely formed above a mantle plume that intruded and erupted onto Farallon oceanic crust inferred to be of Early Cretaceous age (Ghosh, 1990; Kerr et al., 1998; Pindell and Kennan, 2009; Buchs et al., 2018; Boschman et al., 2019). Results from dredging, drilling, and outcrop sampling from different areas of the CLIP showed at least three distinct pulses of eruptive activity: 1) a localized Albian (112 Ma) eruptive event (Lapierre et al., 2000; Escuder-Viruete et al., 2007); 2) a Cenomanian–Santonian (94–83 Ma) pulse that formed the bulk of the CLIP (Kerr et al., 1997; Sinton et al., 1998; Hastie et al., 2008, 2009); and 3) a youngest, localized, eruptive phase during the Campanian–Maastrichtian (80–68 Ma) (Révillon et al., 2000; Sandoval et al., 2015). These three eruptive events have not been definitively mapped over the entire plateau, but several other lines of evidence supported that multi-stage CLIP evolution was regional in scale: 1) variable CLIP crustal thicknesses ranging from 8 to 20 km (Ewing et al., 1960; Corbeau et al., 2017); 2) large differences in basement acoustic character of the CLIP (Figure 2.6–2.8); and 3) widespread presence of

Figure 2.1 Plate evolution reconstruction of the Caribbean, modified from Gomez (2018). **a)** At 112 Ma, multiple arc systems that will eventually coalesce to form the GAC in the Late Cretaceous marked the subduction zones along the margins of the Farallon/Caribbean, the Mackinley, the Mezcalera, and the proto-Caribbean seaway. Eastward motion of these arc systems consumed areas of the proto-Pacific Ocean. **b)** At 90 Ma, the newly erupted Caribbean Large Igneous Province (CLIP) translated eastwards along with the Farallon plate and caused the arc systems to collide, coalesce, and form a continuous GAC system. **c)** By 75 Ma, the Chortis continental block, Siuna/MCOT island arcs, CLIP oceanic plateau, and GAC island arcs accreted to form the stable core of the proto-Caribbean plate, and the GAC became more arcuate as the plate moved northeastwards to consume areas of the proto-Caribbean seaway. **d)** During the period of 65–38 Ma, the collision of the northeastward-migrating proto-Caribbean plate with the thickened crust and lithosphere beneath the Bahamas carbonate platform reoriented the plate into a more eastward direction and initiated the east–west trending Cayman Trough pull-apart basin along the Caribbean plate’s northwestern strike-slip boundary; the east-facing Lesser Antilles volcanic arc formed the leading edge of the Caribbean plate and subducted oceanic crust of the proto-Caribbean Sea and the west-central Atlantic Ocean. **e)** From 38 to 6 Ma, south to southeastward amagmatic subduction of oceanic and oceanic plateau crust of the southern Caribbean plate occurred beneath northern South America and formed the SCDB as an accretionary prism.

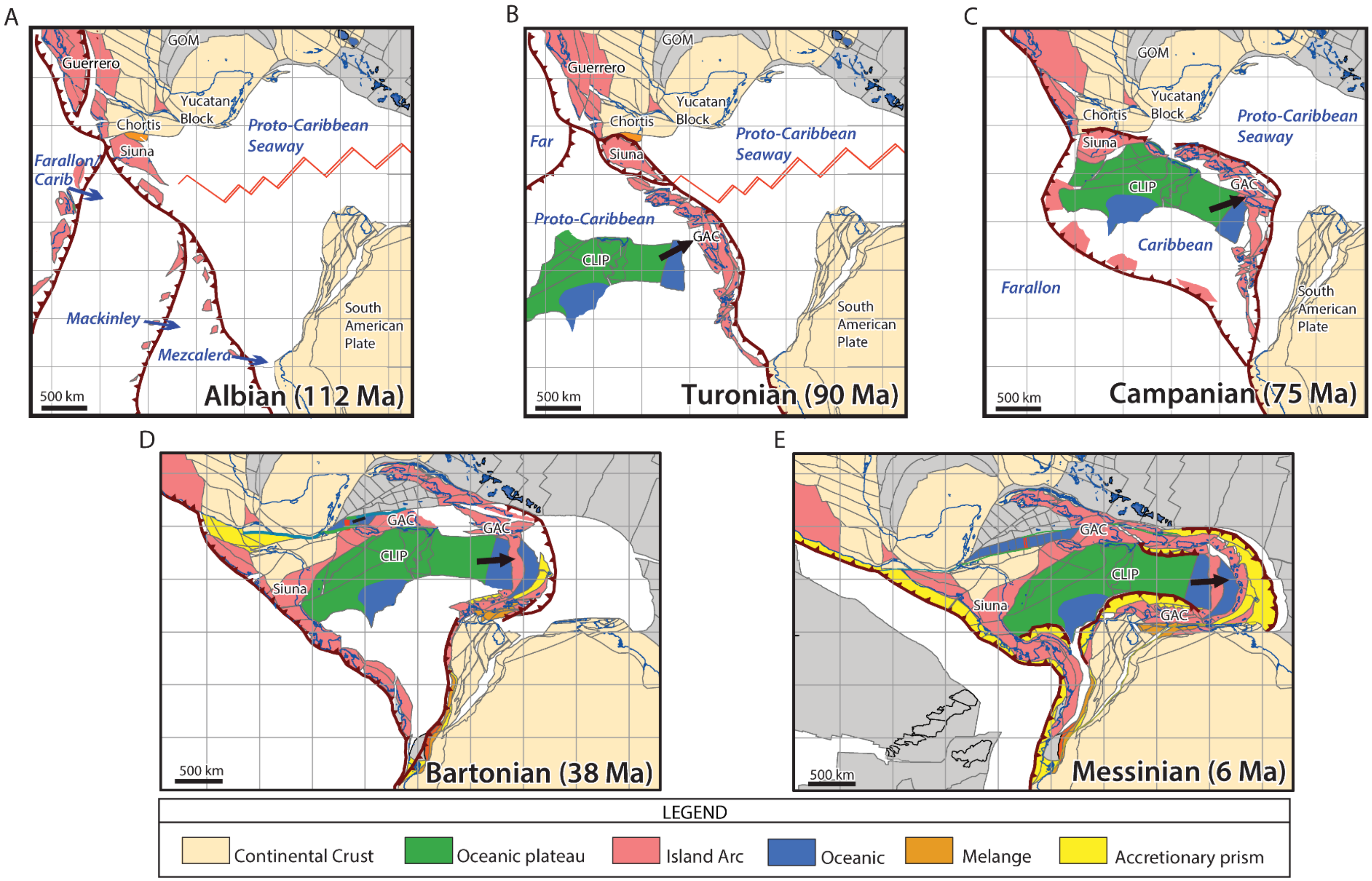
A
Albian (112 Ma)
Guerrero
GOM
Yucatan Block
Chortis
Siuna
Proto-Caribbean Seaway
Farallon/ Carib
Mackinley
Mezcalera
South American Plate
500 km
B
Turonian (90 Ma)
Guerrero
GOM
Yucatan Block
Chortis
Siuna
Far
Proto-Caribbean Seaway
Proto-Caribbean
CLIP
GAC
South American Plate
500 km
C
Campanian (75 Ma)
GOM
Yucatan Block
Chortis
Siuna
Proto-Caribbean Seaway
CLIP
GAC
Caribbean
Farallon
South American Plate
500 km
D
Bartonian (38 Ma)
GAC
GAC
CLIP
Siuna
500 km
E
Messinian (6 Ma)
GAC
CLIP
Siuna
GAC
500 km
LEGEND
Continental Crust
Oceanic plateau
Island Arc
Oceanic
Melange
Accretionary prism

volcanic seamounts that were created during the youngest event and are now found across the Beata Ridge and the Lower Nicaraguan Rise (Carvajal-Arenas, 2017) (Figure 2.6).

During the late Cretaceous, the Chortis block translated from west to east along the southern continental margin of Mexico (Schaff et al., 1995; Pindell and Kennan, 2009) and collided with the Siuna/MCOT island arc terrane (Venable, 1994; Rogers et al., 2007a, 2007b; Sanchez et al., 2016; Lewis et al., 2011) (Figure 2.1b–c). The Chortis block continued to rotate counterclockwise into its current position within the northwestern Caribbean plate (Rosencrantz et al., 1988; Donnelly et al., 1990; Mann et al., 2006; Molina-Garza et al., 2019). Eastward translation of the CLIP from 80 to 75 Ma across the eastern Pacific Ocean led to the collision of multiple island arc chains and coalescence into a single GAC system (Escuder-Viruete et al., 2013; Andjić et al., 2019b) that collided with northern Central America and the northwestern margin of South America (Pindell et al., 1988; Mann et al., 2006; Pindell and Kennan, 2009) (Figure 2.1b–c). The now amalgamated CLIP, Chortis, and Siuna/MCOT/GAC rotated counterclockwise, translated northeastward, and continued to subduct oceanic proto-Caribbean seaway crust (Burke, 1988; Pindell et al., 1988; Kerr et al., 2003; Hastie and Kerr, 2010). Generation of subduction-related melts continued along the GAC and recorded this southwestward subduction (Fox and Heezen, 1985; Pinet et al., 1985; Bouysse, 1988; Aitken et al., 2011; Neill et al., 2011).

The collision of the GAC with thickened crust and lithosphere beneath the Bahamas carbonate platform in the northeastern Caribbean reoriented plate motion from northeastward to eastward during the Paleocene and Eocene (Pindell and Dewey, 1982; Mann et al., 1995) (Figure 2.1d–e). This change in direction initiated the Cayman Trough, which evolved from an oblique pull-apart basin extending arc and continental crust into a short, 110 km-long oceanic spreading center that opened at rates ranging from 7.5 to 15 mm/yr. (Rosencrantz et al., 1988; Leroy et al., 2000). Paleocene to Miocene arc migration of the volcanic axis of the GAC led to the abandonment of the Aves Ridge as a remnant arc, the opening of the Grenada and Tobago basins, and the initiation of magmatism along the Lesser Antilles (Aitken et al., 2011; Neill et al., 2013; Allen et al., 2019) (Figure 2.1e).

Progressive, west-to-east arc-continent collision from the Paleogene to the Neogene led to the emplacement of allochthonous GAC fragments and ophiolites along the edges of both the North and South American continents (Dewey and Pindell, 1986; Burke, 1988; Pindell et al., 1988; Snoke and Noble, 2001) (Figure 2.1d–e)

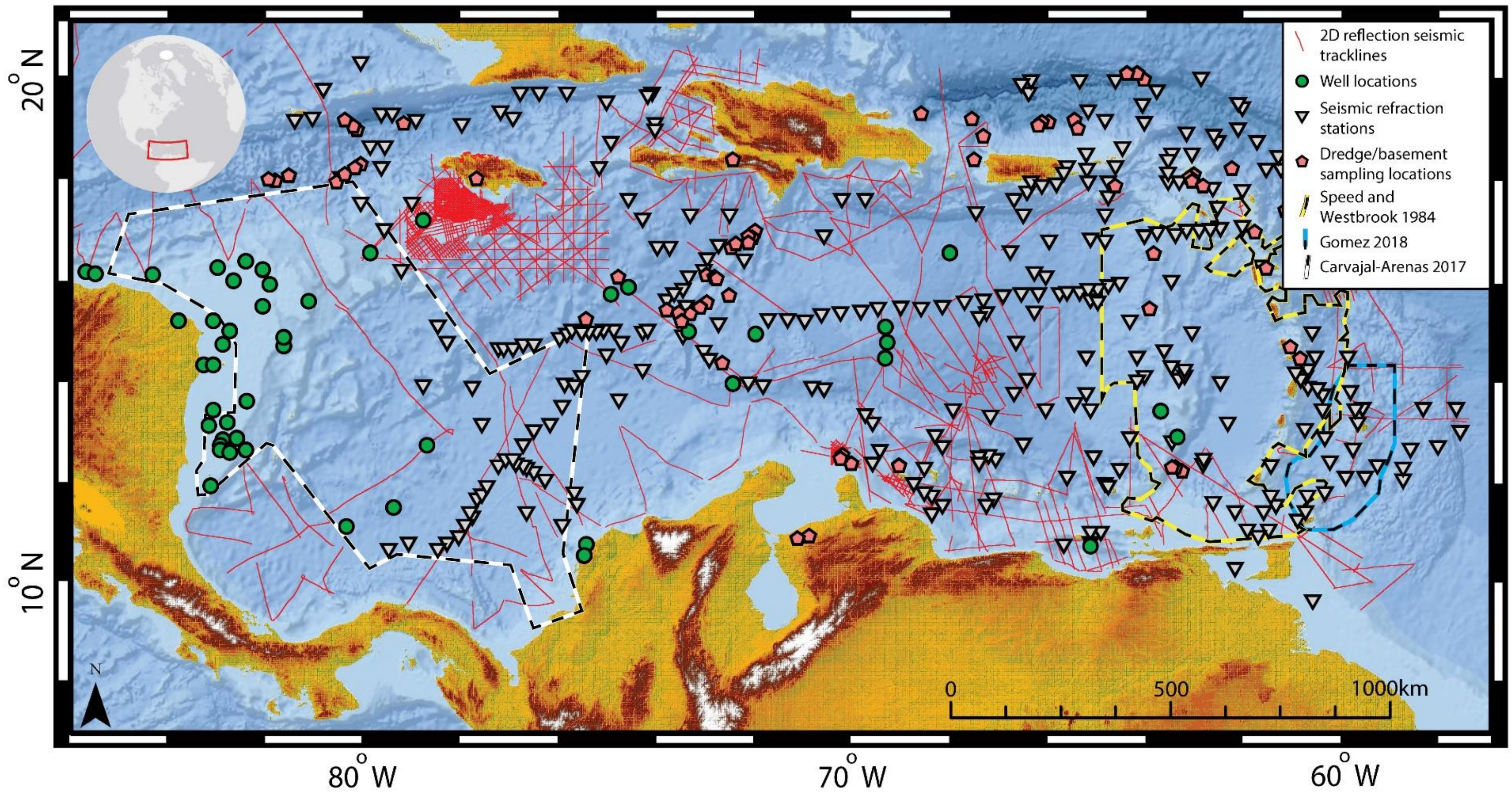

Figure 2.2 Map of seafloor bathymetry of the Caribbean Sea (Weatherall et al., 2015) and the surrounding surface topography (Amante and Eakins, 2009) with inset map showing the extent. Red lines show locations of 2D seismic reflection lines; green circles are well locations; pink pentagons show locations of basement samples from dredges or wells; inverted grey triangles are seismic refraction stations I used for this study. Dashed polygons show locations of published work compiled for this study: study area of Carvajal-Arenas (2017) in the white and black polygon; study area of Speed and Westbrook (1984) in the yellow and black polygon; and study area of Gomez (2018) in the blue and black polygon.

2.2 Data and methodology

Time-migrated seismic reflection data for this study of the Caribbean plate (Figure 2.2, Table 2.1) included vintage seismic surveys acquired in 1983 and reprocessed by Spectrum Geo in 2007, and various vintage seismic surveys acquired by: 1) the Gulf Oil Company in 1975; 2) the University of Texas at Austin's Institute for Geophysics and Rice University (BOLIVAR project) between the 1970s and early 2000s (Watkins et al., 1975; Talwani et al., 1976; Ladd et al., 1977, 1981; Diebold et al., 1981; Lu and McMillen, 1982; Bowland, 1984; Westbrook et al., 1988; Rosencrantz, 1990; Mann et al., 1995; Diebold and Driscoll, 1999; Bangs et al., 2003; Aitken, 2005); and 3) industry in the late 1970s and early 1980s, later catalogued by the United States Geological Survey (USGS) (Triezenberg et al., 2016).

I included two industry depth-migrated seismic reflection surveys reprocessed by Spectrum Geo in 2010 and 2015, respectively: the first acquired in 2006 by the vessel Akademik Shatskiy with a streamer length of 7950 m and a shot interval of 25 m; the second acquired by the MV Discoverer in 2009 with a streamer length of 9450 m and a shot interval of 25 m (Table 2.1). Other data incorporated into my study included: 1) 47 academic and industry exploration wells (Bader, 1970; Edgar et al., 1973; Cann et al., 1983; Sigurdsson et al., 1997; Carvajal-Arenas, 2017) (Figure 2.2, Table 2.2); 2) 366 reversed and unreversed seismic refraction stations (Officer et al., 1952, 1959; Ewing and Worzel, 1954; Ewing et al., 1957, 1960; Edgar et al., 1971; Kearey, 1974; Ludwig et al., 1975; Westbrook, 1975; Houtz and Ludwig, 1977; Boynton et al., 1979; Diebold et al., 1981; Case et al., 1990) (Figure 2.2, Table 2.3); 3) 74 dredges and other basement samples (Fox et al., 1970, 1971; Ramos, 1975; Uchupi, 1975; Nagle et al., 1976; Perfit, 1977; Perfit et al., 1980; Bouysse et al., 1985; Sen et al., 1988; Curet, 1992; Sigurdsson et al., 1997; Dürkefälden et al., 2019a, 2019b) (Figure 2.2); 4) regional magnetic and gravity anomaly grids (Bankey et al., 2002; Sandwell et al., 2014; Meyer et al., 2017) (Figure 2.3); and 5) regional time-maps of top basement from other work where my compilation of seismic data was lacking within the Lesser Antilles (Speed and Westbrook, 1984; Gomez, 2018) and western areas of the Nicaraguan Rise (Carvajal-Arenas, 2017) (Figure 2.2).

Initial Caribbean terrane characterization included interpretation of gravity and magnetic anomalies (Figure 2.3) and the total horizontal derivative of the 5 km-upward-continued Bouguer gravity anomaly (Figure 2.4). To create this derivative surface, I performed a standard Bouguer terrain correction using the Cryosat gravity anomaly grid (Sandwell et al., 2014) and applied an upward-continuation of 5 km to remove near-surface effects. Within the MAGMAP module of Geosoft® Oasis Montaj, I calculated the grid's total horizontal derivative using the following formula from Cooper and Cowan (2008):

$$\text{Equation 2.1: Total Horizontal Derivative} = \sqrt{(\frac{\partial G}{\partial x})^2 + (\frac{\partial G}{\partial y})^2}$$

where G is the gravity anomaly, and x and y denote the horizontal direction of the first derivatives. I further refined the terrane boundaries I inferred from gravity and magnetic methods with seismic interpretation, well log reports, and dredged samples from seafloor areas of the exposed submarine basement (Figure 2.5–2.8).

	Jamaica 2015	*Jamaica 2010*	*Jamaica 2007*	*EW0404*	*EW9501*	*EW9803*	*RC2604*	*W-8-82-CB*	*FM0502*	*W-1-79-CB*	*W-3-79-CB*
Vessel	MV Discoverer	Akademik Shatskiy	Various	R/V Maurice Ewing	R/V Maurice Ewing	R/V Maurice Ewing	R/V Robert Conrad	N/A	R/V Fred Moore	N/A	N/A
Vintage	2009, reproc. 2015	2006, reproc. 2010	1983, reproc. 2007	2004	1995	1998	1985	1982	1980	1979	1979
Source	Air gun array	Air gun array	Various	20 air gun array	20 air gun array	20 air gun array	4 air gun array	Air gun array	4 air gun array	Air gun array	Air gun array
Streamer	25 m spacing	25m spacing	Various	480 channels at 12.5 m spacing	160 channels at 25 m spacing	164 channels at 100m spacing	48 channels at 50 m spacing	N/A	48 channels at 70 m spacing	N/A	N/A
Record Length	10	9	Various	10–14	9–13	13	14–15	4–8	6–10	4–8	4–8
Depth Units	PSDM (depth)	PSDM (depth)	PSTM (time)	Time	Time	Time	Time	Time	Time	Time	Time
Archived	Spectrum Geo	Spectrum Geo	Spectrum Geo	UTIG	UTIG	UTIG	UTIG	USGS	UTIG	USGS	USGS

Table 2.1 Summary of acquisition parameters for reflection seismic data sets

FM0107	*IG2901*	*IG2904*	*IG2401*	*IG2408*	*RC2103*	*IG1503*	*IG1504*	*IG1505*	*IG1506*	*RC1904*	*GULFREX*
R/V Fred Moore	R/V Ida Green	R/V Ida Green	R/V Ida Green	R/V Ida Green	R/V Robert Conrad	R/V Ida Green	R/V Ida Green	R/V Ida Green	R/V Ida Green	R/V Robert Conrad	N/A
1979	1978	1978	1977	1977	1977	1975	1975	1975	1975	1975	1974
3 air gun array	3 air gun array	4 air gun array	2 air gun array	4 air gun array	4 air gun array	3 air gun array	1–2 air gun array	4 air gun array	3 air gun array	4 air gun array	Air gun array
24 channels	24 channels	24 channels	24 channels	24 channels	24 channels at 100 m spacing	24 channels	24 channels	24 channels	24 channels	24 channels at 100 m spacing	N/A
9–10	4–11	6–12	9–10	6–10	12	8–12	6–8	3–5	9–10	11–12	8
Time	Time	Time	Time	Time	Time	Time	Time	Time	Time	Time	Time
UTIG	UTIG	UTIG	UTIG	UTIG	UTIG	UTIG	UTIG	UTIG	UTIG	UTIG	UTIG

Table 2.1 continued

I created three 2D forward gravity and magnetic models along representative seismic lines to constrain basement depth where sedimentary lithology and thicknesses (Figure 2.9b) and/or vintage seismic with lower depth penetration (Figure 2.9c–d) prevented sufficient resolution to image the top basement surface accurately. I used the GM-SYS module within Geosoft® Oasis Montaj to develop cross-sections across the models. GM-SYS assumes each structural block extends infinitely perpendicular and ± 30 000 km along the profile to reduce or eliminate edge-effects. I constrained block velocity and density from seismic refraction station measurements and available well log information (Tables 2.2 and 2.3). Magnetic susceptibility averages for each terrane were compiled from Arden (1975) and Sanchez et al. (2019) (Figure 2.9a). 2D seismic reflection data, seismic refraction profiles, well logs, and terrane contacts constrained iterative modifications to the crustal model until achieving an optimal result, defined as a close fit between the calculated and observed anomalies. Total error tolerated between modeled and observed gravity and magnetic anomalies, respectively, was ±10 mGal and ±20 nT. I used the NAmag regional grid (1 km resolution, Bankey et al., 2002) as the observed magnetic control for models 2 and 3 (Figure 2.9c–d), and EMAG2v3 (2-arc-minute resolution, Meyer et al., 2017) as the control for model 1 (Figure 2.9b). Gravity control relied on the Cryosat gravity anomaly grid (Sandwell et al., 2014). Figure 2.10–2.12 compare these results with their colinear seismic lines. I then extrapolated the resultant crustal structure to adjacent datasets and included other interpretations where data coverage was sparse (Speed and Westbrook, 1984; Carvajal-Arenas, 2017; Gomez, 2018). I combined all the above data types to generate a plate-wide time-to-basement map (Figure 2.13a).

To depth-convert this surface, I created an interval velocity cube of 50 ms slices, from 0 to 18 s, with all available velocity information throughout the Caribbean Sea. I converted 14 sonic logs, 12 from the Nicaraguan Rise and two from the Magdalena fan in the Colombian basin, and 366 seismic refraction velocities to interval velocities. I integrated these velocities to create the final velocity cube within CGG® VelPro software (Figure 2.2; Tables 2.2 and 2.3), depth-converted the final time surface (Figure 2.13b), and then subtracted the depth surface from the seafloor to generate a total sedimentary thickness map (Figure 2.13c).

Well name	Latitude	Longitude	TD (m)	Operator	Status	Terrane
Atlantico-1	13.17	82.795	3232	Shell	Dry hole with gas show	Island arc; Siuna/MCOT/GAC
Berta-1	16.2208	82.0758	2265	Colombia	Dry hole	Continental; Chortis
Caribe-1	16.4	82.4388	3065	Pecten/Chevron	Dry hole	Continental; Chortis
Caribe-2	16.2617	83.0226	3449	Pecten/Chevron	Dry hole	Continental; Chortis
Caribe-3	16.0142	82.6737	2813	Pecten/Chevron	Dry hole	Continental; Chortis
Cartagena-2	3.2101	67.8553	3762	Texas	Gas show	Island arc; Siuna/MCOT/GAC
Cartagena-3	3.1919	68.0614	4810	Amoco-Ecopetrol	Gas show	Island arc; Siuna/MCOT/GAC
Castana-1	16.16	85.5472	4000	Texaco/Amerada	Dry hole	Continental; Chortis
Castilla-1	16.1961	85.6982	3708	Texaco/Amerada	Dry hole	Continental; Chortis
Centeno-1	11.929	83.162	Unknown	Texaco	Dry hole	Island arc; Siuna/MCOT/GAC
Coco Marina-1	15	82.725	3047	Unocal	Gas show	Island arc; Siuna/MCOT/GAC
Diamante-1	15.9408	81.9328	2498	Mobil	Dry hole	Continental; Chortis
DSDP 146/149	15.117	69.378	4711	DSDP	Dry hole	Oceanic plateau; CLIP
DSDP 147	10.708	65.175	1081	DSDP	Dry hole	Continental; Chortis
DSDP 148	13.419	63.721	1504	DSDP	Dry hole	Island arc; Siuna/MCOT/GAC
DSDP 150	14.511	69.356	4725	DSDP	Dry hole	Oceanic plateau; CLIP
DSDP 151	15.017	73.41	2410	DSDP	Dry hole	Oceanic plateau; CLIP
DSDP 152	15.879	74.608	4376	DSDP	Dry hole	Oceanic plateau; CLIP
DSDP 153	13.972	72.435	4708	DSDP	Dry hole	Oceanic plateau; CLIP
DSDP 154	11.085	80.379	3616	DSDP	Dry hole	Oceanic plateau; CLIP
DSDP 29	14.785	69.323	3050	DSDP	Dry hole	Oceanic plateau; CLIP
DSDP 30	12.882	63.383	1651	DSDP	Dry hole	Island arc; Siuna/MCOT/GAC
DSDP 31	14.943	72.027	3674	DSDP	Dry hole	Oceanic plateau; CLIP
DSDP 502	11.49	79.38	3266	DSDP	Dry hole	Oceanic plateau; CLIP
Gorda Bank-1	15.5002	82.0564	1971	Unocal	Dry hole	Island arc; Siuna/MCOT/GAC
Ledacura-1	14.79	82.8948	3792	Unocal	Oil and gas show	Island arc; Siuna/MCOT/GAC
Main Cape-1	15.2511	83.0919	3475	Unocal	Oil and gas show	Continental; Chortis
Miskito-1	14.8733	81.6867	2050	Signal/Occidental	Oil and gas show	Island arc; Siuna/MCOT/GAC
Miskito-2	14.733	81.6638	1967	Western/Occidental	Dry hole	Island arc; Siuna/MCOT/GAC
Mosquitia-1	15.2017	83.83	4263	Pure	Dry hole	Continental; Chortis
Nica-1	12.609	82.726	Unknown	Mobil	Dry hole	Island arc; Siuna/MCOT/GAC
ODP 1000	1000	79.867	1610.9	ODP	Dry hole	Continental; Chortis
ODP 1001	1001	74.91	3781.8	ODP	Dry hole	Oceanic plateau; CLIP
ODP 1002	1002	65.17	1074	ODP	Dry hole	Continental; Chortis
Pedro Bank 1	16.946	78.791	1978	Occidental	Dry hole	Island arc; Siuna/MCOT/GAC
Perlas-1	12.815	82.918	Unknown	Shell	Plugged oil	Island arc; Siuna/MCOT/GAC
Perlas-2	12.757	82.976	Unknown	Shell	Dry hole	Island arc; Siuna/MCOT/GAC
Perlas-3	12.654	82.963	Unknown	Shell	Dry hole	Island arc; Siuna/MCOT/GAC
Prinzapolka-1	13.4317	83.1067	2251	Chevron	Gas show	Island arc; Siuna/MCOT/GAC
Punta Patuca-1	16.1235	84.3301	3132	Esso	Dry hole	Continental; Chortis
Rama-1	13.1383	83.2117	2179	Shell	Dry hole	Island arc; Siuna/MCOT/GAC
Tinkham-1	13.6383	82.4331	1971	Mobil	Gas show	Island arc; Siuna/MCOT/GAC
Toro Cay-1	14.3367	83.115	2265	Mobil	Gas show	Island arc; Siuna/MCOT/GAC
Turquesa-1	15.6413	81.1462	2039	Mobil	Dry hole	Island arc; Siuna/MCOT/GAC
Twara-1	14.3417	83.2917	1910	American	Gas show	Island arc; Siuna/MCOT/GAC
Tyra-1	12.9083	82.6383	2623	Mobil	Dry hole	Island arc; Siuna/MCOT/GAC

Table 2.2 Caribbean wells used within this study

2.3 Results

2.3.1 Four major terranes underlie most of the Caribbean plate

I subdivided the present-day area of the Caribbean plate into four major terranes based on their distinctive seismic reflection basement character, crustal thickness variations and velocities, geometry of their overlying basins, and gravity/magnetic anomaly signal. These four terranes include: 1) the Chortis continental terrane of northern Central America and extending eastward and offshore beneath the Upper Nicaraguan Rise (Arden, 1975; Draper et al., 1994; Rogers et al., 2007a, 2007b; Sanchez et al., 2016, 2019); 2) the Siuna/MCOT/GAC island arc terrane underlying elongate areas of the Upper Nicaraguan Rise and along the Antilles island chains, the SCDB, and the Aves Ridge (Arden, 1975; Brown and Westbrook, 1987; Larue and Warner, 1991; Baumgartner et al., 2008; Lewis et al., 2011; Flores et al., 2015; Ott, 2015; Andjić et al., 2019a, 2019b; Sanchez et al., 2019); 3) the CLIP within the central core of the Caribbean plate, underlying the Lower Nicaraguan Rise and the Venezuelan, Colombian, and Haitian basins (Diebold et al., 1981; Stoffa et al., 1981; Diebold and Driscoll, 1999; Sanchez et al., 2019); and 4) poorly studied oceanic crust within the Venezuelan and Colombian basins (Stoffa et al., 1981; Ghosh, 1990; Diebold and Driscoll, 1999; Kroehler et al., 2011; Carvajal-Arenas, 2017; Sanchez et al., 2019). Workers have recognized other areas of oceanic crust within the Cayman Trough (Rosencrantz and Sclater, 1986; Leroy et al., 1996) and the Grenada basin (Pinet et al., 1985; Holcombe et al., 1990; Bird et al., 1993, 1999; Gomez et al., 2018). In the following subsections, I summarized the main basement characteristics for each of these four terranes.

Figure 2.3 a) Satellite-derived free-air gravity (Sandwell et al. 2014) showing high-positive, free-air anomalies that are characteristic of the elongate Great Arc of the Caribbean terrane that underlies a large area of the Greater, Lesser, and Leeward Antilles. Negative and elongate free-air gravity lows mark subduction zones along the SCDB, the Muertos trench, the North Panama Deformed Belt (NPDB), and the Lesser Antilles subduction zone. **b)** Caribbean magnetic anomaly map from NAmag magnetic compilation from Bankey et al. (2002); characteristic magnetic anomalies are not directly correlatable to the proposed Caribbean basement types, but the wavelengths of the anomalies do indicate relative depth variations to basement magnetic sources. For example, longer wavelength anomalies in the Colombian and Venezuelan basins suggest a more deeply buried oceanic and CLIP substrate. In contrast, shorter wavelengths in the Beata Ridge area of the CLIP and the GAC areas of the Lesser Antilles suggest a more shallowly buried magnetic surface. **c)** Caribbean magnetic anomaly map from EMAG2v3 magnetic compilation by Meyer et al. (2017) showing the same relationships between the wavelength of anomalies and source depth for each terrane, as shown in Figure 2.3b. Note a much smoother, and lower resolution, signal than NAmag. Free-air gravity anomaly units are mGal, magnetic anomaly is displayed in nT.

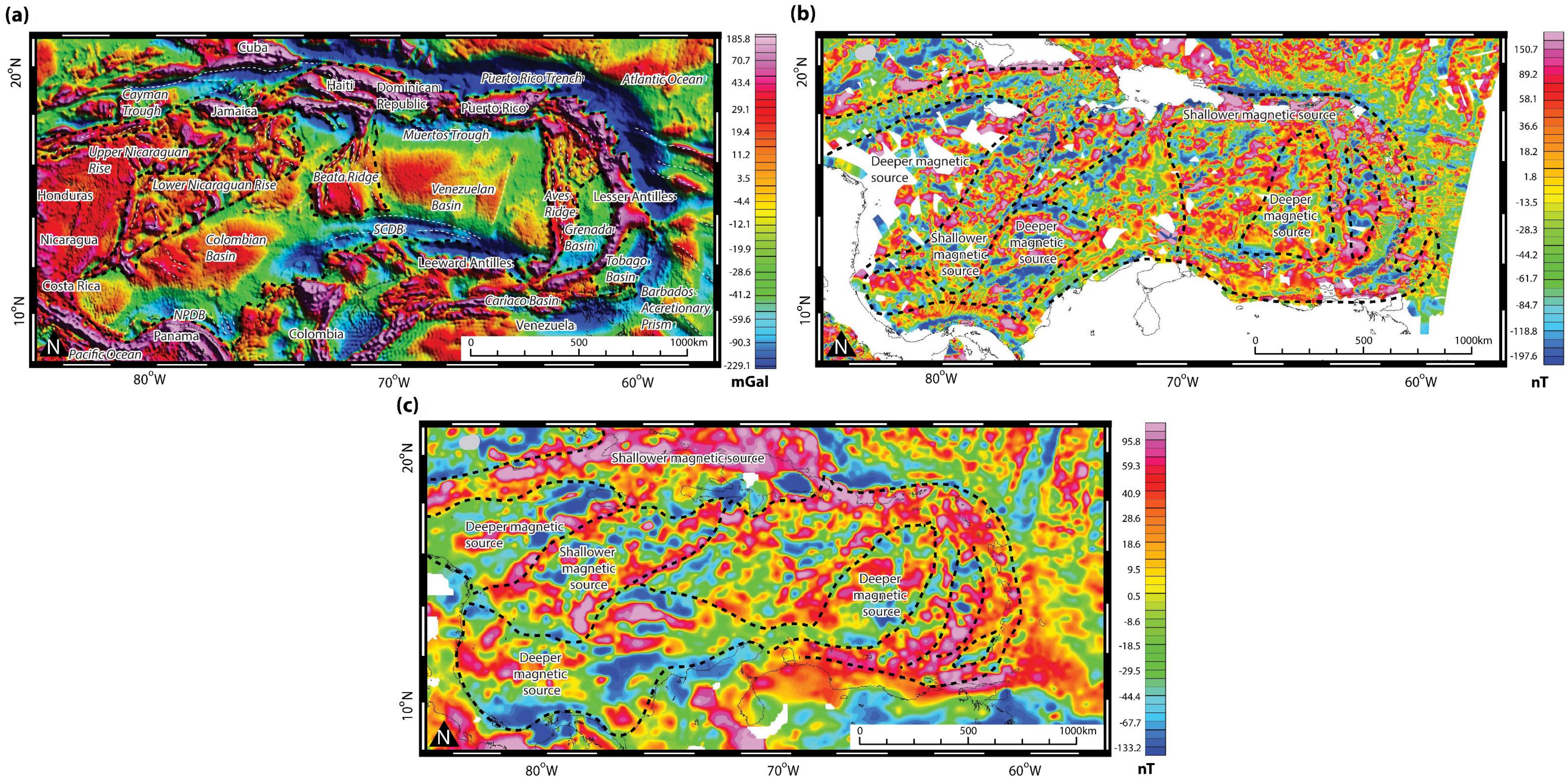
(a)
Cuba
Haiti
Dominican Republic
Puerto Rico Trench
Atlantic Ocean
Cayman Trough
Jamaica
Puerto Rico
Muertos Trough
Upper Nicaraguan Rise
Lower Nicaraguan Rise
Beata Ridge
Venezuelan Basin
Honduras
Aves Ridge
Lesser Antilles
Grenada Basin
Nicaragua
Colombian Basin
SCDB
Leeward Antilles
Tobago Basin
Costa Rica
Cariaco Basin
Barbados Accretionary Prism
NPDB
Venezuela
Panama
Colombia
Pacific Ocean
mGal
(b)
Deeper magnetic source
Shallower magnetic source
nT
(c)
Shallower magnetic source
Deeper magnetic source
nT
20°N
10°N
80°W
70°W
60°W
0
500
1000km

2.3.1.1 Continental Chortis terrane

The Chortis block is the only continental area recognized within the limits of the modern Caribbean plate (Arden, 1975; Rogers et al., 2007a, 2007b) (Figure 2.4 and 2.5) and is bounded to the north by the 1100 km-long Cayman Trough and to the east and south by accreted island arc terranes (Figure 2.5). My criteria to identify the Chortis as a continental terrane was based on: 1) seismic refraction measurements (Figure 2.2, Table 2.3); 2) wells drilled to the top of basement that revealed a continental affinity (Carvajal-Arenas, 2017; Sanchez et al., 2019; Torrado et al., 2019) (Figure 2.2, Table 1.2); and 3) the presence of a widespread and persistent gravity anomaly between + 30 and + 70 mGal consistent with the more than 20 km-thick continental crust interpreted from seismic refraction (Carvajal-Arenas, 2017) (Figure 2.3a).

The top basement surface of the Chortis is shallower than other adjacent oceanic-derived terranes due to its greater crustal thickness (Figure 2.6). The seismic character and structure of this crust have been interpreted as a northwest-verging Late Cretaceous–Paleogene fold belt (Sanchez et al., 2019) underlying the thick carbonate platform that caps the Upper Nicaraguan Rise (Droxler et al., 1991) that have since inverted as normal faults within the active zone of Cenozoic transtension along the Cayman Trough that bounds the northern edge of the Upper Nicaraguan Rise (Sanchez et al., 2016, 2019). Sedimentary basins overlying the thicker crust of the continental Chortis block are more laterally extensive and contain a thinner sedimentary fill in comparison with the smaller and deeper basins that overlie the neighboring GAC and CLIP terranes (Figure 2.6 and 2.13b). The total horizontal

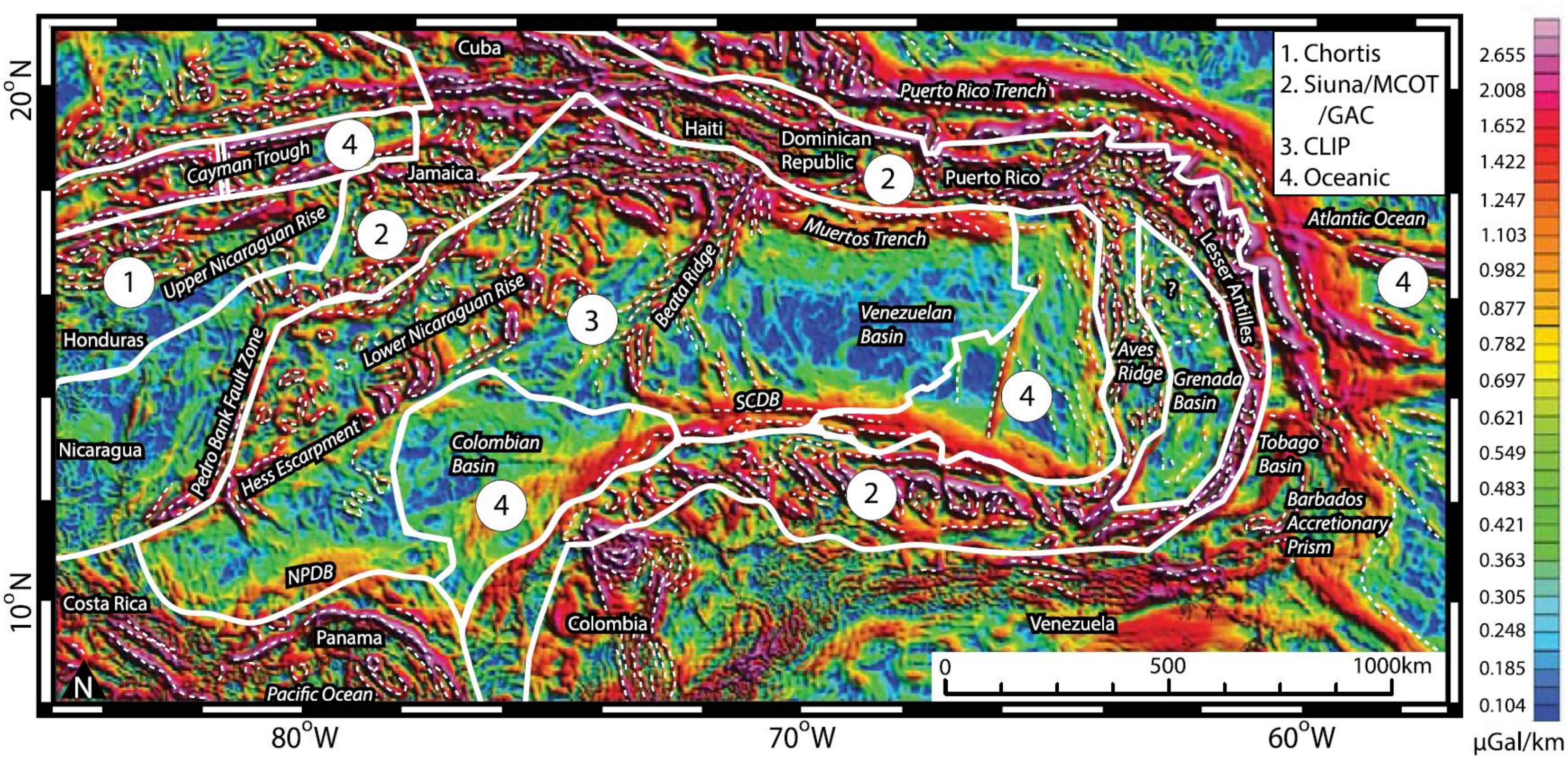

Figure 2.4 Total horizontal derivative of the 5 km-upward-continued Bouguer gravity anomaly that provided edge-detection of sub-bathymetric structural controls on the numbered Caribbean terranes, delineated by white lines. The signal within island arc terranes [2] indicates a highly deformed and intruded crust. Areas of continental and oceanic crust [1, 4] exhibit a flatter, less deformed appearance. Signal over areas of the oceanic plateau [3] is more varied on gravity than areas of the nearby continental or oceanic crust, caused by multiple emplacement events and varying basement structure.

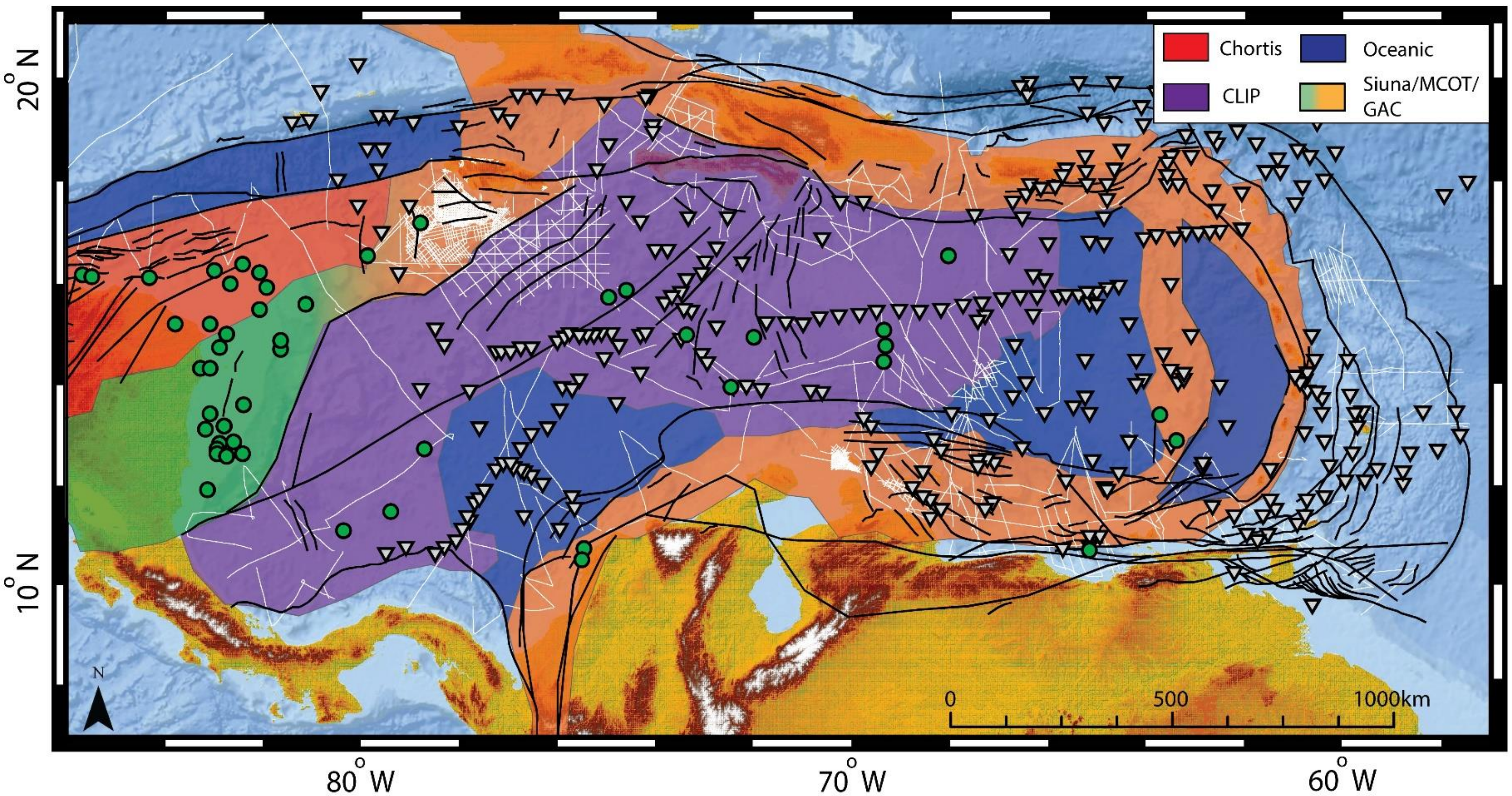

Figure 2.5 Map of four proposed Caribbean terranes as delineated by their magnetic/gravity anomaly, seismic reflection character, gravity and magnetic modeling results, refraction velocities, and basement geochemistry. Thin black lines show mapped faults, thin white lines show 2D seismic reflection track lines, green circles and grey triangles show well and refraction control.

derivative gravity map revealed the linear northern and western boundaries (Figure 2.4). The location of the southern edge of the Chortis block is less defined because of the thick and deformed sedimentary cover and similar crustal thickness of the adjacent, accreted Siuna/MCOT arc terrane. Wells with basement perforations and on-land geochemical work on magmatic rocks within northern Nicaragua and southern Honduras more accurately defined this suture zone (Baumgartner et al., 2008, 2018; Flores et al., 2015).

2.3.1.2 Siuna/MCOT/GAC island arc terranes

The GAC and the related, older oceanic island arc Siuna/MCOT (Baumgartner et al., 2018) accreted to the southern and eastern edge of the Chortis during the Late Cretaceous (Sanchez et al., 2016, 2019) (Figure 2.5). Current plate models interpreted periods of both east- and west-facing subduction during its formation and accretion (Escuder-Viruete et al., 2013; Andjić et al., 2019b) (Figure 2.1). I interpreted the GAC free-air anomaly signal as commonly exceeding + 70 mGal and the magnetic signal as dominated by short wavelengths, indicating a shallow, thick basement (Aitken et al., 2011) (Figure 2.3b–c). GAC basement is generally comparable in seismic reflection character to the Chortis block, with the notable difference that island arc basement exhibits large seamounts inferred to have formed during periods of arc activity (Ott, 2015). Horizontal changes in the filtered gravity signal within the GAC exhibit elliptical patterns that may reflect relict, arc-related, sub-circular, volcanic and plutonic features (Figure 2.4). Moreover, basins overlying the thinner crust of the GAC terrane contain localized, deeper basins in comparison to the shallower and more areally extensive basins overlying the Chortis block (Figure 2.6, 2.7 and 2.13c).

		Velocity ranges (km/s)			
Reference publication	*Total stations*	*Sediment*	*Plateau and crust*	*Upper mantle*	*Type of data*
Ewing et al. (1957)	47	1.7–4.47	4.8–6.88	7.36–8.32	unreversed and reversed shipborne refraction
Officer et al. (1959)	136	1.64–4.4	4.51–7.63	7.58–8.64	unreversed and reversed shipborne refraction
Ewing et al. (1960)	43	1.7–4.4	4.6–7.6	7.8–8.5	unreversed and reversed shipborne refraction
Edgar et al. (1971)	63	1.76–4.75	4.5–7.24	7.86–8.53	reversed shipborne refraction
Ludwig et al. (1975)	44	1.55–4	4.5–6.43	N/A	reversed shipborne refraction
Westbrook (1975)	2	1.7–4	6.7–6.73	8.02	reversed shipborne refraction
Houtz and Ludwig (1977)	27	1.6–4.6	4.85–7.3	8.1	sonobuoy
Mauffret and Leroy (1997)	4	1.7–4.3	5.1–7.45	7.8–8.1	sonobuoy

Table 2.3 Velocity information from multiple authors for the sediment and lithosphere of the Caribbean plate

Up to 3 km-thick sections of sedimentary rocks within the Upper Nicaraguan Rise cover the thickened, 15–20 km crust of the Siuna/MCOT, resulting in a similar free-air gravity and magnetic signature as the Chortis block (Sanchez et al., 2019). Only two seismic reflection lines (CT1-10C and CT1-10D) in my compilation traversed the Siuna/MCOT, and these vintage seismic lines were not able to image the basement character beneath the overlying carbonate platform. Interpretation of the Siuna/ MCOT terrane boundaries in Central America and on the Nicaraguan Rise incorporated geochemical and radiometric results from outcrops and drilled, magmatic rocks (Baumgartner et al., 2008, 2018; Lewis et al., 2011; Flores et al., 2015).

2.3.1.3 CLIP oceanic plateau terrane

The gravity and magnetic signatures over the CLIP are highly variable in both strength and wavelength (Figure 2.3 and 2.4). For this reason, I primarily characterized the CLIP using seismic reflection and refraction data integrated with borehole and dredge basement sampling.

The seismic reflection character of the top CLIP surface is generally smooth and continuous, defined as the 'smooth B" reflector' (Diebold et al., 1981). Early DSDP drilling by Edgar et al. (1971) established the smooth B" reflector as representing the impedance contrast at the top of Late Cretaceous basalt flows. Subsequent, deep-sea drilling and dredging of the Lower Nicaraguan Rise, Beata Ridge and parts of the Colombian and Venezuelan basins recovered basaltic rocks with oceanic flood basalt characteristics and ages ranging from Albian to Maastrichtian (112–68 Ma) that established these areas as part of the CLIP (Dürkefälden et al., 2019a, 2019b).

Refraction station measurements in the Venezuelan and Colombian basins over this thickened CLIP crust also recognized significant differences in structure and velocity when compared to typical oceanic crust (Ewing et al., 1960; Ludwig et al., 1975; Diebold et al., 1981). Refraction measurements within the Colombian basin indicated that the crust in this area is composed of three layers (Mauffret and Leroy, 1997); an upper layer with a velocity of 4.5–5 km/s, within the range of vesicular basaltic velocities and CLIP basement sampled at ODP 1001 (Sigurdsson et al., 1997), and two underlying crustal layers between 5.8–7 km/s, more in-line with typical oceanic velocities that are inferred to be part of the Farallon plate (White et al., 1992). This underlying Farallon oceanic crust has also been seismically imaged in the Aruba Gap region of the Venezuelan basin (Stoffa et al., 1981).

Within the CLIP, intra-basement 'wedging reflectors' (Ott, 2015; Carvajal-Arenas, 2017) (Figure 2.6) are prominent features on seismic reflection lines across wide areas of the Lower Nicaraguan Rise and the Beata Ridge. I interpreted these reflectors as large, conical volcanic features similar to those described from western Pacific oceanic plateaus like the Shatsky Rise (Zhang et al., 2015). Sedimentary basin sizes that overlie the CLIP vary from laterally restricted, between areas of surrounding seamounts, to deep, elongate basins formed by subduction-related flexure along the amagmatic Muertos and SCDB subduction zones (Kroehler et al., 2011; Ott, 2015) (Figure 2.13).

2.3.1.4 Normal and extended areas of likely Early Cretaceous oceanic crust

I mapped normal to thin oceanic crust in the core of the plate within the Colombian and Venezuelan basins (Figure 2.5), which I interpreted as the same Farallon oceanic crust that formed the substrate to the Late Cretaceous CLIP (Ghosh, 1990; Kerr et al., 1998). These areas exhibit crustal thicknesses of 3–8 km, as determined by refraction measurements, modeling, and seismic reflection interpretation (Ewing et al., 1960; Diebold and Driscoll, 1999; Kroehler et al., 2011; Frost, 2018; Sanchez et al., 2019). Within the Colombian basin, the oceanic crust was proposed to an extinct spreading ridge (Frost, 2018) of Early Cretaceous age (Ghosh, 1990); in the easternmost Venezuelan basin, the oceanic crust was proposed to have thinned through Aves Ridge back-arc extension (Kroehler et al., 2011; Allen et al., 2019).

The Venezuelan and Colombian basins display two differing, free-air gravity anomalies. Over the Colombian basin, the gravity anomaly signal reflects a general decrease in intensity as the crust transitions from thicker, smooth-surfaced CLIP crust with a thinner sedimentary cover to thinner, rough-surfaced, normal oceanic crust overlain by thicker sediments. (Figure 2.3a, 2.6–2.8). Over the Venezuelan basin, a prominent, north-striking fault is reflected on the free-air gravity and separates northeastern sections of the CLIP from extended oceanic crust to the east (Driscoll and Diebold, 1999; Kroehler et al., 2011) (Figure 2.3a).

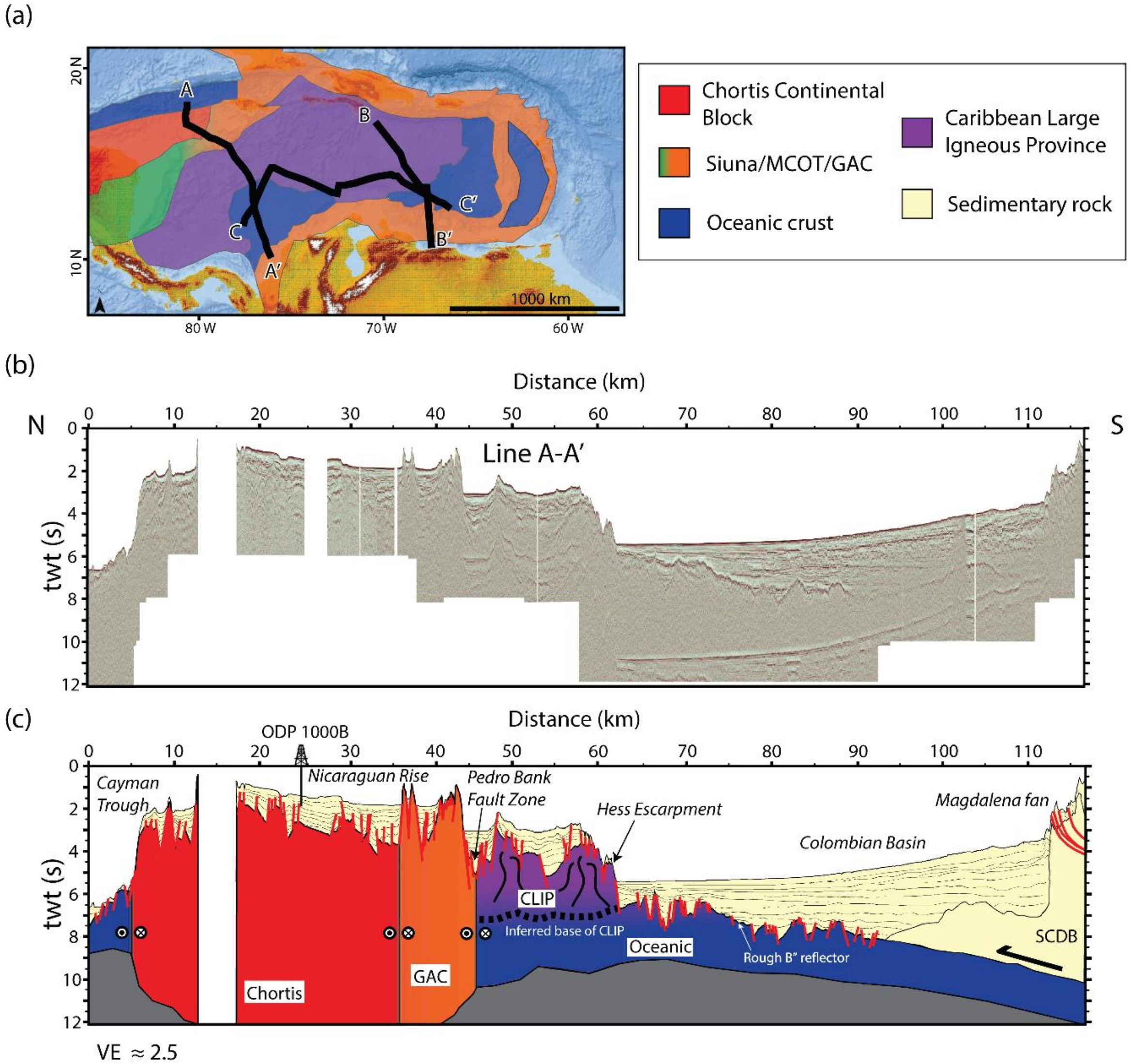

Figure 2.6 a) Location of three, mega-regional lines overlain on a base map of the four Caribbean terranes, and figure key. **b)** Uninterpreted, mega-regional seismic line A–A′ extending from the Cayman Trough to the north and the Magdalena deep-sea fan in the Colombian basin to the south; the regional line includes the following individual seismic reflection lines: CT1-27A, B, C, D, E; CT-28A, B, C; CT-29A, B, C. **c)** Interpreted, mega-regional seismic line A–A' showing variations in basement acoustic character and sedimentary rock thickness across all four of the Caribbean terrane crustal types: continental, island arc, oceanic plateau, and oceanic. twt, two-way travel.

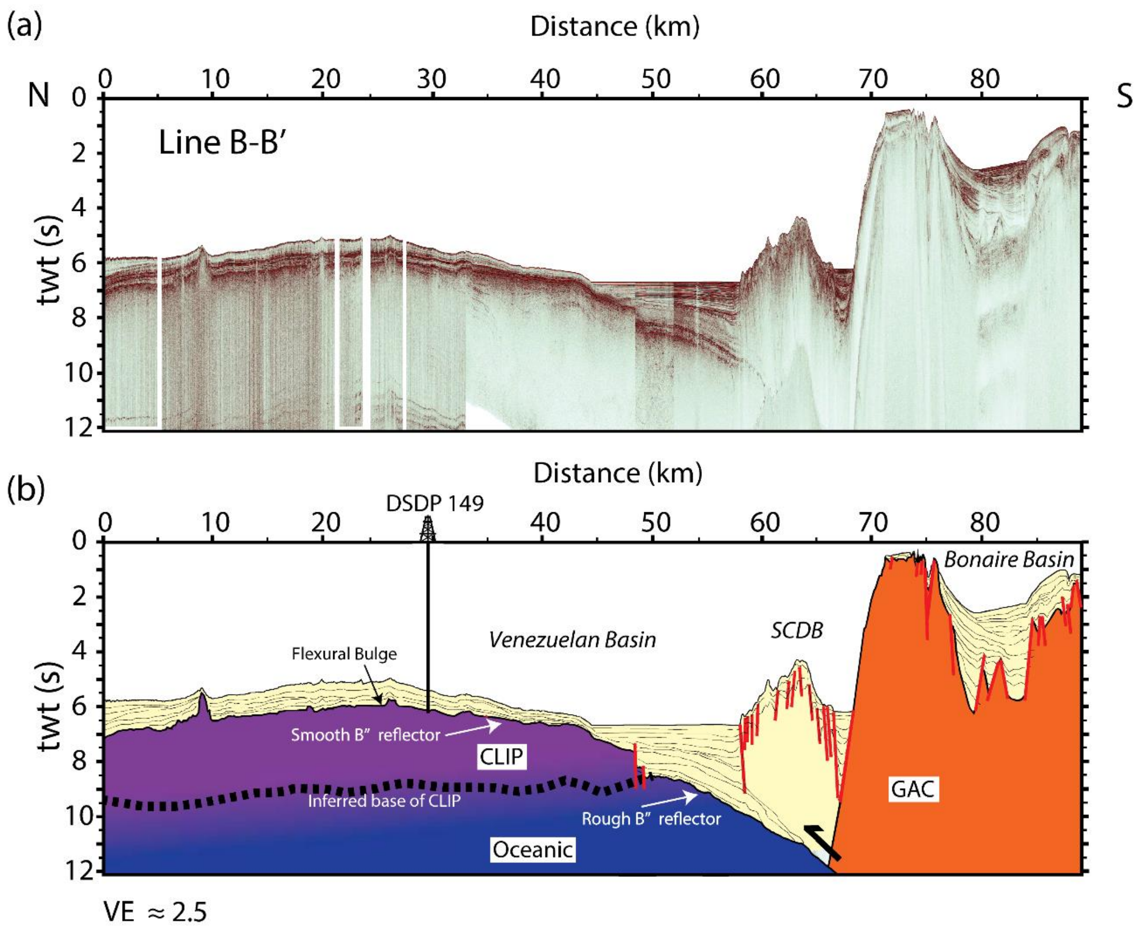

Figure 2.7 a) Uninterpreted, mega-regional seismic line B–B′ extending from the Muertos trench to the north and the Bonaire basin to the south near northern South America; the regional line includes the following individual, seismic reflection lines: 1304; 1316; bol12; VB-3NA, -3NB, -3NC, -3ND, -3NE, -3SA. **b)** Interpreted, mega-regional seismic line B–B' showing how basement acoustic character and sediment thickness varies across three of the four crustal types that underlie the Caribbean: island arc, oceanic plateau, and oceanic. Key to the colored terranes and the line location are shown in Figure 2.6a. twt, two-way travel.

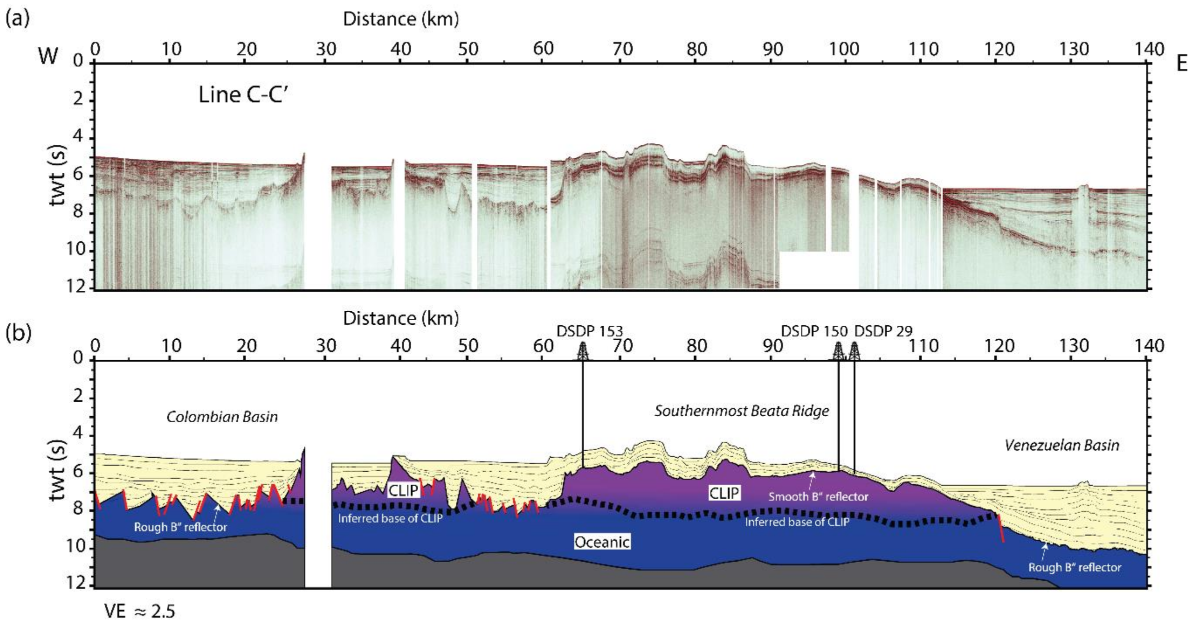

Figure 2.8 a) Uninterpreted, mega-regional seismic line C–C' extending west to east from the Colombian basin to the Venezuelan basin; this regional line includes the following individual, seismic reflection lines: 120; 121; 122; 123; 137; C6-1A, -1B, -1C, -1D. **b)** Interpreted, mega-regional seismic line C–C' showing variations of basement acoustic character and sediment thickness across two of the four Caribbean terrane types: oceanic plateau and oceanic. Key to the colored terranes and line location are shown in Figure 2.6a. twt, two-way travel.

Magnetic anomalies over either the Colombian or Venezuelan basins exhibit increasingly long wavelengths, indicating a substantial increase in source depth relative to the shorter wavelengths within the CLIP (Alldredge and Van Voorhis, 1961) (Figure 2.3b–c). On seismic reflection profiles, the rough B" reflection character reflects a heavily faulted basement surface (Figure 2.6–2.8) that is typical of oceanic crust (Diebold et al., 1981; Bowland, 1993; Kroehler et al., 2011).

2.3.2 Gravity and magnetic 2D forward modeling: Crustal structure across terrane boundaries on the edges of the Caribbean plate

I created 2D gravity and magnetic forward models along three seismic reflection profiles that imaged the contact between the Chortis block and GAC island arc crust (Figure 2.9b), the active subduction of oceanic and CLIP crust southward beneath the SCDB and northern South America (Figure 2.9c), and the northward subduction of the CLIP crust along the Muertos trench and Greater Antilles (Figure 2.9d). My models incorporated constraints from 2D seismic reflection lines, nearby seismic refraction stations and well logs.

To constrain depth to the crystalline basement on these profiles, I matched the observed gravity and magnetic signal to a total calculated error in the range of 10 mGal and 20 nT, respectively. I integrated model constraints of sediment and crustal layer density, velocity and susceptibility based on other work (Arden, 1975; Sanchez et al., 2019), nearby refraction station measurements, and available well logs (Figure 2.9a). Each profile and its constraints were discussed in detail below, displayed in depth within Figure 2.9, and compared to their colinear, depth or time seismic reflection line in Figure 2.10–2.12.

2.3.2.1 Model 1: Offshore southwestern Jamaica, from the Chortis to the GAC (Figure 2.9b)

I used Spectrum Geo reprocessed pre-stack depth migration data (PSDM) seismic reflection profiles WB06-209C, WI09RE-112TP, and WB06-209 to construct a composite, 185 km-long seismic line. This model incorporated three wells – ODP 1000, Pedro Bank-1, and Arawak-1 – and three seismic refraction stations – 20S, 20N, and 21E (Ewing et al., 1960) – to constrain a crustal model across the GAC–Chortis suture offshore Jamaica. It is important to note that, due to a large data gap in the higher resolution NAmag magnetic survey (Figure 2.3b), I instead used the highly smoothed EMAG2v3 magnetic survey (Figure 2.3c), leading to the difference in wavelengths between the higher-resolution modeled signal and lower-resolution observed signal.

A low-amplitude gravity anomaly (0–20 mGal) was observed over the Pedro Basin that increased to the northeast over a lateral distance of 30 km to reach a maximum value of 60 mGal over the Pedro Bank (Figure 2.9b). This positive gravity anomaly increase was inferred to be controlled by the localized increase in crustal thickness away from the Campanian suture zone that was reactivated and extended during the Late Cretaceous to Recent, and now forms a boundary zone between the GAC to the east and the Chortis terrane to the west (Ott, 2015). This crustal thickness change also manifests in the moderate bathymetric slope change along the southwestern flank of the Pedro Bank. Magnetic wavelengths from EMAG2v3 display a steady 60 km wavelength that I inferred as indicative of the relatively similar basement depths throughout the northern Nicaraguan Rise, at least within the resolution of the highly smoothed EMAG2v3 grid (Figure 2.3c and 2.9b).

2.3.2.2 Model 2: Offshore northern Venezuela, from the GAC to the CLIP (Figure 2.9c)

Model 2 was based on time seismic reflection line bol3 and constrained by four seismic refraction profiles: 77W, 78S, 78N and 79E (Edgar et al., 1971). Gravity anomalies vary from 0 and –80 mGal over the GAC, with each positive inflection corresponding to a basement high and each negative inflection corresponding to a small sedimentary depocenter. The anomalies reach a low of about -100 mGal along the SCDB subduction trace and its elongate, parallel, subduction-related, flexural basin. As the modeled line extends 150 km northward, the gravity anomaly increases to 0 mGal. I inferred that the gravity response over the GAC is controlled by the changing crustal thickness and influence of overlying sedimentary basins. The gravity signal across the CLIP also indicates a northward shallowing of its top basement surface that was affected by both thickening of the CLIP and the peripheral bulge imparted by subduction-related plate flexure (Figure 2.9c). This flexural effect was discussed later in this chapter.

Short (20–35 km) magnetic anomaly wavelengths characterize areas of the GAC and CLIP and reflect a shallow top basement surface (Figure 2.9c). Along the SCDB subduction trace, the magnetic wavelengths are longer (60 km), indicative of a deeper basement surface.

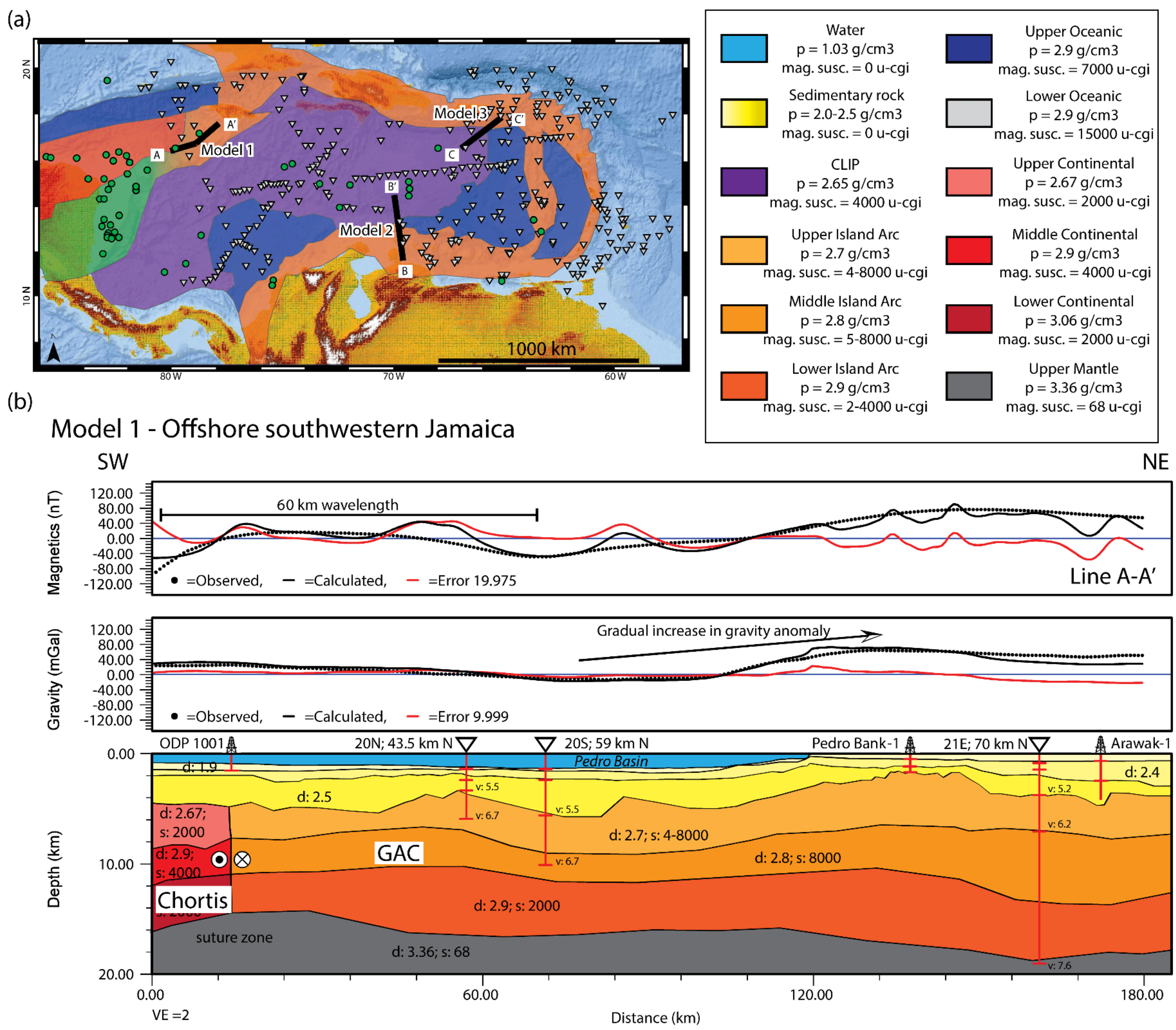

Figure 2.9 2D gravity and magnetic forward models across deformed edges of the Caribbean plate. **a)** Line locations, density values, and magnetic susceptibilities used for modeling. **b)** Model 1 traverses a 185 km-long, southwest–northeast transect in the transpressionally-deformed offshore area of southwestern Jamaica. The three seismic reflection lines used to constrain model 1 are the PSDM Spectrum lines WB06-209C, WI09RE-112TP, and WB06-209A. **c)** Model 2 traverses a 335 km-long, south–north transect across the SCDB subduction zone along the northern margin of South America. The one seismic reflection line used to constrain model 2 is the UTIG line bol3. **d)** Model 3 traverses a 240 km-long, south–north transect across the Muertos trench along the southern margin of Puerto Rico. The three seismic reflection lines used to constrain model 3 are the UTIG lines CT2-39A, CT2-39B, and CT2-39C.

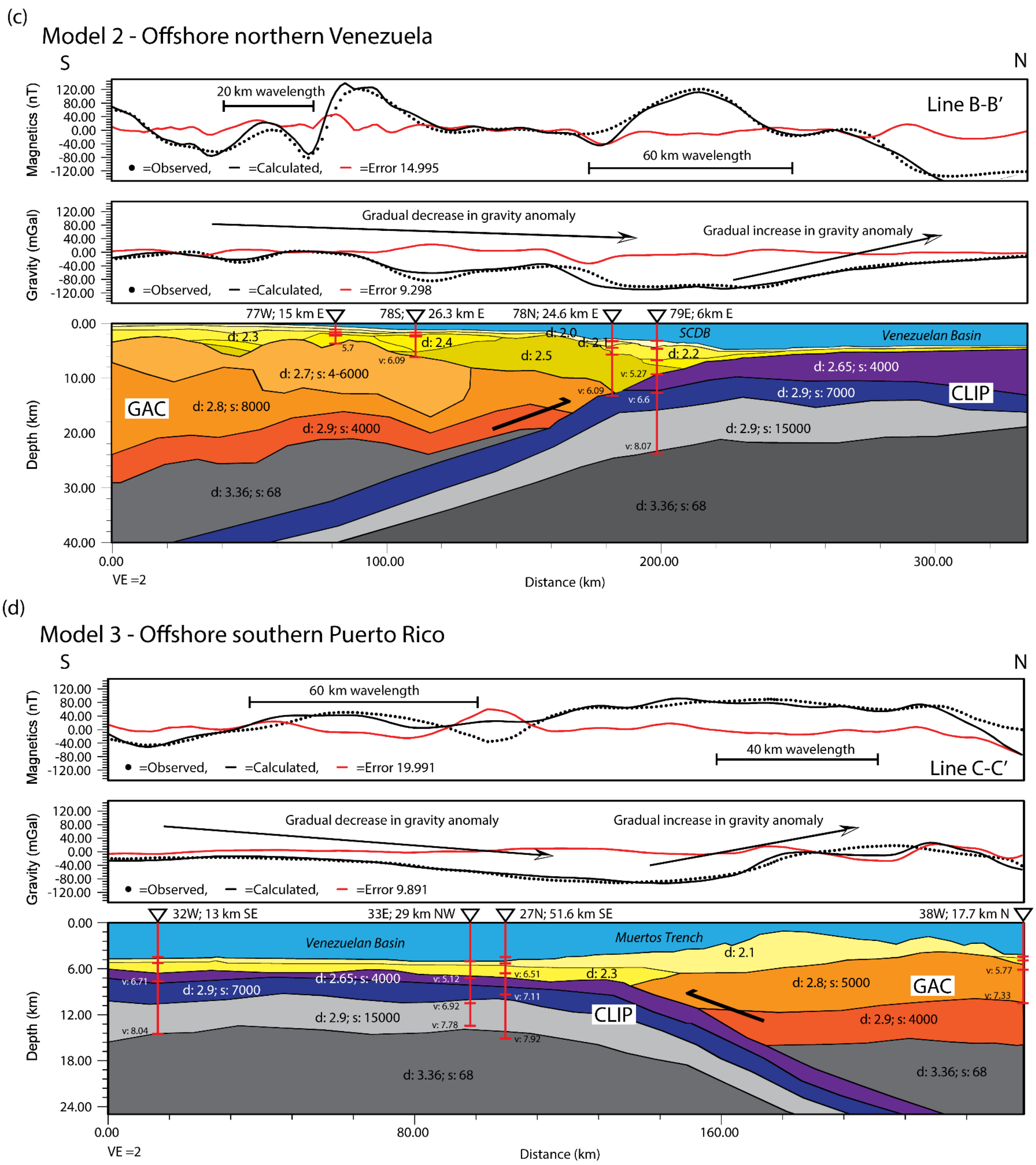

Figure 2.9 continued

2.3.2.3 Model 3: Offshore southern Puerto Rico, from the CLIP to the GAC (Figure 2.9d)

Seismic reflection profiles CT2-39A, CT2-39B, and CT2-39C, and four refraction profiles, 32W, 33E, 27N, and 38W (Officer et al., 1959), constrained model 3 in the offshore area of the Muertos Trough located south of Puerto Rico (Figure 2.9a). The CLIP observed on this line was recognized as oceanic plateau from its distinctive, smooth seismic character of the top basement surface (Figure 2.12). Refraction data and modeling indicated that the crust is slightly thicker than 8 km and much thinner than areas of the Beata Ridge to the west, where the CLIP is up to 20 km in thickness (Driscoll and Diebold, 1999) (Figure 2.9c).

Gravity anomalies over the model 3 line across the Muertos trench display a similar signature to the model 2 line across the SCDB. Both models showed a gradual decrease across the deepening CLIP basement, from –20 to –85 mGal in this model, produced by the subduction of oceanic plateau crust beneath the GAC that underlies the forearc basin. As the model 3 line crosses the GAC in Puerto Rico, the anomaly reaches >0 mGal, and reflects the thickening island arc crust of Puerto Rico and its sedimentary cover. Magnetic anomaly wavelengths decrease northward from 60 to 40 km and reflect the shallowing basement across the subducting CLIP and the overriding Puerto Rico arc crust.

2.3.2.4 Comparison of results from crustal models 1–3

These three models constrained depths to the magnetic basement and were compared with their colinear seismic profiles (Figure 2.10–2.12). Modeled subduction along the SCDB and Muertos trench displayed key differences. For the SCDB subduction zone along model 2: 1) the down-going CLIP of the Caribbean plate has a crustal thickness of 16 km; and

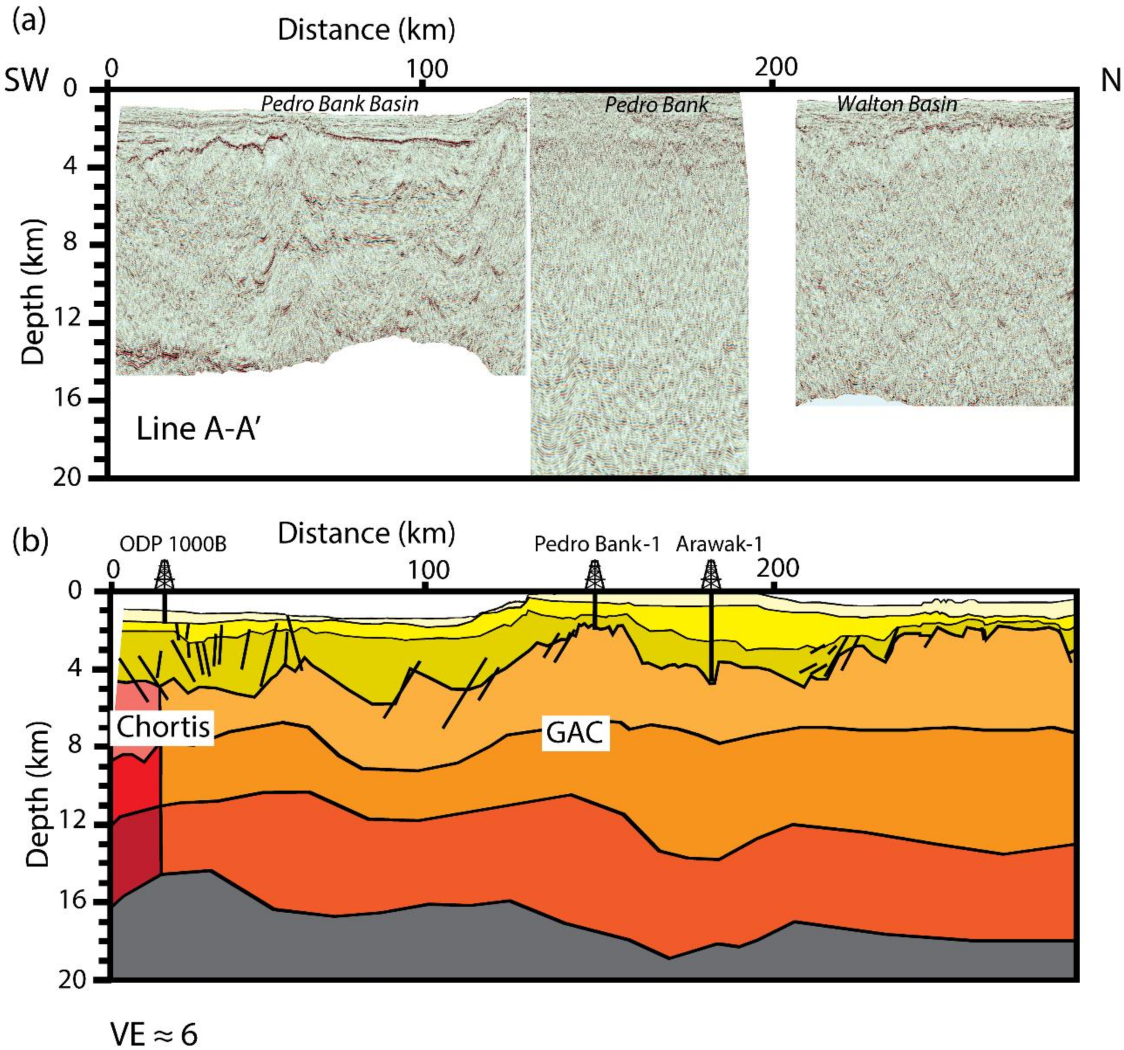

Figure 2.10 a) Uninterpreted, seismic line A–A′ extending southwest–northeast to the southwest of Jamaica and within the Upper Nicaraguan Rise and Pedro Bank area. **b)** Interpreted, seismic lines A–A′ using the results from the gravity and magnetic model 1 shown in Figure 2.9b and extended 100 km to the northeast; this line indicates the location of the suture zone between the GAC to the east and Chortis to the west.

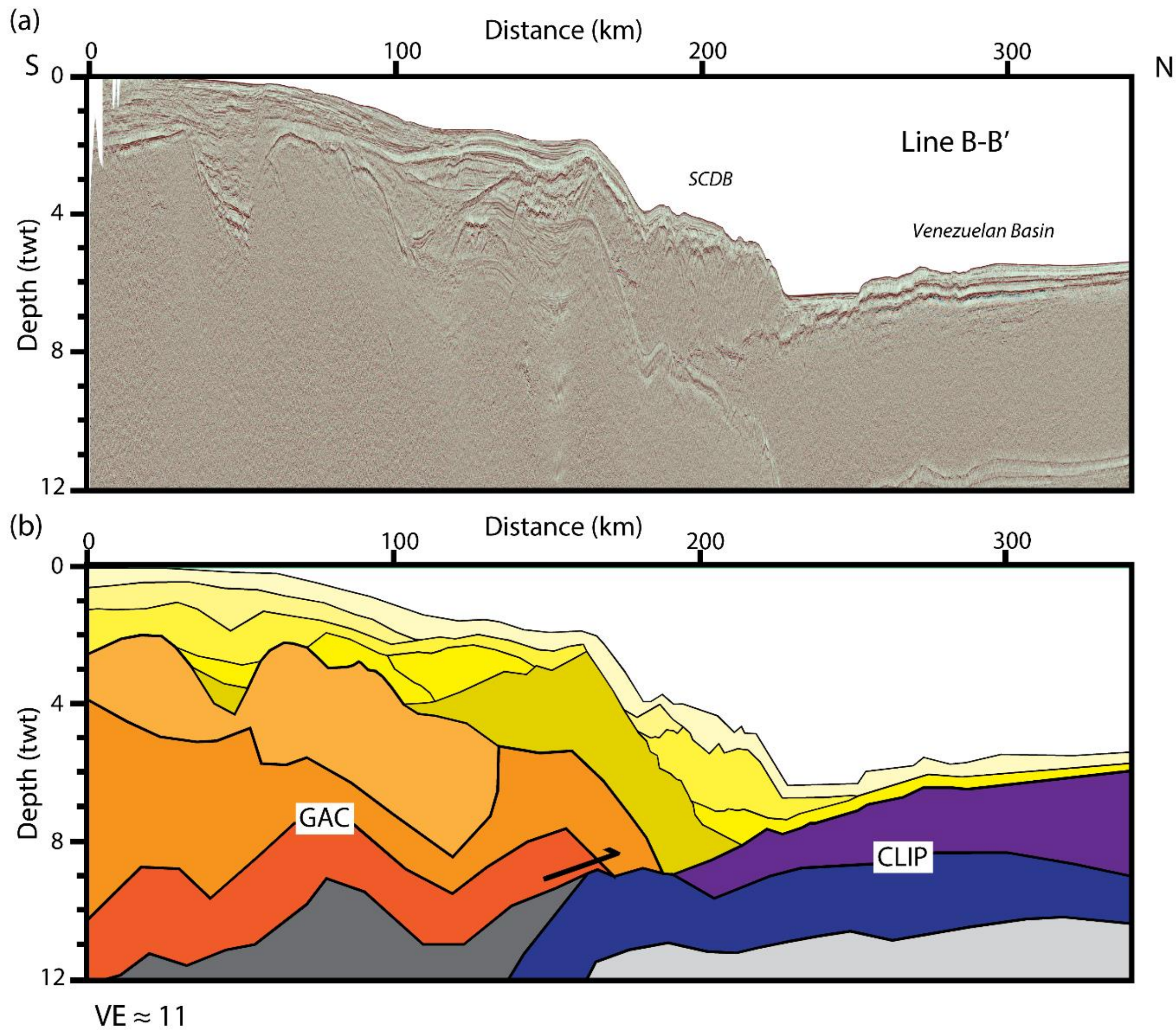

Figure 2.11 a) Uninterpreted, seismic line B–B′ extending from south–north across the subduction zone of the SCDB, north of Venezuela, and into the Venezuelan basin. **b)** Interpreted, seismic lines B–B′ using the results from the gravity and magnetic model 2 shown in Figure 2.9c; this line shows that the CLIP terrane is flexing and subducting southward beneath the SCDB and the northern margin of South America. twt, two-way travel.

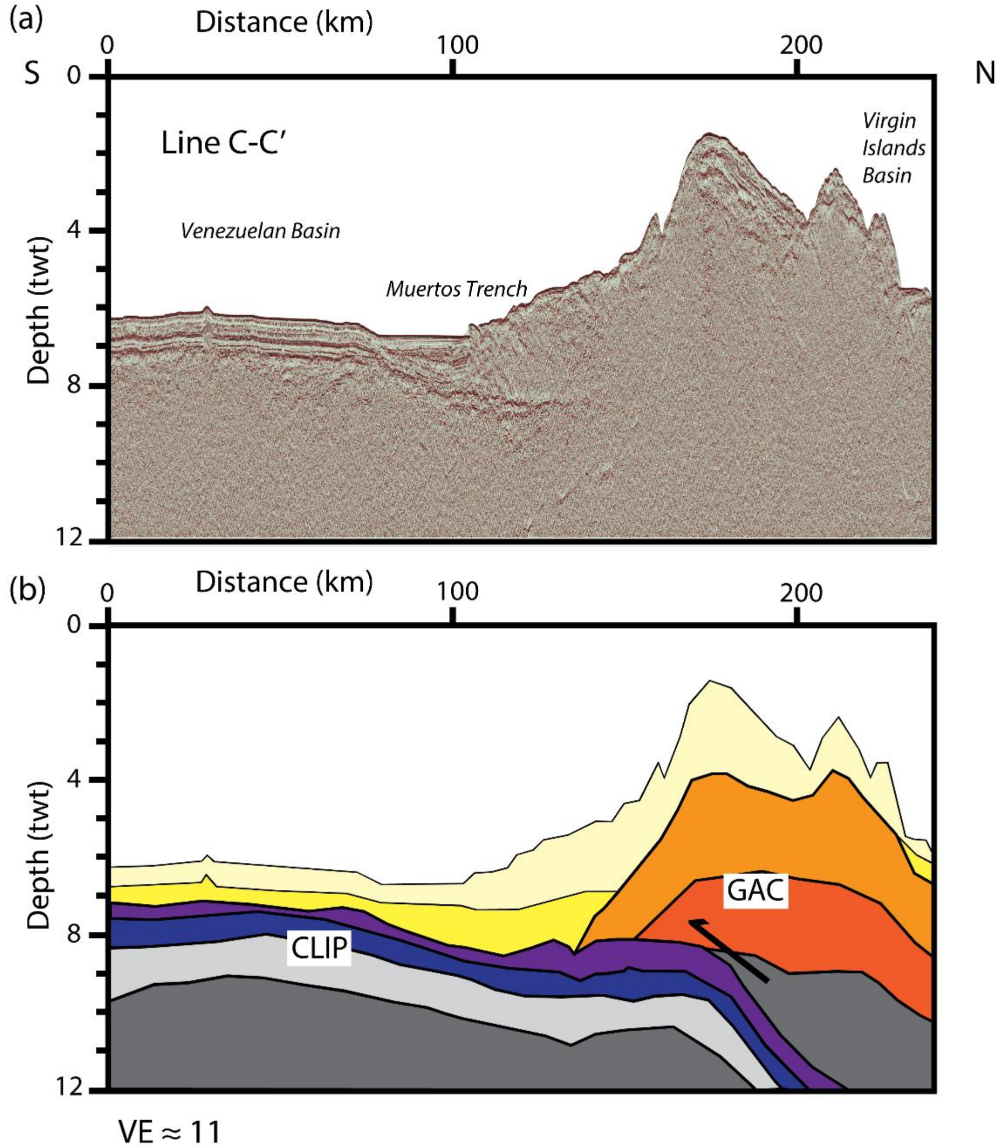

Figure 2.12 a) Uninterpreted, seismic line C–C′ extending from south–north from the Venezuelan basin across the Muertos subduction zone and the Virgin Islands basin in the eastern Greater Antilles. **b)** Interpreted, seismic lines C–C′ using the results from the gravity and magnetic model 3 shown in Figure 2.9d; this line indicates northward subduction of the CLIP terrane beneath the GAC terrane underlying the Greater Antilles. twt, two-way travel.

2) accreted sediments of the SCDB are 8 km in thickness (Figure 2.9c). In comparison, the Muertos subduction zone along model 3 showed: 1) a down-going CLIP that is much thinner (c. 8.2 km), only slightly thicker than 6–8 km normal oceanic crust; and 2) the Muertos accretionary prism forms a narrower belt that is less than 4 km thick (Figure 2.9d).

2.3.3 Caribbean top basement morphology and overlying sedimentary thickness

Following 2D gravity and magnetic model interpretations of the Caribbean basement terranes shown in Figure 2.9, I interpreted the top basement reflector in the Caribbean plate and its overlying sedimentary thickness using my compilation of seismic reflection surveys (Figure 2.13a), which I depth converted (Figure 2.13b). I then used the depth-converted, composite depth-to-basement map to calculate the total plate-wide sedimentary thickness (Figure 2.13c).

2.3.3.1 Regional depth to basement variations within the Caribbean plate

Depths to the tops of the crystalline basement of the four terranes making up the Caribbean plate vary from 18 km near the subduction-flexure controlled depocenter along the SCDB to near sea-level just offshore of the Leeward and Lesser Antilles (Figure 2.13b). Basement type and crustal thicknesses control variations in the depth to top basement; the continental crust of the Chortis block and the thickened Siuna/MCOT arc-type crust both display shallower top basement depths between 1 and 5 km (Ott, 2015; Sanchez et al., 2019), while CLIP and oceanic top basement depths range from 3 to 18 km below sea level (Figure 2.13b).

The GAC basement exhibits highly variable relief with highs near sea-level and basement lows plunging to depths of more than 12 km, such as within fault-controlled sub-basins northeast of Colombia and along the southern Aves Ridge (Figure 2.13b). Explanations for this variability of the GAC by Escalona and Mann (2011) and Ott (2015) included: 1) the origin of the GAC as an intra-oceanic island arc composed of high-relief arc volcanoes; and 2) the susceptibility of the GAC crust to a horst-and-graben style of extension that was described by Escalona and Mann (2011) in the Leeward Antilles and by Ott (2015) on the Nicaraguan Rise.

In the central and western Caribbean plate, the top of the CLIP basement is shallowest in areas with numerous seamounts, as on the Lower Nicaraguan Rise and the Beata Ridge, and along an axis sub-parallel to the SCDB trace (Figure 2.13c). Depths range from 3 km in those areas to 9 km southwards within the area of downward-flexed CLIP basement entering the SCDB subduction zone.

The deepest basement, ranging from 5 to 18 km below sea-level, occurs within the SCDB flexural basins. I interpreted this crustal terrane as faulted, normal to thinned, oceanic crust and propose that it is strongly flexed by the adjacent subduction zone because of its thin and pliant, subducting oceanic crust.

Areas of subduction along the SCDB, Muertos Trough, North Panama Deformed Belt (NPDB) and Lesser Antilles subduction zones exhibit strong flexural effects that formed the deepest areas seen on the top basement map of the Caribbean plate (Figure 2.13b). The depth of the basement along the NPDB is deepest at the distal ends of the subduction zone near Panama and Colombia and likely reflects complex crustal deformation at these terminations of the subduction zone on other types of plate boundary faults (Figure 2.14b). The top CLIP basement surface entering the Muertos Trough remains at a similar depth along the length of that physiographic trench (Figure 2.14b). Basement depths along the SCDB subduction vary widely from a maximum depth of 13 km on oceanic crust within the Colombian basin to 18 km on oceanic crust within the Venezuelan basin (Figure 2.14b).

Depth to the basement also increases within zones of Cenozoic, subduction-related, back-arc extension as observed in both the Lesser Antilles area (Grenada and Tobago basins) and the easternmost Venezuelan basin (Figure 2.13b). Depths within the Grenada back-arc basin generally increase southeastward and support a maximum fault displacement along the eastern and southern ends of the Lesser Antilles (Christeson et al., 2008; Aitken et al., 2011). Basement depths within the Tobago basin slightly increase southwestwards and support an increase in fault displacement in that direction (Christeson et al., 2008; Aitken et al., 2011). The basement of the eastern Venezuelan basin deepens towards the east and may be influenced by an early period of east–west-directed back-arc extension west of the Aves Ridge (Kroehler et al., 2011; Allen et al., 2019).

Shallow basement is generally associated with areas of thicker crust, such as continental, thickened oceanic plateau, or Siuna/MCOT/GAC crust (i.e., Upper and Lower Nicaraguan Rise, Beata Ridge, Greater and Lesser Antilles) (Figure 2.13). However, one of the most extensive and prominent shallow basement features is an east–west trending, linear, flexural bulge affecting the top basement of CLIP and oceanic crust in the Colombian and Venezuelan basins and related to the subduction along the SCDB and Muertos trenches (Figure 2.7 and 2.13b). The axis of this flexural bulge parallels the arcuate trace of the SCDB, although the distance from the bulge to the subduction increases westwards into the Colombian basin. The origins and controls of this regional basement flexure were examined through modeling and discussed in a later section.

Figure 2.13 a) Basement depth in two-way travel (twt) time as interpreted for this study from seismic reflection surveys (white lines) and integration of results from other workers, as shown in the colored and hatched lines. Fault compilation is shown in black. **b)** Top basement depth map following the time-to-depth conversion performed using VelPro software of data shown in Figure 2.13a. Areas of the Yucatan basin and eastern Cayman Trough were added without change from the original mapping of the top basement surface by Rosencrantz (1990) and Leroy et al. (1996). The anticlinal symbol in black marks the trace of the regional flexural bulge recognized in mapping and calculated from flexural modeling. White dashed lines delineate sub-basins where basement depths far exceed the average surrounding depth. **c)** Total sedimentary thickness across the Caribbean plate as interpreted from seismic reflection data shown in Figure 2.2. Basement terrane contacts shown in dashed white lines, and fault traces shown in thin black lines. Map contour interval is 750 units across all figures.

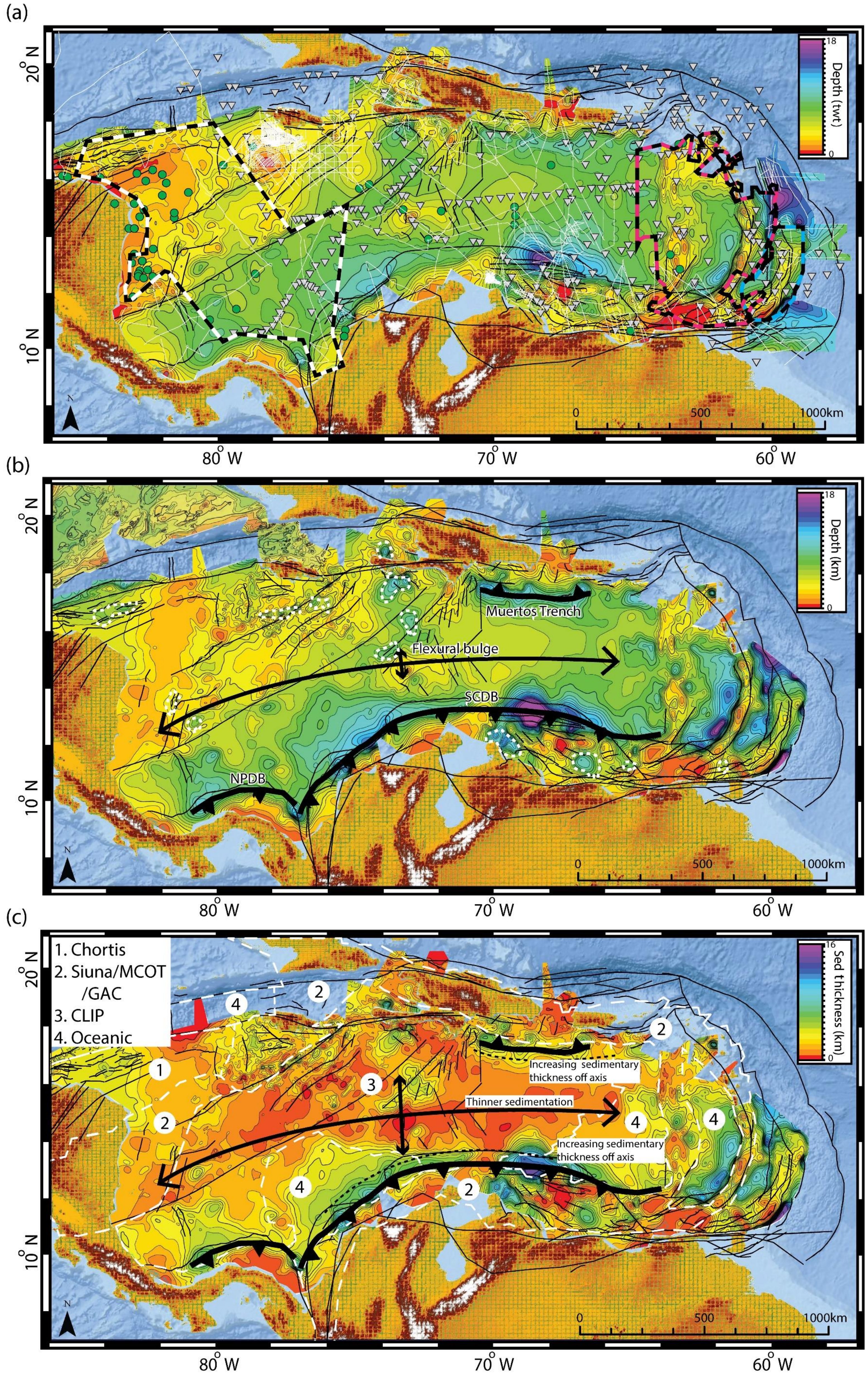
(a)
Depth (twt)
18
0
20° N
10° N
80° W
70° W
60° W
0
500
1000km
(b)
Depth (km)
Muertos Trench
Flexural bulge
SCDB
NPDB
(c)
1. Chortis
2. Siuna/MCOT
/GAC
3. CLIP
4. Oceanic
Sed thickness (km)
16
Increasing sedimentary thickness off axis
Thinner sedimentation
Increasing sedimentary thickness off axis

2.3.3.2 Subduction-related flexural and back-arc extensional effects on Caribbean sedimentary thicknesses

Sedimentary thicknesses are greatest within the subduction-related, flexural trough aligned with the SCDB subduction zone (Figure 2.6, 2.7 and 2.13), the subduction-related Tobago and Grenada basins (Figure 2.13), and the small but deep basins overlying the GAC (Figure 2.6, 2.7 and 2.13). Thicknesses in basins on the Caribbean terrane types range from: 1) 1 to 3 km over the Siuna/MCOT; 2) 0 to 5 km over the Chortis; 3) 0 to 12 km over the GAC; 4) 0 to 7 km over the CLIP; 5) 1 to 16 km over the extended oceanic crust within the Venezuelan and Colombian basins; and 6) 4–12 km over oceanic crust within the Grenada basin. The flexural bulge area traversing the center of the Caribbean plate in an east–west direction shows onlapping thinner sediments (0–3 km) along its structural axis, with downdip thickening into the subduction zones of the SCDB (10–16 km) and the Muertos trench (5–7 km) (Kroehler et al., 2011) (Figure 2.13c).

2.4 Discussion

2.4.1 Comparison of subsidence patterns of Caribbean terranes

I analyzed the subsidence of 17 wells on the Nicaraguan Rise that penetrated basement using previously interpreted stratigraphic constraints on paleo-water depths over three Caribbean terranes: the Chortis block, Siuna/MCOT/GAC and CLIP (Figure 2.14e, Table 2.2). These wells sampled large areas of the western Caribbean plate and revealed varying subsidence rates based on these three underlying crustal terrane types: continental, island arc, and oceanic plateau (Figure 2.14a–c); no well has been drilled into the oceanic crust in the

Venezuelan and Colombian basins. I calculated subsidence and corrected for sediment compaction using Schlumberger 1D PetroMod software.

On the Upper Nicaraguan Rise, the continental Chortis block exhibits a crustal thickness of 20–25 km and subsided at the slowest average rate of c. 25 m/Ma (Figure 2.13a). Within this same region of the northwestern Caribbean, the thinner, 15–25 km thick, Siuna/MCOT/GAC island arc terranes subsided at an average rate of c. 31 m/Ma (Figure 2.13b). ODP site 1001 on the Nicaraguan Rise penetrated oceanic plateau basement intercalated by sedimentary units, providing the only complete, publicly available benthic foraminiferal control on CLIP paleo-water depth (Sinton et al. 2000). These data constrained an average subsidence rate of c. 41 m/Ma for the 8–20 km thick CLIP, with rapid subsidence in the first 10 Ma followed by subsidence rates closely resembling those of normal oceanic crust (Figure 2.14c). Within the Caribbean plate area sampled by wells, thinner oceanic plateau crust in the thickness range of 8–20 km displayed faster average rates (41 m/Ma) than either continental (25 m/Ma) or island arc crust (31 m/Ma). I interpreted the CLIP subsidence history recorded at ODP site 1001 as a result of its initial rapid pulse of subsidence that likely represented a cooling response similar to normal oceanic crust (Figure 2.14a–c).

2.4.2 Comparison of CLIP subsidence patterns to western Pacific and Indian Ocean oceanic plateaus

The similarity between subsidence rates of oceanic plateau crust and normal oceanic crust has been noted by previous workers. Subsidence modeling in areas of the western Pacific and the Indian Ocean closely resembled the average subsidence of age-equivalent oceanic crust (Detrick et al., 1977; Coffin, 1992a, 1992b; Ito and Clift, 1998). As a result, these studies have shown that long-term oceanic plateau subsidence rates do not match analytical solutions for initial, rapid plateau formation above the head of a mantle plume. Thermal models by Ito and Clift (1998) predicted anomalous initial crustal uplift of 1 to 5 km and subsequent rapid subsidence after plume head emplacement events. Oceanic plateaus, including the CLIP, were predicted to exhibit a similar response; my subsidence models instead showed CLIP subsidence rates similar to Parsons and Sclater's (1977) normal oceanic rates.

To address the discrepancy between numerical predictions and observations of the long-term subsidence patterns of oceanic plateaus, Ito and Clift (1998) used DSDP/ODP well sites to quantify subsidence across the Ontong Java, Manihiki, and Shatsky oceanic plateaus in the western Pacific Ocean. These well sites also recorded subsidence at rates similar to long-term rates for normal oceanic crust (as I have shown for the CLIP in Figure 2.14c). Ito and Clift (1998) proposed that the multi-stage accretion of oceanic plateaus was the likely explanation for these subsidence patterns; each emplacement event and associated uplift effectively nullified the thermal subsidence of the prior emplacement. I postulate that this same multi-stage process has controlled the long-term subsidence of the CLIP, as evidenced by its at-minimum three-stage formation (Kerr et al., 1997; Lapierre et al., 2000; Révillon et al., 2000).

2.4.3 Comparisons between subsidence histories of the CLIP drill sites

This similarity in subsidence history between the two differing crustal types, normal oceanic and oceanic plateau, was strengthened by the subsidence curve of the Late Cretaceous CLIP sampled at ODP 1001, which closely resembled the normal oceanic subsidence curve of

Parsons and Sclater (1977) for oceanic crust of Late Cretaceous age (Figure 2.14c). The next logical step was to compare known CLIP basement ages and depths from Caribbean DSDP and ODP cruises, to the normal oceanic subsidence curve from Parsons and Sclater (1977) and make predictions on original plateau emplacement depth (Figure 2.14d). These CLIP subsidence histories were based on sampled areas of the top igneous layers of the CLIP from the Beata Ridge (DSDP 151, 153), south of the Hess Escarpment (DSDP 152, ODP 1001), and within the Venezuelan basin (DSDP 146/149, 150) (Figure 2.14e).

Comparisons yielded estimates of Late Cretaceous oceanic plateau emplacement depths that ranged from: 1) 1000 m above sea-level at DSDP site 151; 2) 500 m below sea-level at ODP site 1001; and 3) 1000–1500 m below sea-level at DSDP sites 146/149, 150, 152, and 153 (Figure 2.14d).

I propose that DSDP 151, drilled on an elevated area on the footwall of a large normal fault on the western flank of the Beata Ridge, has been overprinted by Cenozoic faulting effects. This structural overprint that included c. 3750 m of basement offset (Driscoll and Diebold, 1999), could explain the anomalous predicted emplacement depth of 1 km above sea-level. The plateau at DSDP 151 was likely emplaced much deeper; well reports suggested that the vesicular basalts recovered at this site deposited in water depths between 1 and 2 km (Edgar et al., 1973) and were similar to the vesicular basalts recovered at ODP site 1001 (Sigurdsson et al., 1997).

Preservation of calcareous and siliceous fossils provided some paleo-bathymetric constraints on the CLIP area sampled at DSDP 152 and suggested that its overlying sedimentary rocks accumulated well above the lysocline. Using this observation and assuming a similar relationship to the carbonate compensation depth (CCD) as today, I infer that

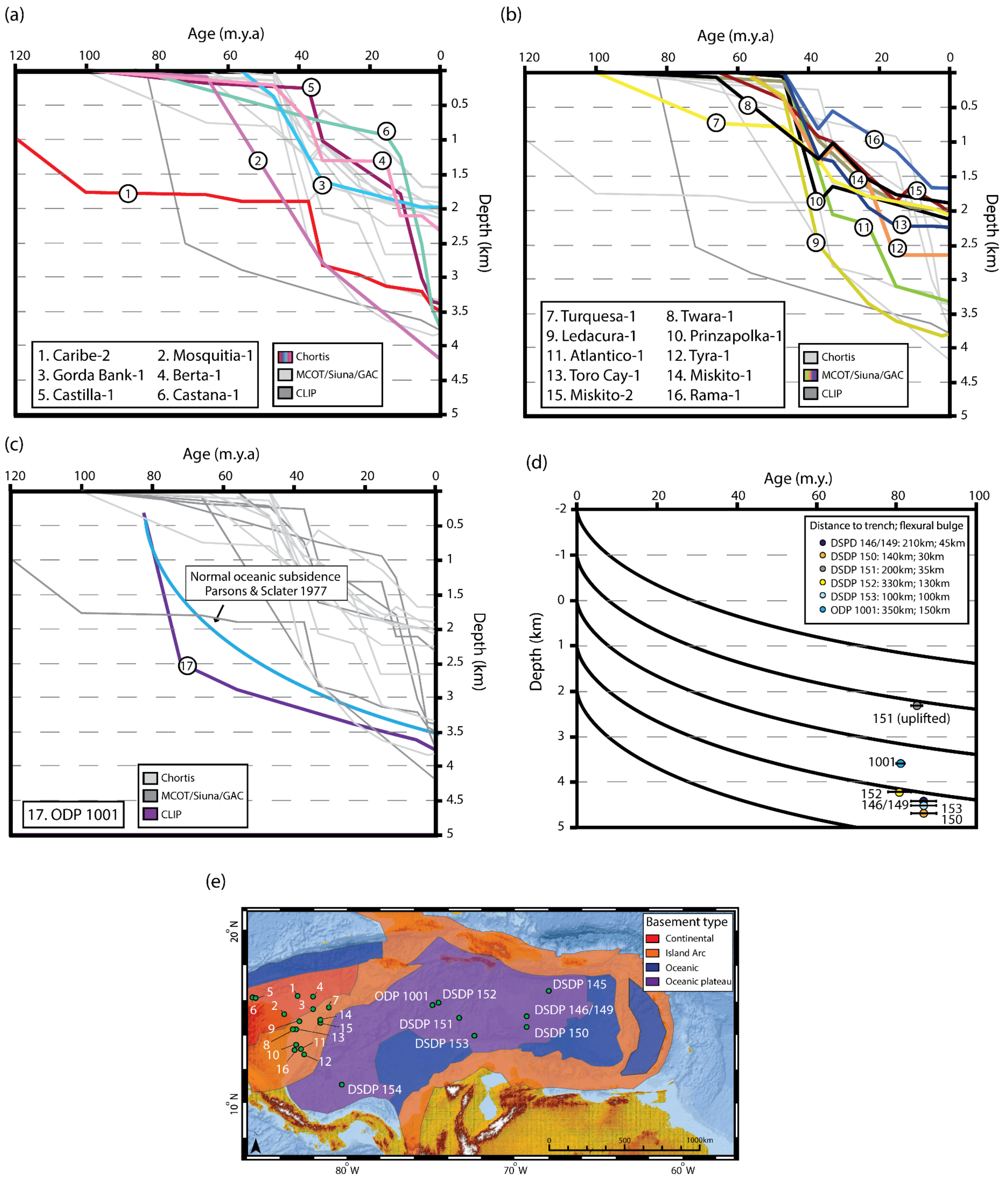

Figure 2.14 Comparison of subsidence from 17 selected wells that overlie Caribbean terranes with three crustal types: continental, island arc, and oceanic plateau. The subsidence rate of the Caribbean terranes is primarily dependent on crustal thickness and age, with the thicker, older continental Chortis block subsiding the slowest and the thinner, younger CLIP plateau crust subsiding the fastest. **a)** 44 dated horizons from six, on- and offshore wells within the continental Chortis terrane on the northwestern Nicaraguan Rise. **b)** 71 dated horizons from ten offshore wells within the island arc Siuna/MCOT/GAC terrane in Central America and along the northern, eastern, and southern edges of the Nicaraguan Rise. **c)** Six dated horizons from one offshore ODP (site 1001) well on the Lower Nicaraguan Rise and along the Hess Escarpment. Normal oceanic subsidence, after Parsons and Sclater (1977), is shown as a blue curve for comparison. **d)** Compilation of data from oceanic plateaus suggested that this crustal type subsides at similar rates to normal ocean crust (Detrick et al. 1977; Coffin 1992a, b; Ito and Clift 1998). Restoration of dated basement points suggested oceanic plateau emplacement depths between 0.5 m and 1.5 km below sea-level. All points account for sediment loading through a simple isostatic correction, from Crough (1983). Black lines indicate typical oceanic subsidence curves from Parsons and Sclater (1977) at different starting depths, while data points and error bars indicate basement depths and ranges of error for dated CLIP basement from Caribbean plate DSDP and IODP cruises (Donnelly et al. 1973; Sinton et al. 2000). **e)** Area map of the four Caribbean terranes and locations of the selected wells.

DSDP 152 remained at water depths above 3 km since the Santonian (Edgar et al., 1973). This would indicate much slower subsidence than described from the other DSDP and ODP wells. The predicted subsidence and depth of this site are thus suspect, likely as the result of a structural overprint similar to DSDP site 151.

At the remaining DSDP and ODP wells with little exact paleo-water depth control, predictions of CLIP formation ranged from depths of 1 to 1.5 km below sea-level (Figure 2.14d). Analyses of DSDP 146/149, 150, and 153 well reports suggested that Cenozoic sediment deposition occurred at or near the CCD. Estimates of the CCD at those times indicated an environment of deposition, soon after plateau emplacement, of around 4 km below sea-level (Ramsay and Finch, 1973). These wells likely experienced a period of rapid initial subsidence down to the CCD followed by a period of much slower subsidence at normal oceanic rates, as observed at ODP 1001 (Figure 2.14c).

2.4.4 Importance of subduction-related flexure on the basement structure of the Caribbean plate

The basement of the central Caribbean Sea displays an arcuate, east–west trending structural high that parallels the shape of the south-dipping subduction zone along the SCDB and resembles flexural bulges in other active subduction settings (Marotta and Mongelli, 1998) (Figure 2.13b–c). To establish the subduction-related flexural origin for this regional high traversing the Caribbean Sea and the associated lows running the lengths of the SCDB and Muertos trench, I created five flexural models perpendicular to the axis of the SCDB that matched the observed Caribbean basement bathymetry (Figure 2.15).

Flexural theory implies that a competent lithosphere acts as a rigid beam overlying a fluid asthenosphere and that this lithosphere responds isostatically to imposed tectonic loads that include large seamounts and subduction zones. To model the transects, I applied the analytical solution for the deflection of an infinite plate affected by a line load qa(x) (Turcotte and Schubert, 1982):

Equation 2.2: $q_a(x) = D\left(\frac{d^4w}{dx^4}\right) + (\rho_m - \rho_b)gw(x)$

where the w(x) is the vertical displacement of the lithosphere along strike, D is the flexural rigidity of the lithosphere, g is the acceleration due to gravity, and mantle and overburden densities are ρm and ρb, respectively.

The top Caribbean basement surface was modeled for all five transects using the Toolbox for Analysis of Flexural Isostasy (TAFI) script in MATLAB (Jha et al. 2017). I assumed a constant ρm of 3360 kg/m^3 and a constant ρb of 1800 kg/m^3. Because of the sole dependence of the flexural bulge location on the flexural rigidity/elastic thickness (Te) of the underlying terranes, load magnitude could be varied independently to fit the interpreted basement signal and determine the Te for each profile. Total flexural response was thus only dependent on the Te for my purposes, with a larger Te indicating a thicker lithosphere that was more resistant to bending (Burov and Diament, 1995).

Profile 1 (2.15a) displays a top Caribbean basement surface in the Colombian basin that dips southwards into the subduction zone along the northern margin of South America (SCDB) over a vertical distance of 5 km. Using a modeled elastic thickness of 80 km, the model predicted a positive flexural bulge 450 km away from the subduction zone, located in the area between the Pedro Banks fault zone and the Hess Escarpment fault zone.

Profile 2 (Figure 2.15b) displays a top basement surface that increases in dip over a vertical distance of 10 km towards the SCDB with a predicted flexural bulge 425 km away from the subduction zone, near to the Hess Escarpment fault zone. Basement along this line is mainly oceanic or oceanic plateau crust that is overall thinner than the crust shown in model 1 (Figure 2.15a) and resulted in a decrease in the elastic thickness to a value of 63 km.

The remaining three profiles of the oceanic and oceanic plateau Caribbean crust subducting at the SCDB (Figure 2.15c–e) dip steeply over an average vertical distance of 7 km with predicted flexural bulges 150–250 km away from the subduction zone and elastic thicknesses ranging between 14 and 29 km.

Crustal types along the transects shown in Figure 2.15 include thicker, stronger, continental and island arc crust in the western Caribbean areas of the Nicaraguan Rise and Colombian basin (Sanchez et al., 2019) and thinner, weaker, oceanic and oceanic plateau crust underlying the eastern area in the Venezuelan basin (Kroehler et al., 2011). My flexural modeling showed that the thinner oceanic and oceanic plateau crust was more responsive to loading and flexure within the Venezuelan basin and created a deeper and narrower basin (18 km maximum depth) than within the Colombian basin (13 km maximum depth) (Figure 2.13b and 2.15).

Kroehler et al. (2011) interpreted Late Cretaceous–Cenozoic sedimentary megasequences and faulting of the Colombian and Venezuelan basins to determine the initiation of subduction under the SCDB, which began in the Late Cretaceous to the southwest of the Colombian basin and became as young as the Miocene within the southeastern portion of the Venezuelan Basin. Seismic reflection profiles (Figure 2.6–2.8) supported this interpretation by showing progressively younger trench deformation in the eastern Caribbean

Figure 2.15 Flexure modeling across the interior of the present-day Caribbean plate along lines perpendicular to the south and southeastward subduction direction of the Colombian and Venezuelan basin beneath the SCDB and northern South America. The models supported the flexural bulge interpretation and showed thicker, competent crust in the west and weaker, less competent crust in the east. Colors along the bottom identify the underlying crustal terrane. Inset map shows locations of the five profiles relative to the two trench areas and the central flexural bulge. LNR, Lower Nicaraguan Rise; UNR, Upper Nicaraguan Rise; PBFZ, Pedro Bank Fault Zone; MDB, Muertos Deformed Belt.

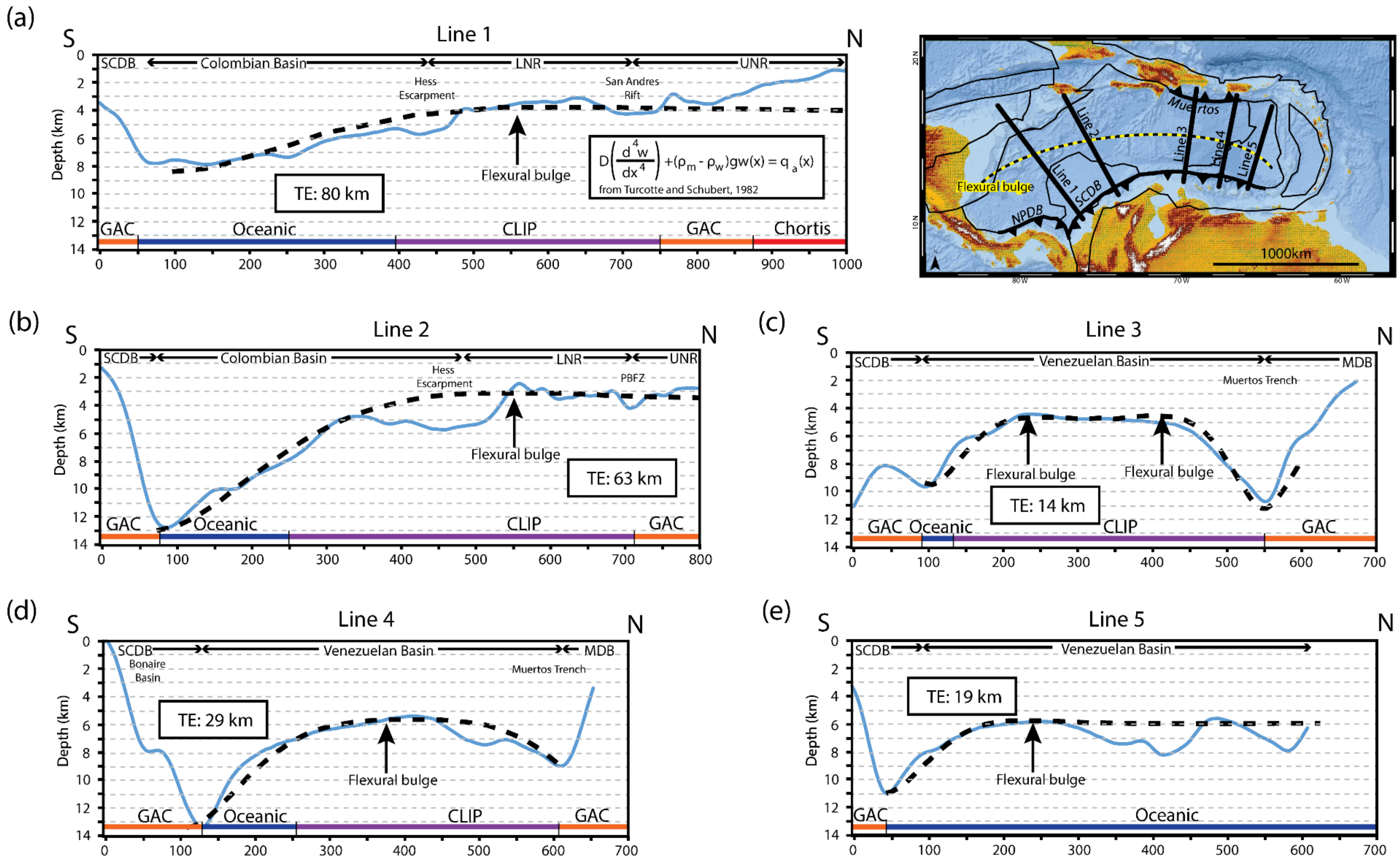

Vertical Exaggeration ≈ 37

and progressively younger age of onlap onto the central, peripheral bulge in the Venezuelan basin (Figure 2.8).

2.4.5 Links between hydrocarbon distribution and the underlying Caribbean terranes

Caribbean terranes are overlain by differing sedimentary sequences, with unique facies types and subsidence histories, that controlled source-rock distribution and richness, kerogen types, and hydrocarbon types. I compared the areas of known marine hydrocarbon source rocks identified by previous workers (Erlich et al., 2003; Bernardo and Bartolini, 2015; Carvajal-Arenas et al., 2015; Torrado et al., 2019) with my Caribbean basement map that showed the extents of the four Caribbean terranes (Chortis, CLIP, GAC/Siuna/MCOT, normal oceanic). This comparison of basement terranes with their overlying source rocks and seeps (Hill and Schenk, 2005; Sánchez and Permanyer, 2006; Yang and Escalona, 2011; Barnard et al., 2015; Carvajal-Arenas et al., 2015; Carvajal-Arenas, 2017; Castillo and Mann, 2021) revealed which basement terranes have provided the most favorable substrate for hydrocarbon generation (Figure 2.16a).

2.4.5.1 Central and eastern Caribbean source rocks

In the central and eastern Caribbean plate, a 0.5 cm to 12 m interval of organically-rich (total organic carbon (TOC) 2.5–11%) Late Cretaceous pelagic limestone deposited immediately above the top of CLIP and potentially over oceanic crust (Figure 2.16a). DSDP and ODP well reports described a type II kerogen that was immature over the drilled structural highs in the area of the Beata Ridge and Hess escarpment (Bernardo and Bartolini, 2015). Researchers proposed this interval as the expression of the Oceanic Anoxic Event (OAE 3) of Coniacian–Santonian age (c. 86.3 Ma) (Erlich et al., 2003). The mechanism of the

OAE 3 in the Caribbean Sea was likely related to the depletion of oxygen due to increased nutrient flux and continual development of paleobathymetric barriers along both margins of the translating Caribbean plate (Erlich et al., 2003).

The lack of hydrocarbon indicators within the elevated areas of the CLIP in the central and eastern Caribbean suggests that Cretaceous source rocks generally do not reach depths required for hydrocarbon production. The most promising area for the maturation of Late Cretaceous source rocks is the 10–18 km-deep, elongate, subduction-flexure basin adjacent to the SCDB (Figure 2.16b). Kroehler et al. (2011) mapped the Cretaceous interval over a large area of the CLIP and oceanic crust that included this deep SCDB basin, although the actual presence of such a thin source rock interval (<1–12 m) was difficult to image at these depths. However, the presence of gas chimneys emanating from near the top basement contact may indicate that these type II marine source rocks are present and have matured (Frost, 2018).

2.4.5.2 Western and northern Caribbean source rocks

In contrast to the marine, pelagic source rocks on the central and eastern Caribbean plate, hydrocarbon source rocks on the western and northern Caribbean plate are not associated with a global OAE event but are instead associated with localized sedimentation within lagoonal/marine settings. In these higher-standing areas that overlie the thicker crust of the Chortis, GAC, and CLIP on the Lower Nicaraguan Rise, documented source rocks in exploration wells deposited in 100–500 m-thick intervals of lagoonal limestone and deep marine calcareous shale with average TOCs of 2–4% and type II/III and III/II kerogen of Eocene to Miocene age (Bernardo and Bartolini, 2015; Torrado et al., 2019). Oil and gas seeps are commonly reported from the edges of the 3–6 km-deep depocenters (Carvajal-

Arenas et al., 2015) that my top basement mapping has also highlighted (Figure 2.16b). Reservoirs within these western regions include algal-rich reefs, dolomitized and fractured carbonates, and fluvio-deltaic sandstones. Poor sealing potential and lack of source-rock maturation pose the largest exploration risks (Torrado et al., 2019).

2.4.5.3 Northern Nicaraguan Rise and Jamaica

Unmapped, inferred, Jurassic and Cretaceous marine source rocks have been geochemically linked to seeps on- and offshore Jamaica and across the northern Nicaraguan Rise (Ott, 2015; Carvajal-Arenas, 2017; Skarstein, 2018). Recent geochemical work on the biomarkers of marl-derived oils in Jamaica suggested a Jurassic source (Skarstein, 2018). This finding is problematic, as no rocks older than Cretaceous have been found either exposed or in wells drilled on- or offshore Jamaica (Arden, 1975, Skarstein, 2018).

Drilled Cretaceous intervals offshore of Honduras recovered high maturity, low TOC, type IV source rock, indicating that the Cretaceous petroleum potential is limited (Bernardo and Bartolini, 2015). On- and offshore Jamaica, Cretaceous source intervals are slightly more promising, with up to 1.6% TOC and with thermal maturities that span the entire oil-window phase. These values are encouraging, but the type VI/III kerogen reduces their hydrocarbon potential (Bernardo and Bartolini, 2015).

2.4.5.4 Source rocks associated with the GAC in the southern Caribbean

Nearly all major discoveries along the shelf and slope of northern South America from Panama to northwestern Trinidad have been either biogenic or thermogenic gas. This belt of gas-prone basins closely follows the underlying trend of the GAC, which collided with the continental margin of northern South America in a west-to-east direction from Late

Cretaceous to Recent (Escalona and Mann, 2011). Useful comparisons can be made by describing major producing gas discoveries along this margin: the Chuchupa and La Perla fields offshore Colombia, and the North Coast Marine area (NCMA) offshore northern Trinidad (Figure 2.16b)

The Chuchupa gas field in the shelfal area of offshore Colombia has produced several trillion cubic feet (TCF) of gas since its discovery in 1977 (Katz and Williams, 2003) (Figure 2.16b). The gas was trapped in Miocene sandstone and limestone and is predominantly biogenic with a minor thermogenic component. Petroleum system modeling has shown that the possible underlying source rocks are not thermally mature; significant thermogenic gas creation only occurs in sedimentary thicknesses exceeding 3.5 km, greater than the available rock thicknesses in the immediate area (Katz and Williams, 2003).

The La Perla field, 200 km to the east along the trend of the GAC, is a world-class giant with 17 TCF of gas in place (Figure 2.16b). The discovery was made in 2009 in a late Eocene–early Oligocene shelfal limestone and is the largest gas discovery ever made in Venezuela (Castillo et al., 2017). Geochemical analyses of gas at the La Perla field indicated a thermogenic source from the Early Tertiary with type II/ III and III/II kerogen, 1–2% TOC, a maturity range between 0.8–1.9% and hydrocarbon generation that began in the latest Miocene to Present (Castillo et al., 2017).

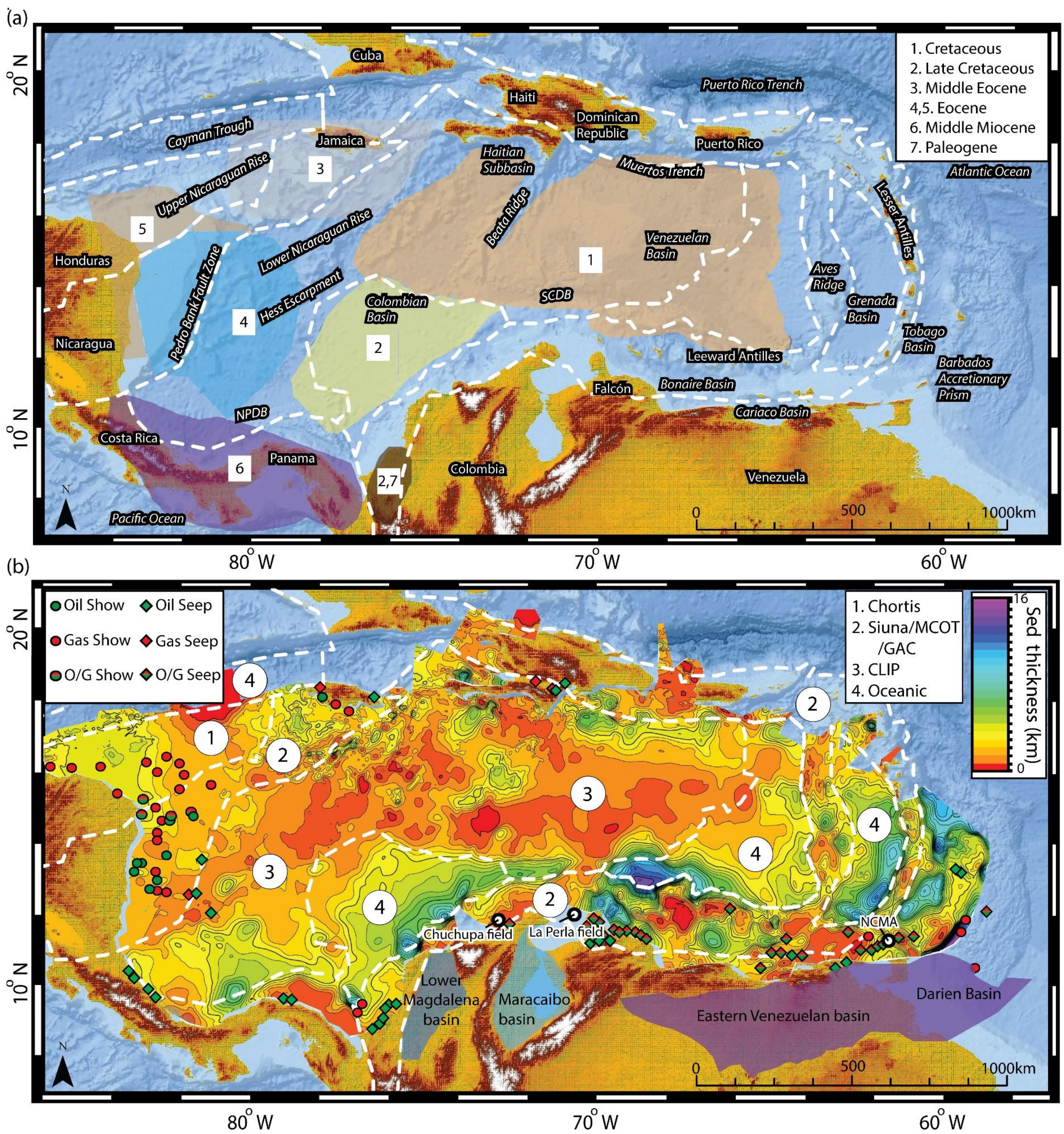

Figure 2.16 a) Caribbean plate terrane map compared to known or inferred source rocks as compiled from other authors (Erlich et al. 2003; Bernardo and Bartolini 2015; Carvajal-Arenas et al. 2015). Known Coniacian–Santonian OAE 3 source rocks deposited on the CLIP and its adjacent, Early Cretaceous extended oceanic crust. Late Cretaceous source rocks are known to be immature in the DSDP wells of the Colombian and Venezuelan basins; subduction-related, flexural, sediment-filled basins along the SCDB and Muertos trench may have provided sufficient overburden for the maturation of these source rocks at depth. Younger, more terrestrial Cenozoic source rocks were preferentially deposited over elevated continental and island arc basement terranes. **b)** Compilation of known oil and gas seeps and reported well shows from the Caribbean plate indicated that active hydrocarbon systems linked to Cretaceous and Cenozoic source rocks are mature enough to produce hydrocarbons in the deeper basinal depocenters that overlie the terranes (Hill and Schenk, 2005; Sánchez and Permanyer, 2006; Yang and Escalona, 2011; Barnard et al., 2015; Carvajal-Arenas et al., 2015; Carvajal-Arenas, 2017; Castillo and Mann, 2021).

In the far east, and 50 km off the northern coast of Trinidad, the NCMA is well-known for its prolific, biogenic gas fields with more than 3 TCF in place (Figure 2.16b) and little evidence of a thermogenic component. The fields are in structural traps associated with basement highs and reservoired within Pleistocene shoreface and shelfal sandstones (Moonan et al., 2018; Punnette and Mann, 2021).

I conclude that hydrocarbon accumulations along this margin are generally biogenic, and the association of the GAC and thermogenic gas fields is likely more related to the deposition of type II/III and III/II kerogen within deltaic systems aligned along the northern, continental margin of South America than to the underlying GAC basement rocks. Due to the modest burial depths, it is also unlikely that most underlying Cenozoic source rocks are thermally mature. However, sedimentary thicknesses greater than 3.5 km can provide enough overburden to mature the type II/III and III/II kerogen offshore Colombia (Katz and Williams, 2003), with even deeper basins and thick Cenozoic sedimentation able to thermogenically produce La Perla-sized resources (Castillo et al., 2017) (Figure 2.16).

2.5 Conclusions of this chapter

I defined four, largely submarine, Caribbean crustal terranes using seven different sources of regional geological and geophysical data: 1) Pre-stack depth migration (PSDM) and pre-stack time migration (PSTM) regional seismic reflection data provided by Spectrum Geo; 2) vintage multi-channel and single-channel seismic reflection data provided by the University of Texas Institute for Geophysics (UTIG) and the USGS; 3) 2D forward modeling of gravity and magnetic anomalies along the edges of the plate; 4) compilation of industry and academic wells; 5) compilation of seismic refraction stations; 6) regional magnetic and gravity surveys available for public access; and 7) integration of seismic reflection, dredging, geochemical, radiometric, and outcrop studies.

Depth to top basement varies from 0 to 18 km across the Caribbean plate. Basement within the Chortis continental terrane on the Nicaraguan Rise is shallow (1–5 km) and overlain by broad basins containing up to 5 km of sedimentary fill. Depth to the top of basement in Jurassic to Recent arc terranes, including the Great Arc of the Caribbean, is controlled by high-relief arc volcanic structures formed during periods of magmatic activity and later horst-and-graben style extension following arc collision and inactivity. Sedimentary thicknesses on Caribbean arc terranes are highly variable, up to 12 km in localized, fault-controlled basins. Depth to the top of CLIP basement is shallow (0–7 km) but variable due to the presence of Late Cretaceous oceanic seamounts and the widespread effects of lithospheric flexure related to active subduction of the Caribbean plate southward along the SCDB and northward along the Muertos trench. I conclude that subduction-related flexural effects occur in elongate basins along the SCDB and Muertos trench in the Colombian and Venezuelan basins. Greater flexural effects arise in areas of eastern, thinner, and more flexible crust than in western areas of thicker and less flexible crust.

Subsidence of three Caribbean terranes (Chortis, Siuna/MCOT/GAC, and CLIP) was calculated using stratigraphic information from deep wells and varied with crustal type. Thicker continental crust of the Chortis block subsided at slower average rates of 25 m/Ma, while island arc crust of the Siuna/MCOT/GAC subsided at faster average rates of 31 m/Ma. Average subsidence within the CLIP occurred at the fastest observed rates (41 m/Ma) and was similar to age-equivalent normal oceanic crust, with a period of rapid initial subsidence followed by a prolonged period of slow subsidence. Multiple CLIP emplacement events and associated thermal uplift and subsidence are proposed to have a self-cancelling effect on plume-related thermal effects and reduced the CLIP subsidence history to an average path resembling normal oceanic crust. This characteristic had been recognized by past research for Cretaceous oceanic plateaus in the western Pacific and the Indian Ocean. Reconstructions of the initial paleo-bathymetry of DSDP/ODP well sites based on this relationship within the CLIP indicated that sampled areas of the oceanic plateau formed in a marine setting, 0.5–1.5 km below sea-level. This was confirmed through the analysis of stratigraphic and biostratigraphic DSDP/ODP well log reports.

I then compared my mapping to the distribution of source rocks, natural seeps, and commercial hydrocarbon production in the Caribbean to infer relationships between basement terrane types, basement depth, and source-rock maturity. Marine type II and III kerogen source rocks of Eocene to Miocene age are most common on the continental, arc, and oceanic plateau terranes of the western Caribbean plate and over the Nicaraguan Rise. Seeps related to these sources occur adjacent to thicker depocenters that create environments favorable for source rock maturation. In the area of the CLIP, within the Venezuelan and Colombian basins, Late Cretaceous OAE 3 marine source rocks of type II kerogen were documented as immature from the elevated drilling localities on the Beata Ridge. These source rocks can be traced down-dip into the downward-flexed, elongate sediment-filled trough adjacent to the SCDB, where they are likely mature, but remain untested by deepwater drilling. Miocene and younger obliquely-rifted basins that formed during east–west elongation of the GAC in the Leeward Antilles and the southeast Caribbean exhibit little thermogenic hydrocarbon potential, except in older western basins or in thickly-sedimented areas such as north of Falcón or within the Bonaire and Cariaco Basins.

CHAPTER 3: CRUSTAL STRUCTURE OF THE CAMAMU-ALMADA MARGIN ALONG THE NORTHEASTERN RIFT SEGMENT OF BRAZIL FROM AN INTEGRATION OF DEEP-PENETRATION SEISMIC REFLECTION PROFILES, REFRACTION, AND GRAVITY MODELING

A version of the following chapter has been submitted to Tectonics

3.1 Introduction

Rifted-passive margins formed by continental separation have existed on Earth since at least the Paleoproterozoic (Bradley, 2008). Significant questions remain on the evolution from unstretched, full-thickness continental crust, through the rifting phase with necking of the continental lithosphere, to the final stage of the emplacement of oceanic crust along an organized spreading ridge. An important variable during the continental rift phase is the relative amount of magmatic activity that can occur during the necking of the continental lithosphere (e.g., Mutter et al., 1988; White and McKenzie, 1989; Desmurs et al., 2001; Whitmarsh et al., 2001; Péron-Pinvidic et al., 2019). The terms *magma-rich* and *magma-poor* margins define the two endmembers along the spectrum of varying magmatic influence and are synonymous terms with *volcanic* or *non-volcanic* margins and *magmatic* or *amagmatic* margins (e.g., Reston, 2009; Doré and Lundin, 2015).

Typical magma-rich systems are characterized by large volumes of flood basalts, commonly manifested as <10–15 km-thick units of seaward-dipping reflectors (SDRs) interpreted from seismic reflection sections (Eldholm et al., 1989; 2000; White et al., 2008, Quirk et al., 2014; Reuber and Mann, 2019). SDRs commonly overlie high-velocity lower crust (HVLC) generally attributed to lower crustal intrusions (Becker et al., 2014). Typical magma-poor margins are characterized by hyper-extended continental crust that lacks extrusive and intrusive magmatic emplacement during its syn-rift phase. In extreme cases of thinning, tracts of exhumed mantle are exposed at the seafloor surface (Péron-Pinvidic and Manatschal, 2010; Reston, 2009; Péron-Pinvidic et al., 2019). Some rifted margins display a hybrid magmatic evolution with an early magma-poor stage followed by a later magma-rich phase, or vice-versa (Armitage et al., 2011; Lundin and Doré, 2011; Belgarde et al., 2015; Gernigon et al., 2015).

Péron-Pinvidic et al. (2013, 2019) have divided magma-poor margins into four, sub-parallel crustal domains: 1) Proximal domain, the zone where continental crust underlying the land area or shelfal area of the passive margin has undergone limited stretching; grabens and half-grabens bounded by normal faults in this domain sole out at mid-crustal levels. Due to the low amount of extension, only a modest amount of surficial accommodation is created by rifting (Péron-Pinvidic et al., 2013; Tugend et al., 2015); 2) Necking domain, underlies the outer shelf and slope of the passive margin where the thinned continental crust is tapered to a wedge-shape (Péron -Pinvidic and Manatschal, 2009; Mohn et al., 2010; Sutra et al., 2013); 3) Distal domain, underlies the deep basinal area of the passive margin and can include disparate structural domains associated with the ocean-continent transition such as: volcanically-thickened transitional crust; volumes of SDRs; areas of exhumed mantle; and hyperextended zones of continental crust (Péron-Pinvidic et al., 2013; 2019); and 4) Oceanic domain, underlies the distal passive margin and abyssal plain and is marked by the steady-state production of oceanic crust at a spreading ridge; this type of early-formed oceanic crust can vary widely in its thickness, composition, and other geophysical characteristics (Péron-Pinvidic et al., 2013).

Although magma-rich margins are generally less studied than magma-poor margins (Abdelmalak et al., 2015), the defining characteristics of magma-rich margins include: large volumes of extrusive volcanics, including thick SDRs, complex networks of intrusive rocks in the middle crust, and HVLC in the lower crust (Geoffroy, 2005). Volcanic rocks interbedded with layers of sedimentary rocks are expressed as SDRs and are thought to result from the accretion of magma flows during rifting, breakup, and initial seafloor accretion (Hinz, 1981; Mutter et al., 1982; Geoffroy, 2005; Buck, 2017; Reuber and Mann, 2019). Their distinct seismic architecture has been explained by either normal faulting (Hinz, 1981; Geoffroy, 2005; Paton et al., 2017; Quirk et al., 2014) or through a combined effect of volcanic loading and margin subsidence (Bodvarsson and Walker, 1964; Mutter et al., 1982; Buck, 2017; Reuber and Mann, 2019). Some authors have suggested that normal faults, volcanic loading, and subsidence do not occur synchronously but rather at different times during margin evolution (McDermott et al., 2018). Landward, these SDRs onlap and thin onto extended continental crust and possibly over pre-SDR sedimentary basins (Abdelmalak et al., 2015). Oceanward, SDRs overlie HVLC that is inferred to have been emplaced at some time during the rifting process (Schnabel et al., 2008) and is likely related to mantle upwelling prior to the formation of normal oceanic crust (Kelemen and Holbrook, 1995; Boutilier and Keen, 1999; Korenaga et al., 2000).

I interpreted a large seismic reflection dataset over the shelf, slope, and deep basinal area of the Camamu-Almada basin that straddles the area between full-thickness continental crust exposed on the onland area of northeastern Brazil and normal oceanic crust of the deepwater abyssal plain. The seismic dataset included: 1) two 200 km-long, high-resolution, long-offset, pre-stack depth migration (PSDM) seismic reflection profiles provided by ION Geophysical; and 2) 19,000 line-km of 2D reflection seismic surveys and well logs provided by the Brazilian Agência Nacional do Petróleo, Gás Natural e Biocombustíveis (ANP).

2D gravity models were created to test four simple crustal transitions described by workers from the study area (Blaich et al., 2010; Loureiro et al., 2018) or from other analogous margins (Gillard et al., 2015; Torrado, 2018; Reuber and Mann, 2019). Following these results, a more complex crustal model was proposed for the Camamu-Almada rifted margin and compared the proposed crustal structure to that of its west African conjugate, the South Gabon margin (Epin et al., 2021). The Camamu-Almada rifted-passive margin was then contrasted to a very similar, magma-poor margin in the Gulf of Lion within the western Mediterranean Sea (Jolivet et al., 2015). Seafloor spreading rates and heat flow were then measured in the zone of transitional crust of the Camamu and the Almada sub-basins and compared to other margins worldwide (Maliverno, 1991; Goff, 1991, 1992; Goff et al., 1995; Neumann and Forsyth, 1995; Minshull 1999; Weigelt and Jokat, 2001; Ehlers and Jokat, 2009; Sauter et al., 2011; Sauter et al., 2018; Lucazeau, 2019).

Figure 3.1 a) General location map showing the conjugate northeastern coast of Brazil and southwestern coast of Africa. The conjugate Camamu-Almada and South Gabon basins are located within a Paleoproterozoic orogenic belt that included the now separated Archean São Francisco craton of eastern Brazil and the Congo craton of western Africa. Generalized structural trends from these cratons shown in black (Gray et al., 2008), large igneous provinces in ochre (Coffin and Eldholm, 1994), and large salt-filled sag basins in pink (Davison, 2007). Ages of oceanic crust were based on magnetic isochrons from Seton et al. (2020) and are contoured on a 30 My interval. **b)** Total horizontal derivative map of the Bouguer gravity map over the rifted-passive margin of northeastern Brazil. Solid black lines denote interpretations from Péron-Pinvidic et al. (2013) and dashed black lines denote interpretations from this study. Giant hydrocarbon field locations from a compilation by Merrill and Sternbach (2017) are shown as white dots. Black dotted line denotes 108 Ma Q2 seafloor spreading anomaly within oceanic crust from Granot and Dyment (2015). **c)** Total horizontal derivative map of the Bouguer gravity over the western African margin with same features shown on the map in Figure 3.1b.

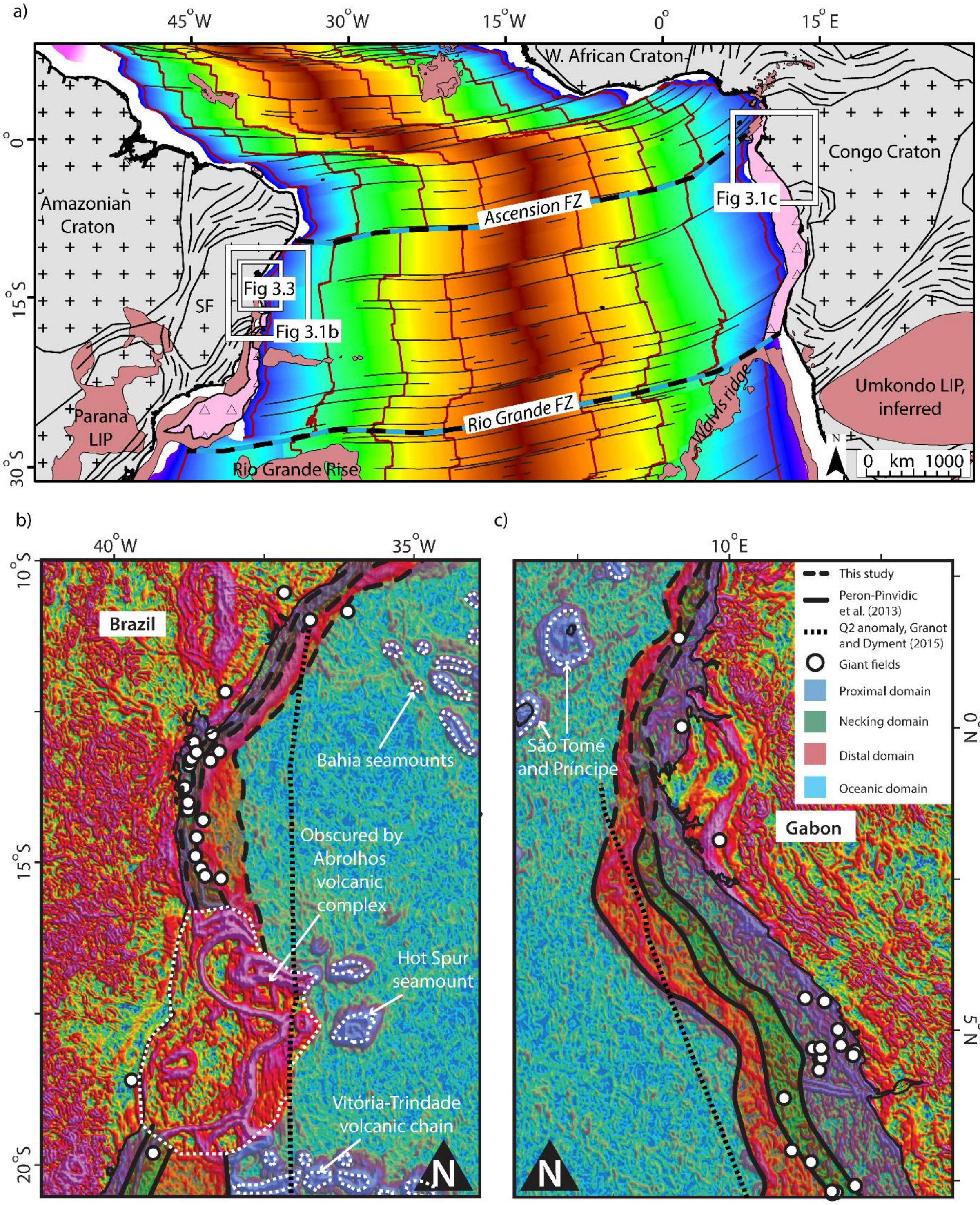
a)
45°W
30°W
15°W
0°
15°E
0°
15°S
30°S
W. African Craton
Congo Craton
Amazonian Craton
Ascension FZ
Fig 3.1c
Fig 3.3
Fig 3.1b
SF
Parana LIP
Rio Grande FZ
Walvis ridge
Rio Grande Rise
Umkondo LIP, inferred
0 km 1000
b)
40°W
35°W
10°S
15°S
20°S
Brazil
Bahia seamounts
Obscured by Abrolhos volcanic complex
Hot Spur seamount
Vitória-Trindade volcanic chain
N
c)
10°E
0°N
5°N
São Tomé and Príncipe
Gabon
N
This study
Peron-Pinvidic et al. (2013)
Q2 anomaly, Granot and Dyment (2015)
Giant fields
Proximal domain
Necking domain
Distal domain
Oceanic domain

3.1.1 Previous interpretations, problems, debates, and open questions

The rifted-passive margins of the South Atlantic contain examples of both magma-rich and magma-poor endmembers. Magma-rich rifted margins are found 1,800 km to the south of the Camamu-Almada in the Pelotas basin and 200 km to the north of the margin within the Sergipe-Alagoas basin. These magma-rich margins are characterized by <10 to more than 15 km-thick, magmatic "seaward-dipping reflectors" or "SDRs" that overlie large intrusives into thinned continental or thickened, oceanic crust (McDermott et al., 2018; Reuber and Mann, 2019). 1000 km south of the Camamu-Almada, most workers consider the Campos, Santos, and Espírito Santo basins to be non-volcanic margins where exhumed mantle may have unroofed in the distal zone (Zalán et al., 2011; Zalán, 2015), although other workers have proposed differing interpretations (Kumar et al., 2012; Evain et al., 2015; Klingelhoefer et al., 2014).

Understanding the tectonic and geologic history of the Camamu-Almada margin has proven difficult because there have been limited deepwater geological study and exploration (Scotchman and Chiossi, 2009). Understanding of its conjugate Gabonese margin is somewhat more advanced than Camamu-Almada, although thick Aptian salt deposits obscure the deeper crustal imaging of syn- and pre-rift strata in offshore Gabon (Rao and Yang, 2019). Limited data from both conjugate margins have led to multiple hypotheses for the crustal structure and compositions of the disparate basement blocks within the rifted transition zone.

The Camamu-Almada-Gabon conjugate pair has been classified as either a magma-poor rifted margin (Loureiro et al., 2018), a magma-rich rifted margin (Coelho et al., 2019), or a rifted margin with both characteristics (Blaich et al., 2010). Magma-poor proponents for the

Camamu-Almada basin point to: 1) interpretations of 2D and 3D seismic reflection datasets that showed a lack of extensive SDR development; 2) the absence of an adjacent, onland, large igneous province (LIP); and 3) the presence of hyperextended continental crust (Gordon et al., 2013). Proponents for a magma-rich Camamu-Almada rifted margin point to extrusive syn-rift volcanics drilled in the Sergipe-Alagoas to the north and correlative events inferred from seismic and gravimetric data throughout the Camamu-Almada (Caixeta et al., 2014). Blaich et al. (2010) proposed a hybrid margin with an initial magma-poor environment that was superimposed by a later stage of magmatic activity and emplacement of igneous crust before breakup.

Figure 3.2 a) Free-air gravity anomaly map from Sandwell et al. (2014) of the Camamu-Almada rifted-passive margin and its surrounding areas. Black dashed lines denote proposed structural/compositional contacts based on this study. **b)** Total horizontal derivative of the Bouguer gravity anomaly with white dashed lines marking on- and offshore structural features. Paleozoic structural grain of basement rock is roughly north-south and orthogonal to the Berriasian-Albian direction of rifting. **c)** On this EMAG 2v3 magnetic anomaly map (Meyer et al., 2017) of the study area, the longer wavelengths can be explained by deeper basement and shorter wavelengths by shallower basement. Black hatched line delineates rough boundary between the two; **d)** Comparison of proposed continental-oceanic boundary, or COB, of Müller et al. (2016) and Blaich et al. (2009), later re-interpreted as a continental-transitional boundary in Blaich et al. (2010). Pink polygon is the salt-filled sag basin (Davison, 2007), black polygon is a large seamount (Davison, 2007), and the ochre polygon is the extent of the Abrolhos Magmatic Province of Eocene to Miocene age as defined by Coffin and Eldhom (1994). Topographic basemap was modified from Amante and Eakins (2009).

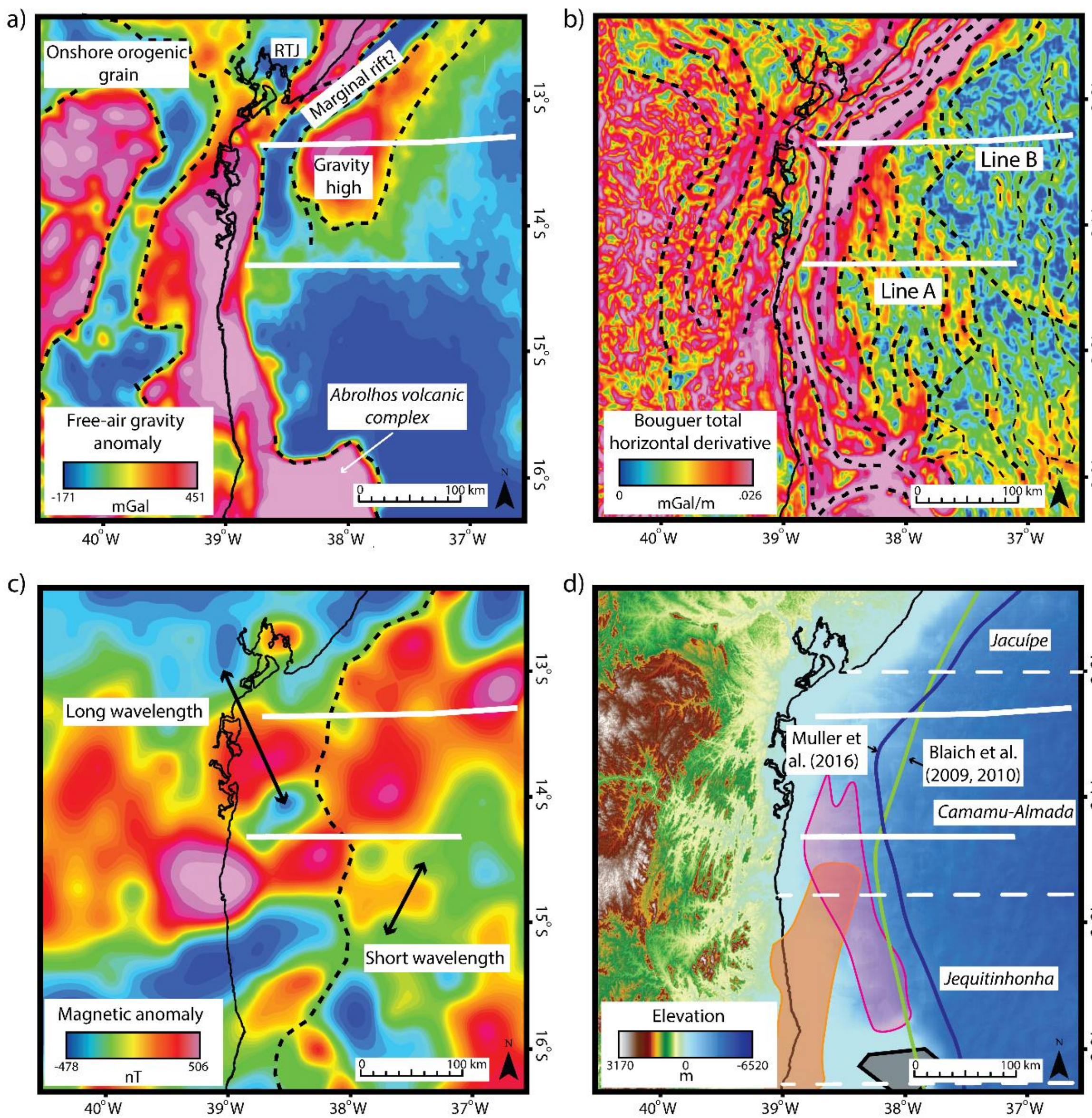
a)
Onshore orogenic grain
RTJ
Marginal rift?
Gravity high
Abrolhos volcanic complex
Free-air gravity anomaly
-171
451
mGal
0
100 km
b)
Line B
Line A
Bouguer total horizontal derivative
0
.026
mGal/m
c)
Long wavelength
Short wavelength
Magnetic anomaly
-478
506
nT
d)
Jacuípe
Muller et al. (2016)
Blaich et al. (2009, 2010)
Camamu-Almada
Jequitinhonha
Elevation
3170
0
-6520
m
40°W
39°W
38°W
37°W
13°S
14°S
15°S
16°S

3.1.2 Geologic setting of the Camamu-Almada passive-rifted margin

The Camamu-Almada basin, and its conjugate South Gabon basin of western Africa, formed as part of a continuous, Paleoproterozoic orogenic belt of the 40 km-thick Archean São Francisco-Congo cratons (Assumpção et al., 2013) (Figure 3.1). These orogenic belts, the Eastern Bahia orogenic belt in Brazil and the West Central African orogenic belt in Africa, collectively formed during the Paleoproterozoic period of Gondwana collision and amalgamation of the São Francisco and Congo cratons (Alkmim and Martins-Neto, 2012). The Berriasian-Albian rift-parallel, orogenic grain of the Paleoproterozoic orogenic belt is prominent in the onshore area Brazil from gravity, magnetic, and digital elevation model (DEM) maps (Figure 3.2–3.3). There is a slight variation in the orogenic trends from north-south along the Almada sub-basin to a slightly southwest-northeast trend along the Camamu sub-basin (Figure 3.2–3.3).

The Cretaceous break-up of Gondwana propagated diachronously from south to north (Rabinowitz and LaBrecque, 1979; Matos, 2000). Wider rift zones formed where the rift tip encountered relatively stronger orogenic grains at a high angle, whereas more narrow rifts formed where the rift tip opened parallel to the relatively weaker orogenic trends, as in the Camamu-Almada area (Reuber and Mann, 2019). The inverted V-shaped area of South Atlantic oceanic crust that resulted from the northward propagation of the rifting and formation of oceanic crust is subdivided into four areas of oceanic crust bounded by large oceanic fracture zones: 1) the southernmost **Falkland segment** of oceanic crust located south of the Falklands-Alguhas fracture zone; 2) the **South segment** formed between the Falklands-Alguhas and the Rio Grande fracture zones; 3) the **Central segment** between the Rio Grande and the Ascension fracture zones, containing the Camamu-Almada and Gabon conjugate margins; and 4) the northernmost **Equatorial segment** between the Ascension and the Marathon fracture zones (Figure 3.1).

Within the northern Central segment, initial amagmatic rifting in the Neocomian (135 to 122 Ma) occurred along a triple junction whose three arms included the Recôncavo-Tucano-Jatobá rift (RTJ), the Jequitinhonha-Almada-Camamu rift (JAC), and the Jacuípe-Sergipe-Alagoas (JSA) (Netto, 1978; Netto and Oliveira, 1985; Milani and Davison, 1988; Chang et al., 1992; Magnavita et al., 1994) (Figure 3.1). This triple junction remained active until the RTJ rift was abandoned in the Aptian, and the JAC underwent several pulses of concurrent rifting punctuated by periods of quiescence (Ferreira et al., 2011). During this time, widespread magmatism affected the Sergipe-Alagoas segment of the rifted-passive margin in northeastern Brazil. Faulting and rifting propagated eastward along the JAC until the advent of early Albian marine incursions that accompanied crustal break-up and initial emplacement of oceanic crust (Caixeta et al., 2014).

3.2 Data used in this study

The centerpiece of the dataset used in this study were two high-resolution long-offset Kirchhoff pre-stack depth migrated seismic reflection lines acquired and processed by ION Geophysical. These two dip profiles extend a total of 415 km across the rifted-passive margin and were collected by ION in 2012 as part of their Greater BrasilSPAN program. On both lines, the original pre-stack time-migrated seismic reached a record length of 18 seconds. Kirchhoff pre-stack time and depth migrations were performed by ION following their processing workflows, summarized by Sauter et al. (2016). I also interpreted older time-migrated seismic reflection data that were provided by ANP and included four seismic reflection surveys. Three surveys were acquired by GECO AS, two in 2001 and one prior to 1998, with seismic record lengths between 12 to 18 seconds. The fourth seismic dataset was acquired by multiple operators, reprocessed by Gaia in 2001, and included seismic lines of various vintages and record lengths (Table 1) (Figure 3.3).

Well data used within this study were also obtained from ANP and included 105 boreholes within the area of the Jacuípe, Camamu, Almada, and Jequitinhonha basins (Figure 3.3). Well locations were mainly from the shelf (water depths < 50 m) with only a few deepwater wells (water depths > 2000 m). Over half these wells were dry holes, with the remainder reporting hydrocarbon shows, technical successes, and commercial successes, especially from those wells drilled on the shelf (Table 2). Total depth ranges for wells vary from 100 m to more than 6500 m, with a few wells penetrating Paleoproterozoic basement beneath the rift section.

On- and offshore seismic refraction data from Rivadeneyra-Vera et al. (2019) and Loureiro et al. (2018) were integrated into the 2D and 3D modeling of the Camamu-Almada basins. Potential fields data were also integrated and included regional magnetic and gravity anomaly grids from Sandwell et al. (2014) and Meyer et al. (2017).

Table 3.1 Reflection seismic data and selected acquisition parameters

	Greater BrasilSPAN	0258_2D_SPEC_BM_CAL	0258_2D_SPEC_BM_J	R0003_BAHIA_SUL	0239_BAHIA_SUL_15A
Vintage	Since 2009	21/06/2001	21/06/2001	Various, reprocessed 1/12/2001	Pre-1998
Processing	Pre-stack depth migrated	Time-migrated	Time-migrated	Time-migrated	Time-migrated
Acquisition Company	ION Geophysical	GECO AS	GECO AS	Gaia	GECO AS
Offset	10 km	Unknown	Unknown	Unknown	Unknown
Record Length	18 s	12 s	12 s	Various	17.5 s
Total Length	415 km	6,193 km	2,732 km	9,225 km	375 km
Depth units	Depth	Time	Time	Time	Time
Archived	ION Geophysical	ANP	ANP	ANP	ANP

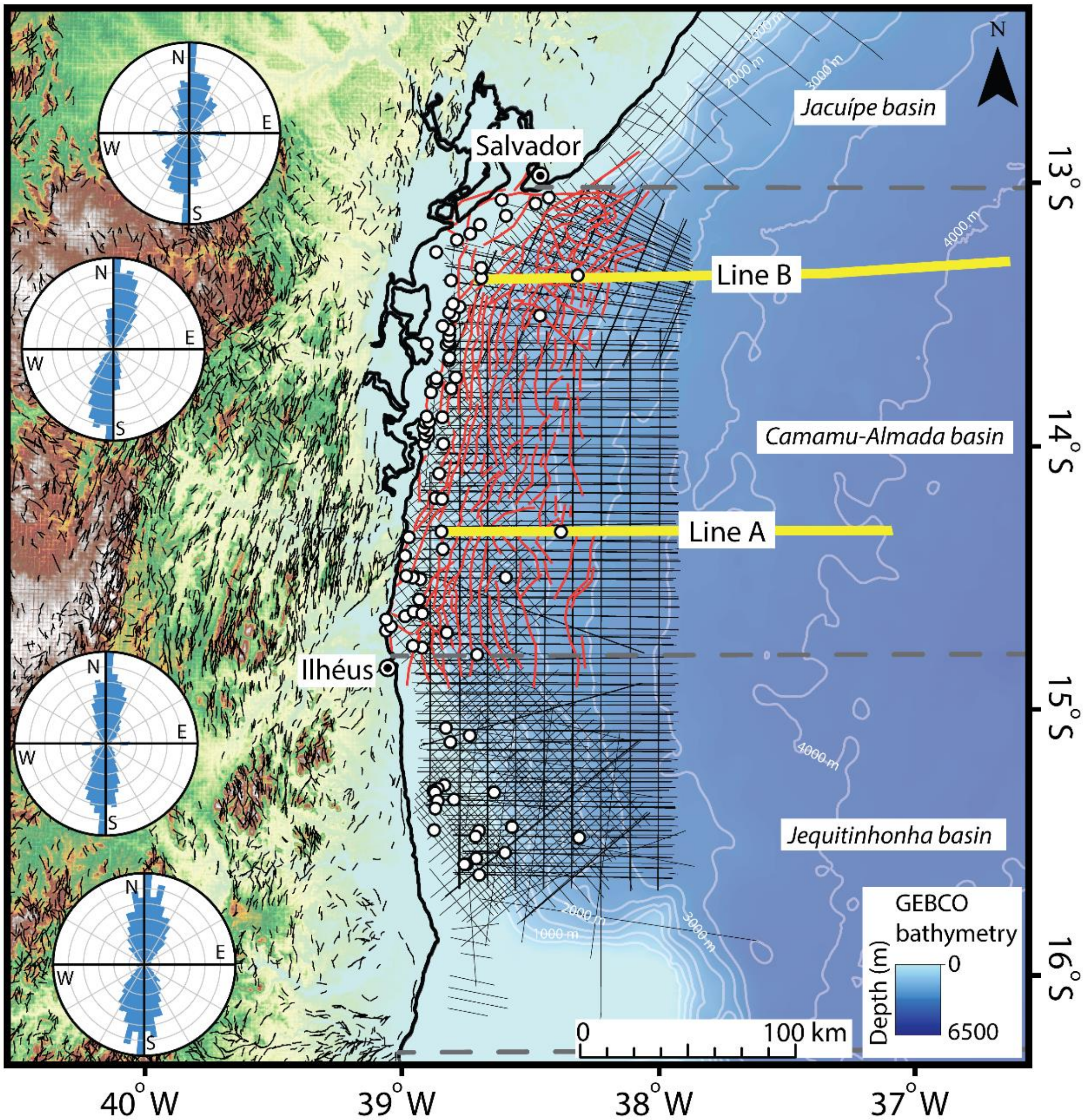

Figure 3.3 Map showing the dataset used for the study area that included 2D time reflection seismic shown as thin black lines, well logs shown as white circles, and PSDM reflection seismic lines in the area shown by the yellow lines. Mapped offshore basement faults compiled from Ferreira (2009) are shown as red lines and show a roughly east-west opening direction for the Almada sub-basin with a more northwest-southeast opening direction for the Camamu sub-basin. Rose diagrams summarize orientation of basement fabric and Cretaceous rift-related normal faults within the Precambrian São Francisco craton (black lines).

Table 3.2 ANP wells used in the study

Well name	Latitude	Longitude	Basin	Year	Status	Driller depth	Archived
1-BAS-3-BA	-38.96	-14.61	Almada	1971	Dry	3526	ANP
1-BAS-4-BA	-38.61	-13.06	Camamu	1972	Dry	2827	ANP
1-BAS-5-BA	-38.78	-13.21	Camamu	1971	Gas, subcommercial	2343	ANP
1-BAS-7-BA	-38.70	-16.07	Jequitinhonha	1971	Dry	3874	ANP
1-BAS-8-BA	-38.71	-15.54	Jequitinhonha	1972	Dry	2881	ANP
1-BAS-9-BA	-38.83	-15.79	Jequitinhonha	1972	Dry	3104	ANP
1-BAS-13-BA	-38.96	-14.49	Almada	1973	Dry	2680	ANP
1-BAS-14-BA	-38.92	-14.62	Almada	1972	Dry	2071	ANP
1-BAS-19-BA	-38.99	-14.40	Almada	1973	Dry	960	ANP
1-BAS-20-BA	-38.80	-13.77	Camamu	1973	Oil, subcommercial	3548	ANP
1-BAS-21-BA	-38.82	-13.67	Camamu	1973	Dry	3397	ANP
1-BAS-27-BA	-38.70	-15.60	Jequitinhonha	1976	Dry	2215	ANP
1-BAS-29-BA	-38.42	-13.06	Camamu	1976	Dry	2937	ANP
1-BAS-30-BA	-38.73	-15.79	Jequitinhonha	1975	Dry	3890	ANP
1-BAS-32-BA	-38.69	-13.32	Camamu	1976	Dry	3044	ANP
1-BAS-35-BA	-38.83	-15.06	Jequitinhonha	1977	Dry	2891	ANP
1-BAS-37-BAS	-38.87	-15.29	Jequitinhonha	1979	Oil	1750	ANP
1-BAS-51A-BA	-38.86	-15.32	Jequitinhonha	1979	N/A	110	ANP
1-BAS-51-BA	-38.86	-15.32	Jequitinhonha	1979	N/A	141	ANP
1-BAS-51B-BA	-38.86	-15.32	Jequitinhonha	1979	N/A	112	ANP
1-BAS-51C-BA	-38.86	-15.33	Jequitinhonha	1979	Dry	1950	ANP
1-BAS-52-BA	-38.84	-15.27	Jequitinhonha	1979	Oil, subcommercial	2277	ANP
1-BAS-53-BA	-37.95	-12.70	Jacuípe	1980	Dry	2533	ANP
1-BAS-56-BA	-38.87	-15.35	Jequitinhonha	1979	Dry	1920	ANP
1-BAS-57-BA	-38.87	-15.43	Jequitinhonha	1980	Dry	2110	ANP
1-BAS-62-BA	-38.97	-14.33	Almada	1980	Dry	1076	ANP
1-BAS-63-BA	-38.79	-13.73	Camamu	1981	Dry	3942	ANP
1-BAS-64-BA	-38.87	-13.74	Camamu	1981	Oil	3457	ANP
1-BAS-65-BA	-38.81	-15.10	Jequitinhonha	1984	Dry	3025	ANP
1-BAS-67-BA	-38.86	-14.09	Camamu	1981	Dry	2646	ANP
1-BAS-68-BA	-38.71	-15.45	Jequitinhonha	1985	Oil/Gas show	4567	ANP
1-BAS-69-BA	-38.80	-16.05	Jequitinhonha	1982	Dry	1874	ANP
1-BAS-71-BA	-38.99	-14.63	Almada	1982	Dry	2942	ANP
1-BAS-72-BA	-38.86	-13.26	Camamu	1982	Dry	1288	ANP
1-BAS-73-BA	-38.87	-13.75	Camamu	1982	Gas	2560	ANP
1-BAS-74-BA	-38.88	-13.75	Camamu	1983	Oil	2830	ANP
1-BAS-75-BA	-38.82	-13.66	Camamu	1984	Dry	3595	ANP
1-BAS-77-BA	-38.87	-14.19	Camamu	1985	Oil, subcommercial	3399	ANP
1-BAS-78-BA	-38.98	-14.48	Almada	1985	Dry	1380	ANP
1-BAS-79-BA	-38.94	-14.57	Almada	1985	Oil, subcommercial	2956	ANP
1-BAS-80-BA	-38.63	-15.29	Jequitinhonha	1987	Dry	3513	ANP
1-BAS-81-BA	-38.80	-15.32	Jequitinhonha	1988	Dry	3710	ANP
1-BAS-82-BA	-38.96	-14.75	Almada	1988	Dry	2215	ANP
1-BAS-83-BA	-38.92	-14.75	Almada	1988	Dry	2904	ANP
1-BAS-84-BA	-38.59	-13.12	Camamu	1990	Dry	3952	ANP
1-BAS-88-BA	-38.93	-14.49	Almada	1993	Dry	4339	ANP
1-BAS-97-BA	-38.90	-13.94	Camamu	1992	Oil	2975	ANP
1-BAS-102-BA	-38.70	-14.77	Almada	1993	Dry	5200	ANP
1-BAS-107-BA	-38.84	-13.88	Camamu	1994	Oil show	2394	ANP
1-BAS-112-BA	-38.47	-13.08	Camamu	1996	Dry	2100	ANP
1-BAS-113-BA	-38.69	-13.16	Camamu	1995	Gas show	3819	ANP
1-BAS-118-BA	-38.84	-14.38	Almada	1996	Dry	4392	ANP
1-BAS-120-BA	-38.59	-15.51	Jequitinhonha	1997	Dry	3703	ANP
1-BAS-121-BA	-38.70	-15.44	Jequitinhonha	1998	Oil, subcommercial	3531	ANP
1-BAS-126-BA	-38.59	-14.49	Almada	2000	N/A	3438	ANP
1-BP-10-BAS	-38.37	-14.31	Camamu	2013	Dry	6725	ANP
1-BRSA-14-BAS	-38.81	-13.49	Camamu	2000	N/A	1828	ANP
1-BRSA-267-BAS	-38.73	-15.08	Jequitinhonha	2004	Dry	4575	ANP
1-BRSA-28-BAS	-38.45	-13.50	Camamu	2001	Oil show	5221	ANP
1-BRSA-5A-BAS	-38.73	-13.19	Camamu	2000	Gas	1773	ANP
1-BRSA-5-BAS	-38.73	-13.19	Camamu	2000	N/A	136	ANP
1-BRSA-614-BAS	-38.83	-14.69	Almada	2008	Dry	2825	ANP
1-BRSA-637D-BAS	-38.85	-14.19	Almada	2008	Oil/Gas, subcommercial	3225	ANP
1-BRSA-669-BAS	-38.30	-15.46	Jequitinhonha	2009	Oil	4618	ANP
1-BRSA-702-BAS	-38.69	-13.36	Camamu	2009	Gas	4625	ANP

1-BRSA-734-BAS	-38.85	-14.31	Almada	2009	Gas, subcommercial	4025	ANP
1-BRSA-748-BAS	-38.81	-13.37	Camamu	2009	Oil show	2428	ANP
1-BRSA-768-BAS	-38.56	-15.42	Jequitinhonha	2009	Oil	4425	ANP
1-COST-3-BAS	-38.84	-13.98	Camamu	2001	Dry	2029	ANP
1-ELPS-16D-BAS	-38.88	-13.79	Camamu	2007	N/A	3020	ANP
1-ELPS17DA-BAS	-38.88	-13.79	Camamu	2007	Gas	2896	ANP
1-ELPS-17D-BAS	-38.88	-13.79	Camamu	2007	N/A	2896	ANP
1-ELPS-5-BAS	-38.91	-13.88	Camamu	2001	Dry	1350	ANP
1-QG-5A-BAS	-38.74	-15.56	Jequitinhonha	2011	Gas	4700	ANP
1-QG-5-BAS	-38.75	-15.56	Jequitinhonha	2011	N/A	4700	ANP
1-STAT-7-BAS	-38.30	-13.35	Camamu	2011	Dry	3651	ANP
1-STAT-7i-BAS	-38.30	-13.35	Camamu	2011	N/A	2500	ANP
2-VBST-1-BA	-38.90	-13.61	Camamu	1962	Dry	1381	ANP
3-BAS-49-BA	-38.86	-15.28	Jequitinhonha	1979	Oil, subcommercial	1786	ANP
3-BAS-49D-BA	-38.86	-15.28	Jequitinhonha	1979	Oil, subcommercial	2025	ANP
3-BAS-50DA-BA	-38.87	-15.29	Jequitinhonha	1979	Dry	2160	ANP
3-BAS-50D-BA	-38.87	-15.29	Jequitinhonha	1979	N/A	1704	ANP
3-BAS-55D-BA	-38.87	-15.29	Jequitinhonha	1980	Dry	2160	ANP
3-BAS-61D-BAS	-38.87	-15.29	Jequitinhonha	1980	Oil	1889	ANP
3-BAS-99-BA	-38.91	-13.95	Camamu	1992	Oil/Gas	947	ANP
3-BAS-100-BA	-38.91	-13.94	Camamu	1992	Gas	909	ANP
3-BAS-101-BA	-38.90	-13.95	Camamu	1992	Dry	1050	ANP
3-BAS-108-BA	-38.89	-13.92	Camamu	1994	Oil	983	ANP
3-BAS-109-BA	-38.90	-13.96	Camamu	1994	Dry	999	ANP
3-BAS-110-BA	-38.90	-13.93	Camamu	1994	Gas	903	ANP
3-BAS-111-BA	-38.89	-13.90	Camamu	1994	Oil show	1281	ANP
3-BRSA-106-BAS	-38.82	-13.57	Camamu	2001	Oil	1651	ANP
3-BRSA-115-BAS	-38.80	-13.45	Camamu	2002	Gas	1670	ANP
3-BRSA-128-BAS	-38.84	-13.54	Camamu	2002	Oil/Gas show	1853	ANP
3-BRSA-135-BAS	-38.81	-13.55	Camamu	2002	Oil show	1536	ANP
3-BRSA-141-BAS	-38.80	-13.50	Camamu	2002	Oil	1860	ANP
3-BRSA-599DP-BAS	-38.77	-13.47	Camamu	2008	Oil	3506	ANP
3-ELPS-11-BAS	-38.82	-13.61	Camamu	2003	Oil	1543	ANP
3-ELPS-6-BAS	-38.91	-13.90	Camamu	2001	Oil show	1020	ANP
4-BAS-116-BA	-38.91	-13.98	Camamu	1996	Dry	942	ANP
4-BRSA-529-BAS	-38.77	-13.47	Camamu	2008	Oil, subcommercial	3746	ANP
4-ELPS-10-BAS	-38.82	-13.60	Camamu	2003	Oil/Gas, subcommercial	1420	ANP
4-ELPS-12-BAS	-38.82	-13.61	Camamu	2003	Oil/Gas	1500	ANP
4-ELPS-13-BAS	-38.81	-13.61	Camamu	2003	Oil show	1500	ANP
6-BAS-115-BA	-38.92	-13.92	Camamu	1995	Dry	1048	ANP

Table 3.2 continued

3.2.1 Methods

3.2.1.1 Gravity interpretations

Initial regional gravity interpretations were based on the total horizontal derivative (THD) of the Bouguer gravity anomaly (Figure 3.2b). This filter represents the direct measure of the lateral changes of the gravity signal, with maximum gravity values corresponding to source edges (Cordell, 1979; Cordell and Grauch, 1985). This surface was created using a standard Bouguer terrain correction applied within Geosoft® Oasis Montaj to the gravity grid of Sandwell et al. (2014). Using the MAGMAP module, the THD of the Bouguer anomaly grid was calculated using the method of Cooper and Cowan (2008):

Equation 3.1: $THD = \sqrt{(\frac{\partial G}{\partial x})^2 + (\frac{\partial G}{\partial y})^2}$

where G is the gravity anomaly, and x and y signify the horizontal direction of the first derivatives.

3.2.1.2 Seismic interpretation methodology

Interpretation of the two PSDM seismic reflection lines relied on stratigraphic tops interpreted from well logs, surfaces interpreted from the 2D seismic grid, and mapped surfaces compiled from published work (Cobbold et al., 2010; Ferreira, 2018; Loureiro et al., 2018). Following Tugend et al. (2015; 2018), the steps used for seismic interpretation included: 1) definition of first-order interfaces that included the seafloor, top of each rift stage, top of the basement, and seismic Moho in areas where it was recognizable (Figure 3.4 and 3.5); and 2) division of crustal types into normal continental, transitional crust of either oceanic or continental origin, and normal oceanic crust based on seismic character, crustal thickness, depth of their underlying seismic Moho, and refraction constraints from Loureiro et al. (2018) (Figure 3.4–3.5).

3.2.1.3 2D modeling methodology

The Almada sub-basin PSDM seismic Line A was chosen as the location for 2D forward gravity modeling because of its anomalously wide (110 km) transitional zone between thinned to hyperextended continental crust to the west and normal oceanic crust to the east (Figure 3.4). Along this line and within the GM-SYS module in Oasis Montaj, a 2D model was created and extended by 200 km to the east and west.

Block density was constrained with: 1) fifteen well logs compiled for this study; 2) results from published work (Loureiro et al., 2018; Rivadeneyra-Vera et al., 2019); and 3) average values based on global studies (Carlson and Raskin, 1984; Mooney et al., 1998) (Table 3). Detailed block geometries and internal layering for the 2D gravity model were interpreted based on first-order interfaces mapped across the 2D seismic grid and two, deep-penetration seismic lines, correlated well tops, and integration of refraction results (Loureiro et al., 2018; Rivadeneyra-Vera et al., 2019). Gravity control relied on the gravity grid of Sandwell et al. (2014) and magnetic data were obtained from the global study by Meyer et al. (2017).

Limitations on the interpretation of the seismic reflection data that I used to constrain the models fall into three categories: 1) errors associated with velocities, as the data were recorded in seismic travel time and not in depth; 2) errors associated with the imaging of a 3D geobody in 2D-space; and 3) errors associated with the recording and processing of the data (Tucker and Yorston, 1973).

3.2.1.4 3D modeling methodology

The initial input Moho structural grid was derived from the isostatic calculation following the method of Blakely (1995):

Equation 3.2: $d_m = h * \frac{\rho_t}{\Delta\rho} + d_s$

where d_m is the Moho depth, h is the elevation with regards to sea level, ρ_t is the load, $\Delta\rho$ is the density contrast at the base of the crust, and d_s is the isobaric Moho depth. The combined load includes thicknesses and densities of water, sediment, and crystalline crust. I took the density of water as 1.03 g/cc, the average density of the crust as 2.825 g/cc, and sediment density was approximated using an exponential decay function tied to well-derived density values. Total sediment thickness was calculated from the final seafloor and basement surfaces.

Depth conversion of the seafloor surface assumed a P-wave seawater velocity of 1500 m/s. Depth conversion of the basement surface was constrained by sonic logs from 65 wells that were calibrated by checkshots and compared to the PSDM seismic profiles and refraction results. The final bathymetric grid was merged with the satellite topography grid from Smith and Sandwell (1997). The final basement grid included the depth-converted basement surface derived from seismic interpretation merged with: 1) satellite-derived, onshore topographic grids of the exposed, mountainous areas (Smith and Sandwell, 1997); 2) basement depths of the onland Recôncavo basin integrated from work by Milani and Davison (1988); and 3) estimates of basement depth compiled from the CRUST 1.0 compilation in the deepwater, oceanic areas (Laske et al., 2013).

Structural inversion within Oasis Montaj GM-SYS 3D employed a Fourier transform technique for calculating potential field anomalies produced by uneven layers using the method of Parker (1973). Using the topographic, top basement, and sediment density grids as control, the isostatic Moho surface was inverted to a gravity anomaly convergence limit of 0.1 mGal. This surface was then constrained using Moho estimates from refraction stations and PSDM seismic reflection lines.

Table 3.3 Density information of sediment and lithospheric layers from multiple sources and authors

	Density ranges (g/cc)			
Source	Sediment	Crust	Upper Mantle	Type of data
Well data (ANP)	2.1-2.6			Density logs
Loureiro et al. (2018)	2.2-2.58	2.66-3.25 (continental)	3.32-3.33	Converted from seismic refraction velocities
Carlson and Raskin (1984)		2.86 - 3 (oceanic)		Worldwide estimates

Table 3.4 Magma-rich vs. magma-poor; a spectrum between two end members (modified from Gillard et al. 2015)

Margin Type	Defining features	Types of Crust	Processes	Type locations
Magma-poor	- Few magmatic additions - No or poorly-resolved seismic Moho - No or poorly-defined magnetic lineations	- Hyperextended continental crust - Unroofed lower continental crust - Exhumed continental mantle	- Low magmatic budget - Unroofing of deep crustal rocks	Newfoundland-Iberia (e.g., Druet et al., 2018); Gulf of Lion (e.g., Jolivet et al., 2015); Australian-Antarctic (e.g., Gillard et al., 2015)
Mixed	- Complex internal and compositional structure - Well-defined magnetic lineations - No or poorly-resolved seismic Moho	- Mixture of magma-poor and magma-rich types of crust	- Combination of magmatic accretion and tectonic exhumation	NW shelf of Australia (e.g., Belgarde et al., 2015); Mid-Norwegian (e.g. Lundin and Doré, 2011); India–Seychelles (e.g., Armitage et al., 2012)
Magma-rich	- Large volume of magmatic additions - Visible Moho - Well-defined magnetic lineations	- Magmatic underplating - Intrusive/extrusive (SDR) additions - Volcanic crust	- High magmatic budget - Adiabatic decompression melting of mantle	Pelotas basin (e.g., McDermott et al., 2018); Argentinian passive margin (e.g., Paton et al., 2017)

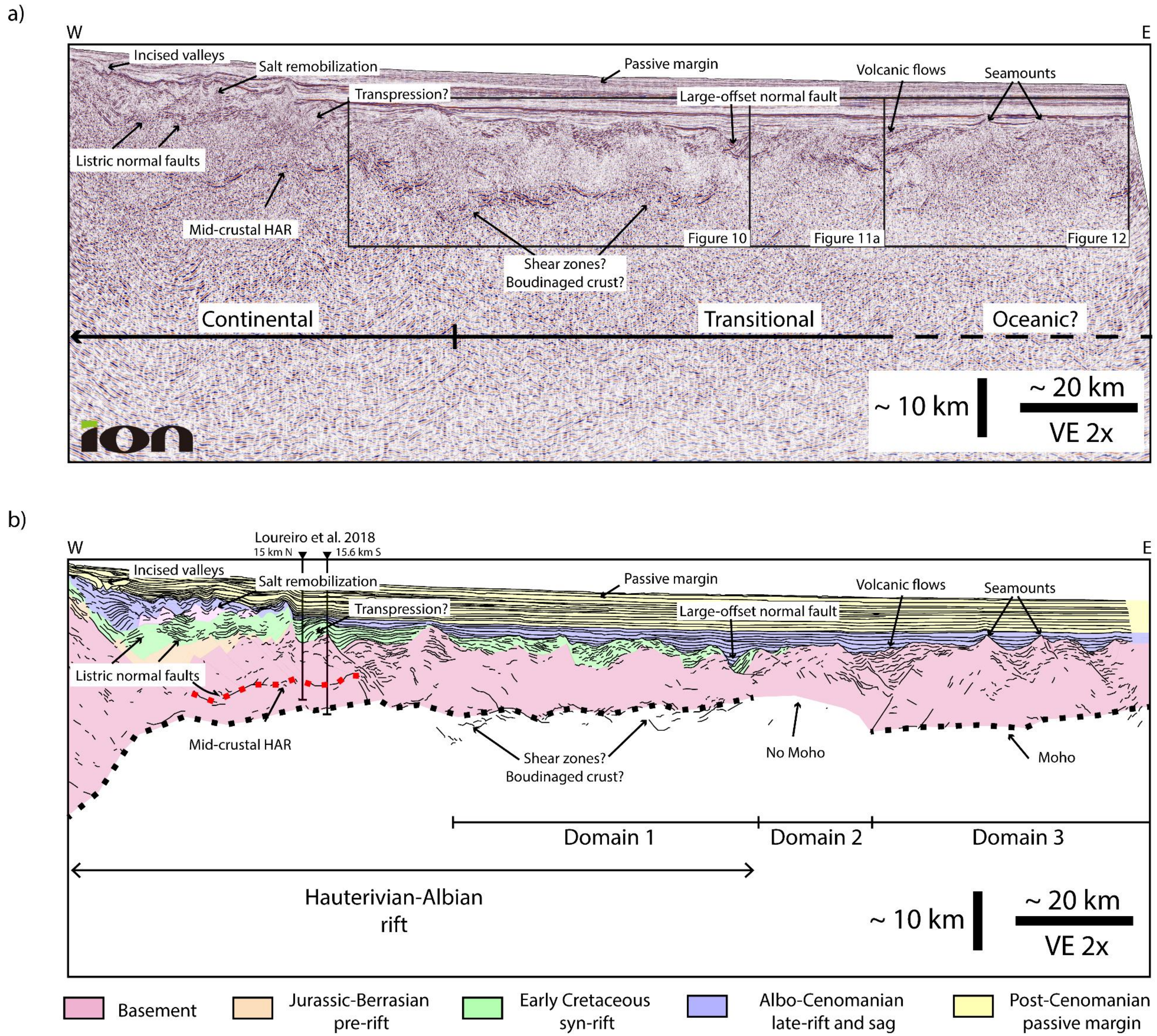

Figure 3.4 a) Seismic reflection Line A over the Almada sub-basin (see Figure 3.3 for location). **b)** Line drawing and interpretation of Line A showing major structures and stratigraphic packages. Note laterally varying seismic Moho signal and changes in the top crystalline crust reflector. Exact scales not included to protect data anonymity.

a)

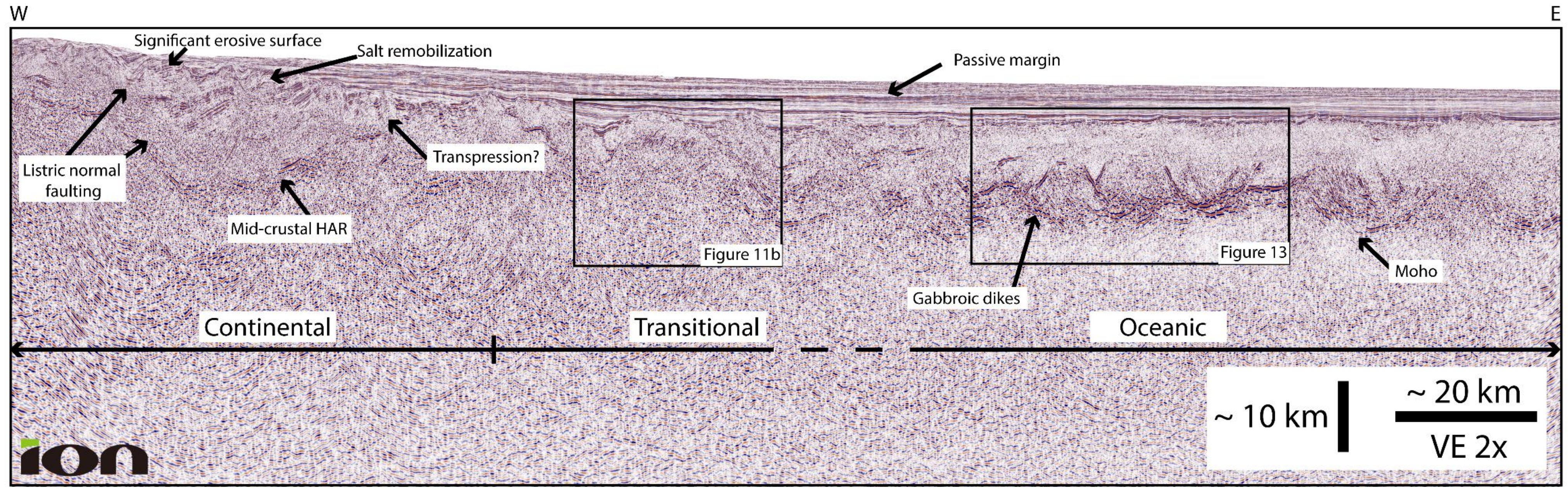

b)

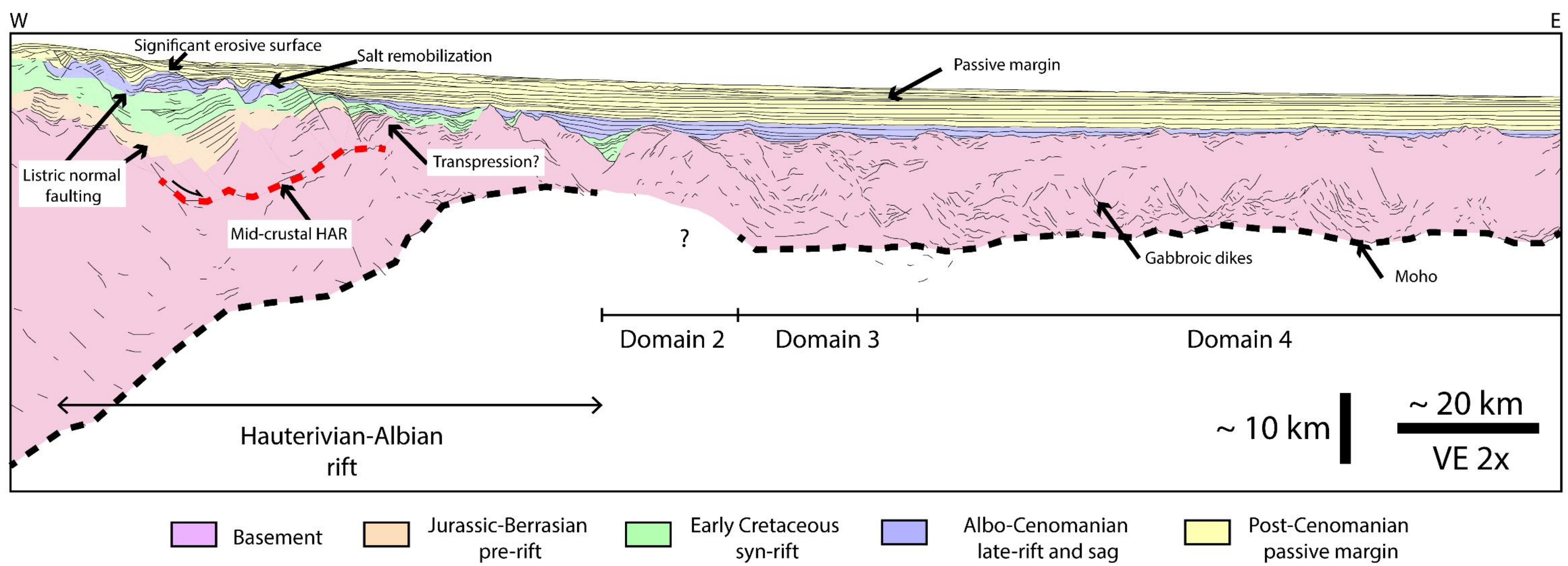

Figure 3.5 a) Seismic reflection Line B over the Camamu sub-basin (see Figure 3.3 for location). **b)** Line drawing and interpretation of Line B showing major structures and stratigraphic packages. Note laterally varying seismic Moho signal and changes in the top crystalline crust reflector. Exact scales not included to protect data anonymity.

3.3 Results and interpretation

3.3.1 Seismic observations

For interpretation of the two PSDM deep-penetrating reflection seismic, both seismic lines were subdivided based on seismically observable crustal features. The continental domain was defined as continental crust thicker than 5 km with thick overlying rifts; the transitional zone was defined as crust of indeterminate crustal composition, as thin as 3.5 km with highly faulted sediments, and having a laterally varying seismic Moho reflection; and the oceanic zone was defined as oceanic crust 6–8 km-thick with a strong Layer 2/3 differentiation and clear seismic Moho (Figure 3.4–3.5).

3.3.1.1 Line A; Almada sub-basin

Deeply-penetrating seismic reflection Line A traverses 190 km across the northernmost Almada sub-basin (Figure 3.3) and is located south of the area of lineated, free-air gravity anomaly lows and highs (Figure 3.2a). Both the total horizontal derivative interpretation and the basement fault interpretations of Ferreira (2009) in the Almada displayed south to north-trending structures indicative of a west-to-east Cretaceous rift direction (Figure 3.2b and 3.3).

Magnetic anomalies decrease in wavelength seawards, suggestive of a shallowing of the source depth of the underlying crust (Alldredge and Van Voorhis, 1961) (Figure 3.2c). This change in magnetic character roughly corresponds to previously proposed compositional/structural boundaries, including the continent-ocean boundary proposed by Müller et al. (2016) and the continent-transitional boundary proposed by Blaich et al. (2009;

2010) (Figure 3.2d). This seismic line is within the Aptian salt basin region defined by Davison (2007) and north of any large magmatic emplacements (Figure 3.2d).

The record depth of seismic Line A reached 40 km. Within the continental domain, crustal thicknesses decrease rapidly from 18 km to 10 km across a distance of 20 km, forming the necked zone. Sedimentary thicknesses and ages within grabens and half-grabens that overlie the necked zone indicate a seaward migration of the rift system (Ferreira, 2018).

As Davison (2007) noted, salt and salt-withdrawal mini-basins are present above this necked zone of continental crust. Large listric normal faults terminate across an area of sub-parallel, laterally continuous, high-amplitude reflectors (HAR; e.g., Mortimer et al., 2020) that is interpreted here as the mid-crustal boundary that separates the upper, brittle continental crust and the lower, ductile continental crust (Clerc et al., 2015) (Figure 3.4). Refraction control from Loureiro et al. (2018) was used to validate the observed seismic Moho interpretation present in this extended area (Figure 3.4).

In the seaward direction, the transitional zone can be separated according to the seismic Moho character that changes from a strong reflector, to area of indeterminate Moho reflector, and, finally, to an area where only a weak seismic reflector is observed (Figure 3.4). The strong seismic Moho appears as sub-parallel, wavy reflectors reminiscent of a sheared or boudinaged zone.

Crustal thicknesses above the strong Moho reflectors vary from 4 to 3.5 km, and the basement is overlain by 6 km of highly faulted sedimentary rock and unfaulted sag and passive margin sedimentary rocks (Figure 3.4).

40 km offshore, the seismic Moho either disappears or shallows dramatically (Figure 3.4). This change in Moho reflection character coincides with the location of several large-offset listric normal faults in the upper crust. The top of the crystalline crust across this 20 km-wide zone displays chaotic, intra-basement reflectors, mounding at the top basement surface, and overlying unfaulted sag and passive margin sedimentary rocks.

Near the easternmost end of the line, a weak seismic Moho is observed underlying a 6 to 7 km-thick crust. In this area, 1 km-high seamounts flanked by packages of divergent reflectors are observed overlying the top of the crystalline crust. Undeformed, thin sag deposits and thick passive margin sedimentation deposited over the top of crystalline basement and reach a maximum thickness of 5 km (Figure 3.4).

Figure 3.6 Summary of the contrasting crustal elements of the four crustal models for the broad rift zone of the Almada basin in the area vicinity of Line A that separates full thickness continental crust of the Brazilian craton and normal oceanic crust. **a)** Hyperextended continental crust with a sharp transition to oceanic crust. **b)** Hyperextended continental crust with an exhumed lower crust and a sharp transition to oceanic crust; the unroofing of lower continental crust likely occurs by the process of depth-dependent extension. **c)** Hyperextended continental crust, exhumed mantle, and a sharp transition to oceanic crust. **d)** Hyperextended continental crust, a broad transition zone into igneous/incipient oceanic crust, and normal oceanic crust.

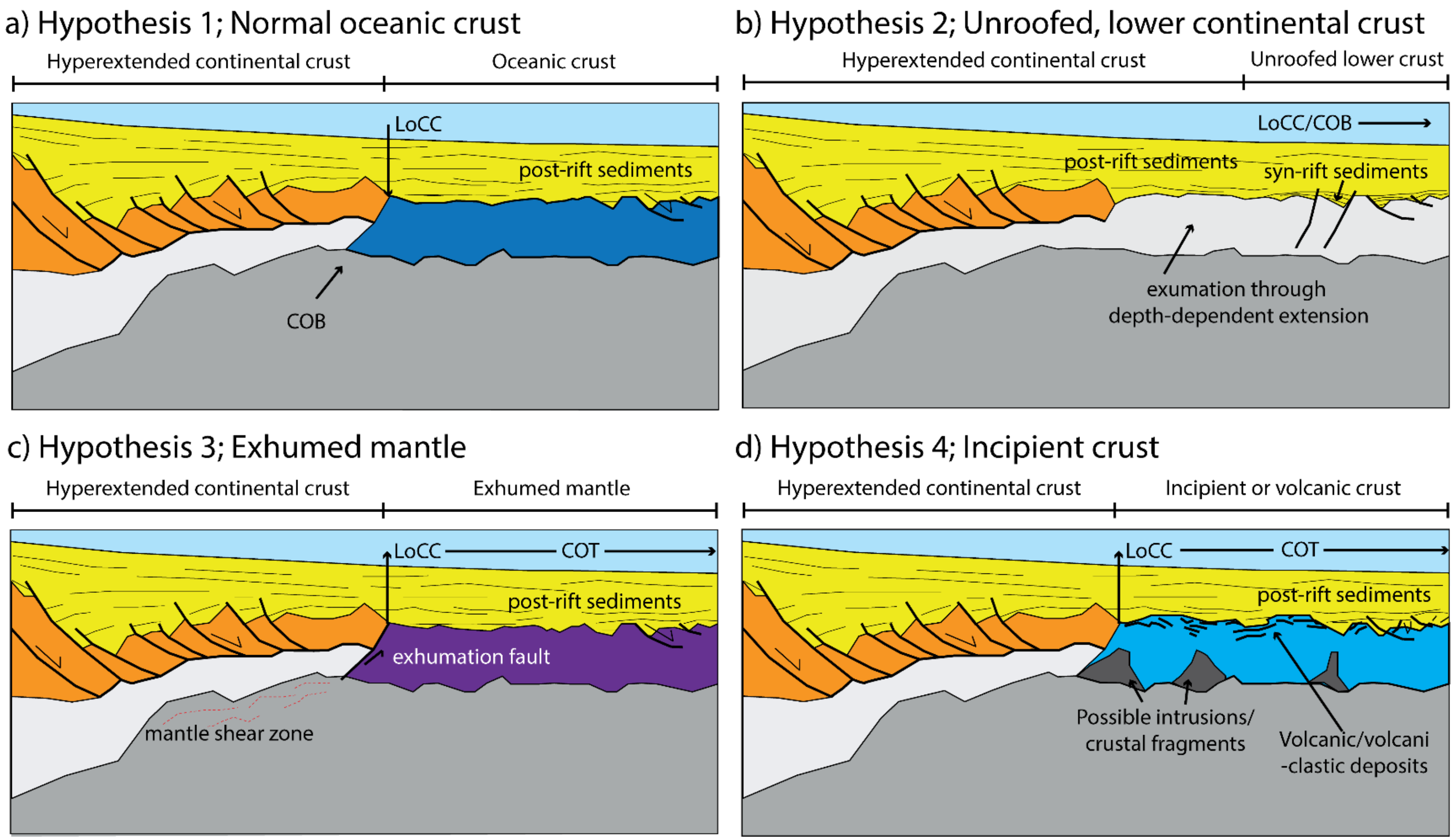
a) Hypothesis 1; Normal oceanic crust
Hyperextended continental crust
Oceanic crust
LoCC
post-rift sediments
COB
b) Hypothesis 2; Unroofed, lower continental crust
Hyperextended continental crust
Unroofed lower crust
LoCC/COB
post-rift sediments
syn-rift sediments
exumation through
depth-dependent extension
c) Hypothesis 3; Exhumed mantle
Hyperextended continental crust
Exhumed mantle
LoCC
COT
post-rift sediments
exhumation fault
mantle shear zone
d) Hypothesis 4; Incipient crust
Hyperextended continental crust
Incipient or volcanic crust
LoCC
COT
post-rift sediments
Possible intrusions/
crustal fragments
Volcanic/volcani
-clastic deposits

3.3.1.2 Line B; Camamu sub-basin

Deeply-penetrating seismic reflection Line B traverses 225 km across the Camamu sub-basin (Figure 3.3). Line B is located across a nearshore, linear free-air gravitational low that likely marks a narrow rift zone of extended continental crust (Figure 3.2a). Both the total horizontal derivative of free-air gravity and previous basement fault interpretations display southwest to northeast-lineated basement trends, indicative of a northwest-to-southeast opening direction (Figure 3.2b and 3.3). Magnetic anomalies decrease in wavelength seawards and match closely to previously mapped compositional/structural boundaries (Figure 3.2d). Line B is north of the previously-interpreted limit of Aptian salt and is also north of any large seamounts or magmatic plateaus in the marginal rift zone (Davison, 2007) (Figure 3.2d).

Crustal thicknesses within the continental zone are thicker than along line A and taper from 25 km to 8 km across a distance of 60 km. The tapered or necked continental crust is attributable to several, large, listric normal faults that terminate downward on the HAR. In contrast to the general acceptance of a lack of salt within these rift basins and overlying sag basins as summarized by Davison (2007), seismic reflection evidence suggests the presence of both salt pillows and salt-withdrawal mini-basins (Figure 3.5).

The zone of transitional crust within the Camamu basin is considerably narrower (40 km) than observed in the Almada basin (110 km). Moreover, the area of strong, divergent seismic Moho reflectors seen along Line A in the Almada basin (Figure 3.4) is not apparent along Line B crossing the Camamu basin (Figure 3.5).

At the western edge of the transitional zone in the Camamu sub-basin, a 20 km-wide zone of mounded, chaotic basement without a seismic Moho is apparent (Figure 3.5), strikingly similar to the equivalent area within the transitional crust of the Almada sub-basin (Figure 3.4). Overlying this zone, the 4 km-thick sedimentary sections display parallel-sided and conformable geometries that typify the sag and passive margin-style sedimentation (Figure 3.5).

Further seawards, a region of weak seismic Moho varies in depth from 6-8 km and is similar in thickness and seismic character to the deepwater crust of the Almada basin seen along Line A (Figure 3.4). The top of the crystalline crust displays low relief (400 m) mounded topography with a chaotic inner seismic character and small, flanking packages of divergent reflectors (Figure 3.5).

The easternmost portion of the Camamu sub-basin PSDM seismic line images a rough-surfaced crust with a strong Moho reflection (Figure 3.5) that was not seen along Line A within the Almada sub-basin (Figure 3.4). Two well-defined layers within the crust were interpreted: an upper layer about 2 km-thick with mostly homogeneous and transparent facies, and a lower layer about 6 km-thick with high-amplitude curvilinear reflections (Figure 3.5). Thin sag-related sedimentary deposits progressively thin and onlap onto this top crystalline crust. The total thickness of passive margin sedimentary rocks above the top basement reach a maximum thickness of 3.5 km.

3.3.2 2D gravity forward modeling

To understand the lateral changes in crustal composition across the Camamu-Almada margin, I tested four different hypotheses that have been proposed either specifically within the Camamu-Almada margin or elsewhere along the South Atlantic: 1) normal oceanic crust (e.g., Foz do Amazonas basin, Torrado, 2018); 2) unroofed lower continental crust (e.g., South China Sea, Deng et al., 2020); 3) exhumed mantle (e.g., West Galicia margin, Boillot et al., 1980; 1989; Druet et al., 2018); and 4) thickened igneous crust (e.g., South Pelotas Basin, Reuber et al., 2019) or "incipient" oceanic crust (e.g., Santos Basin, Klingelhoefer et al., 2014). These four hypotheses were tested by creating four seismically-constrained gravity models (Figure 3.7).

The four gravity models were created along the 190 km-long ION PSDM seismic reflection line within the Almada sub-basin (Figure 3.4). To ensure that each of the four gravity models tested the composition of the crust rather than structural differences, the seismically-interpreted structure shown in Figure 3.4 was kept constant and only the block densities were varied. Each model was extended 200 km both on- and off-shore. The onshore surface geology from the Geological Survey of Brazil showed that the Archean and Paleoproterozoic basement has been exposed at the landward end of the gravity transect, while the seaward end of the line is devoid of seamounts and was assumed to be normal ocean crust as shown on the CRUST1.0 global model (Laske et al., 2013). Refraction control from Loureiro et al. (2018) and Rivadeneyra-Vera et al. (2019) measured an onshore continental basement thickness and Moho depth of 40 km and an offshore continental basement thickness and Moho depth of 8 and 12 km, respectively (Figure 3.7).

Patterns in the magnetic character of the crust (Meyer et al., 2017) over Line A vary in wavelength and amplitude oceanward and can be roughly divided into four zones: 1) an area of short wavelengths over onshore continental crust, reflecting this extremely shallow or exposed area of basement; 2) a long-wavelength signal coinciding with the area of hyperextended continental crust that suggested locally deep basement within deeper upper crustal rifts; 3) short wavelength, low amplitude, near-zero signal as basement shallows across the area of transitional crust; and 4) short wavelength, high amplitude signal above offshore, normal oceanic crust.

3.3.2.1 Model 1: Normal oceanic crust (Figure 3.7a)

As a continental plate rifts and necks, it will reach a breaking point, and a mid-ocean ridge will form and begins to emplace normal oceanic crust next to the rifted continental crust (Wilson, 1966; Péron-Pinvidic et al., 2017). In this model, the end of the continental rift phase marks the beginning of the oceanic spreading phase (Figure 3.6a).

The hypothesis that the 110 km-wide transitional area of crust in the Almada sub-basin is underlain by normal oceanic crust was tested by the gravity model shown in Figure 3.7a. Several problems for the oceanic crust hypothesis were apparent in the comparison between observed and modeled results: 1) the large mismatch in the observed and modeled gravity anomaly indicated that actual transitional crust is either denser or thinner than modeled; 2) the observed gravity is not consistent with the accepted density range (2.8–2.9) for Layer 2/3 of normal oceanic crust (Carlson and Raskin, 1984); and 3) the varying seismic Moho across the zone.

a) Hypothesis 1: Normal oceanic crust

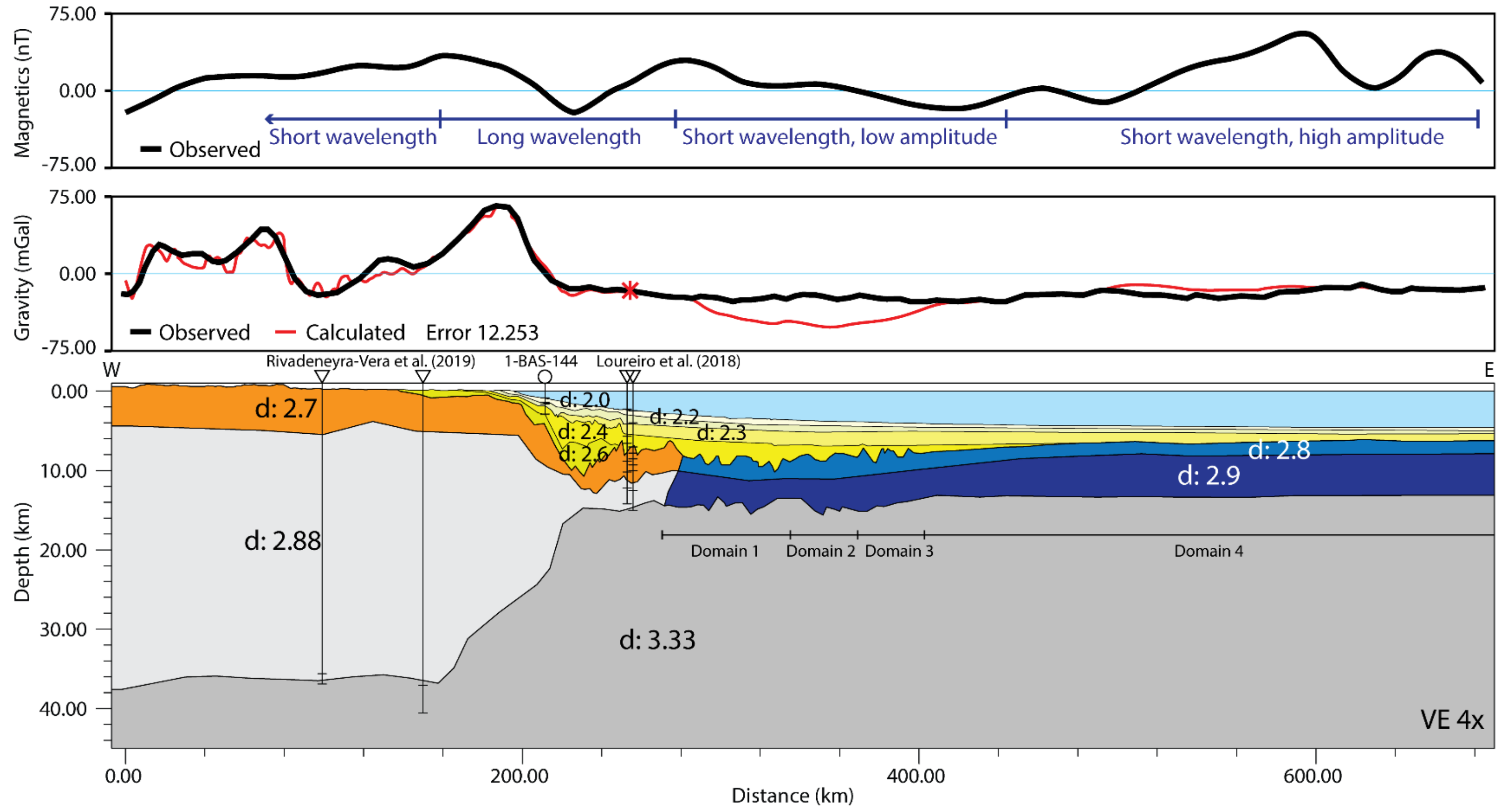

b) Hypothesis 2: Unroofed lower continental crust

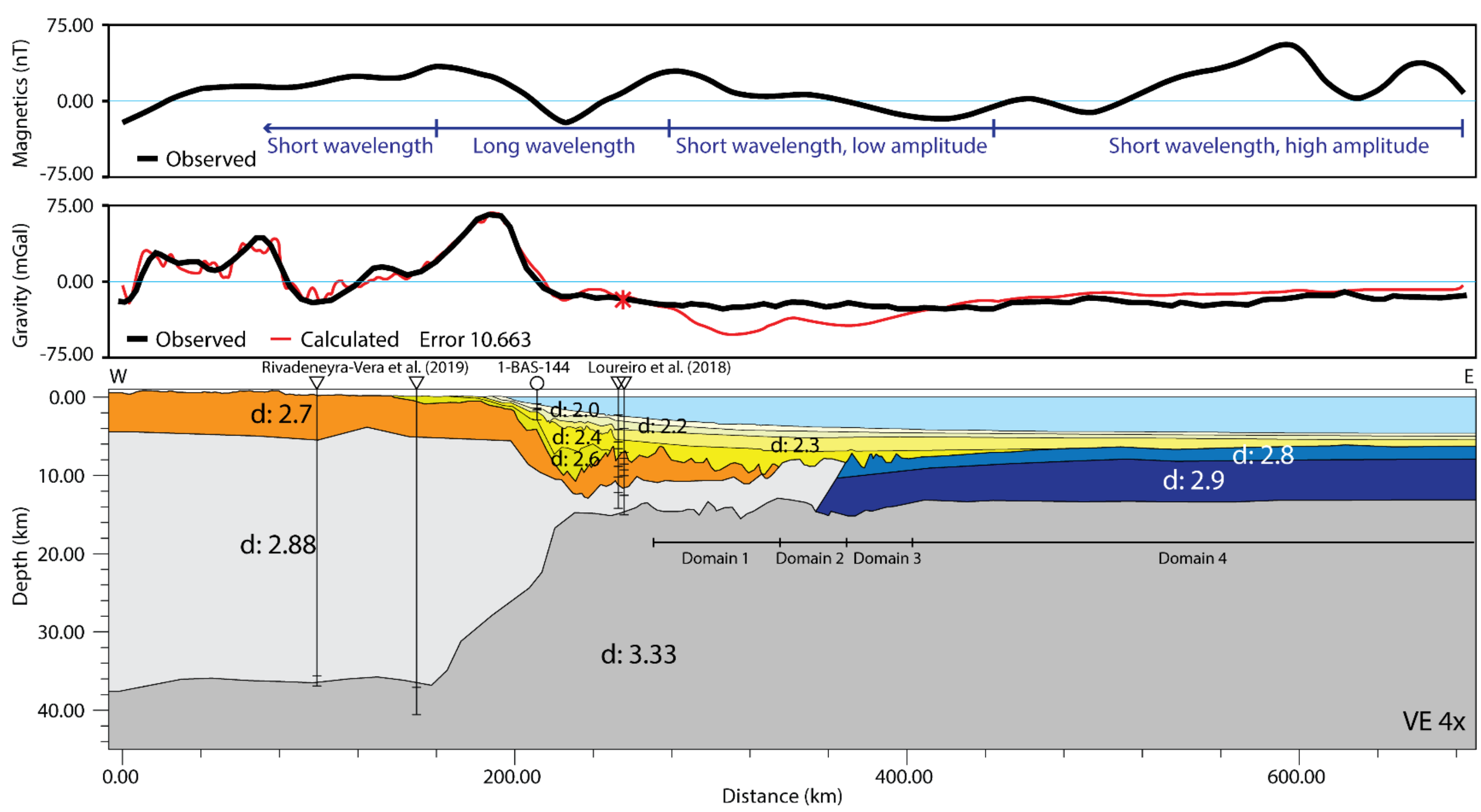

Figure 3.7 Gravity models testing the four differing crustal models shown in Figure 3.6: **a)** For the hyperextended hypothesis in Figure 3.6a, the predicted presence of a large area of normal oceanic crust produced a large gravity deficiency over the center of the transitional crust that was not observed. **b)** For the unroofed continental crust hypothesis in Figure 3.6b, the predicted presence of a large area of lower continental crust produced a large gravity deficiency over the middle of the transitional crust that was not observed. **c)** For the exhumed mantle hypothesis in Figure 3.6c, the predicted presence of exhumed mantle produced gravity variations in the transitional zone that were not observed. **d)** For the igneous/incipient oceanic crust hypothesis in Figure 3.6d, the predicted presence of upper, less dense volcanic flows and lower, denser oceanic or intruded continental crust produced gravity variations in the transitional zone that were not observed.

c) Hypothesis 3: Exhumed mantle

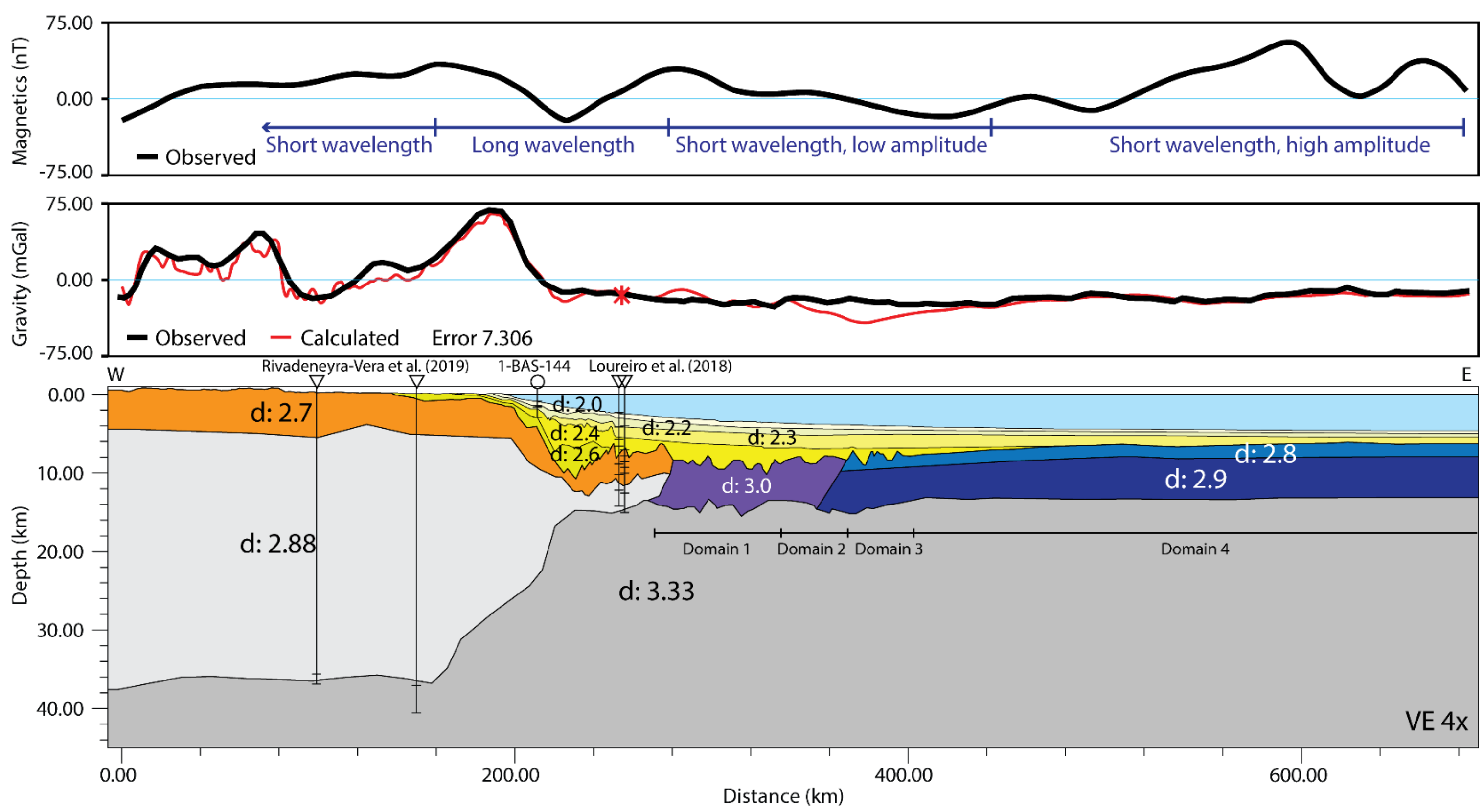

d) Hypothesis 4: Igneous/incipient crust

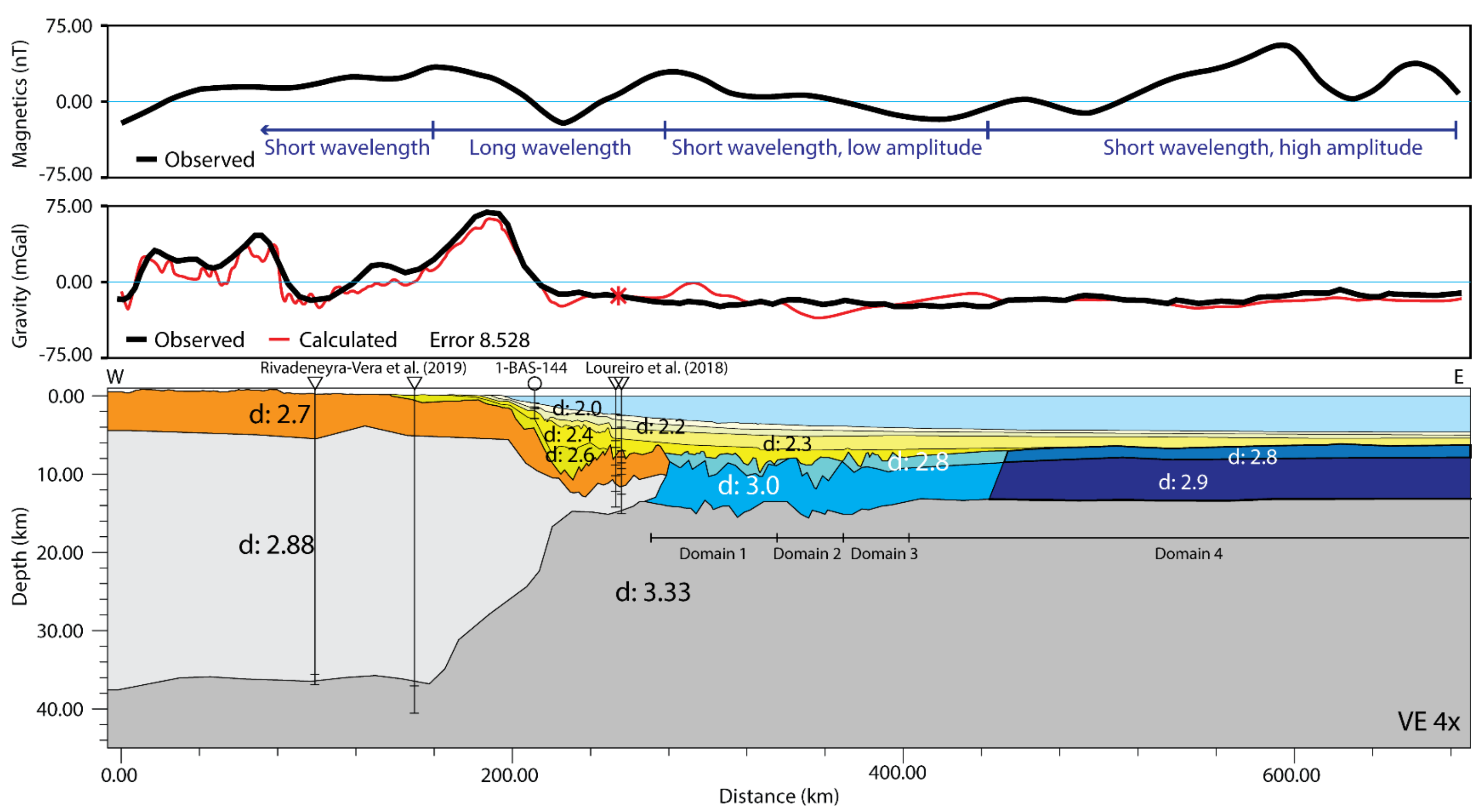

Figure 3.7 continued

3.3.2.2 Model 2: Unroofed lower continental crust (Figure 3.7b)

Theoretical models for the transition from continental necking to oceanic ridge formation began with simple or pure shear of the lithosphere (McKenzie, 1978) and have since been modified. One of these modifications, depth-dependent extension, was defined as lithosphere breakup with variable shear strain with depth (Royden and Keen, 1980; Kusznir and Karner, 2007). According to this model, the upper crust deforms along brittle normal faults while the lower crust deforms in a ductile mode; this difference in strain can lead to much higher strains at depth that are manifested by the preferential removal and exposure of parts of the lower crust and upper mantle (Huismans and Beaumont, 2014). Loureiro et al. (2018) had proposed this process of depth-dependent strain and unroofed, lower continental crust in the Jequitinhonha basin, south and directly adjacent to the study area (Figure 3.3).

The hypothesis that the 110 km-wide transitional area of crust in the Almada formed by depth-dependent stretching was tested in Figure 3.7. The main problem for this hypothesis included: 1) the modeled gravity response displayed a large deficiency across the transitional zone that would require a denser lower continental crust than is supported by estimates in this area (Loureiro et al., 2018), and 2) the lack of a seismic Moho reflector across two 20 km-wide zones in both the Camamu and Almada sub-basins (Figure 3.4–3.5).

3.3.2.3 Model 3: Exhumed mantle (Figure 3.7c)

Mantle exhumation occurs when spreading rates are so low that the continental crust necks and, in the absence of significant magmatic activity, the underlying mantle is exhumed and subsequently serpentinized by seawater (Huismans and Beaumont, 2014; Bodur, et al., 2018). Mantle exhumation has been documented by deep-sea drilling along the West Galicia margin (Boillot et al., 1980; 1989; Druet et al., 2018) and has been proposed within several different rifted-passive margins (Nemčok et al., 2012; Gillard et al., 2015; Tugend et al., 2018; Mortimer et al., 2020).

The hypothesis that the 110 km-wide transitional area of crust in the Almada contains exhumed mantle was tested in Figure 3.7c. This model resulted in the lowest total error out of any of the four models, with a minor gravity surplus over the continent-transitional contact and a moderate deficiency over the transitional-oceanic contact. Additionally, the magnetic signal over this zone is low amplitude and disorganized, perhaps suggesting a weakly-magnetic body as predicted for exhumed mantle lithologies (Bronner et al., 2014). However, while the intra-crustal seismic character can be explained by exhumed mantle's inner reflectivity and faulting (see seismic examples in Gillard et al., 2015; Tugend et al., 2018; McCarthy et al., 2020), this model was not supported by the semi-continuous and subhorizontal Moho observed underneath most of the crust within the transitional zone along Line A (Figure 3.4) and B (Figure 3.5).

3.3.2.4 Model 4: Igneous crust/incipient oceanic crust (Figure 3.7d)

Igneous crust along magma-rich margins can contain SDRs, intrusive bodies, and magmatic underplating. Reuber et al. (2019) synthesized a four-step model where: 1) lithospheric thinning occurs along with intrusive and extrusive volcanism; 2) the lithosphere completely ruptures and the high magmatic budget manifest in an initial volcanic pile; 3) successive volcanic flows continue to emplace basinward, rotate, and subside, leading to SDR geometries; and 4) oceanic crust begins to emplace as a spreading center forms. This evolution results in a margin with SDRs emplaced both on extended continental crust landward and on “igneous” crust basinward before creation of normal oceanic crust (Schnabel et al., 2008).

Incipient oceanic crust is defined as transitional oceanic crust formed in a magma-poor setting and lacking any clear seismic characteristics or typical velocity gradients (Hopper et al., 2004; Tugend et al., 2018). This type of crust has been documented by deep-sea drilling along the distal Iberia-Newfoundland margin (ODP sites 1070 and 1277; Shipboard Scientific Party, 1998; 2004). Recent drilling has shown that the earliest incipient oceanic crust created at the onset of ultra-slow spreading can include higher-density serpentinite underlying a layer of lower-density MORB-type basalt (Jagoutz et al., 2007; Tucholke and Sibuet, 2007). Incipient oceanic crust has also been described in the field on the Alpine Tethys rifted margin (Lower Platta nappe, Desmurs et al., 2002; Chenaillet ophiolite, Manatschal et al., 2011). It has been interpreted as extremely thin (Klingelhoefer et al., 2014; Bécel et al., 2020), thin with a 2 km thick layer 2 and 2-3 km thick layer 3 (Klingelhöfer et al., 2000), or as thicker crust that included both mantle and oceanic-derived crust (Tugend et al., 2018). Incipient oceanic crust is thought to form in ultraslow spreading centers and can consist of volcanic flows, tilted fault blocks with on-lapping fill, and splintered crustal sections. Compositionally, these can be either basaltic flows, serpentinized mantle, lower continental crust, upper continental fragments, or even a combination of all the above (Odegard et al., 2002). In analogous areas like the Southwest Indian Ocean, basaltic lava flows emplaced directly onto serpentinized mantle crust (Muller et al., 1997).

The hypothesis that the 110 km-wide transitional area of crust in the Almada formed by either igneous activity or non-steady state emplacement of oceanic crust was tested in

Figure 3.7d. The main problems for this hypothesis included: 1) while the overall gravity error is low, gravity surpluses existed over the flanks of the crust while a gravity deficiency is modeled over the middle of the body; 2) there is no evidence for magmatic thickening of the crust as from SDR features; and 3) the magnetic profile lacks large anomalies as expected for magmatically-derived crust (Bronner et al., 2011; Davis et al., 2018).

3.3.2.5 Modeling conclusions

Each of the four models for the transition from continental rifting to oceanic spreading tested for the Almada sub-basin yielded significant weaknesses. A potential explanation for the mismatch is heterogeneity of the crust; sensitivity testing within the gravity models suggested large changes in density across the transitional zone. Likewise, the seismic character across the Almada sub-basin suggested three structurally diverse blocks (Figure 3.8).

These blocks include: 1) a western, lower density block (2.7–2.9 g/cc) characterized by oblique and subparallel reflectors, a strong Moho reflection, and strong, intra-crustal chaotic reflectors; 2) a central block that is either high-density (>3.1 g/cc) or thinned (<4 km-thick) characterized by chaotic upper and strong mid-crustal reflectors, no clear Moho reflection, and a domed top-basement horizon; and 3) an eastern, lower density block (2.7–2.9 g/cc) characterized by a mounded top basement with a chaotic inner seismic character, smaller overlying packages of divergent reflectors, and a weak Moho reflector (Figure 3.4 and 3.8).

3.3.3 3D gravity modeling

3.3.3.1 Basement within the Camamu-Almada basin

Basement elevations across the study area range from 1 km above sea-level onshore in the São Francisco craton to more than 11 km below sea-level within the deepest offshore rift (Figure 3.9a). Two basement highs that divide the Camamu, Almada, and Jequitinhonha basins are resolved; these highs continue up to 100 km offshore and appear to be directly adjacent to onshore areas where the Paleoproterozoic basement fabric runs perpendicular to the opening direction (Figure 3.9a).

3.3.3.2 Moho elevation results and crustal thickness

Through the 3D gravity modeling process, the final constrained result was achieved within a total 0.1 mGal error. Moho elevations range from -65 km onshore to -0.6 km offshore. The deepest Moho and thickest crust onshore are located along the boundaries of the Recôncavo onshore basin and E–W-trending basement fabric and related offshore structures that divide the Camamu-Almada (Figure 3.9b).

The two areas of thinnest crust offshore are centered on the LoCC within the Almada and the Camamu and are 40–60 km-wide (Figure 3.9c). In the Almada sub-basin, the crust thins to 3 km in thickness, coincident with the central, transitional Domain 2 that was recognized through seismic interpretation and 2D gravity modeling (Figure 3.8).

In the Camamu sub-basin, a similar zone of thinned crust coincides with the large gravity high on the free air anomaly map (Figure 3.2a). In this area, the gravity-constrained crustal thickness reaches a minimum of zero and is coincident with a crustal block similar to the Domain 2 imaged within the Almada. No Moho was resolved in the seismic under this crust (Figure 3.5). Other areas of 1–4 km-thick crust trend parallel to the coastline within the Jacuípe rifted-passive margin to the north, while oceanic crust is generally 5–7 km-thick (Figure 3.9c–d).

Figure 3.8 Almada seismic line compared with the observed magnetic and both modeled and observed gravity signals from each model in Figure 3.7. Morphologically diverse blocks based on seismic and gravity modeling are numbered Domain 1–3: For Domain 1, divergent reflectors occur in the upper crust and reflect rifting and strong Moho reflection are present along with clinoform-filled rifts in highly faulted basement. For Domain 2, strong, concordant, highly tilted reflectors are bounded by a listric fault. Chaotic upper reflections and strong mid-crustal reflectors are present but lack an underlying Moho reflection. For Domain 3, mounded top basement with a chaotic inner seismic character, smaller overlying packages of divergent reflectors, and a weak, but observable, Moho reflector. Exact scales not included to protect data anonymity.

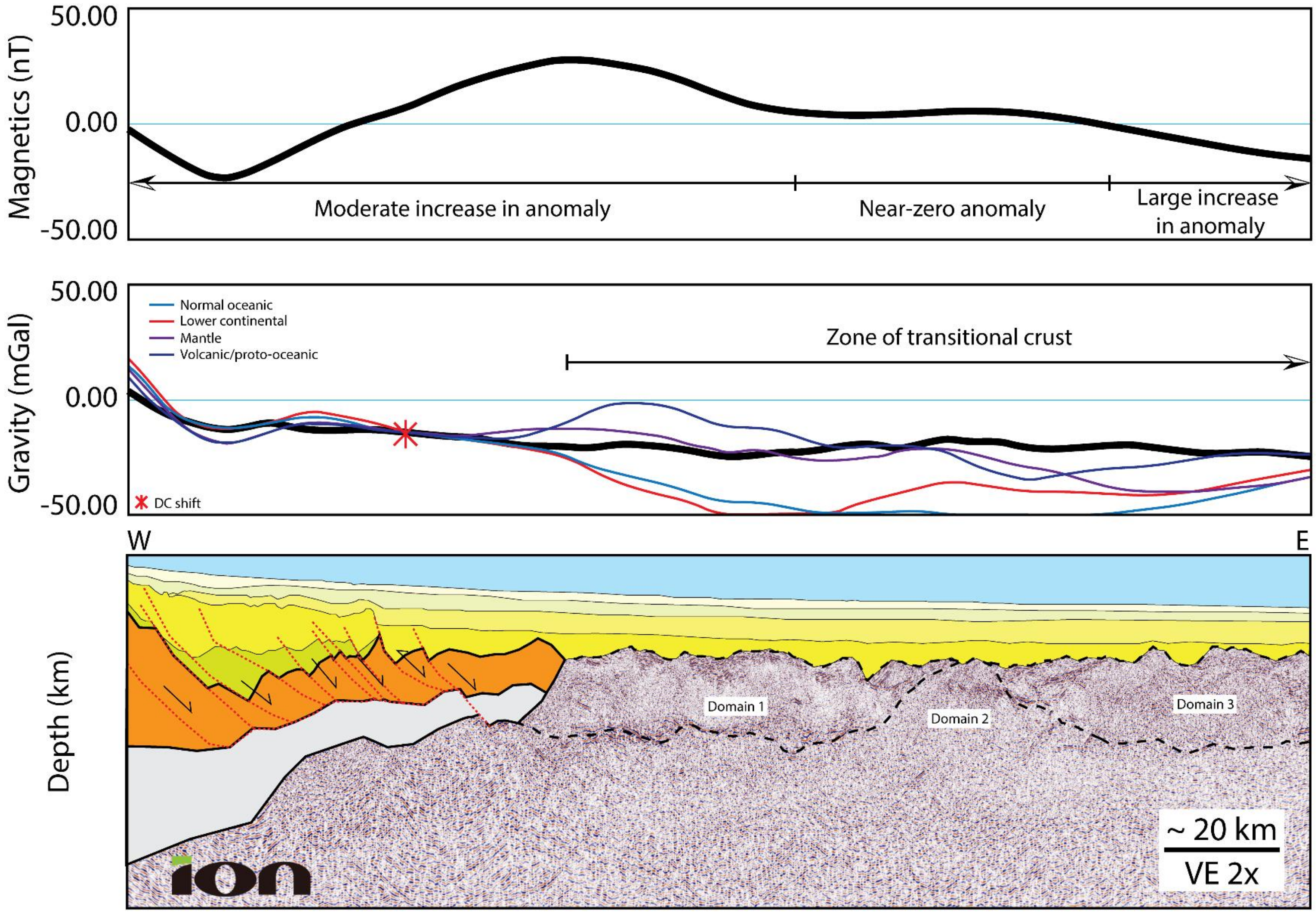

Magnetics (nT)
50.00
0.00
-50.00
Moderate increase in anomaly
Near-zero anomaly
Large increase in anomaly
Gravity (mGal)
50.00
0.00
-50.00
Normal oceanic
Lower continental
Mantle
Volcanic/proto-oceanic
Zone of transitional crust
DC shift
W
E
Depth (km)
Domain 1
Domain 2
Domain 3
~ 20 km
VE 2x

3.3.4 Seismic nature of the basement within the transitional zone

Initial interpretations, 2D modeling, and 3D modeling highlighted different blocks along the crust within the transitional zone. Four domains are defined (Figure 3.10–3.14) based on these results and described below.

3.3.4.1 Domain 1

Domain 1 is best observed on seismic line A across the Almada basin and represents an 80 km-wide crustal section that necks from 6 km to 3.5 km (Figure 3.10). Sedimentary reflections above the top basement were subdivided into three tectonosequences: 1) a syn-rift fill characterized by normally faulted, high-amplitude, subparallel to oblique reflectors; 2) a marine rift and sag fill characterized by continuous, subparallel reflectors that occasionally onlap onto the syn-rift fill and are capped by a high-amplitude reflection; and 3) a passive margin sequence characterized by continuous, horizontal, and sub-parallel reflectors.

The seismic character of the thicker, landward, crust consists of subparallel continuous reflectors that become more chaotic and highly faulted in the thinned crust further offshore. Listric faults dip landward before reaching a basement high where they begin to dip oceanward (Figure 3.4). Two large-offset listric faults were interpreted at the easternmost boundary of this block. The Moho reflection is easily recognizable as a series of subparallel, wavy, divergent, high-amplitude reflectors that disappear at the transition to Domain 2.

3.3.4.2 Domain 2

Domain 2 is present and was imaged along both profiles. It represents a 20 km-wide crustal section with seismically-indeterminate thickness (Figure 3.11). Sedimentary reflections above the basement include all three of the previously recognized sedimentary layers, though syn-rift fill only occurs on the landward-most end of this domain. The top basement surface is domed, with chaotic reflectors in the upper crust, strong mid-crustal reflectors, and no clear seismic Moho reflection.

3.3.4.3 Domain 3

Domain 3 is present along both profiles and especially prominent within the Almada sub-basin where it is 40 km-wide and 6–7 km-thick (Figure 3.12). Sedimentary reflections indicate thick, parallel-sided sag and passive margin deposits with a notable lack of faulted syn-rift sedimentation. Crustal seismic character includes a zone of normally faulted, divergent, landward-dipping reflectors with variable strength and a zone of chaotic internal character with a reflective upper crust and a rugose top basement.

3.3.4.4 Domain 4

Domain 4 was only imaged on the Camamu seismic line B, is 6–8 km-thick, and is at least 80 km-long (Figure 3.13). Sedimentary reflections include the sag and passive margin deposits, with most of the sag deposits onlapping and pinching out along the top of the crystalline crust. The top basement reflector is continuous and slightly rugose with minor normal faulting. Internal seismic character is well layered and split into an upper section that is either chaotic or reflection-free, and a lower section of concave-upward, laterally discontinuous, and divergent reflectors. The seismic Moho is bright and easily interpreted and mapped along the base of the deeper reflective zone.

Figure 3.9 a) Top basement interpretation from seismic reflection data was integrated with onshore topography (Smith and Sandwell, 1997) and offshore crustal thicknesses derived from the CRUST 1.0 model (Laske et al., 2013). Offshore continuations of shallow continental crust occur offshore of E–W trending basement fabric, while the deepest basement occurs along the elongate marginal rift as indicated by the low free-air gravity anomaly in Figure 3.2a. **b)** Final Moho topography as calculated from the 3D gravity inversion using controls from seismic refraction and reflection data. Onshore and elongate areas of a deeper Moho (40 to 50 km below sea level) run parallel to the orogenic grain that can be traced offshore. An area of shallow Moho (4 to 12 km below sea level) parallels the north coast and coincides with the large free-air gravity anomaly seen in Figure 3.2a. **c)** Total crustal thickness derived from basement and Moho topography with the thickest areas occurring along E–W Paleoproterozoic orogenic grain and along the flanks of the Recôncavo failed rift basin. Thinnest crust occurs along the two basinward-younging rifts, as shown in colored polygons. LoCC = limit of continental crust. **d)** Total crustal thickness with values > 10 km removed. Past the LoCC, thin areas contain the interpreted exhumed mantle as shown by the white hatched polygons. Domains 1–4 are demarcated by black dotted lines.

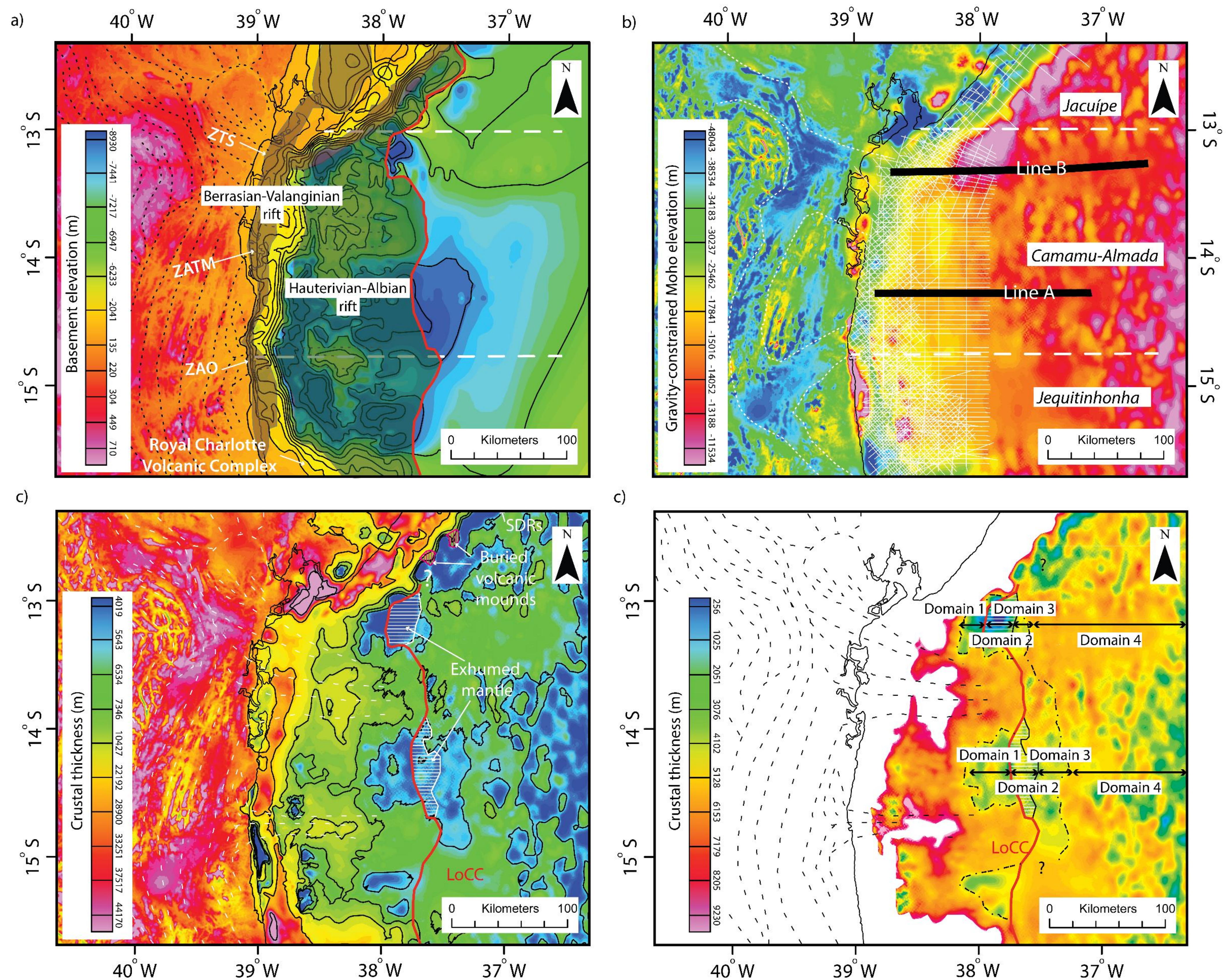

a)
b)
c)
c)
40° W
39° W
38° W
37° W
13° S
14° S
15° S
N
Basement elevation (m)
-8930
-7441
-7217
-6947
-6233
-2041
135
220
304
449
710
ZTS
Berrasian-Valanginian rift
ZATM
Hauterivian-Albian rift
ZAO
Royal Charlotte Volcanic Complex
0 Kilometers 100
Gravity-constrained Moho elevation (m)
-48043
-38534
-34183
-30237
-25462
-17841
-15016
-14052
-13188
-11534
Jacuípe
Line B
Camamu-Almada
Line A
Jequitinhonha
Crustal thickness (m)
4019
5643
6534
7346
10427
22192
28900
33251
37517
44170
SDRs
Buried volcanic mounds
Exhumed mantle
LoCC
256
1025
2051
3076
4102
5128
6153
7179
8205
9230
Domain 1
Domain 2
Domain 3
Domain 4

3.4 Discussion

3.4.1 Modeling results

Seismic mapping identified three basement horst blocks that separate the Camamu and Almada basins. These elongate blocks are parallel the east-west-trending basement fabric lineaments of the onshore Paleoproterozoic orogenic belt (Ferreira, 2009) (Figure 3.9a). The crust in these east-west trending zones is on average 10 km thicker than the surrounding crust and may have acted as a barrier to the northward-propagating rift system (Courtillot, 1982; Reuber and Mann, 2019) (Figure 3.9c).

Crustal thicknesses identified two lobate areas of thin crust to the east of the limit of continental crust (LoCC): 1) a 1,300 km^2 area in the Almada sub-basin with a crustal thickness of 3 km; and 2) a 1,200 km^2 area in the Camamu sub-basin with a thickness of 0 km (Figure 3.9c). These results suggested that the crust within these areas is exhumed mantle. Both lobate areas are coincident with the interpreted Domain 2, best seen along Line A, where the seismic Moho was not resolvable underneath the domed top basement reflector, identical to other worldwide examples of exhumed mantle (Gillard et al., 2015; Tugend et al., 2018; McCarthy et al., 2020).

Other explanations for this result were the potential biases imparted by the seismic time-to-depth conversion or overlying sediment densities (Figure 3.4–3.5 and 3.9). Careful inspection of the 3D modeling result and the seismic coverage showed that the basement lows and thinned crust were coincident with the location of the offshore ION seismic. If the seismic time-to-depth conversion used velocities that were too slow, the basement would appear deeper than it really is. This, in turn, would influence the 3D model and result in an artificially shallower Moho and thinner crust in these regions. Similarly, if sediment densities over these zones were higher than estimated by my depth-density function, the inversion would likewise result in a thicker crust in these localized areas. While I recognized these scenarios as possibilities, the integration of the 3D model with regional geology, 2D modeling, gravity/magnetic interpretation, and seismic interpretation reduced the associated uncertainty.

Work in both the Sergipe-Alagoas and northern Jacuípe basin imaged hyperextended crust with inferred SRD reflections in the transitional crustal area (Mohriak et al., 1998). In the 3D gravity model for the southern Jacuípe basin, areas of crust as thin as 1 km were present in the model (Figure 3.9c–d). This area is further complicated by buried volcanic rocks interpreted by Nunes and Holz (2019) as a “volcanic plug” of indeterminate age (Figure 3.9c–d). The 3D modeling suggests that the Jacuípe basin was the transition between the magma-rich Sergipe-Alagoas margin to the north (Mohriak et al., 1988) and the magma-poor margin of the Almada-Camamu basin to the south (Figure 3.9).

3.4.2 Nature of the basement composition seen along the Camamu and Almada seismic lines

Deep-penetration seismic reflection observations supported by 2D and 3D gravity modeling allowed subdivision of the transitional crust across the Camamu and the Almada sub-basins into four crustal domains that were described below and shown in Figure 3.10–3.13.

3.4.2.1 Domain 1: Hyperextended to unroofed lower continental crust

Blaich et al. (2010) used an extensive 2D seismic reflecting dataset in this same distal Domain 1 of the Camamu-Almada basin and proposed that these crustal blocks were volcanic buildups rather than normal oceanic crust or exhumed mantle. I reinterpret Domain 1 as hyperextended, possibly unroofed continental crust based on the following observations (Figure 3.4 and 3.10): 1) a strong seismic Moho that marks the base of this domain and defines a density contrast between the crust and the mantle; 2) the distinctive, seismic reflection character of the Moho suggesting boudinaged crustal lozenges; 3) the 2.88 g/cc density supported by refraction velocities within comparable crust along the southern, adjacent Jequitinhonha basin (Loureiro et al., 2018) that matched the lower density required by the 2D gravity modeling (Figure 3.8); 4) the presence of well-developed normal faults that crosscut both the top of basement and the syn-rift delta fill sediments, consistent with extreme thinning; and 5) the presence of a landward-dipping detachment between brittle upper continental crust and ductile lower continental crust (Péron-Pinvidic et al., 2017).

The crust across Domain 1 thinned to minimum thickness of 3.5 km, from an original continental crust thickness of 40 km in the onland area of the Camamu-Almada basin (Assumpção et al., 2013) (Figure 3.4 and 3.10). The seaward limit of this domain is marked by large-offset listric normal faults, discontinuous and rafted blocks of continental crust (e.g., Deng et al., 2020), and a discontinuity in the seismic Moho reflection (Figure 3.10).

a) Line A, Domain 1, uninterpreted seismic

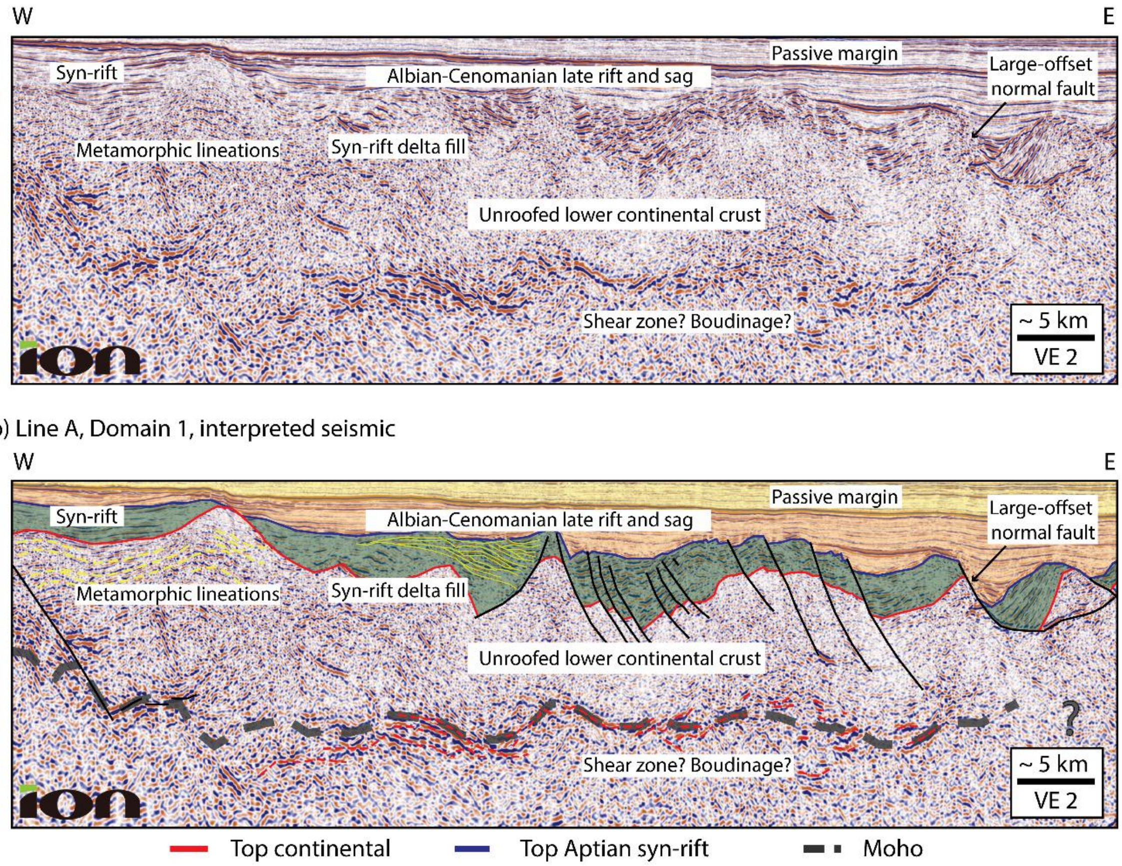

Figure 3.10 a) Zoom of a 60 km-long, uninterpreted deep-penetration seismic Line A crossing the broad rift zone of the Almada basin. **b)** Interpreted zoom of Line A showing seismic evidence for hyperextended, potentially unroofed lower continental crust and highly faulted rifts with clinoformal, clastic sedimentary rocks. Scales not included to protect data anonymity.

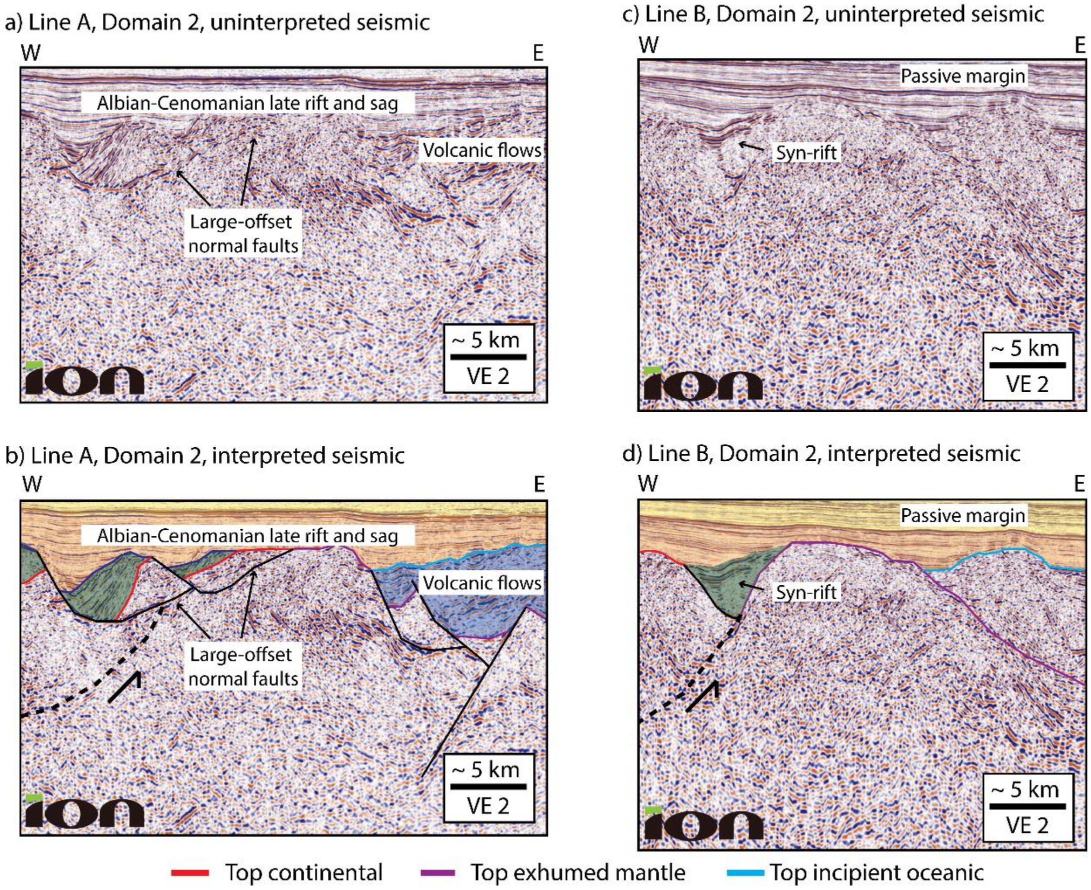

Figure 3.11 a) Uninterpreted zoom of a 20 km-long, uninterpreted, deep-penetration seismic Line B crossing the broad rift zone of the Camamu basin**. b)** Interpreted zoom of Line B showing seismic evidence for exhumed mantle. **c)** Uninterpreted zoom of a 20 km-long, uninterpreted deep-penetration seismic Line A crossing the broad rift zone of the Almada basin. **d)** Interpreted zoom of Line A showing seismic evidence for exhumed mantle. Scales not included to protect data anonymity.

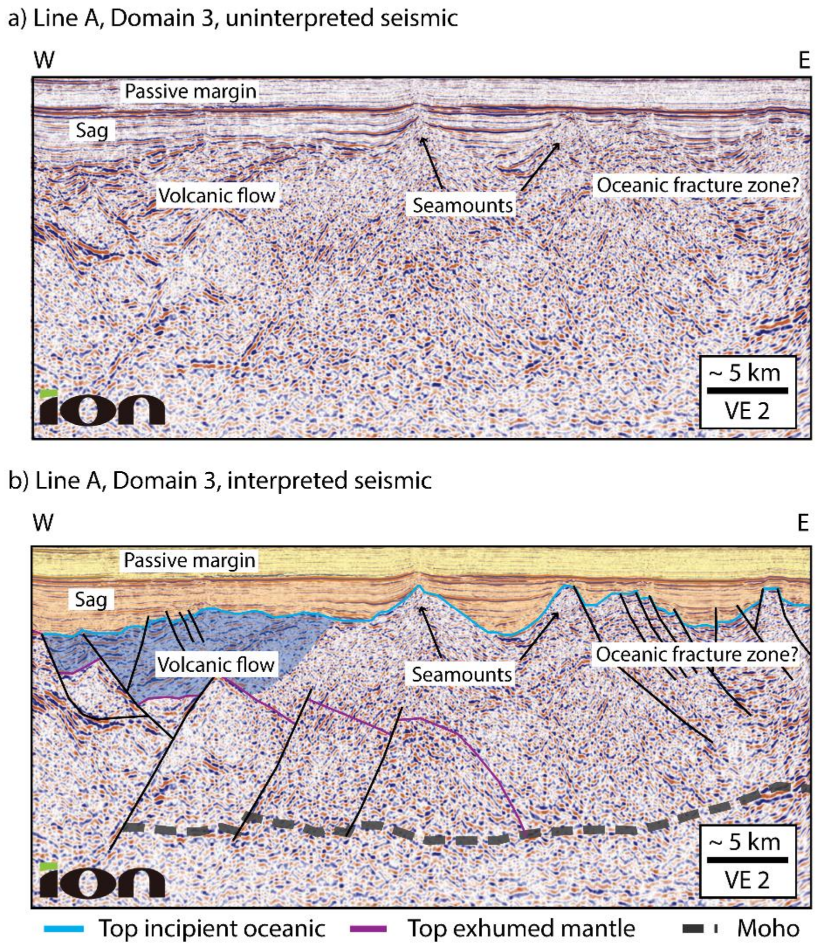

Figure 3.12 a) Uninterpreted zoom of a 25 km-long, uninterpreted deep-penetration seismic Line A crossing the broad rift zone of the Almada basin. **b)** Interpreted zoom of Line A showing seismic evidence for volcanic flows and seamounts within incipient oceanic crust. Scales not included to protect data anonymity.

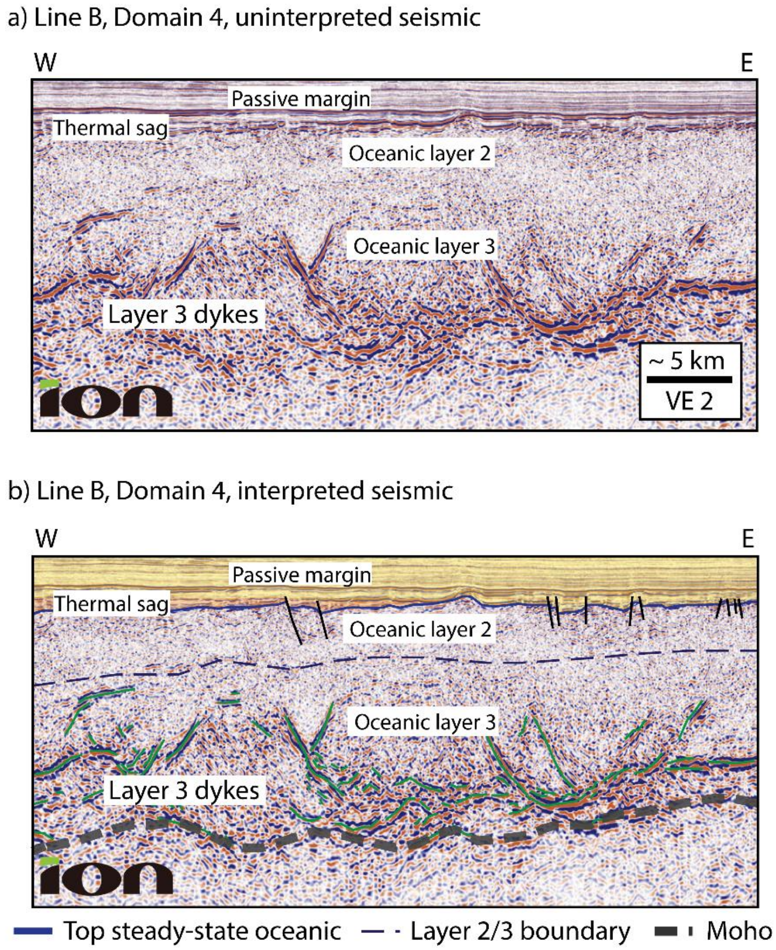

Figure 3.13 a) Uninterpreted zoom of a 45 km-long, uninterpreted deep-penetration seismic Line B crossing the broad rift zone of the Camamu basin. **b)** Interpreted zoom of Line B showing seismic evidence for oceanic crust with an upper faulted oceanic Layer 2 and intrusive dikes within the lower oceanic Layer 3. Scales not included to protect data anonymity.

3.4.2.2 Domain 2: Exhumed mantle

Domain 2 is interpreted as exhumed, serpentinized mantle crust based on the following observations (Figure 3.4 and 3.11): 1) a reflective upper crust with no clear Moho reflections suggestive of similar impedance as mantle; 2) a lack of a strong, organized magnetic signal characteristic of magnetic isochrons over oceanic crust (Gillard et al., 2015); 3) the correspondence of the density range of exhumed mantle (3.1-3.2 g/cc) that fit the high densities required by the 2D gravity modeling (Figure 3.8); and 4) the mounded, top basement morphology that has been described within other interpreted areas of exhumed mantle worldwide (Unternehr et al., 2010; Gillard et al., 2015; Jolivet et al., 2015).

The crust of Domain 2 is 20 km-wide across both the Camamu and Almada sub-basins and is of indeterminate thickness due to the lack of a seismic Moho (Figure 3.11). This domain may have exhumed due to slow extension in the absence of magmatism and exists in localized areas of 1,200–1,300 km^2 of the Camamu and Almada, as identified on the 3D gravity model (Figure 3.9d).

While exhumed mantle is our preferred interpretation, an alternative model for Domain 2 would be a zone of thinned, oceanic crust. In this scenario, the thin oceanic crust would produce a similar gravity response to that of a thick, dense, serpentinized mantle. This scenario will be modeled and discussed in a later section.

3.4.2.3 Domain 3: Incipient oceanic crust

Domain 3 is interpreted as non-steady-state, incipient oceanic crust based on the following observations (Figure 3.4 and 3.12): 1) evidence from seismic reflection data for seamounts and volcanic flows in the upper crust; 2) the lower density of oceanic crust (2.9 g/cc) that fits the lower density required by the 2D modeling (Figure 3.8); 3) complex internal seismic character without an oceanic Layer 2/Layer 3; 4) the faint seismic Moho surface suggesting slight differentiation with mantle velocities; and 5) undeformed, overlying sag and passive margin sedimentary units.

Domain 3 represents the most magmatic part of the transitional zone, interpreted as the earliest ocean floor sequence that formed during a period of unfocused and transient melt supply at low spreading rates (Odegard et al., 2002). Incipient oceanic crust is interpreted within the Camamu-Almada basin as a 40–60 km-wide zone of oceanic crust overlain by a zone of basaltic flows and underlain by a weak seismic Moho (Figure 3.4–3.5, and 3.12).

3.4.2.4 Domain 4: Normal oceanic crust

Domain 4 is interpreted as steady-state, normal oceanic crust based on the following observations (Figure 3.5 and 3.13): 1) the Moho is clearly visible with the crustal thickness ranging from 6–8 km; 2) the top basement surface character is high-amplitude, continuous, and mostly unfaulted; 3) the overlying sedimentary units are largely undeformed, either sag or passive margin related, and onlap the top basement surface; and 4) the strong, organized magnetic anomalies over this domain suggestive of a highly magnetized crust (Figure 3.15).

Figure 3.14 a) Gravity model colinear with deep-penetration seismic Line A across the Almada sub-basin to test the hypothesis for a crustal transitional zone of unroofed lower continental crust, exhumed mantle, and incipient oceanic crust. **b)** Block model over Line A across the Almada sub-basin according to this scenario. **c)** Gravity model over Line A across the Almada sub-basin to test a transitional zone of unroofed lower continental crust, thin oceanic crust (down to 3.4 km-thick), and incipient oceanic crust. **d)** Block model over Line A across the Almada sub-basin according to this scenario. Exact scales not included to protect data anonymity.

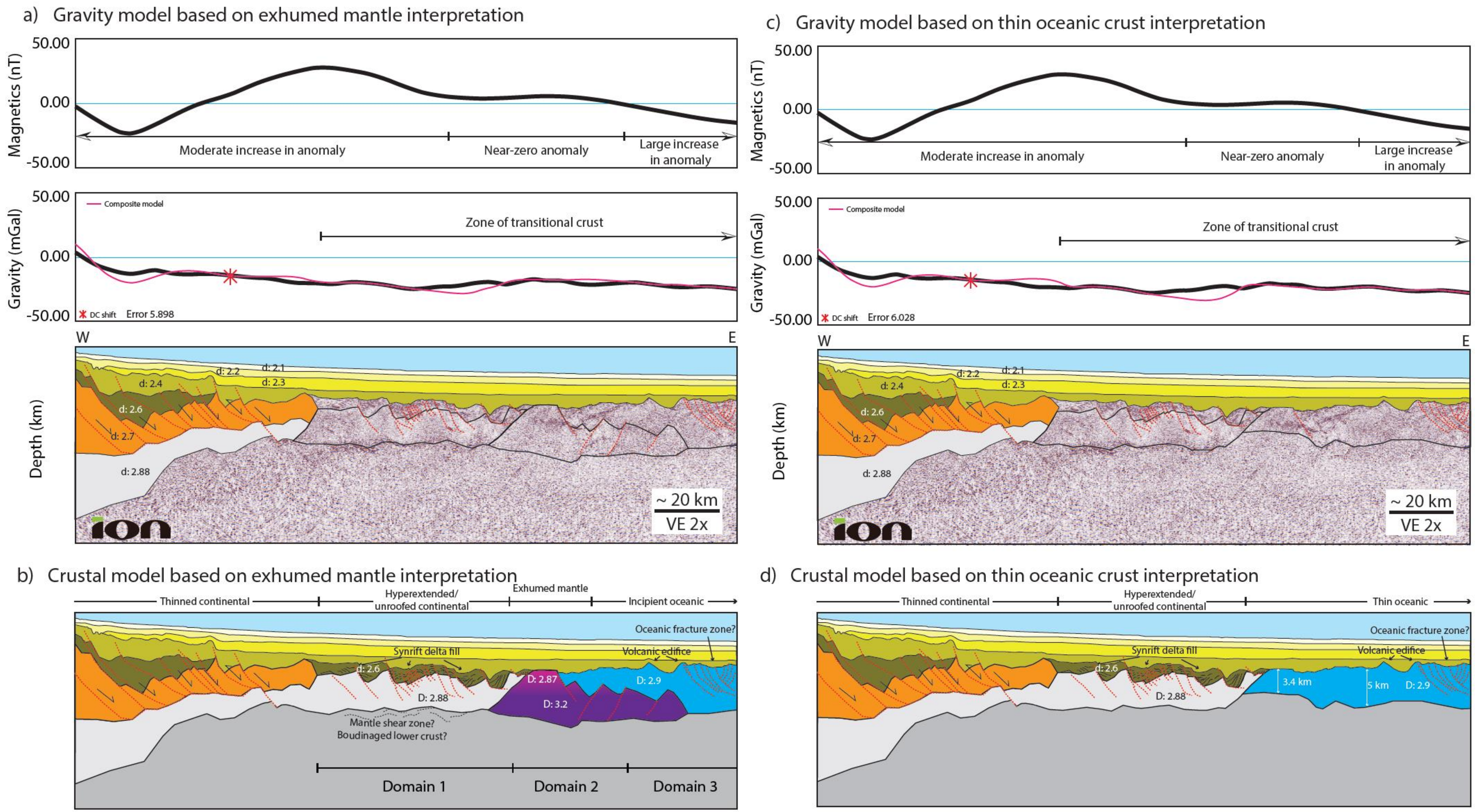
a) Gravity model based on exhumed mantle interpretation
Magnetics (nT)
50.00
0.00
-50.00
Moderate increase in anomaly
Near-zero anomaly
Large increase in anomaly
Gravity (mGal)
Composite model
Zone of transitional crust
DC shift
Error 5.898
W
E
Depth (km)
d: 2.2
d: 2.1
d: 2.4
d: 2.3
d: 2.6
d: 2.7
d: 2.88
~ 20 km
VE 2x
b) Crustal model based on exhumed mantle interpretation
Thinned continental
Hyperextended/ unroofed continental
Exhumed mantle
Incipient oceanic
Oceanic fracture zone?
Synrift delta fill
Volcanic edifice
d: 2.6
D: 2.87
D: 2.9
D: 2.88
D: 3.2
Mantle shear zone? Boudinaged lower crust?
Domain 1
Domain 2
Domain 3
c) Gravity model based on thin oceanic crust interpretation
Magnetics (nT)
50.00
0.00
-50.00
Moderate increase in anomaly
Near-zero anomaly
Large increase in anomaly
Gravity (mGal)
Composite model
Zone of transitional crust
DC shift
Error 6.028
W
E
Depth (km)
d: 2.2
d: 2.1
d: 2.4
d: 2.3
d: 2.6
d: 2.7
d: 2.88
~ 20 km
VE 2x
d) Crustal model based on thin oceanic crust interpretation
Thinned continental
Hyperextended/ unroofed continental
Thin oceanic
Oceanic fracture zone?
Synrift delta fill
Volcanic edifice
d: 2.6
3.4 km
5 km
D: 2.9
D: 2.88

Figure 3.15 a) Gravity model colinear with deep-penetration seismic Line B across the Camamu sub-basin to test the hypothesis for a crustal transitional zone of unroofed lower continental crust, exhumed mantle, and incipient oceanic crust. **b)** Block model over Line B across the Camamu sub-basin according to this scenario. **c)** Gravity model over Line B across the Camamu sub-basin to test a transitional zone of unroofed lower continental crust, thin oceanic crust (down to 4 km-thick), and incipient oceanic crust. **d)** Block model over Line B across the Camamu sub-basin according to this scenario. Exact scales not included to protect data anonymity.

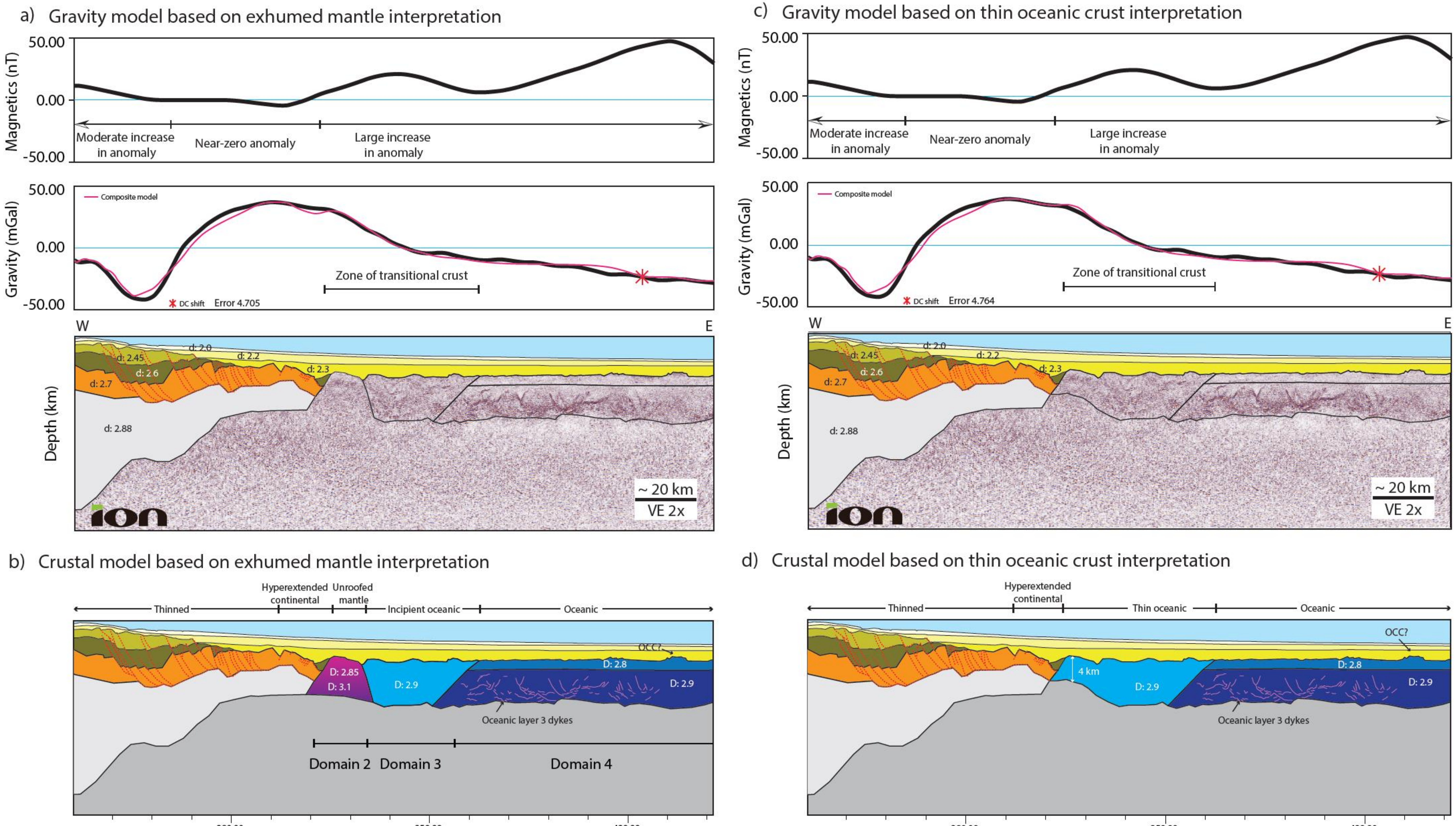
a) Gravity model based on exhumed mantle interpretation
Magnetics (nT)
50.00
0.00
-50.00
Moderate increase in anomaly
Near-zero anomaly
Large increase in anomaly
Gravity (mGal)
Composite model
Zone of transitional crust
DC shift
Error 4.705
W
E
Depth (km)
d: 2.0
d: 2.2
d: 2.3
d: 2.45
d: 2.6
d: 2.7
d: 2.88
~ 20 km
VE 2x
b) Crustal model based on exhumed mantle interpretation
Thinned
Hyperextended continental
Unroofed mantle
Incipient oceanic
Oceanic
OCC?
D: 2.85
D: 3.1
D: 2.9
D: 2.8
Oceanic layer 3 dykes
Domain 2
Domain 3
Domain 4
280.00
350.00
420.00
c) Gravity model based on thin oceanic crust interpretation
Magnetics (nT)
Gravity (mGal)
Error 4.764
d) Crustal model based on thin oceanic crust interpretation
Thin oceanic
4 km

An interesting feature that I observed within Domain 4 crust is the clear division between oceanic crust layers 2 and 3 (Figure 3.13). Layer 2 is about 2 km-thick with mostly homogeneous and transparent facies. Layer 3 is about 6 km-thick with high-amplitude curvilinear reflections. These seismic reflections are interpreted as gabbroic dykes within the coarse-grained gabbros that make up the lower crust (Perfit, 2018). Analogs of these high-amplitude curvilinear reflections within the lower oceanic crust have been seismically imaged within oceanic crust offshore of other South Atlantic rifted margins (Unternehr et al., 2010; Hoggard et al., 2017)

3.4.3 Proposed composite model for the imaged transitional zone of the Camamu-Almada

This study suggests that the Camamu-Almada was magma-poor throughout Berriasian-Albian rifting, and is characterized by exhumed mantle with no obvious SDRs, intrusions, or underplating (Table 3.4). The proposed model for the transitional crust along the Camamu-Almada margin includes four domains: **Domain 1**: hyperextended continental to potentially unroofed lower continental crust (wider and better imaged in the Almada); **Domain 2**: exhumed mantle (restricted to small, lenticular, isolated areas within the Camamu and Almada); **Domain 3**: incipient oceanic crust (varying areal extent); and **Domain 4**: normal oceanic crust. The presence and location of these domains are supported by seismic interpretation (Figure 3.4–3.5, 3.10–3.13), 2D modeling (Figure 3.7–3.8), 3D modeling (Figure 3.9), and interpretation of magnetic and gravity grids (Figure 3.2).

Within the Almada sub-basin, gravity modeling suggests a rapidly thinning continental crust, from an initial 18 km-thick crust down to a 10 km-thick crust across a 20 km-wide necking zone. This zone is characterized by upper crustal listric normal faults that terminate on an HAR (Figure 3.4 and 3.5). As the continental crust hyperextended and lower continental crust potentially unroofed through depth-dependent extension, the crust cooled and underwent brittle normal extension to a final thickness of 3.5 km (Figure 3.4 and 3.5). When crustal breakup occurred between Brazil and Africa, a 20 km-wide block of mantle locally exhumed and serpentinized (Figure 3.9c). Emplacement of incipient oceanic crust occurred during a period of unfocused and transient melt supply at low spreading rates before transitioning to steady-state normal oceanic crust (Figure 3.14a–b).

100 km to the north of the Almada, rift evolution was similar within the Camamu sub-basin. The gravity model suggested rapidly thinning crust from an initial 25 km downward to 8 km across a 60 km wide necking zone with a similar pattern of listric normal faults and HAR geometry as observed in the Almada basin (Figure 3.4). Continental crust hyperextended throughout rifting before crustal break-up locally occurred and a 20 km-wide tract of mantle was locally exhumed (Figure 3.5 and 3.9c). Emplacement of incipient oceanic crust began with smaller seamounts and likely lower amounts of magmatism than within the Almada before transitioning to the more ordered emplacement of steady-state normal oceanic crust (Figure 3.15a–b).

3.4.3.1 An alternative model for the ultrathin crust

An alternative to the exhumed mantle within Domain 2 is instead the presence of thinned oceanic crust (Figure 3.14–3.15). As shown in the 2D models, 4 km-thick oceanic crust in the Camamu and 3.4 km-thick oceanic crust in the Almada (Figure 3.14–3.15) achieved a similar gravity response to the exhumed mantle model. However, as has been discussed, multiple lines of evidence suggest the presence of exhumed mantle. Additionally, within the Almada basin, magnetic anomalies over the domain appear to lack a strong, organized magnetic signal, suggesting against strongly magnetized oceanic crust (Figure 3.16b). Within the Camamu sub-basin the presence of mantle is suggested by both a large gravity anomaly (Figure 3.16a) and the 0 km-thick crustal thickness resolved in the 3D model (Figure 3.9c–d).

3.4.4 Evidence for ultrathin crust and exhumed mantle along the South Gabon conjugate margin

Recent studies of the west African conjugate, offshore South Gabon basin resulted in contrasting interpretations of its crustal structure. Péron-Pinvidic et al. (2017) interpreted a transitional zone of hyperextended continental crust and exhumed mantle. Fernandez et al. (2020) interpreted similar hyperextended continental crust, but instead argued for large volumes of breakup volcanics that extruded before emplacement of oceanic crust, similar to the Blaich et al. (2010) model.

Epin et al. (2021) revisited the interpretation of the transitional crust along the South Gabon basin using a PSDM 3D seismic reflection survey with a seismic record length of 20 km. These data imaged the sub-salt continent-ocean transition in precise detail and identified a small zone of exhumed mantle with weak or absent Moho located between the hyperextended continental crust and unorganized, oceanic-derived crust. This interpretation is very similar to the interpretation of the conjugate Camamu-Almada basin put forward herein (Figure 3.15 and 3.17).

Figure 3.16 The continent-ocean transition along the Camamu-Almada rifted-passive margin as defined by 2D and 3D gravity modeling. Exhumed continental crust is imaged in two separate areas (1,200–1,330 km^2) of the Camamu-Almada basins. The crust within the southern Jacuípe basin is not well imaged or modeled using gravity but appears to represent the transition between the magma-rich northern Jacuípe and Sergipe-Alagoas basins and the magma-poor Camamu-Almada basin. **a)** Results of 3D gravity model on a basemap of the Bouguer gravity anomaly whose gravity low corresponds to the near-coastal Berriasian-Albian rift and whose gravity high marks the 1,200 km^2 area of exhumed mantle within the Camamu sub-basin. **b)** Results of the 3D gravity model on a basemap of the EMAG 2v3 magnetic anomaly. The magnetic wavelengths change from a large amplitude continental character to smaller amplitude oceanic crust with a zone of weak magnetic lineations centered on the 1,300 km^2 area of exhumed mantle in the Almada sub-basin. **c)** Results of the 3D gravity model on a basemap of the 3D gravity model.

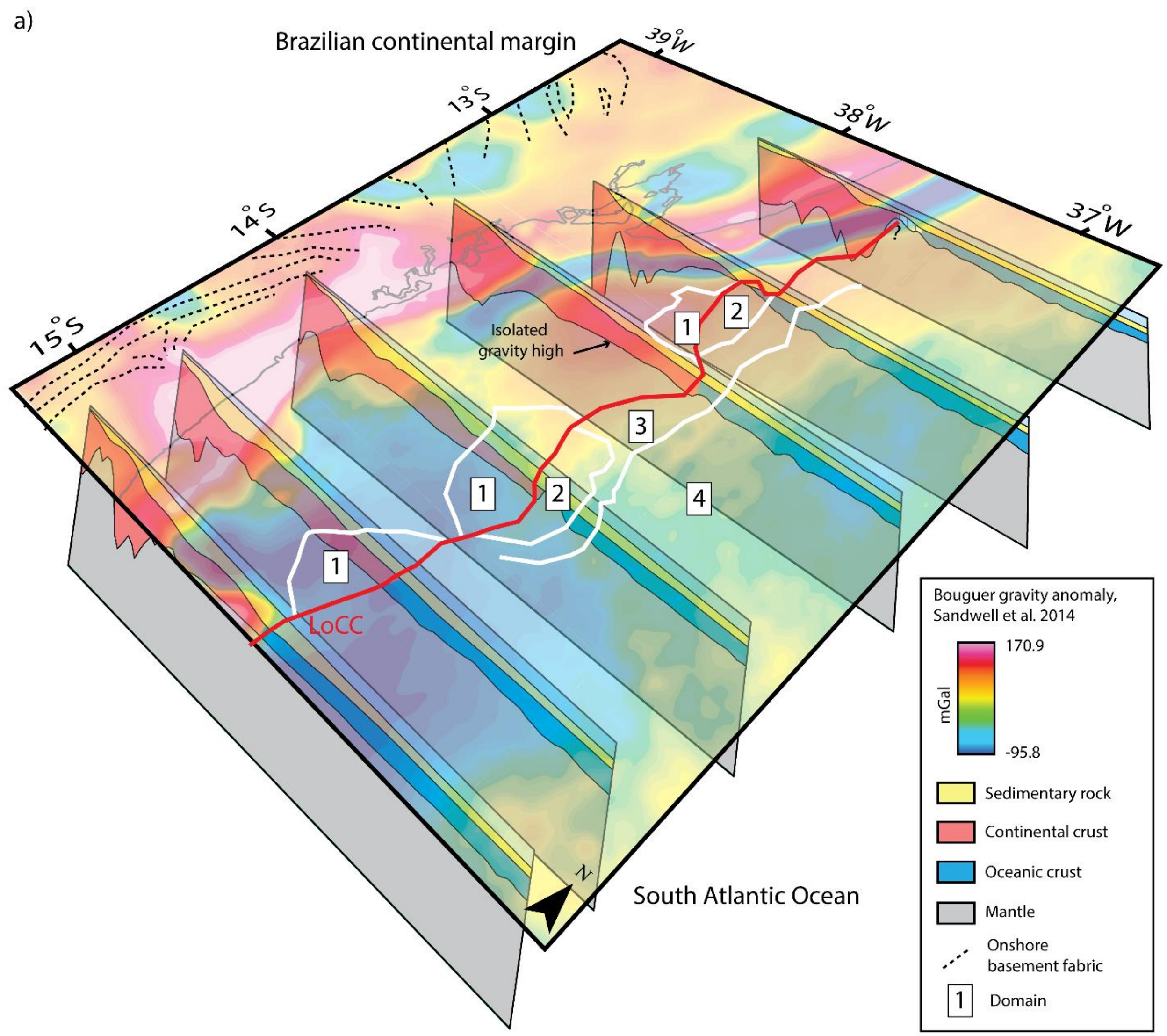
a)
Brazilian continental margin
39°W
38°W
37°W
13°S
14°S
15°S
Isolated gravity high
LoCC
1
2
1
2
3
4
1
South Atlantic Ocean
N
Bouguer gravity anomaly, Sandwell et al. 2014
mGal
170.9
-95.8
Sedimentary rock
Continental crust
Oceanic crust
Mantle
Onshore basement fabric
Domain

b)

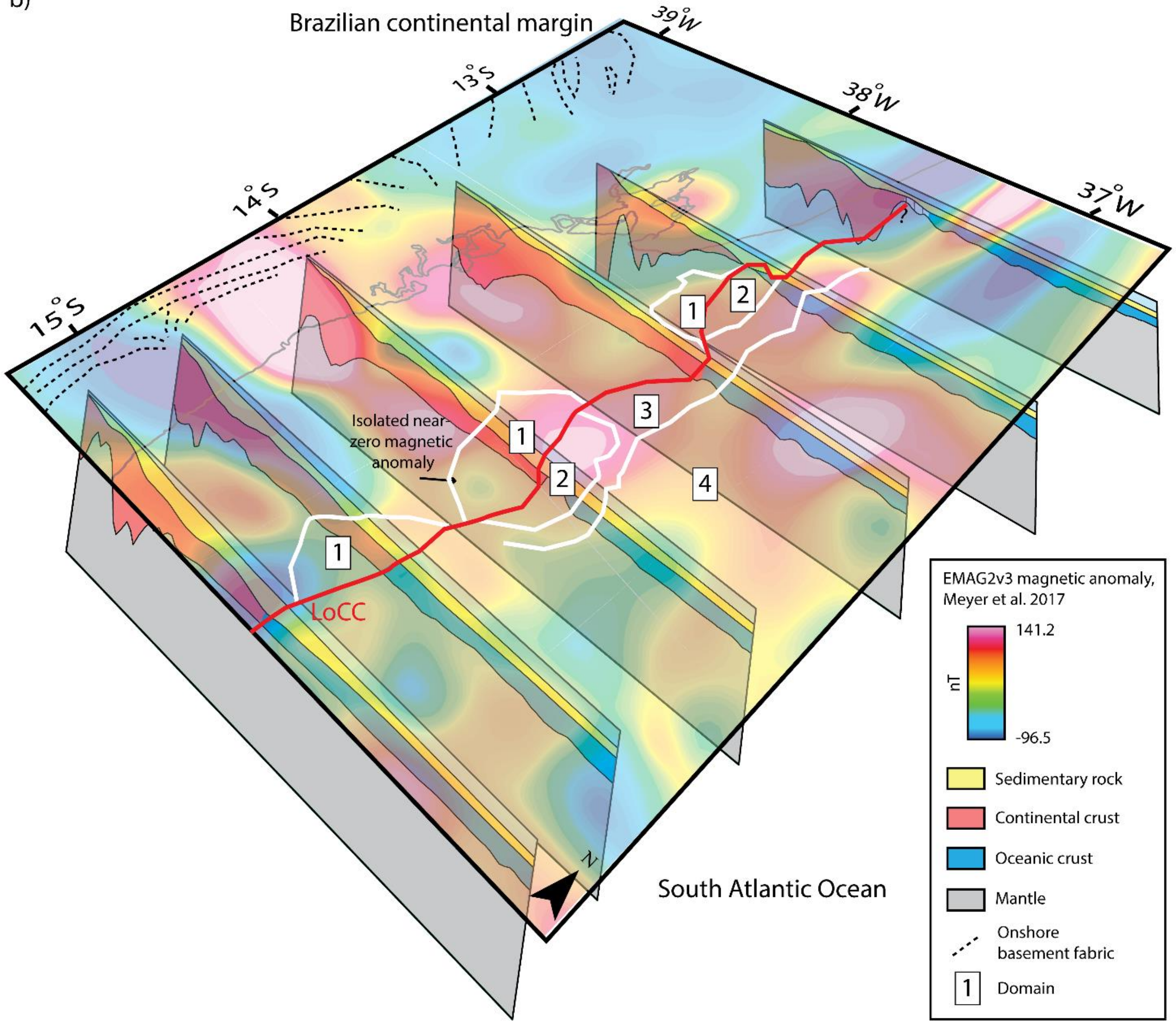
Brazilian continental margin
39°W
38°W
37°W
13°S
14°S
15°S
Isolated near-zero magnetic anomaly
1
2
3
4
LoCC
N
South Atlantic Ocean
EMAG2v3 magnetic anomaly, Meyer et al. 2017
141.2
nT
-96.5
Sedimentary rock
Continental crust
Oceanic crust
Mantle
Onshore basement fabric
Domain

c)

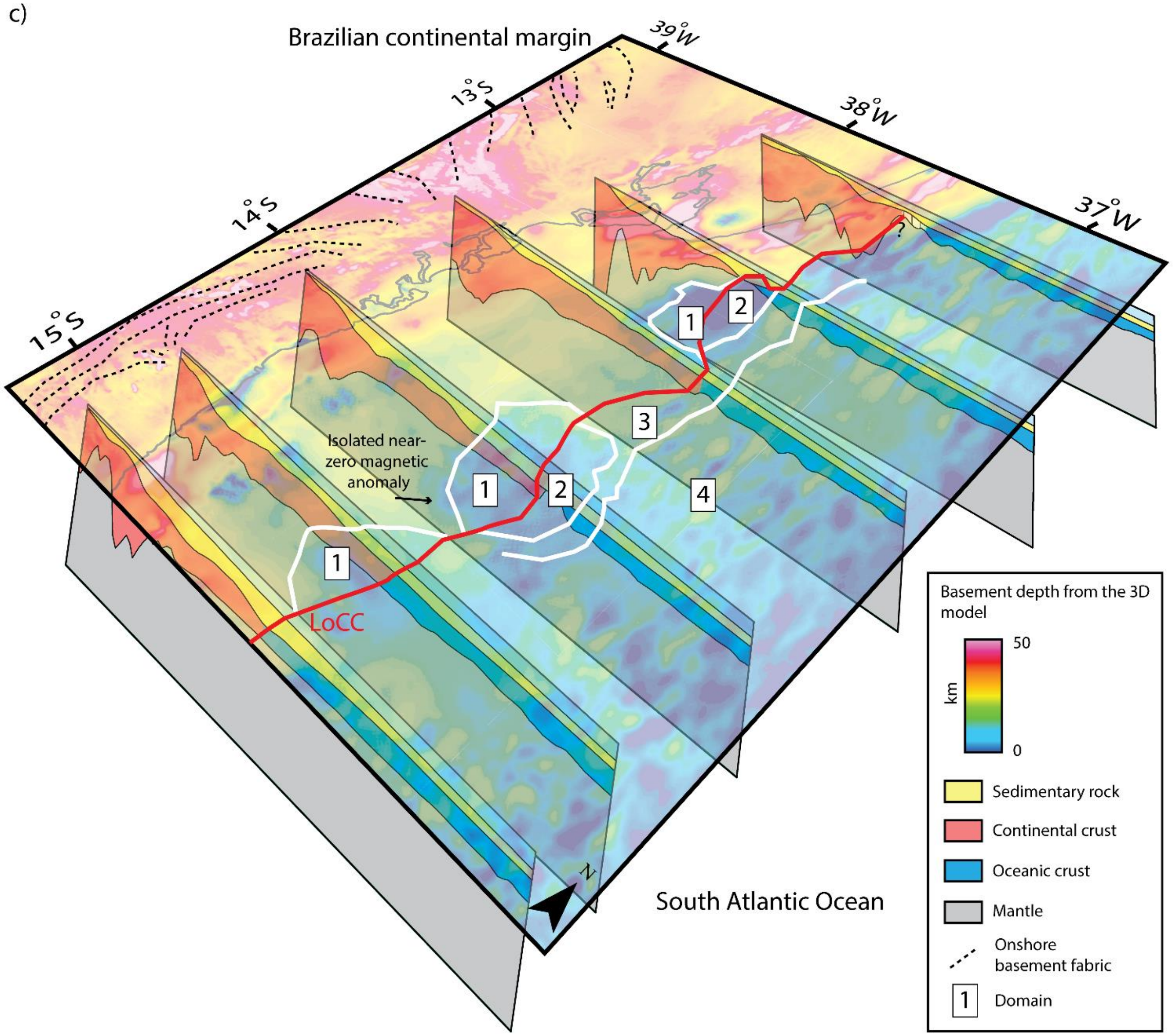
Brazilian continental margin
39°W
38°W
37°W
13°S
14°S
15°S
Isolated near-zero magnetic anomaly
1
2
3
4
LoCC
N
South Atlantic Ocean
Basement depth from the 3D model
km
50
0
Sedimentary rock
Continental crust
Oceanic crust
Mantle
Onshore basement fabric
Domain

3.4.5 An analog for the crustal structure of the Camamu-Almada basin from the western Mediterranean

A similar crustal structure to the Camamu-Almada basin from unstretched continental crust to hyperextended continental crust, unroofed lower continental crust, and exhumed mantle has been described in the Gulf of Lion, western Mediterranean Sea, by Jolivet et al. (2015). The Gulf of Lion rifted-passive margin formed as a back-arc basin during the Oligocene-Miocene retreat of the Apennine subducted slab (Réhault et al., 1984; Gueguen et al., 1998). Oceanic crust formed in the early Miocene until the earliest middle Miocene (Westphal et al., 1976; Vigliotti and Kent, 1990). Magnetic anomalies indicated that this Miocene oceanic crust occupies the center of the basin (Le Douaran et al., 1984; De Voogd et al., 1991), while the continent-ocean transition is characterized by a complicated crustal section with abnormal velocities and low-amplitude magnetic anomalies, suggestive of lower crustal material or exhumed mantle (Gailler et al., 2009).

Jolivet et al. (2015) interpreted long-offset seismic across this distal area and recognized a similar continent-ocean transition to the proposed model across the Camamu-Almada (Figure 3.17). Both margin interpretations resolved hyperextended continental crust with listric normal faulting, a high-amplitude reflector (HAR), and possibly exhumed lower continental crust that was heavily faulted by half-grabens filled by wedge-like syn-rift sedimentation. Both interpretations suggested the presence of a mantle shear zone and/or lower boudinaged zone below the hyperextended continental crust and exposed serpentinized mantle. This analog illustrates the similarities between these two crustal transitional zones formed by slow, amagmatic rifting (Figure 3.17).

3.4.6 Along-margin variations in the continent-ocean transition of northeastern Brazil

Distinct changes occur in the crustal architecture across the Camamu-Almada margin that are expressed in the gravity and magnetic anomalies (Figure 3.2). Comparisons to the Bouguer-corrected gravity anomaly revealed a gravity low that runs parallel to the coastline and marks the deepest Barremian-Albian rift as recognized from the 3D gravity model (Figure 3.9). Isolated gravity highs overlie the zone of exhumed mantle within the northern Camamu sub-basin (Domain 2) (Figure 3.16a).

Correlations between the magnetic anomalies and geologic features are less obvious, as the magnetic wavelengths lengthen over deeper continental crust, shorten over shallower oceanic crust, and are disorganized above the interpreted exhumed mantle domain (Domain 2) in the Almada sub-basin (Baranov and Naudy, 1964).

A key result of the modeling is that the mantle did not exhume as a continuous band along the margin, as observed for the Iberian-Newfoundland conjugate (Boillot et al., 1980, 1989; Druet et al., 2018). Instead, the exhumed mantle is only apparent within localized areas of 1,200–1,300 km^2 in the Camamu and Almada sub-basins, flanked by zones of thinned continental and oceanic crust (Domain 3 and 4, Figure 3.16). This raises the question of whether this mantle is subcontinental (Boillot et al., 1980) or oceanic in nature (Pressling et al., 2012).

Serpentinized peridotite along similar exhumed mantle domains was previously interpreted as having a continental affinity (Piccardo et al., 1990; Trommsdorff et al., 1993; Rampone et al., 1995; Müntener and Hermann, 1996). The interpreted seismic lines in Figure 3.11 shows a possible area of sheared and exhumed mantle along a normal fault (Figure 3.11), although this could also be interpreted as boudinage within the lower continental crust as proposed for the Jequitinhonha basin (Loureiro et al., 2018).

A competing hypothesis is that the mantle was ocean-derived and exhumed concurrently with the formation of adjacent oceanic crust, similar to an oceanic core complex (Pressling et al., 2012). This latter hypothesis is supported by the geometries shown in the 3D model; Domain 2 exhumed mantle zones are not continuous across the margin and instead occur in localized, lenticular areas (Figure 3.9c).

Figure 3.17 a) Interpretation of the crustal structure of the rifted-passive margin of the Gulf of Lion in the western Mediterranean Sea, modified from Jolivet et al. (2015), showing a rifted zone comparable to the Camamu-Almada basin including blocks of extended continental crust, unroofed lower continental crust, exhumed mantle, and oceanic crust. **b)** Interpretation across line A in the Almada sub-basin displayed in a similar style. Notice the similar syn-rift reflections over the faulted and unroofed lower continental crust, and landward dipping normal faults within the exhumed and serpentinized mantle.

a) Gulf of Lion, offshore southeastern France, modified from Jolivet et al. 2015

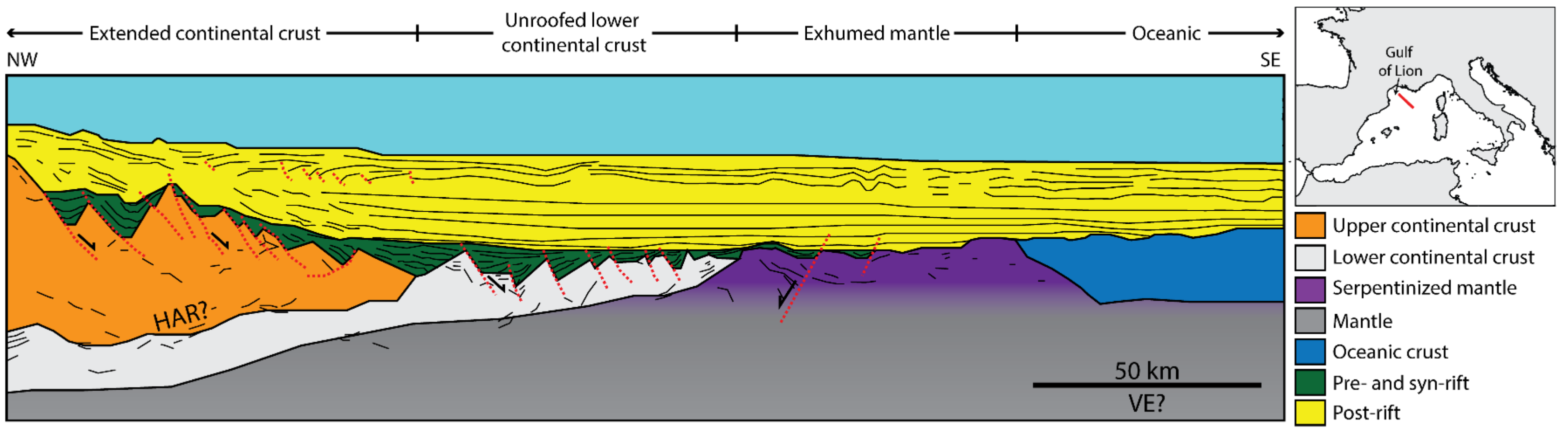

b) Line A, Almada sub-basin, offshore northeastern Brazil

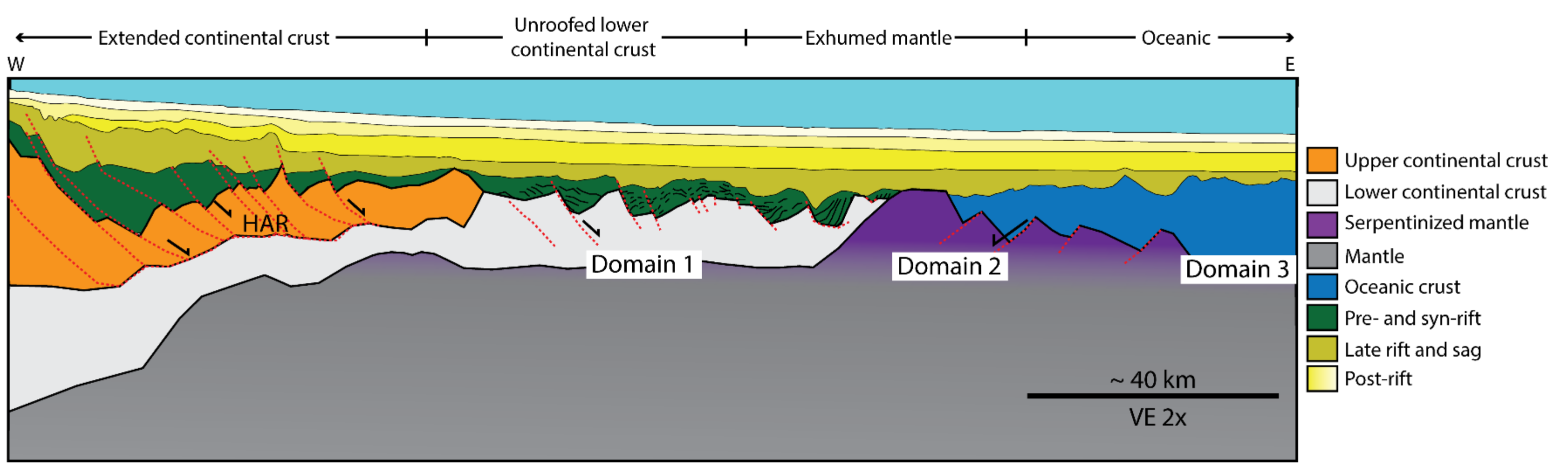

3.4.7 Rates of oceanic spreading in the early post-rift period of the Camamu-Almada basin

Initial spreading rates are a key piece of the puzzle when it comes to mantle exhumation, thought to only occur within some ultra-slow-spreading margins (Sauter et al., 2018). The direct estimation of oceanic spreading rates over the incipient and normal oceanic crust in the Camamu-Almada basin was not possible given the lack of nearby magnetic isochrons (Figure 3.1). However, it was possible to use oceanic basement roughness to estimate spreading rates. Malinverno (1991) first noted that the roughness of the top oceanic basement surface increased with a decrease in spreading rates; while there was scatter in the results, this general trend has been upheld by later studies (Goff, 1991, 1992; Goff et al., 1995; Neumann and Forsyth, 1995; Minshull, 1999; Weigelt and Jokat, 2001; Ehlers and Jokat, 2009; Sauter et al., 2011, 2018). Limitations for this method result from the de-trending process, the conversion of seismic reflection data from two-way time to depth, mantle temperature, and presence of fracture zones (Bécel et al., 2020).

Roughness along the two PSDM seismic lines was defined as the root-mean-square (RMS) deviation from the overall trend of the basement (Bécel et al., 2020). I interpreted the top basement surface along the incipient and normal oceanic crust along both seismic lines and used a second-degree polynomial fit to remove longer wavelength trends. I then subdivided the Camamu into three sections roughly 40 km-long (encompassing Domains 3 and 4) and considered the entire Almada incipient oceanic domain (Domain 3) as one 35 km-long section to compute roughness RMS values. These values were then compared to comparable studies from other rifted margins (Figure 3.18).

In their study of ultraslow spreading crust emplaced at the Mid Atlantic Ridge, Mid-Cayman Spreading Center, Southwest Indian Ridge, and other divergent margins, Sauter et al. (2018) concluded that roughness values greater than ~300 m are suggestive of magma-poor, ultra-slow spreading ridges where mantle exhumation can occur. Roughness values across the northern Camamu (RMS = 306) and Almada (RMS = 387) over Domain 3 incipient oceanic crust suggest ultra-slow spreading rates of 8-20 mm/yr (Figure 3.18), and the potential for mantle exhumation.

Roughness values within the areas of normal oceanic crust (Domain 4) are more complex. Along a seismic reflection line crossing the Camamu sub-basin, the first 40 km of oceanic crust had a roughness value of 82, while over the next 40 km this increased to 248. This would imply large variations of spreading rates along strike, which seems unlikely; these results were hard to confirm along strike because of the lack of imaged normal oceanic crust within the Almada (Figure 3.18).

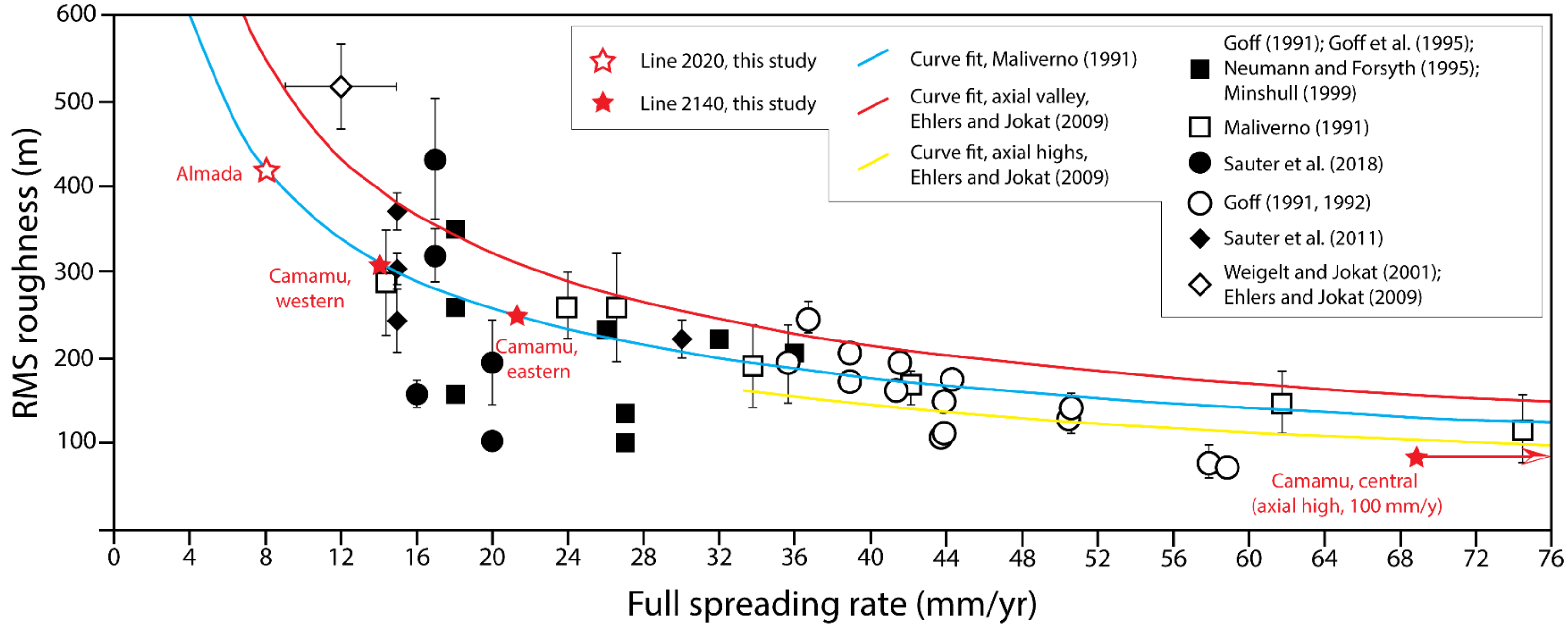

Figure 3.18 Oceanic-derived crustal roughness values, compiled from the world's ocean basins by Bécel et al. (2020), can be used to estimate relative velocity in seafloor spreading in the study area of southeastern Brazil. Comparisons of curve fits by Maliverno (1991) and Ehlers and Jokat (2009) to roughness values along the incipient oceanic crust measured along both PSDM ION seismic lines indicate initial, ultra-slow spreading at rates of 8 to 14 mm/yr within Domain 3 incipient oceanic crust and an increase to more than 20 mm/yr over Domain 4 normal oceanic crust.

3.4.8 Hydrocarbon implications of this study for the Camamu-Almada basin

A major factor for the generation of hydrocarbons along rifted-passive margins is the past and present heat flow that can act as primary control for hydrocarbon maturation (Palumbo et al., 1999). The Camamu-Almada margin exhibits highly variable Moho elevations like those described in Péron-Pinvidic et al. (2013); I extended their interpretations across an extensive area of the South American and African conjugate margins (Figure 3.1b–c).

On this same regional rift domain map, I combined the most recent worldwide heat flow model from Lucazeau (2019) (Figure 3.19a). Heat flow, on average, tended to decrease offshore, but there was considerable overlap between values across each of the four domains (Figure 3.19b–e). Large variations in heat flows (24–95 mW/m^2) occurred within the distal domain (Domain 1–3, Figure 3.10–3.12) because this domain can encompass different types of crust including: hyperextended continental crust, unroofed lower continental crust, exhumed mantle, igneous crust, and SDRs. Comparisons to giant hydrocarbon discoveries showed that most of these largest oil discoveries (500 MBOE) are within the proximal, necking, and at the landward edge of the distal domain (Figure 3.1b–c). This concentration may be partly influenced by shallower drilling depths in this more landward area rather than viability of source rock (Figure 3.19f).

Figure 3.19 a) Regional map showing the four structural domains (proximal, necking, distal, and oceanic) of eastern South America-western Africa conjugate, rifted-passive margin pair based on the definitions and mapping of Peron-Pivinidic et al. (2015) and the results of this study shown on a basemap of modern global heat flow modeled by Lucazeau (2019). **b)** The proximal domain of continental crust displays an average heat flow of 68.8 mW/m^2. **c)** The necking domain of continental crust displays an average heat flow of 65.1 mW/m^2. **d)** The distal domain of thinned continental crust and possibly oceanic crust displays an average heat flow of 57.5 mW/m^2. **e)** The oldest oceanic crust displays an average heat flow of 56.6 mW/m^2. **f)** Comparison of the structural domains across northeastern Brazil margin, as imaged in the Almada sub-basin, to its conjugate margin along the South Gabon basin, based on my depth conversion of time-migrated seismic from Scott (2015).

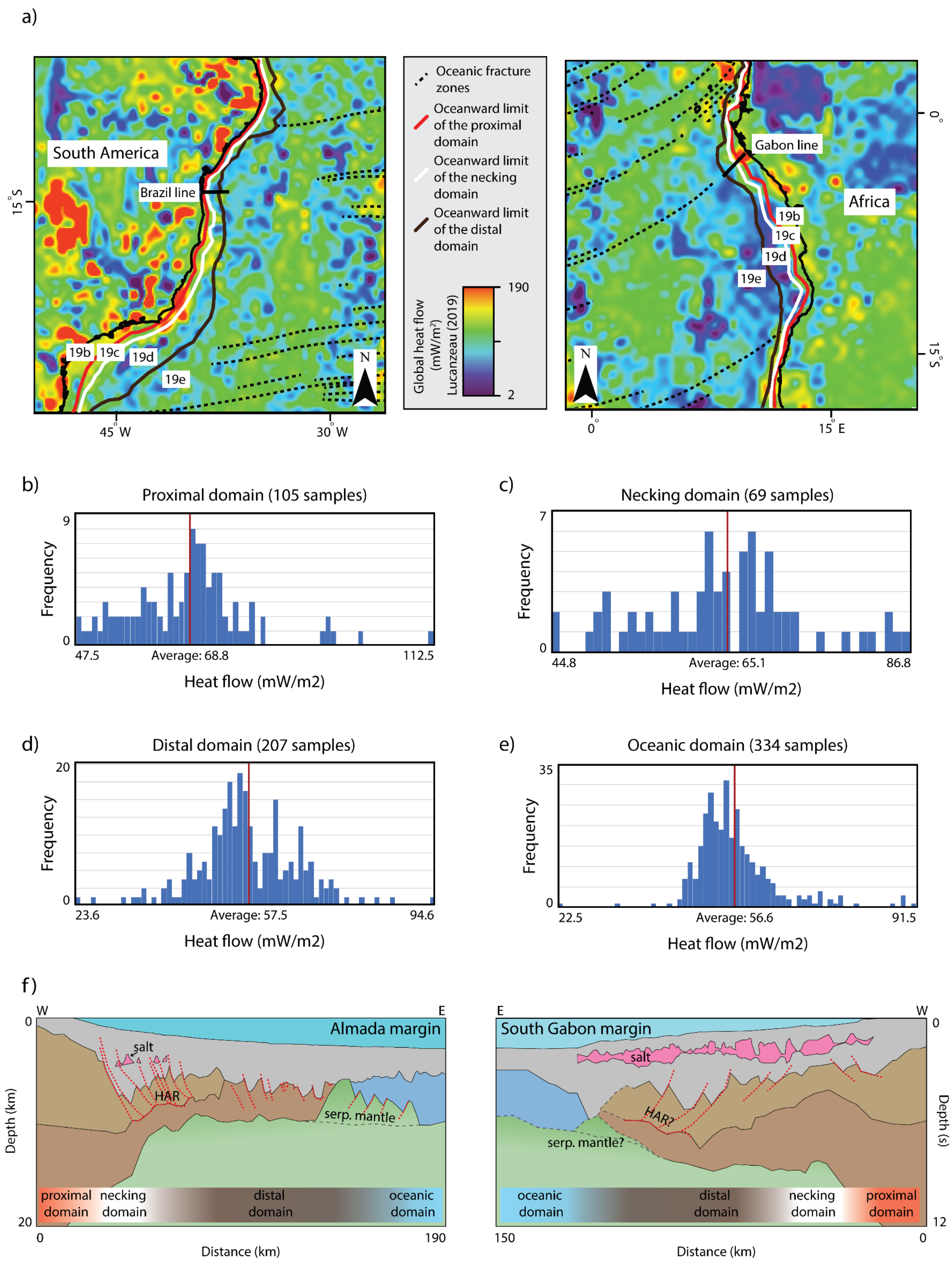
a)
South America
Brazil line
19b
19c
19d
19e
15° S
45° W
30° W
Oceanic fracture zones
Oceanward limit of the proximal domain
Oceanward limit of the necking domain
Oceanward limit of the distal domain
Global heat flow (mW/m²) Lucanzeau (2019)
190
2
Gabon line
Africa
0°
15° S
15° E
N
b)
Proximal domain (105 samples)
Frequency
9
0
47.5
Average: 68.8
112.5
Heat flow (mW/m2)
c)
Necking domain (69 samples)
Frequency
7
0
44.8
Average: 65.1
86.8
Heat flow (mW/m2)
d)
Distal domain (207 samples)
Frequency
20
0
23.6
Average: 57.5
94.6
Heat flow (mW/m2)
e)
Oceanic domain (334 samples)
Frequency
35
0
22.5
Average: 56.6
91.5
Heat flow (mW/m2)
f)
W
E
Almada margin
salt
HAR
serp. mantle
Depth (km)
0
20
proximal domain
necking domain
distal domain
oceanic domain
0
190
Distance (km)
E
W
South Gabon margin
salt
HAR?
serp. mantle?
Depth (s)
0
12
oceanic domain
distal domain
necking domain
proximal domain
150
0
Distance (km)

Another important factor for the creation of a functioning deepwater hydrocarbon system is the thickness of the overburden. For the Camamu-Gabon conjugates the thickness of sediments covering Domain 1 is similar (5.5 km in the Camamu, 8 km in the South Gabon). The base of this deepwater sedimentary sequence could be equivalent to the proved Neocomian lacustrine source rock that has been characterized and drilled nearshore (Gonçalves et al., 2000), and the thick burial and lack of syn-rift volcanic rocks suggest deep-water prospectivity for both conjugates.

3.5 Conclusions of this chapter

Detailed structural and stratigraphic interpretations from two PSDM seismic reflection lines were integrated with 2D and 3D gravity models of the Camamu-Almada and surrounding basins, offshore northeastern Brazil. Four different hypotheses were tested for the composition of the 40–110 km-wide transitional zone separating continental crust onshore and nearshore Brazil and offshore oceanic crust: 1) normal oceanic crust; 2) unroofed lower continental crust; 3) exhumed continental crust; and 4) igneous/incipient crust. 2D gravity modeling across the Almada sub-basin revealed that none of the models matched the observed gravity signal.

A new interpretation was proposed for the transitional zone that included three, distinctive crustal blocks: a high density (> 3.1 g/cc), or thin (< 4 km-thick) central block with no seismic Moho flanked by two, lower density (2.7–2.9 g/cc) blocks. The more landward of these three blocks exhibits a bright and undulating Moho at a depth of 14 km. The more seaward block adjacent to normal, oceanic crust exhibited a faint, but continuous, seismic Moho at a depth of 15 km.

To better understand the spatial relationships of these three blocks outside the areas covered by the two, deep-penetration seismic reflection lines, a 3D gravity model of the entire Camamu-Almada margin that extended over an along-strike-distance of 400 km was created. The 3D gravity model resolved extremely thin crust within a 1,300 km^2 lobate area in the Almada sub-basin and a 1,200 km^2 lobate area in the Camamu sub-basin, herein interpreted as exhumed mantle.

Modeling and interpretation analyses led to a model of crustal evolution from hyperextended continental crust to unroofed lower continental crust, exhumed mantle, and incipient to normal oceanic crust. Seafloor spreading estimates over the incipient oceanic crust also advocated for an ultra-slow spreading history, conducive for mantle exhumation. These interpretations were supported by seismic evidence of exhumed mantle within the conjugate South Gabon basin and a similar crustal structure for the Lion Basin, a magma-poor, ultrathin, rifted margin of Oligocene–Miocene age in the western Mediterranean Sea.

This study demonstrates that the Camamu-Almada is remarkably magma-poor with no obvious SDRs, intrusions, or underplating commonly seen along magma-rich margins. This magma-poor character for the Camamu-Almada basin contrasts with the northernmost Jacuípe and the Sergipe-Alagoas basins, 40 km north of the study boundary, where researchers identified SDRs and more typical magma-rich margin characteristics. The transition between these two margin types, magma-poor and magma-rich, lies somewhere within the 100 km-wide, and intervening, southern Jacuípe basin, where the paucity of seismic coverage, overprint of Cenozoic volcanism related to seamounts, and locally inconclusive modeling obscures the nature of the transition.

The interpretation of crustal structure for the Camamu-Almada basin was compared with the present-day heat flow, a key element for modeling hydrocarbon resources in both the South American and African conjugate margins. Heat flow values generally decrease oceanward, although there is considerable overlap between each of the domains proposed. Relatively high heat flow in the most distal areas (40–70 mW/m^2) of thinned continental crust and thick sedimentary overburden (6-8 km) suggest that large hydrocarbon systems may be present as an “outer kitchen” within the deepwater Camamu-Almada.

CHAPTER 4: CRETACEOUS-CENOZOIC UPLIFT AND EROSION EVENTS OF THE CAMAMU-ALMADA RIFTED-PASSIVE MARGIN, NORTHEASTERN BRAZIL: THEIR TECTONIC ORIGIN AND IMPACT ON HYDROCARBON POTENTIAL

4.1 Introduction

Passive margins are commonly viewed as submarine, sedimentary environments that are the sites of prolonged thermal subsidence, tectonically quiescent for time periods at tens to hundreds of millions of years, and – for these reasons – not subject to the same types of widespread, convergent, uplift and erosional events that affect active plate margins (McKenzie, 1978). However, seismic reflection-based studies of the rifted-passive margin of the North Atlantic Ocean in northwestern Europe and Greenland by Japsen and Chalmers (2000) showed compressional deformation of Cenozoic rocks in the passive margins the British Isles, Scandinavia, and Greenland 160 Ma after the cessation of rifting. Later work by Stoker et al. (2005) used large seismic reflection grids from the northwestern Atlantic margins to confirm anticlinal doming, angular unconformities, and modifications of the physiography of the existing passive-margin basins that re-routed deep-water circulation patterns and even led to the formation of major hydrocarbon traps. This convergent deformation occurred during the Early to Middle Miocene, or about 150 Ma after this segment of the margin formed by rifting with North America. Proposed mechanisms for deformation by these authors included: 1) emplacement of the Iceland hotspot plume in the early Cenozoic; 2) upward flow the mantle; 3) isostatic uplift of continental masses; and 4) regional compressive forces that included the Alpine orogeny of Oligocene to Recent age.

On the western margin of the North Atlantic Ocean in maritime Canada and the eastern USA, Withjack et al. (1995) used seismic reflection and well data to describe post-rift shortening of the Middle Triassic to Early Jurassic Bay of Fundy rift. Shortening structures included several km of reverse displacement on inverted normal faults, broad anticlines on the hanging wall blocks, and the overall synclinal geometry of the present-day Bay of Fundy rift. Although the exact post-rift timing is not known, these authors proposed that the deformation was related to ridge push forces form the Mid-Atlantic spreading ridge that were transmitted to the passive margin.

Other studies on the eastern margin of North America used thermochronology to link the uplifts of coastal areas of pre-rift crystalline basement with pulses of increased oceanic spreading along the oceanic Mid-Atlantic spreading ridge during two periods: 1) the late rift period of Early Jurassic (201-175 Ma) (Spotila et al., 2004); and 2) the passive margin period from the Middle Jurassic through the Late Cretaceous (174-65 Ma) (Roden-Tice et al., 2000). Roden-Tice et al. (2009) proposed that the northernmost New England area was regionally extended and uplifted by the passage of this part of the North American continent over the Great Meteor hotspot during the Late Cretaceous (118-70 Ma).

Figure 4.1 Tectonic and geologic setting of the Camamu-Almada segment of the Cretaceous-Cenozoic passive margin of northeastern Brazil with net Cretaceous-Cenozoic uplift estimates from apatite fission track data in the narrow coastal plain area of the basin ranging from 0.5 to 1.3 kms (Scotchman and Chiossi, 2009), whose datapoints are red squares; Japsen et al. 2012, whose datapoints are yellow circles). Inset map shows the location of this area on the eastern margin of South America. Limit of continental crust (LoCC) shown in yellow, marginal rift in the thin hatched black lines, both based on results from Chapter 3. Aptian salt deposits, shown in pink and compiled from Davison (2007), deposited in an elongate sag basin overlying the Berriasian-Aptian marginal rift. Areas of igneous activity in that may have affected the Brazilian rifted-passive margin are shown in purple: 1) Paraná large igneous province of early Cretaceous (Valanginian age ~132 Ma), related to pre-rift activity of the Tristan hotspot (Coffin and Eldhom, 1994). This Brazilian hotspot track is continuous with the Walvis ridge and Etendeka large igneous province on the conjugate margin of southwest Africa; 2) the adjacent Poxoreu igneous province emplaced in the Late Cretaceous (~84 Ma); 3) the Rio Grande Rise and the early Cenozoic Abrolhos magmatic province (69-32 Ma) and 4) the semi-continuous hotspot trail related to the Tristan hotspot that extended eastward across the Brazilian rifted margin to form the Trindade volcanic chain (50-10 Ma). Black dashed lines in oceanic crust of the South Atlantic Ocean are the mapped seafloor spreading anomalies Q2 (108 Ma) and Q1 (92 Ma) from Granot and Dyment (2015). Boxed areas show the location of the more detailed map of the study area in Figure 4.2.

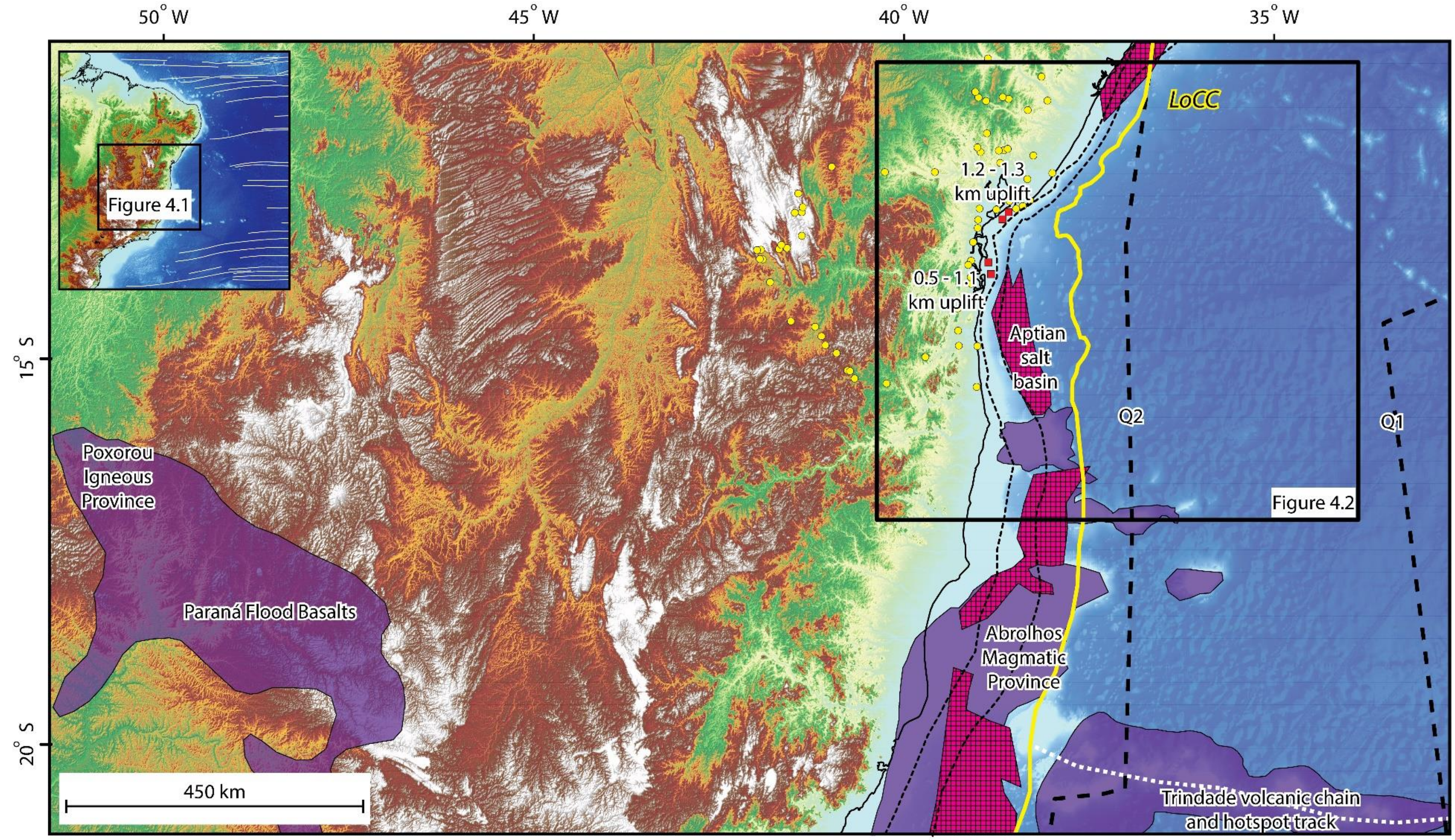
50° W
45° W
40° W
35° W
15° S
20° S
Figure 4.1
LoCC
1.2 - 1.3
km uplift
0.5 - 1.1
km uplift
Aptian
salt
basin
Q2
Q1
Figure 4.2
Poxorou
Igneous
Province
Paraná Flood Basalts
Abrolhos
Magmatic
Province
450 km
Trindade volcanic chain
and hotspot track

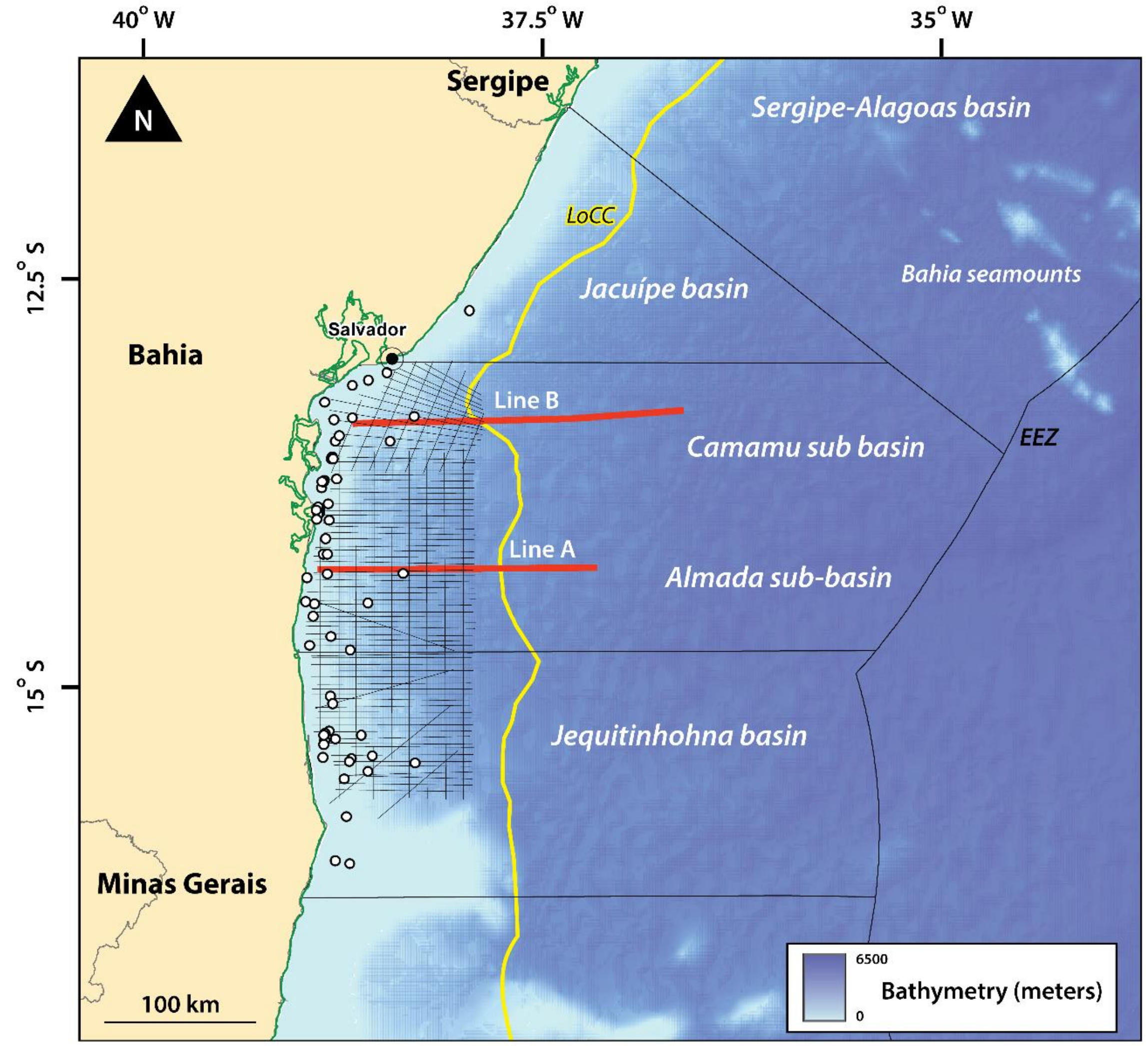

Figure 4.2 Map showing the location of subsurface data used in this study. Line A is a 200 km-long, deep-penetration seismic reflection line across the southern shelf, slope, and deepwater of the Almada sub-basin that was used for the structural restoration described in this chapter. Line B is the 230 km-long line crossing the northern part of the shelf, slope, and deepwater of the Camamu sub-basin that was also used for the structural restoration described in this chapter. Additional seismic reflection control was provided by the seismic grid shown in the black lines and tied to the well logs shown by white circles. The bathymetric grid is from GEBCO (2021).

For the conjugate margin of eastern North America and northwestern Africa, passive margin uplift events have been proposed as a result of: 1) rising mantle anomalies and lithospheric thinning during the late Jurassic and early Cretaceous (163-100 Ma) (Frizon de Lamotte et al., 2009) and during the Paleogene (65-56 Ma); and 2) far field effects of the Africa-Eurasia collision during the Late Cretaceous (100-66 Ma) (Leprêtre et al., 2014) and during the Alpine orogeny from the Oligocene to Recent (30-20 Ma) (Beauchamp et al., 1999).

On the passive, conjugate rifted-passive margins of the South Atlantic Ocean along the eastern margin of South America and the western margin of Africa, discrete Cenozoic deformation events have been similarly proposed based mainly on thermochronological studies of pre-rift, crystalline basement rocks. In a more recent study, Japsen et al. (2012) synthesized geological, landscape, paleothermal, and paleoburial data from the passive margin of northeastern Brazil and identified three passive margin uplift and erosion events beginning in the Late Cretaceous (80–75 Ma), Eocene (48–45 Ma), and Miocene (18–15 Ma) that deeply eroded the onshore. The authors proposed that the uplift events were correlatable across both Africa and Brazil and suggested that the Campanian event coincided with a decline in Atlantic seafloor spreading rates. They concluded that the common cause was the “lateral resistance to plate motion” (Japsen et al., 2012).

4.1.1 Objectives of this chapter

Based on the fundamental and widespread problem of identifying passive margin uplift events and correlating those events to a variety of previously proposed tectonic mechanisms, the objectives of this chapter included the following for the Camamu-Almada segment of the northeastern rifted-passive margin of Brazil:

1) To map 24 individual pre-, syn-, and post-rift (passive margin) surfaces based on 19,000 line-km of 2D seismic data and two, 200-230 km-long, deeply-penetrating seismic lines.

2) To quantitatively restore the 5 km-thick passive margin section observed on two, 200-230 km-long, deeply-penetrating seismic reflection lines recorded to upper mantle depths of 40 km whose crustal structure and tectonic origins are described in Chapter 3 of this dissertation; restorations included a process of unfolding, backstripping, and decompacting sedimentary units and estimating the amounts of erosion.

3) To compare these results to previous work on the timing of uplift and exhumation of the onshore areas of the Camamu-Almada rifted-passive margin and understand the mechanisms for these post-rifting events during the Cretaceous and Cenozoic.

4) To apply this information of erosive events to basin modeling of the offshore area to better understand the deepwater hydrocarbon potential of the established Morro do Barro syn-rift source rock of Berriasian–Valanginian age.

4.1.2 Tectonic and geologic setting of the rifted-passive margin of northeastern Brazil

4.1.2.1 Rift events affecting the Camamu-Almada margin

Opening of the South Atlantic propagated diachronously from south to north (Rabinowitz and LaBrecque, 1979; Matos, 2000; Reuber and Mann, 2019). Initial amagmatic rifting in the Neocomian (135 to 122 Ma) occurred through a triple junction formed by the confluence of the Recôncavo-Tucano-Jatobá rift (RTJ), the Jequitinhonha-Almada-Camamu rift (JAC), and the Jacuípe-Sergipe-Alagoas rift (JSA) (Figure 4.2) (Netto, 1978; Netto and Oliveira, 1985; Milani and Davison, 1988; Chang et al., 1992; Magnavita et al., 1994).

This triple junction remained active in northeastern Brazil until the RTJ rift arm aborted in the Aptian, and the JAC underwent concurrent rifting punctuated by intervals of inactivity (Ferreira et al., 2011). Faulting and rifting propagated east along the JAC until a final, distal marine rift in the early Albian, crustal break-up, and emplacement of oceanic crust (Caixeta et al., 2014; Chapter 4, this dissertation). Post-rift, the South Atlantic Gulf gradually opened as the Walvis ridge was breached and an Albian marine carbonate platform developed. This was followed by open-marine conditions and gradual deepening that drowned the high-energy carbonate platform, establishing bathyal conditions by the end of the Albian-Cenomanian (Chang et al., 1992).

4.1.2.2 Basement structures of the Camamu-Almada rifted-passive margin

The metamorphic basement of the São Francisco craton directly adjacent to the Camamu-Almada displays basement orogenic trends and faults that are oriented roughly north-south within the Paleoproterozoic Eastern Bahia orogenic belt (Alkmim and Martins-Neto, 2012; Ferreira, 2018) (Figs. 4.1 and 4.2). Original crustal thickness of the São Francisco craton was about 40 km, as estimated in the central part of the craton (Rivandeneyra-Vera et al., 2019). The crustal thickness decreases to 32 km at the coastline and 4 km at the deepwater limit of continental crust (Figs. 4.4 and 4.5).

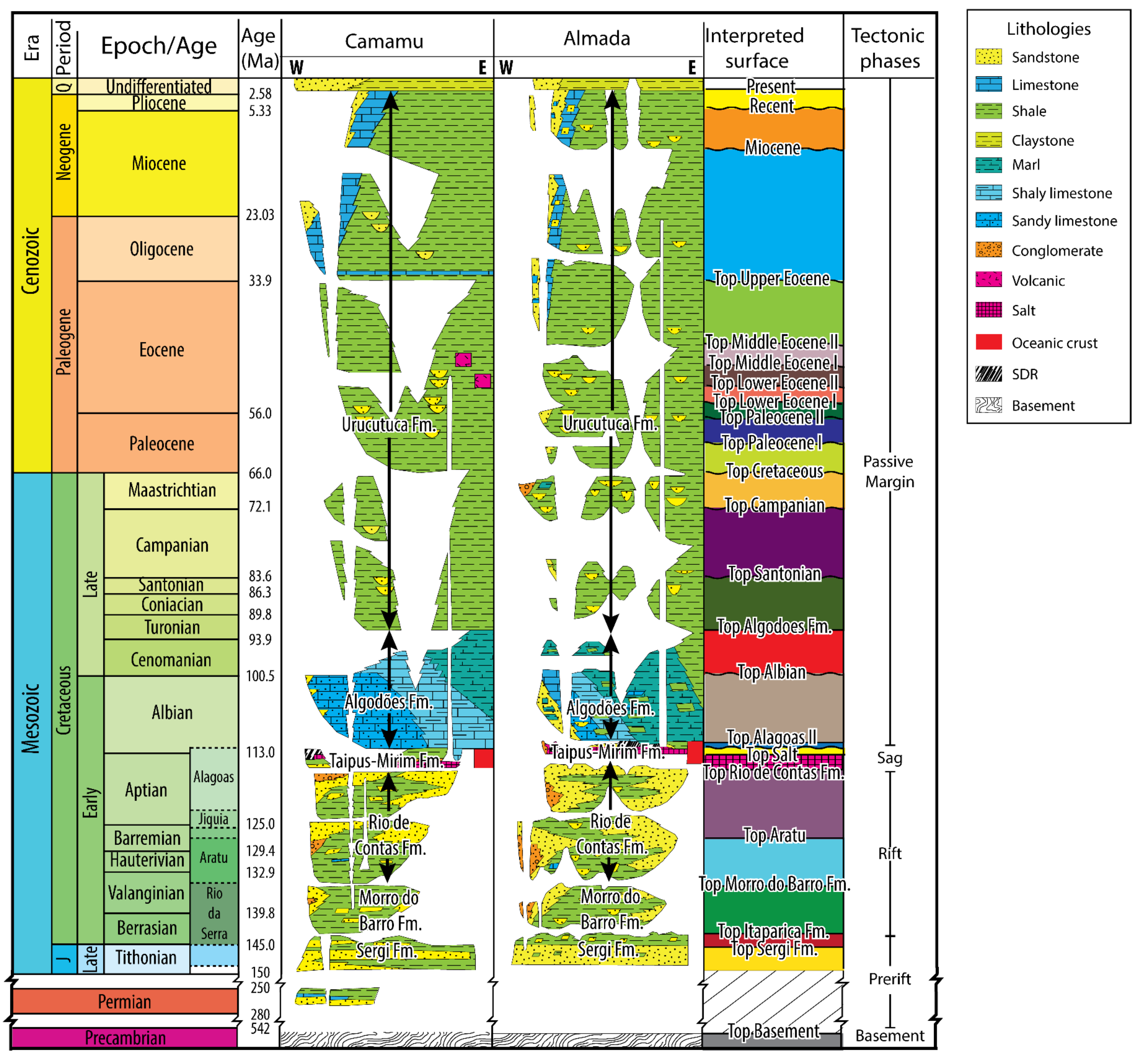

Figure 4.3 Precambrian to Recent stratigraphic column modified from Milani et al. (2007) for the Camamu-Almada rifted-passive margin of northeastern Brazil. The four main tectonostratigraphic sequences include: 1) more sand-rich pre-rift and syn-rift formations of Permian to Aptian age; 2) a brief evaporitic sag phase in the late Aptian; 3) a late syn-rift shallow carbonate phase of Albian age; and 4) a passive margin phase characterized by deepwater shale with sandstone channels from the Cenomanian to Recent. The key to lithologies is shown to the right. Unconformities with missing stratigraphic section affect the passive margin from the late Albian to recent. The names of the 24 individual surfaces that were mapped from the seismic grid and wells shown in Figure 4.2 are indicated. Structural restorations of the chapter focused on the late Aptian to recent late syn-rift, sag, and overlying passive margin phase.

This underlying crystalline fabric in northeastern Brazil was reactivated during the break-up of Gondwana with normal faults nucleating along the pre-existing basement structural trends (Ferreira, 2018). In their interpretation of an extensive seismic reflection dataset, Ferreira et al. (2009) proposed that the syn-rift faults oriented roughly parallel to the onshore basement fabric, N-S in the Almada and trending more to the northeast near the Camamu sub-basin. Additionally, Ferreira et al. (2009) interpreted two structural highs along the same trends as the Itaju do Colônia and Salvador “shear zones”, two roughly E-W basement lineaments that separated the Camamu-Almada sub-basins (Ferreira et al., 2009). The orientation of the underlying orogenic fabric appeared to have had a first-order impact on the syn-rift evolution of the basin (Figure 4.4 and 4.5).

4.1.2.3 Stratigraphic summary of the Camamu-Almada rifted-passive margin

The stratigraphic succession used in this study, summarized on Figure 4.3, was based on previous work by Milani et al. (2007), and my seismic interpretation showed that the maximum stratigraphic thickness in the Camamu sub-basin is 9.3 km (Figure 4.4) and 9.2 km in the Almada sub-basin (Figure 4.5). The overlying sedimentation was divided into four fundamental units: pre-rift, syn-rift, transitional, and post-rift marine (Teisserenc and Villemin, 1989; Gontijo et al., 2007).

The thick pre-, syn-, and post-rift sedimentary sections overlies the Precambrian crystalline basement of the São Francisco craton that is composed of granitic-gneisses that are migmatized with metamorphic facies varying from amphibolite to granulite (Almeida et al., 1981). Offshore, this heterogeneity of the crystalline basement was confirmed in wellbores that have sampled basement to recover gneisses and granulites (Gordon et al., 2013).

Pre-rift sedimentation within the Camamu-Almada deposited in fluvial, deltaic, and aeolian settings from the Jurassic to Berriasian times with a maximum thickness of 500 m (Gontijo et al., 2007; Gordon, 2011). The first interpreted pre-rift interval is the Jurassic Sergi formation, which is one of the most prolific hydrocarbon reservoirs in the basin (Fig. 4.3). This interval is composed of red and gray-green sandstone with cross-stratification and intercalations of shale and conglomerate (Viana et al., 1971). Immediately overlying the Sergi is the second mapped, pre-rift interval – the Itaipé formation, a thin clastic section characterized by shale and rare sandstone lenses that represent the transition from the pre- to syn-rift phase (Netto et al., 1994) (Figure 4.3).

The syn-rift sequence is largely composed of lacustrine deposits, some of which are considered the main source rocks of the region (Milani et al., 2007). Syn-rift thicknesses reach up to approximately 3300 m and was deposited within the progressively younger and offshore-propagating half-grabens (Gontijo et al., 2007; Gordon 2011). The oldest mapped formation in this sequence, the Morro do Barro, contains coarse sandstone and carbonaceous, lacustrine greenish gray to dark brown shale and is the source rock for the proved, successful nearshore Morro do Barro (!) hydrocarbon system (Caixeta et al., 2007) (Fig. 4.3). Other mapped horizons are the top of the local Aratu within the lower Barremian, and the top of the Rio de Contas, a fine sandstone and shale unit with associated conglomerate, dolomite, and marl that was deposited in a deltaic and lacustrine system (Netto et al., 1994) (Fig. 4.3).

The Taipus-Mirim evaporites of Aptian age developed during the Gondwana break-up and opening of the South Atlantic and can be seen today to exhibit pillow and diapir structures that can reach 2500 m in thickness (Gordon, 2011). Other mapped intervals within this section are two overlying unconformities within the Alagoas carbonates (Figure 4.3).

During the post-rift period, the Camamu-Almada basin evolved from a shallow carbonate platform to a deep-water environment (Fig. 4.3). These Albian-Turonian carbonates of the Algodões formation were partially dolomitized, exhibit thicknesses that are generally less than 500 m, and are capped by a Cenomanian to Turonian unconformity (Milani et al. 2007). Both the top of the Albian interval and the top of the formation itself are mapped (Fig. 4.3). The Urucutuca formation unconformably overlies the Algodões and is predominantly composed of shale with interbedded conglomerate, sandstone, and carbonate rocks with occasional turbiditic flows (Netto et al., 1994). The Urucutuca spans the period from the Turonian to Recent – I mapped thirteen different surfaces within this formation for this study (Fig. 4.3).

4.1.2.4 How far north did the Aptian Brazilian salt basin extend and what was its original thickness?

Massive salt, up to several km in thickness, in the Brazilian salt basin formed in a restricted marine environment with poor circulation that was dammed to the south by elevated hotspot track of the submarine Walvis ridge (Beglinger et al., 2012). Basement highs separated these evaporites as they developed diachronously in the Aptian, and deposition was immediately followed by the latest rift and passive margin phases (Davison, 1999). The Camamu-Almada basin is near the thinning, northernmost limit of the Brazilian salt basin, along with its conjugate South Gabon basin, where much thicker, late Aptian salt was deposited (Davison, 2007).

During the rifting process, the northeastern Brazilian segment appears to have behaved as the lower plate, resulting in a narrower margin that limited salt deposition (Davison, 2007).

This is contrasted by the thick salt along the wider margin on the African side (Gordon et al., 2013). Alternatively, Reuber and Mann (2019) proposed that the origin of the wide versus narrow margin is instead related to inherited basement fabrics: the rifting of narrow margins like northeastern Brazil occurred parallel to the inherited basement fabric which was weak and broke easily to form a narrow margin. Wider margins with rifting at a higher angle to the inherited basement fabric, such as the conjugate of northeastern Brazil in Gabon, was stronger, resisted break-up, and formed a broader rift zone.

Evaporites can create accommodation for clastic sedimentation because areas of remobilized and evacuated salt can form deep basins. Salt is mechanically weak, relatively incompressible, and flows like a fluid across geologic time, promoting instability, and because of its inherent weakness, movement is closely tied to regional deformation. The primary driving force behind salt tectonics is differential loading, either induced by gravitational forces, thermal gradients, or tectonic deformation (Hudec and Jackson, 2007).

Widespread salt tectonism characterized post-Albian sedimentation within basins further south along the Brazil passive margin, like the Santos and Campos. Thin-skinned structures within these basins detach on the salt layer between the syn-rift and sag-basin deposition, are deformed by gravity gliding and gravity spreading, and are affected by continental rifting (Mohriak et al., 2008).

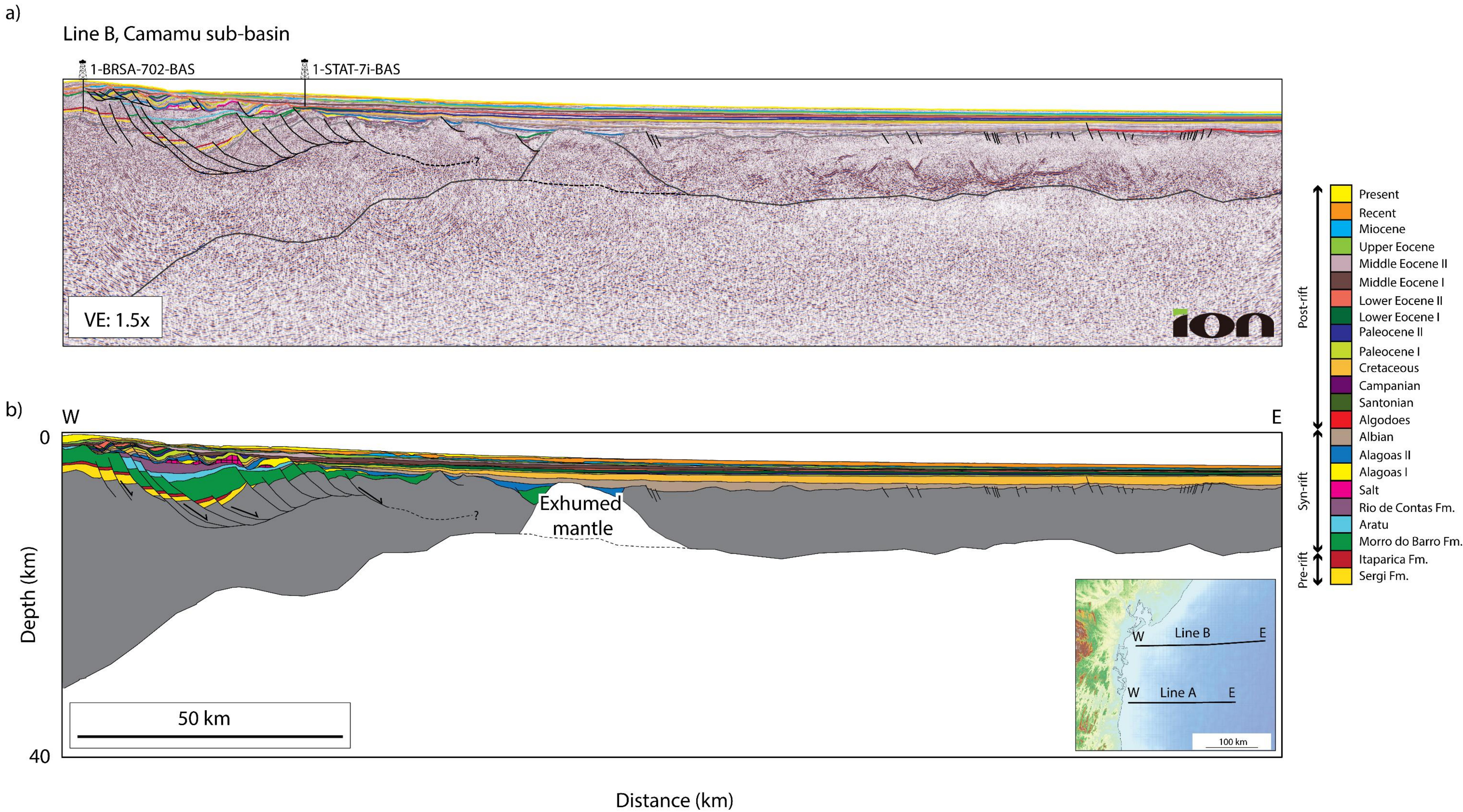

Figure 4.4 a) Structural interpretation of deep-penetration seismic Line B across the Camamu sub-basin of the northern Camamu-Almada rifted-passive margin that is located on the inset map and on the map in Figure 4.2. Colored lines correspond to the 24 mapped surfaces shown in Figure 4.3. **b)** Interpretation of crystalline basement shown in grey and described in detail in Chapter 3. The overlying pre-rift, syn-rift, sag, and passive margin formations are shown by colors that are keyed to the formation names in the stratigraphic column to the right. Structural restorations of Line B through the Camamu sub-basin focused on quantifying the timing and magnitude of multiple normal faulting, uplift and, erosional events that affected late Aptian to recent late syn-rift, sag, and overlying passive margin phases.

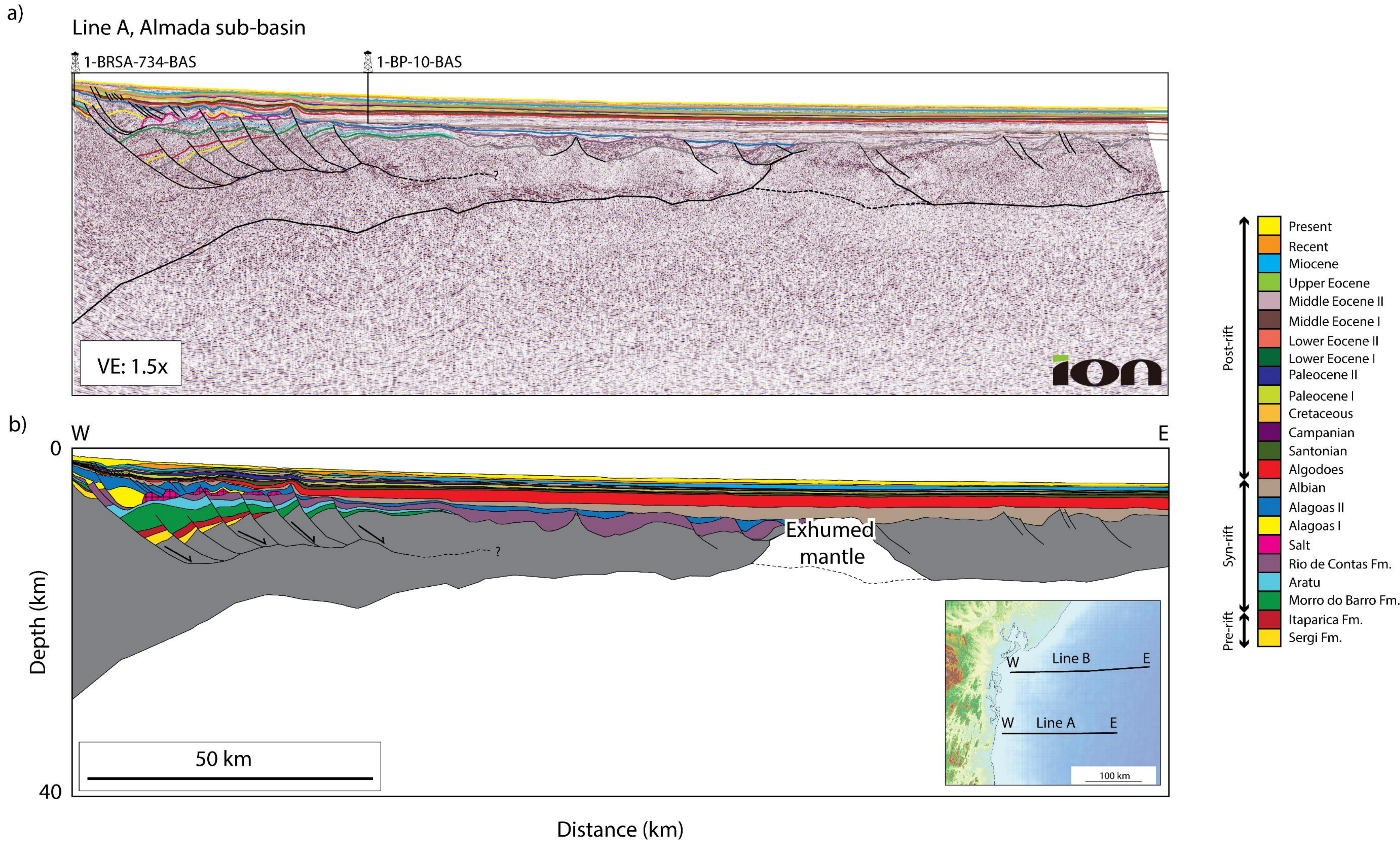

Figure 4.5 a) Structural interpretation of deep-penetration seismic Line A across the Almada sub-basin of the northern Camamu-Almada rifted-passive margin that is located on the inset map and on the map in Figure 4.2. Colored lines correspond to the 24 mapped surfaces shown in Figure 4.3. **b)** Interpretation of crystalline basement shown in grey and described in detail in Chapter 3. The overlying pre-rift, syn-rift, sag, and passive margin formations are shown in color and are keyed to the formation names to the right. Structural restorations of Line A through the Almada sub-basin focused on quantifying the timing and magnitude of multiple normal faulting, uplift, and erosional events that affected late Aptian to recent late syn-rift, sag, and overlying passive margin phases.

As the salt thins to the north around the Camamu-Almada sub-basins, salt tectonism would appear to be less of a factor in its passive margin deformation. However, in a previous study of the Almada sub-basin, Brandão et al. (2020) used a grid of 2D seismic lines to propose various salt structures along with zones of salt inflation and deflation related to salt remobilization. A key objective of the reconstructions in this chapter became: how far north did the Aptian Brazilian salt basin extend and what was its original thickness?

4.2 Data and methodology used in this chapter

4.2.1 Seismic reflection data and wells

For this study, I structurally restored two, high-resolution, long-offset, Kirchhoff pre-stack depth-migrated seismic reflection lines that were acquired, processed, and made available by ION Geophysical. Both lines are dip lines that collectively image 430 km of the Camamu-Almada rifted-passive margin and were acquired in 2012 as part of the Greater BrasilSPAN 2D seismic reflection dataset. Acquisition parameters can be found at ION Geophysical’s website (https://www.iongeo.com/data-library/latin-america/brazil/greater-brasilspan/) and processing workflows were described by Sauter et al. (2016).

To supplement these two ION lines, I also interpreted 2D seismic grids from four, time-migrated, seismic reflection surveys that were provided by the Agência Nacional do Petróleo, Gás Natural e Biocombustíveis (ANP) and included: 1) three separate surveys of which two were acquired by GECO AS in 2001 and one was acquired prior to 1998; the record lengths for these three surveys range from 12 to 18 seconds; and 2) a seismic dataset reprocessed by Gaia in 2001 with data of various vintages and record lengths (Figure 4.2).

66 boreholes were selected from the ANP database based on whether they included operator-picked well tops. These wells were used to interpret the different horizons within the seismic surveys (Figure 4.2). Horizon ages presented in this chapter were approximate because there was a lack of high-resolution biostratigraphic dating for many of these horizon picks. Several unconformities were relatively timed for this reason (e.g., intra-lower/middle Eocene unconformities as occurring sometime within the lower or middle Eocene).

4.2.2 Methodologies used for structural restoration of regional lines

Chamberlin (1910) first described the concept of using constant area for balancing structural cross sections where both the deformed and undeformed sections maintain roughly the same area across a 2D section, and little mass lost or gained out of section. Using this approach, a 2D section is restorable to its pre-deformation geometry, and each time-step can be described and quantified.

The addition of a salt layer within a section to be restored violates this law of constant area, as salt is extremely mobile and can move in and out of the plane of the section. However, the workflow described below using MOVE can accommodate remobilized salt by application of backstripping, isostatic adjustment, thermal adjustment, restoring the horizon, and adjusting the salt area (Fig. 4.6).

Backstripping removes a specific rock thickness and then accounts for sediment compaction using the thickness and density of the remaining sedimentary column (Roberts et al., 1998). Because laboratory measurements have empirically shown that the porosity of a rock exponentially decreases with depth (Stüwe, 2007), I applied the decompaction solution of Sclater and Christie (1980) to approximate the compaction and loss of porosity with increasing depth.

Linked with compaction is isostatic adjustment, which addresses the non-elastic response of Earth's lithosphere due to either loading or unloading. I approximated this response through the calculation of the Airy isostasy. I also considered the effects of thermal subsidence and the effects of changing temperatures on subsidence (McKenzie, 1978). During the rifting process, the crust thins and asthenosphere flows into the space that is created, and as this asthenosphere cools, the crust subsides. Cooling and subsidence are greatest immediately following rifting and decline over time. All three corrections were performed within the MOVE software for each timestep.

4.2.3 Workflow used for structural restoration

Figure 4.6 illustrates a four-step workflow applied to structurally restoring horizons that ranged in age from the Miocene to the Upper Eocene. These steps included the following:

1. Initial Miocene conditions and the starting point for the restoration (Figure 4.5a).
2. Removal of the Miocene, underlying rock decompacted, and section isostatically and thermally adjusted. Hatched red line indicates present-day shelf geometry for next step (Figure 4.6b).
3. Upper Eocene horizon restored to present-day shelf geometry to model underlying salt evacuation. Missing "space" underneath post-rift sediments is filled in with evaporites (Figure 4.6c).

Figure 4.6 Summary of main steps in the structural restoration of Line A of the Camamu sub-basin, as shown in Figure 4.4. **a)** Miocene unit was unfolded and structurally restored. **b)** Miocene unit was backstripped and the underlying section was decompacted and thermally/isostatically adjusted. **c)** Upper Eocene was unfolded and structurally restored to the shape of the present-day shelf geometry; this provided an estimate for the thickness of the Aptian salt interval at this time step. **d)** Erosion of the Upper Eocene was estimated and restored using the shape of the underlying horizons. Section was compacted to account for the restoration of the eroded Upper Eocene rock thickness.

a) Restored Miocene

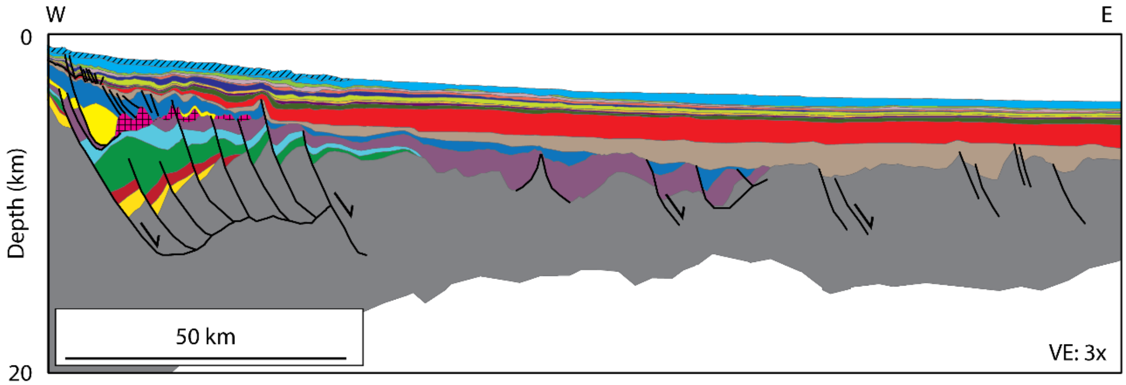

b) Miocene backstripped, section decompacted and thermally adjusted

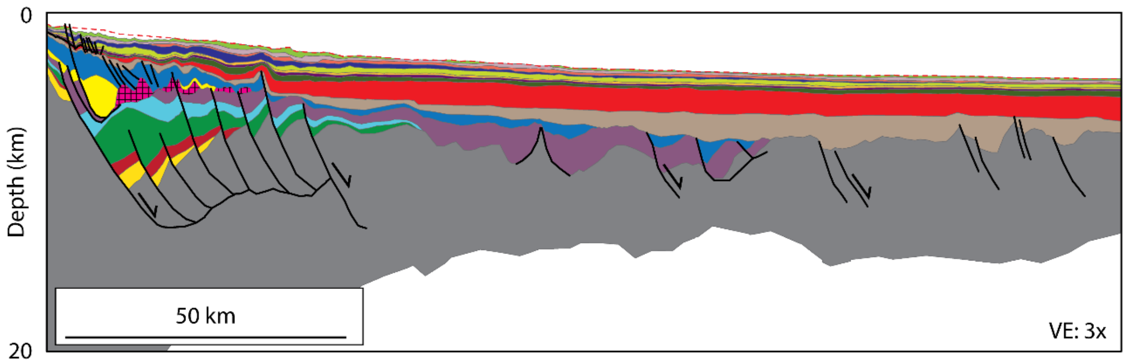

c) Upper Eocene unfolded to present-day shelf geometry to restore original salt thickness

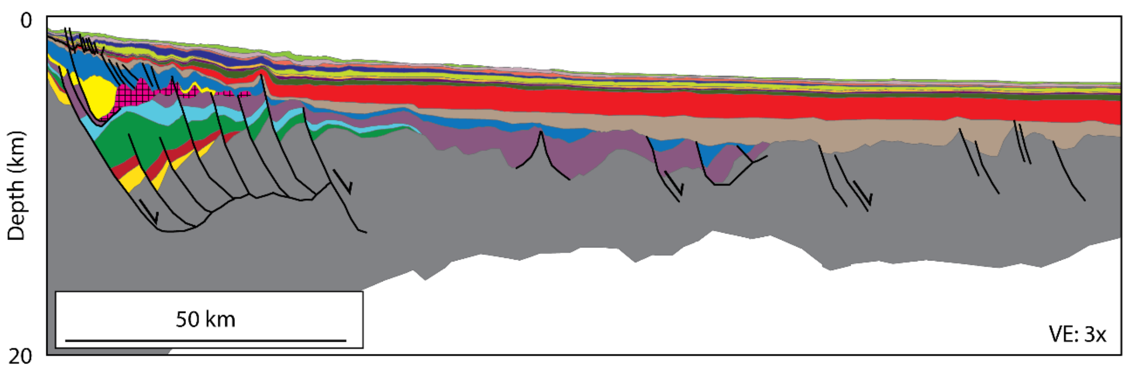

d) Upper Eocene missing section restored, section compacted

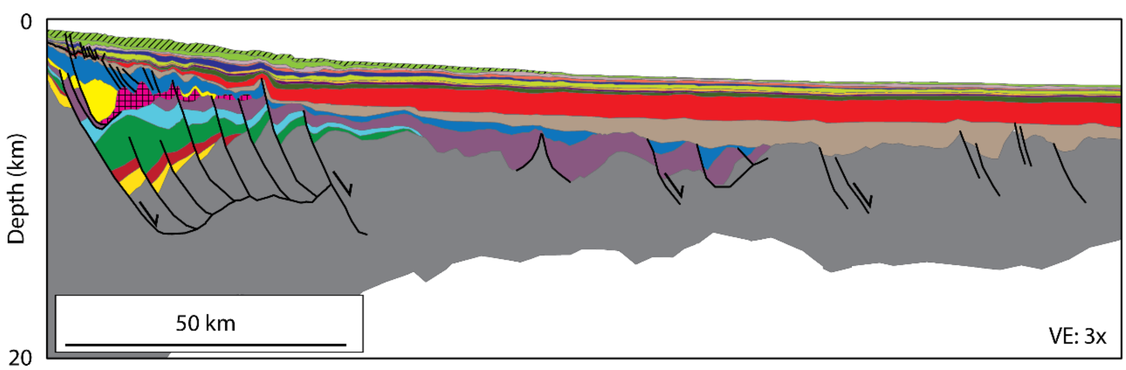

4. Underlying Middle Eocene surface was used as a template to restore eroded Upper Eocene section, representing the minimum eroded interval (Figure 4.6d). Underlying rock was compacted to account for the loading of the restored section.

4.3 Summary of main results from the structural restoration of 18 intervals from the Camamu and Almada sub-basins

The results of the restoration described below model the geological evolution of eighteen mapped, late-rift and post-rift horizons that have been interpreted for the Camamu and Almada sub-basins (Figures 4.7–4.12). Each model was subdivided into six time-steps: Aptian Salt, Alagoas/Albian, Upper Algodões/Cretaceous, Paleocene, Eocene, and Miocene to Present as summarized on the stratigraphic column in Figure 5.3. Each of the steps was described below.

4.3.1 Restoration of Aptian salt unit interval

The thickness and areal extent of the Aptian salt thickness reached 1.75 km and 39.9 km^2, respectively, in the Camamu basin and 3.5 km and 60.3 km^2, respectively, in the Almada basin (Fig. 4.7). This evaporitic layer extended offshore until a topographic high that limited further deposition (Fig. 4.7). These thicknesses and areas were the minimum required to accommodate for the overlying post-rift sedimentation as shown in the following time steps.

The top of the salt layer was restored by assuming a near-horizontal bathymetric expression, as salt is assumed to deposit sub-horizontally in waters shallow enough to promote evaporation and crystallization (Warren, 2006).

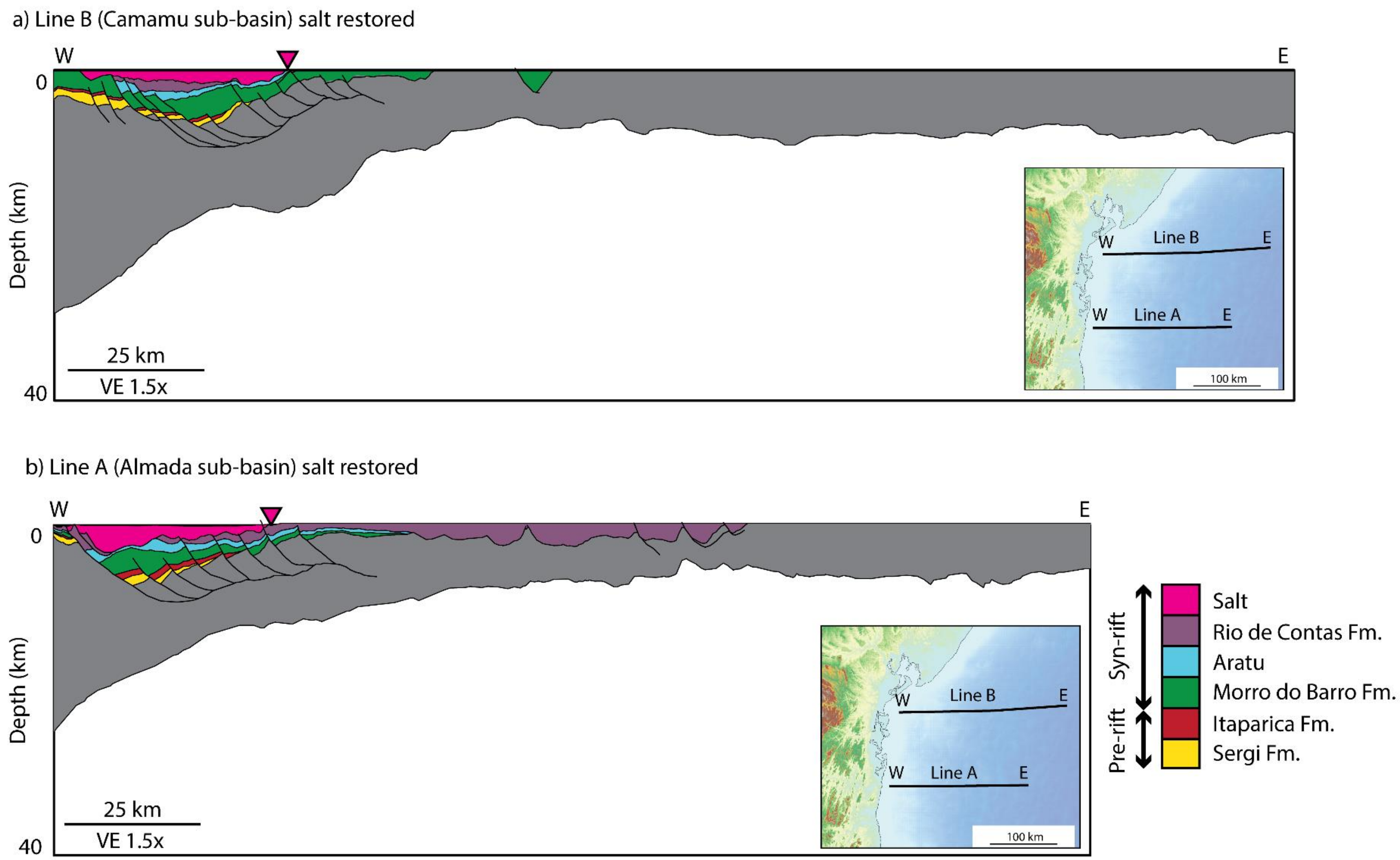

Figure 4.7 a) Restoration of Line B across the Camamu sub-basin during Aptian time when the salt-filled sag basin overlayed the northern area of an elongate, marginal rift and extended over an estimated area of 40 km^2. **b)** Restoration of Line A of the Almada sub-basin during Aptian time when a salt-filled sag basin overlayed the southern area of an elongate marginal rift and extended over an estimated area of 60 km^2.

4.3.2 Restoration of the Alagoas/Albian interval

Within this time interval, I mapped three surfaces across both lines: Alagoas I, Alagoas II, and top Albian (Figure 4.8).

4.3.2.1 Results from the Camamu sub-basin

The first post-salt sedimentary sequences included Alagoas-Albian carbonate and shale section (Figures 4.8a–4.8c). Initial deposition up to Alagoas I time was more restricted before the more regional salt deposition during Alagoas II time. By the end Albian, true regional deposition extended across the model as deepwater sedimentation reached 2.3 km in thickness. Salt tectonism greatly influenced nearshore deposition as the evaporites deflated and formed walls, were pushed out of plane, or were exposed and experienced dissolution in seawater. The final area of salt by the end of the Aptian was diminished to an area of 29.5 km^2.

Two unconformities and erosive events are recognized during this time. The first was associated with the Alagoas I surface eroding up to 820 m of the stratigraphic succession. The second was associated with the Albian surface and eroded up to 1000 m.

.

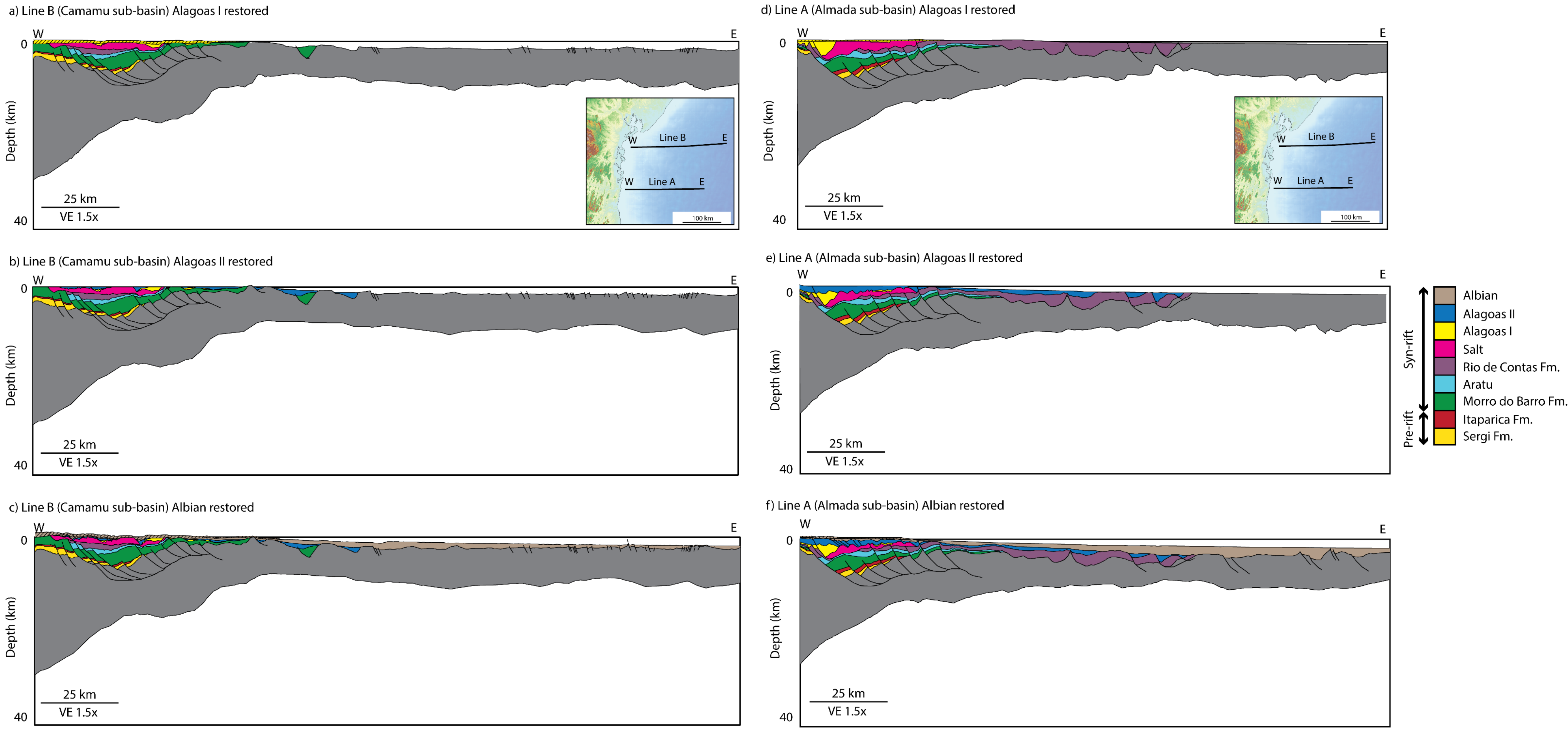

Figure 4.8 Restoration of the Camamu and Almada sub-basins during the late syn-rift Alagoas and Albian intervals, the restoration showed significant erosion and rapid salt deflation across both sub-basins. **a)** The restoration of the Camamu sub-basin during the Alagoas I interval indicated 820 m of erosion and a total salt area of 37.5 km^2. **b)** The restoration of the Camamu sub-basin during the Alagoas II interval indicated no erosion during this time and a total salt area of 35.6 km^2. **c)** The restoration of the Camamu sub-basin during this time indicated 1000 m of erosion and a 29.4 km^2 salt area. **d)** The restoration of the Almada sub-basin during the Alagoas I interval indicated 330 m of erosion and a 54 km^2 salt area. **e)** The restoration of the Almada sub-basin during the Alagoas II interval indicated no erosion and a 33.5 km^2 salt area. **f)** The restoration of the Almada sub-basin during the Albian interval indicated 450 m erosion and a 23.8 km^2 salt area.

4.3.2.2 Results for the Almada sub-basin

Albian deposition followed a similar pattern in the Almada sub-basin except for a thicker Alagoas I block nearshore and more widespread Alagoas II deposition. Salt tectonism also heavily influenced the overlying sediment deformation, with a final salt area of 26.4 km^2 in the Almada sub-basin by the end of the Albian. Two similar erosive events within the Almada model were identified. The first, associated with the Alagoas I surface, eroded up to 330 m, while the second, associated with the Albian surface, eroded up to 450 m.

4.3.3 Restoration of the Upper Algodões/Cretaceous interval

Interpretations within the upper Algodões and Cretaceous intervals across the Almada and Camamu differ in resolution. Within the Almada, discernable Algodões, Santonian, Campanian, and Cretaceous tops are resolvable (Figure 4.9b–4.9e), while within the Camamu only a top Cretaceous surface was interpretable (Figure 4.9a).

4.3.3.1 Results for the Camamu sub-basin

From the Aptian to the Cretaceous, thick sedimentation blanketed the Camamu sub-basin as salt tectonism slowed (but continued) nearshore, and the shelf submerged under at least 50 m of water. Final salt volume across the model reached a volume of 29 km^2.
A large erosive event caps this section, with removal of up to 1300 m of rock.

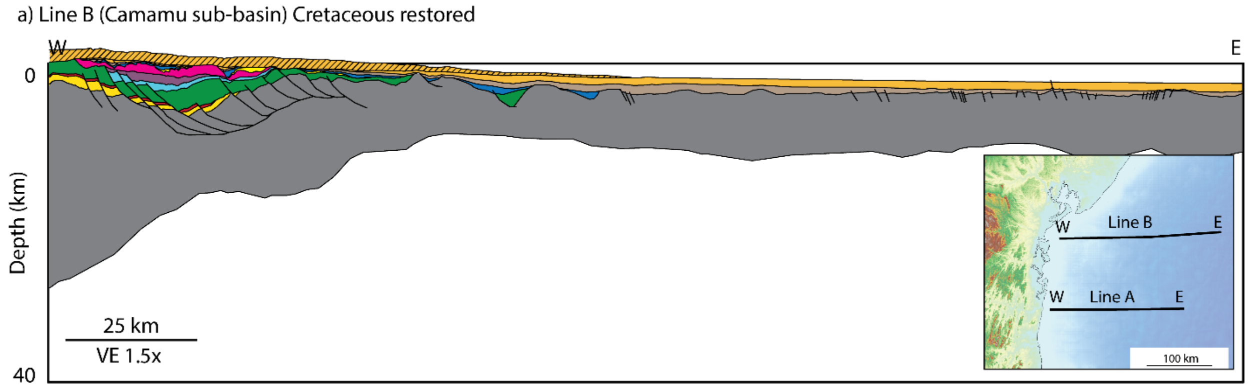

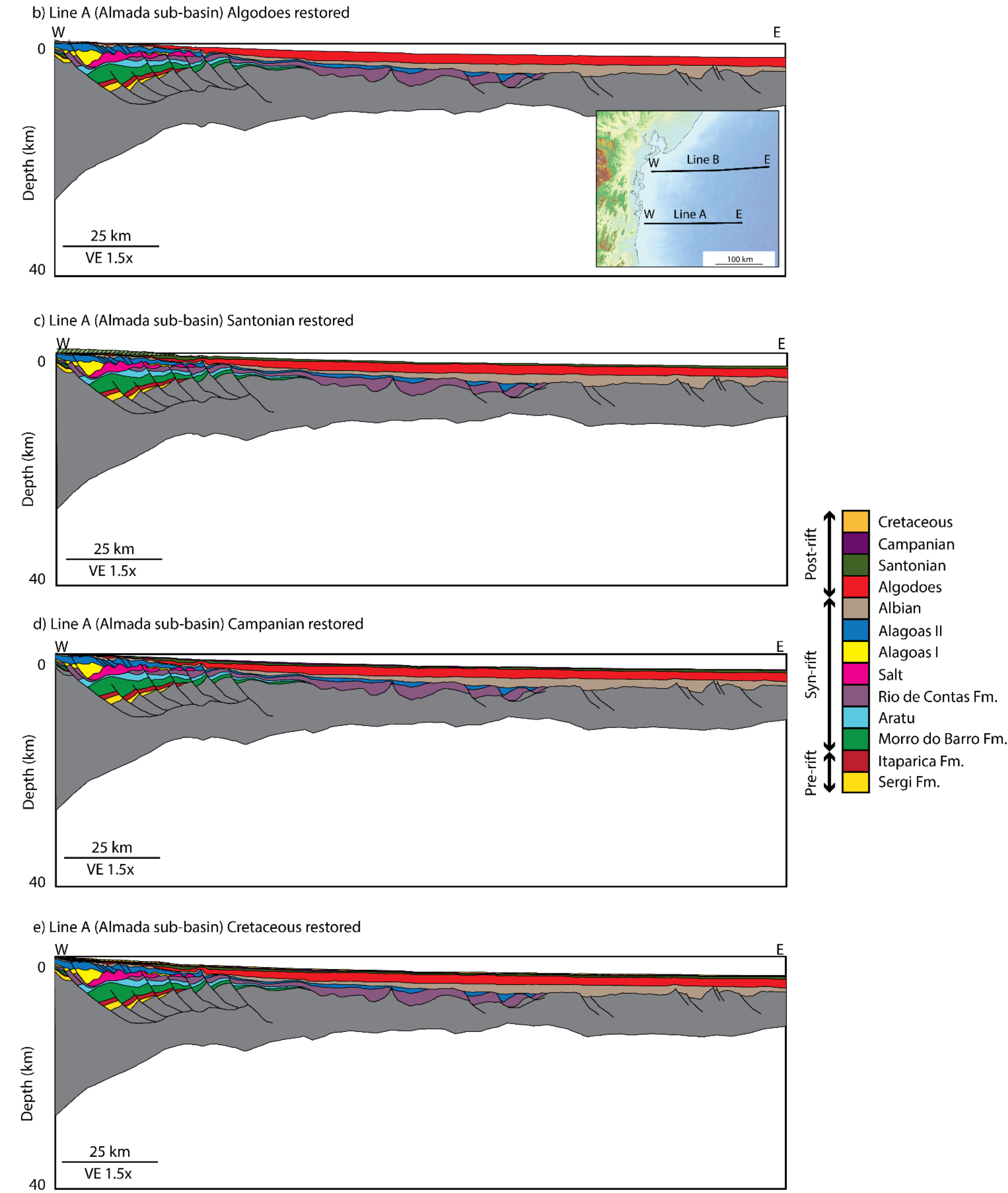

Figure 4.9 Restoration of the Camamu and Almada sub-basins during the post-rift, Cretaceous passive margin period. **a)** The restoration of the Camamu sub-basin during the Cretaceous indicated 1300 m of erosion and a 29 km^2 salt area. **b)** The Almada Algodões restoration indicated no erosion and a total salt area of 23.6 km^2, during a period of increased, deepwater clastic sedimentation. **c)** The restoration of the Almada sub-basin during the Santonian interval indicated 770 m of erosion with a salt area of 21 km^2. **d)** The restoration of the Almada sub-basin during the Campanian interval indicated a possible, but unquantified, amount of erosion as the reflector terminations were not clearly imaged on the seismic grid. Salt area at this time deflated to an area of 21 km^2. **e)** The restoration of the Almada sub-basin during the Cretaceous indicated 240 m of erosion and a 21 km^2 salt area.

4.3.3.2 Results for the Almada sub-basin

Algodões carbonates within the Almada thickened considerably offshore while seismic reflectors do not indicate the presence of any large erosive surface (Figure 4.14). This seems to suggest either a transgression or sediment bypass of the shelf, potentially caused by a large influx of sediments related to erosion from the land area west of the sub-basins. Overlying the Algodões, Urucutuca shales were deposited as water depths increased and thick clastic sedimentation continued into the Santonian, followed by thin Campanian and Maastrichtian clastic sedimentation. By the end Cretaceous, the shelf was submerged under at least 150 m of water with an underlying salt area of 21 km^2.

Two clear erosive events were interpreted during the Santonian and one in the latest Cretaceous. A less clear and third potential event occurred within the Campanian. Santonian erosion reached a maximum of 770 m while the top Cretaceous and possible Campanian were each responsible for less than 250 m of erosion.

4.3.4 Restoration of the Paleocene interval

Within this time interval I interpreted two surfaces, Paleocene I and Paleocene II (Figure 4.10).

4.3.4.1 Results for the Camamu sub-basin

Urucutuca deposition continued into the Paleocene as shales were deposited in increasingly deeper water. By the end of the epoch, water depth over the shelf was at a minimum of 350 m and the salt area deflated to 19.9 km^2. Both Paleocene I and II surfaces were unconformable, with 460 and 1000 m of interpreted erosion, respectively.

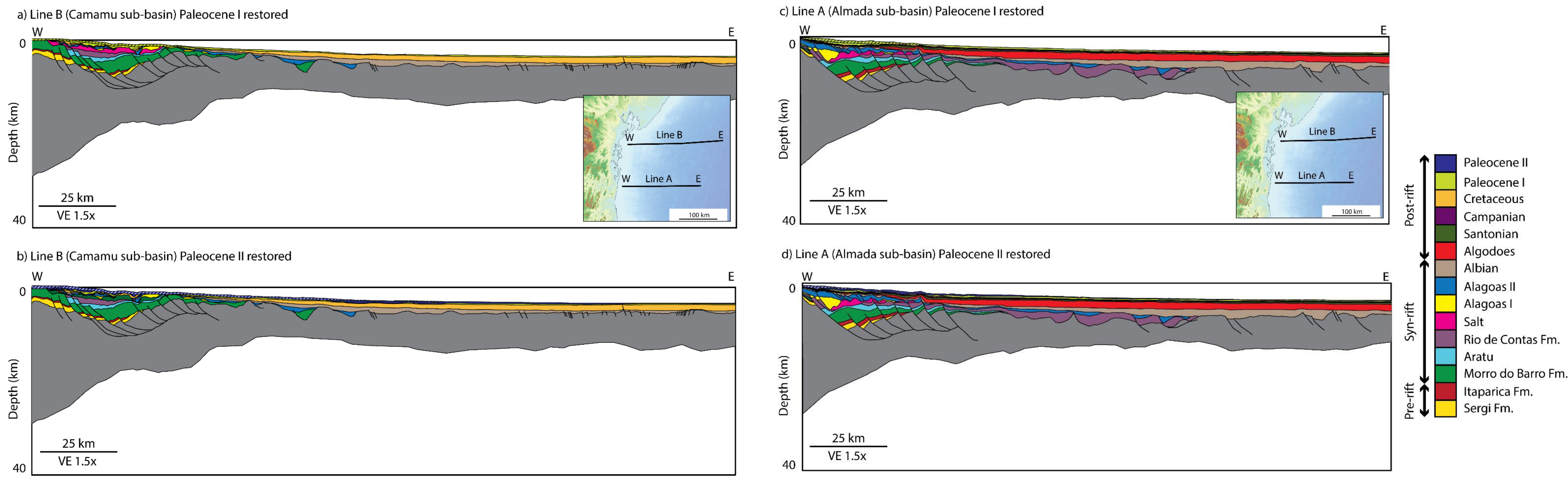

Figure 4.10 Restoration of the Camamu and Almada sub-basins during the Paleocene. **a)** Restoration of the Camamu sub-basin during the Paleocene I indicated 460 m of erosion and a salt area of 24 km^2. **b)** Restoration of the Camamu sub-basin during the Paleocene II interval indicated 1000 m of erosion and a salt area of 19.9 km^2. **c)** Restoration of the Almada sub-basin during the Paleocene I interval indicated 650 m of erosion and a salt area of 17.6 km^2. **d)** Restoration of the Almada sub-basin during the Almada Paleocene II interval indicated 720 m of erosion and a salt area of 15.7 km^2.

4.3.4.2 Results for the Almada sub-basin

Paleocene deposition in the Almada was similar to deposition in the Camamu, with water depths reaching 840 m, a salt area of 15.7 km^2, and erosive estimates of 650–720 m.

4.3.5 Restoration of the Eocene interval

Interpretations of Eocene time differ along the two models. Within the Camamu sub-basin five surfaces were resolved: lower Eocene I, II, middle Eocene I, II, and upper Eocene (Figure 4.11a–4.11e). Within the Almada only the lower Eocene II, middle Eocene II, and upper Eocene (Figure 4.11f–4.11h) were interpreted.

4.3.5.1 Results for the Camamu sub-basin

The Eocene within the Camamu sub-basin was a major period of salt tectonics and erosion. Deposition of the Urucutuca shales continued throughout this age, and salt tectonics was important until a large unconformity within the Eocene (Cobbold et al., 2010) (Figure 4.13). This resulted in a final salt area of 5.6 km^2, or a net deflation of 72% since deposition.

Several unconformable surfaces marked the Eocene. Each horizon of these surfaces was associated with some erosion that was resolved using the seismic data and from estimates based on the structural restorations:

I. Lower Eocene I (Figure 4.11a): 1100 m of erosion

II. Lower Eocene II (Figure 4.11b): 920 m of erosion

III. Middle Eocene I (Figure 4.11c): 500 m of erosion

IV. Middle Eocene II (Figure 4.11d): 600 m of erosion

V. Upper Eocene (Figure 4.11e): 520 m of erosion

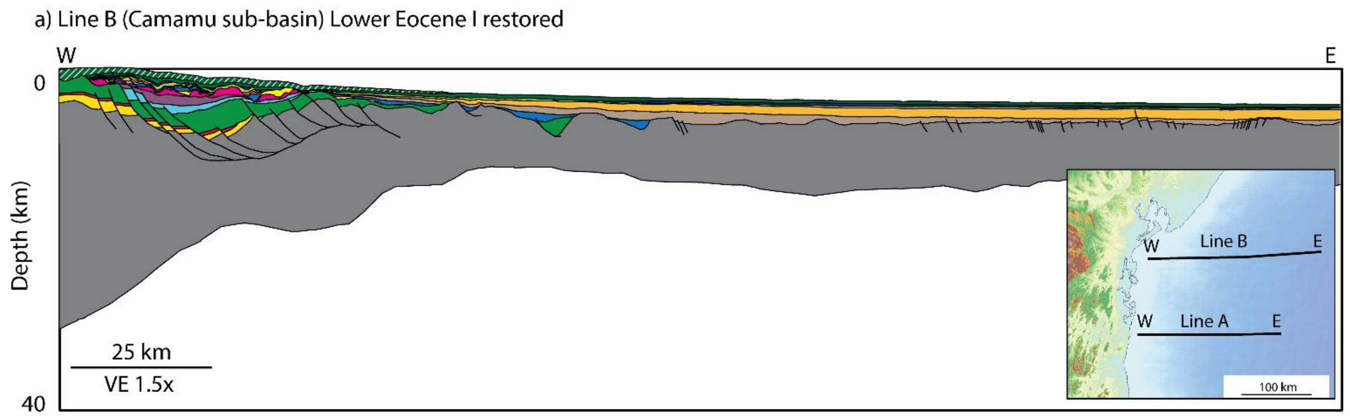

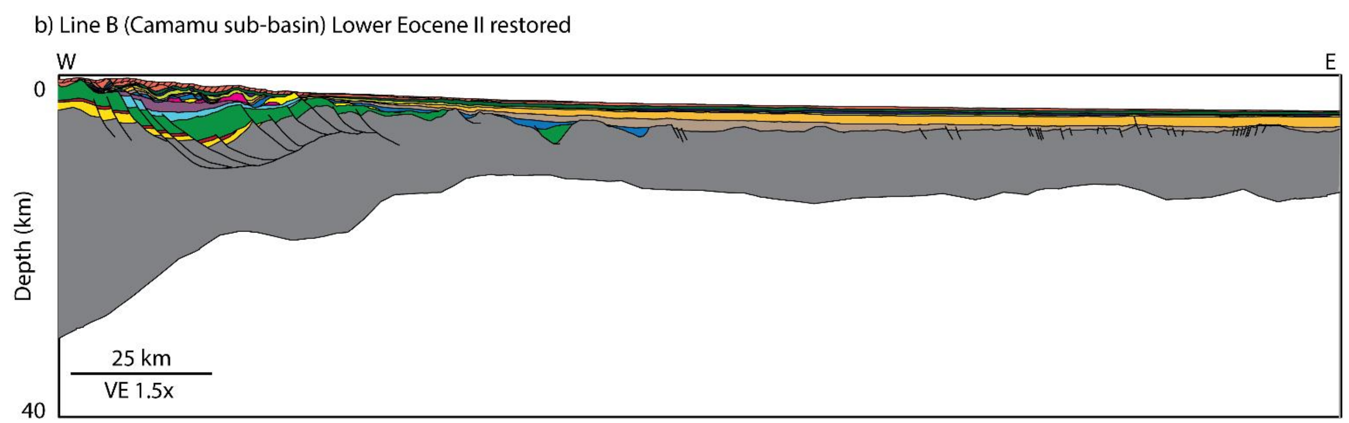

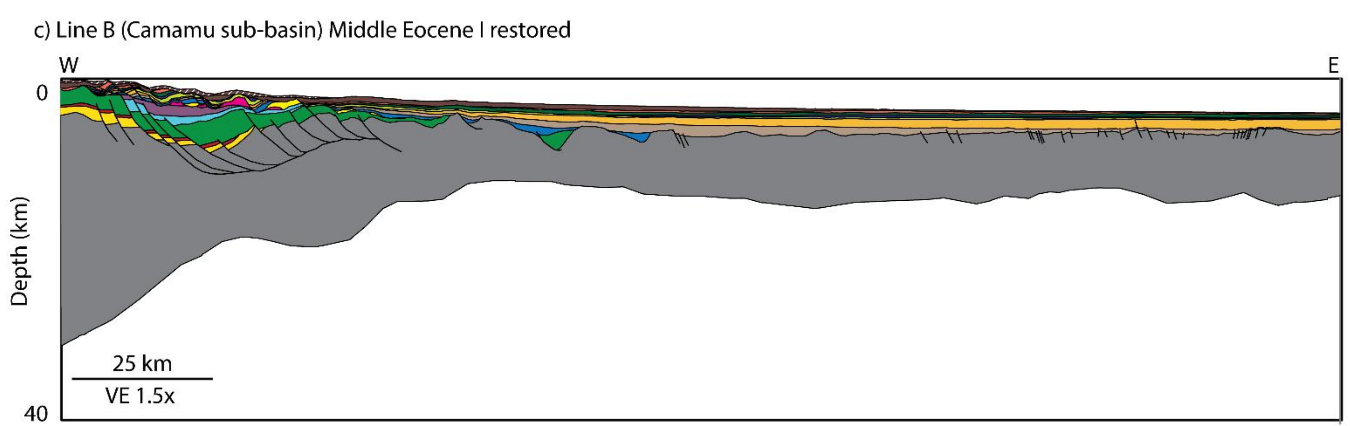

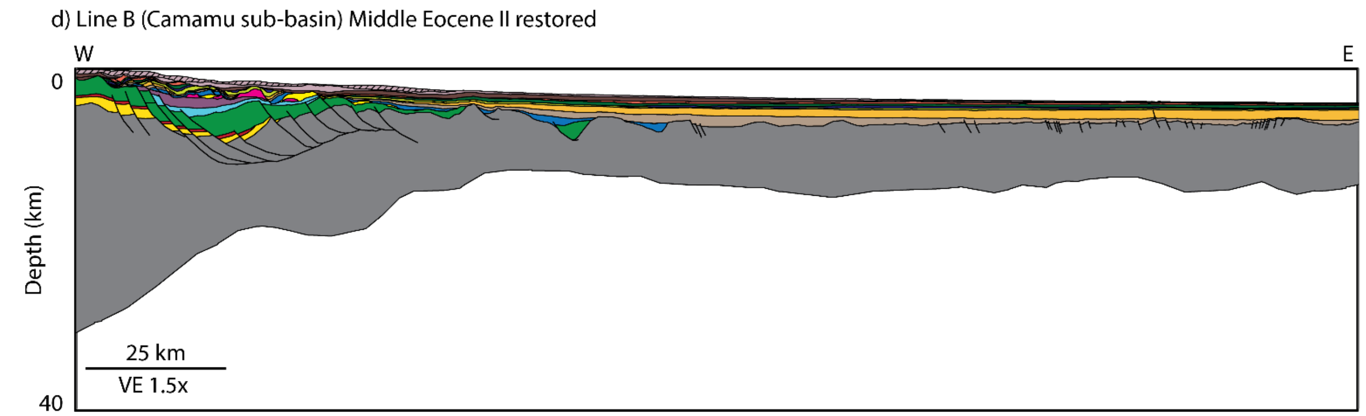

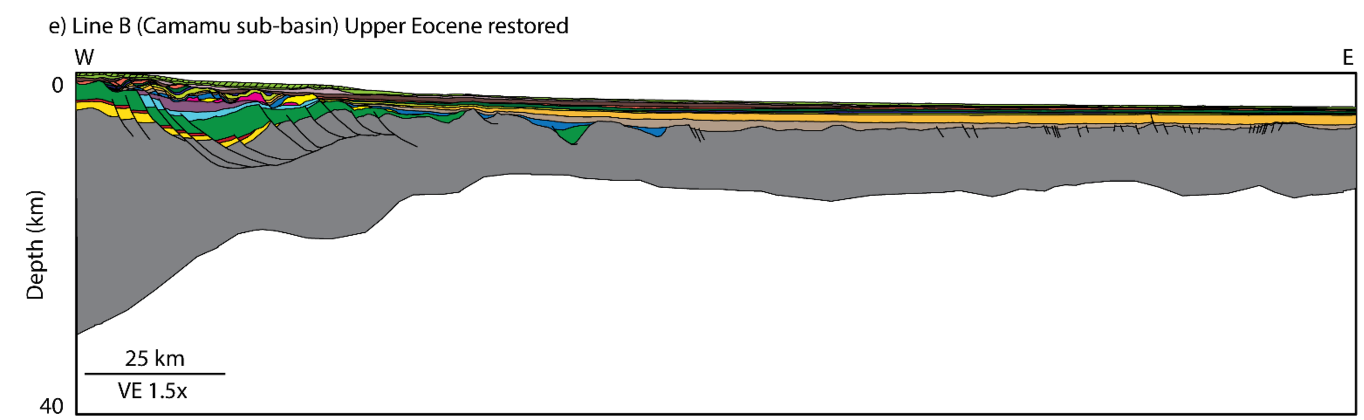

Figure 4.11 Restoration of the Camamu and Almada sub-basins during the Eocene interval. **a)** Restoration of the Camamu sub-basin during the lower Eocene I interval indicated 1100 m of erosion and a salt area of 15.5 km^2. **b)** Restoration of the Camamu sub-basin during the lower Eocene II interval indicated 920 m of erosion and a salt area of 5.7 km^2. Salt-related deformation ended in the Camamu sub-basin after this interval. **c)** Restoration of the Camamu sub-basin during the middle Eocene I interval indicated 500 m of erosion. **d)** Restoration of the Camamu sub-basin during the middle Eocene II interval indicated 600 m of erosion. **e)** Restoration of the Camamu sub-basin during the upper Eocene interval indicated 520 m of erosion. **f)** Restoration of the Almada sub-basin during the lower Eocene II interval indicated 580 m erosion and a salt area of 15.7 km^2. **g)** Restoration of the Almada sub-basin during the middle Eocene II interval indicated 550 m of erosion and a salt area of 15.6 km^2. **h)** Restoration of the Almada sub-basin during the upper Eocene interval indicated 650 m of erosion and a salt area of 14.5 km^2.

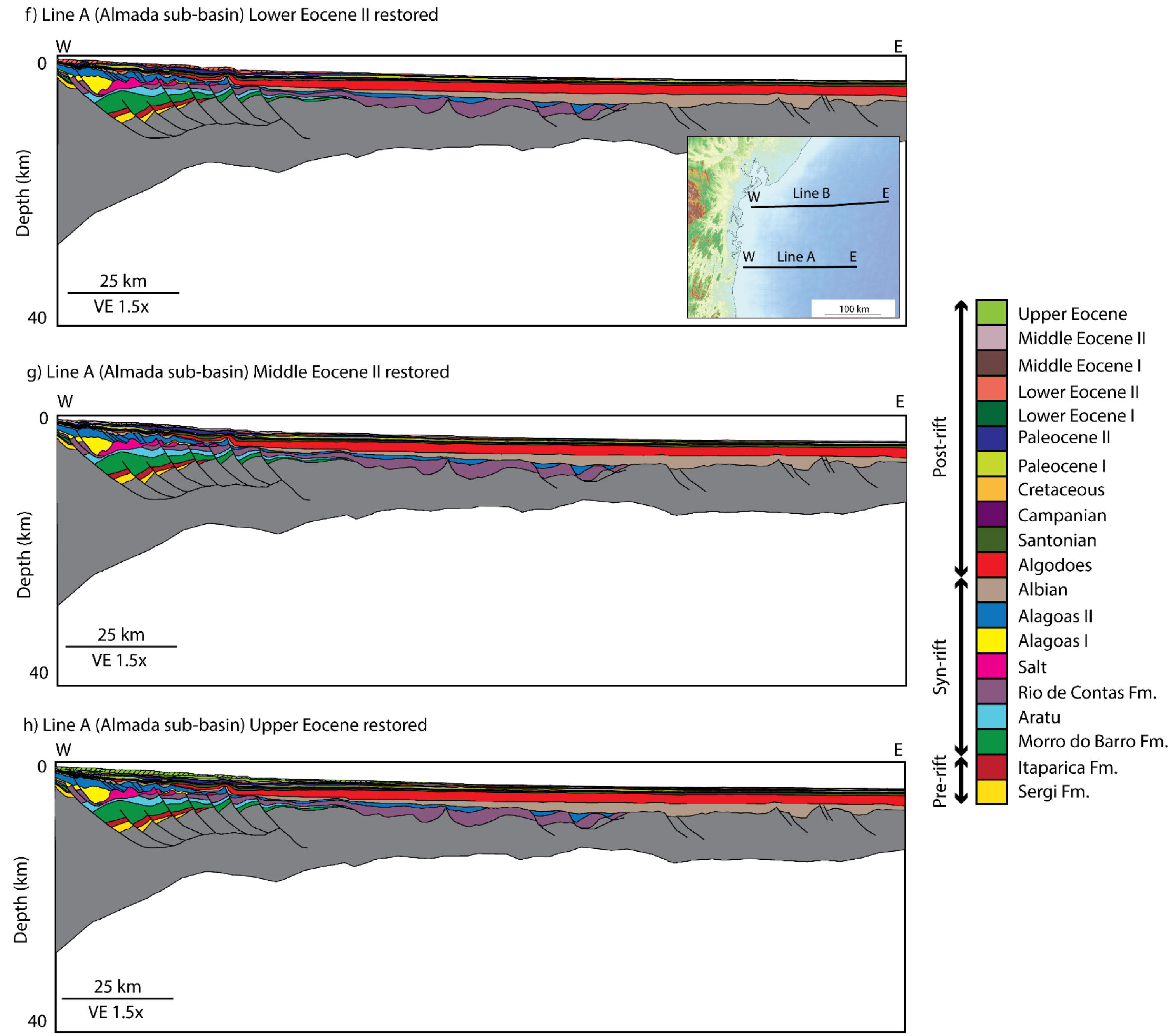

Figure 4.11 continued

4.3.5.2 Results for the Almada sub-basin

Eocene deposition within the Almada differed in a few respects from the Camamu. Only minor salt tectonism occurred within the sub-basin, for an end Eocene salt volume of 14 km^2, and evaporite deflation continued throughout the Eocene. Modeling suggested that the three interpreted unconformities, lower Eocene II, middle Eocene II, and upper Eocene, were responsible for eroding 580 m, 550 m, and 650 m, respectively.

4.3.6 Restoration of the Miocene to Present interval

I interpreted three surfaces from the Miocene to the Present: Miocene, Recent, and Present (Figure 4.12).

4.5.1 Results for the Camamu sub-basin

Deposition and erosion continued into the Miocene and Present within the Camamu basin. Post-Miocene seismic reflectors clearly indicate erosion, such as from large submarine canyon fills (Figure 4.5), that reflects the present-day influence of the Bahia state river system (Figure 4.3). Two major erosive intervals were interpreted, one in the Miocene and one within the Recent section, which eroded 550 m and 640 m, respectively.

4.3.6.1 Results for the Almada sub-basin

A similar geologic story played out within the Almada basin as the Camamu, except for continued salt tectonism until the end of the Miocene and a final salt volume of 11 km^2. Erosion across the two major unconformities removed 450 m in the Miocene and 530 m in the Recent section.

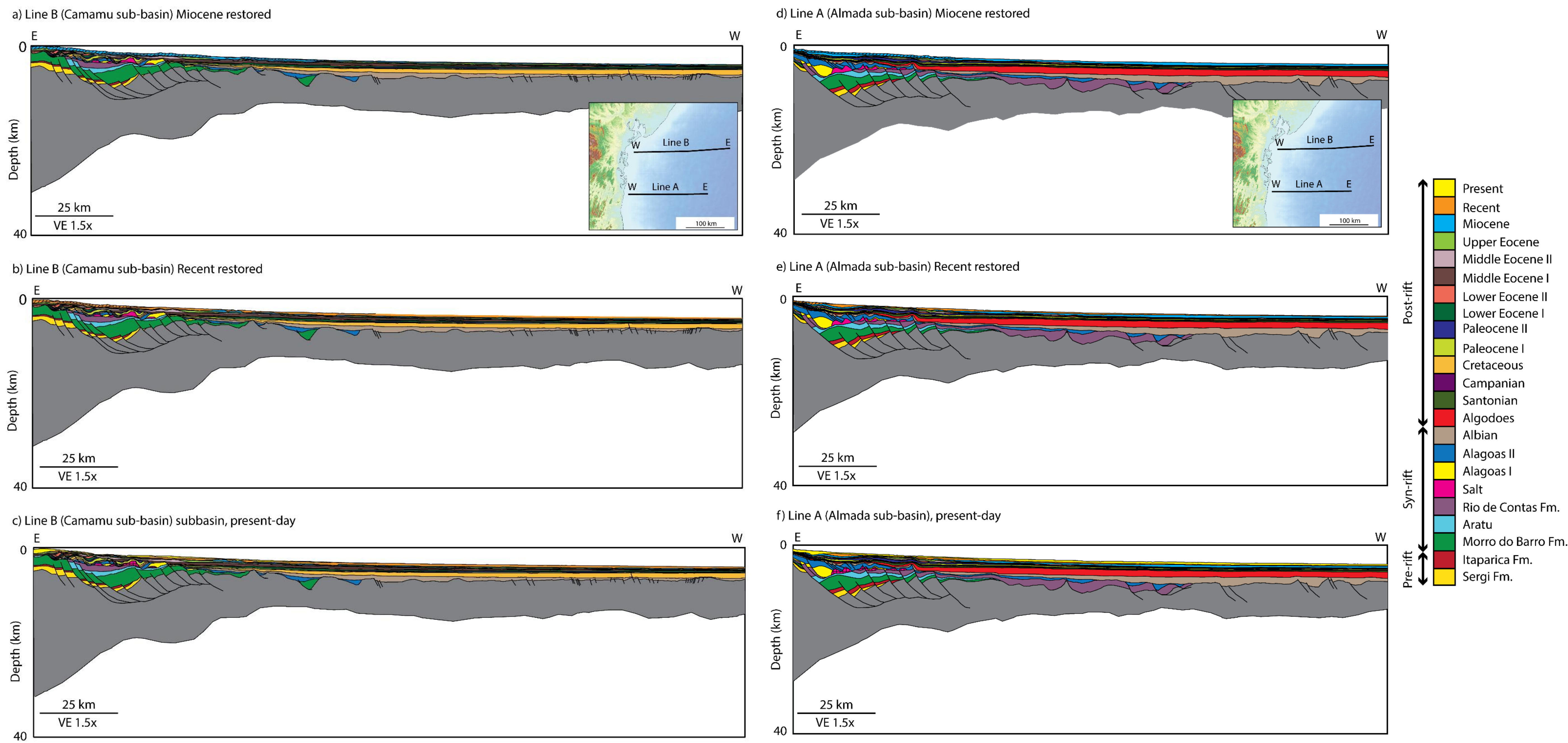

Figure 4.12 Restoration of the Camamu and Almada sub-basins during the interval of Miocene to Present. **a)** Restoration of the Camamu sub-basin during the Miocene interval indicated 550 m of erosion. **b)** Restoration of the Camamu sub-basin during the Recent interval indicated 640 m of erosion. **c)** Restoration of the present-day Camamu sub-basin with the unconformable seafloor surface suggesting active uplift and erosion of the nearshore area. **d)** Restoration of the Almada sub-basin during the Miocene interval indicated 450 m of erosion and a final salt area of 11 km^2. Salt-related deformation ceased in the Almada sub-basin during the Miocene interval. **e)** Restoration of the Almada sub-basin during the Recent interval indicated 530 m of erosion. **f)** Restoration of the present-day Almada sub-basin with the unconformable seafloor surface suggesting active uplift and erosion of the nearshore area.

Figure 4.13 a) Uninterpreted zoom from seismic Line B in the Almada sub-basin with the inset map showing the location of this segment of Line B. **b)** Interpretation of a part of Line B showing the lower Eocene unconformity beveling off more than 1 km clastic sedimentary rocks of the syn-rift Morro do Barro, Rio de Contas, and Taipus-Mirim, and the post-rift Algodões and Turonian–Eocene Urucutuca formations (Fig. 4.3). These formations were originally elevated and rotated in the footwalls of low-angle normal faults during the syn-rift period of Berriasian-and Aptian. This period of lower Eocene erosion within the Camamu sub-basin was the single largest uplift/erosion observed and formed the upper Eocene salt detachment described in more detail in Chapter 5. This uplift and erosive event of Eocene age influenced salt tectonism in the area as salt deflation in the Camamu sub-basin occurred at its fastest rate during the Eocene, as discussed in Chapter 5.

a)

b)

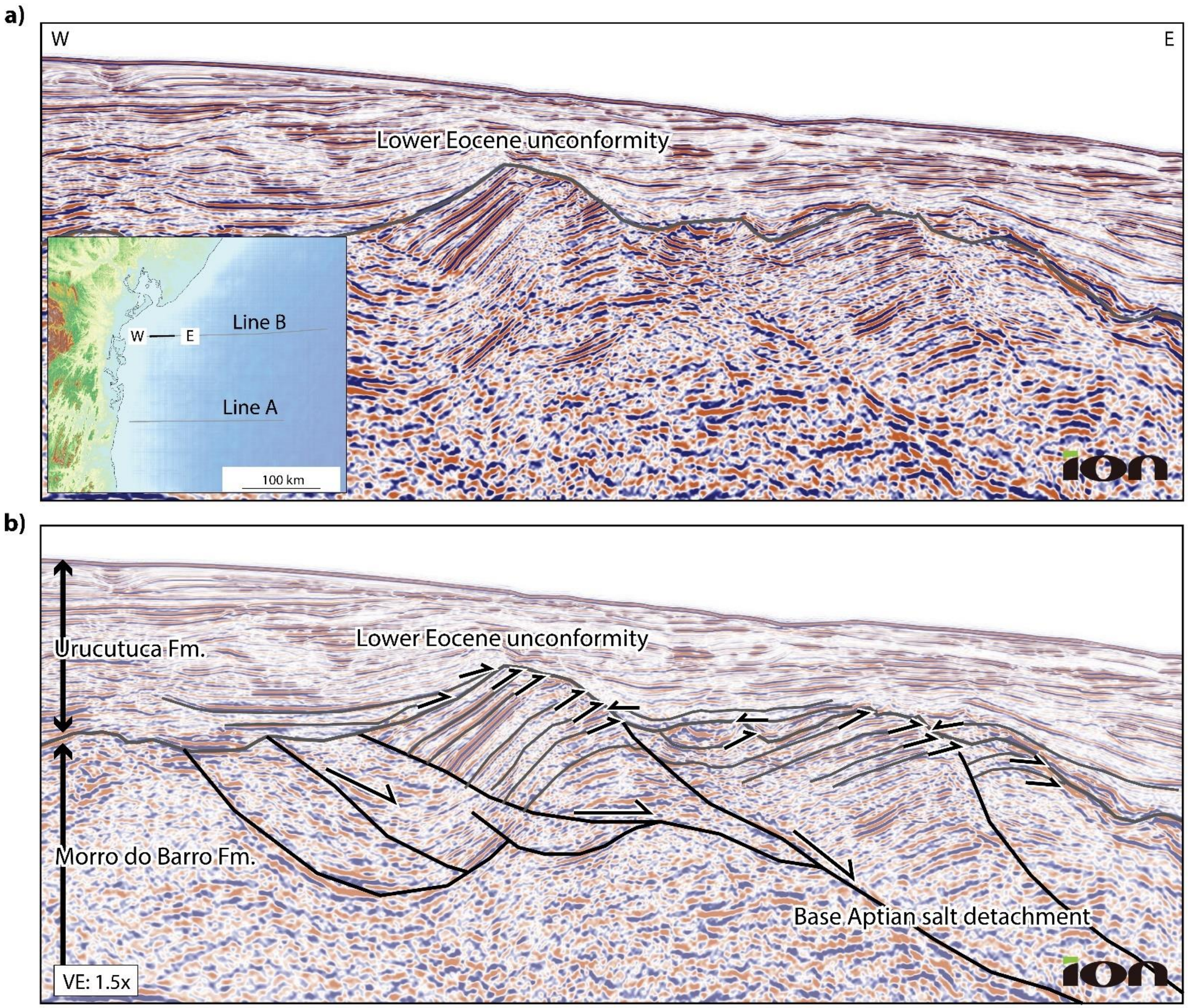

W
E
Lower Eocene unconformity
Line B
W
E
Line A
100 km
ion
Urucutuca Fm.
Lower Eocene unconformity
Morro do Barro Fm.
Base Aptian salt detachment
VE: 1.5x
ion

Figure 4.14 a) Uninterpreted zoom from seismic Line A in the Almada sub-basin with the inset map showing the location of this segment of Line A. **b)** Interpretation of a part of Line A showing the conformity at the top of the post-rift Algodões formation of Late Cretaceous age and the unconformity marking the end of the Albian syn-rift phase. The proximal part of the Algodões formation thins but is conformable while the distal part of the Algodões formation thickens in the basinward direction, likely as the result of erosion of the onshore area and increased sediment supply to the offshore.

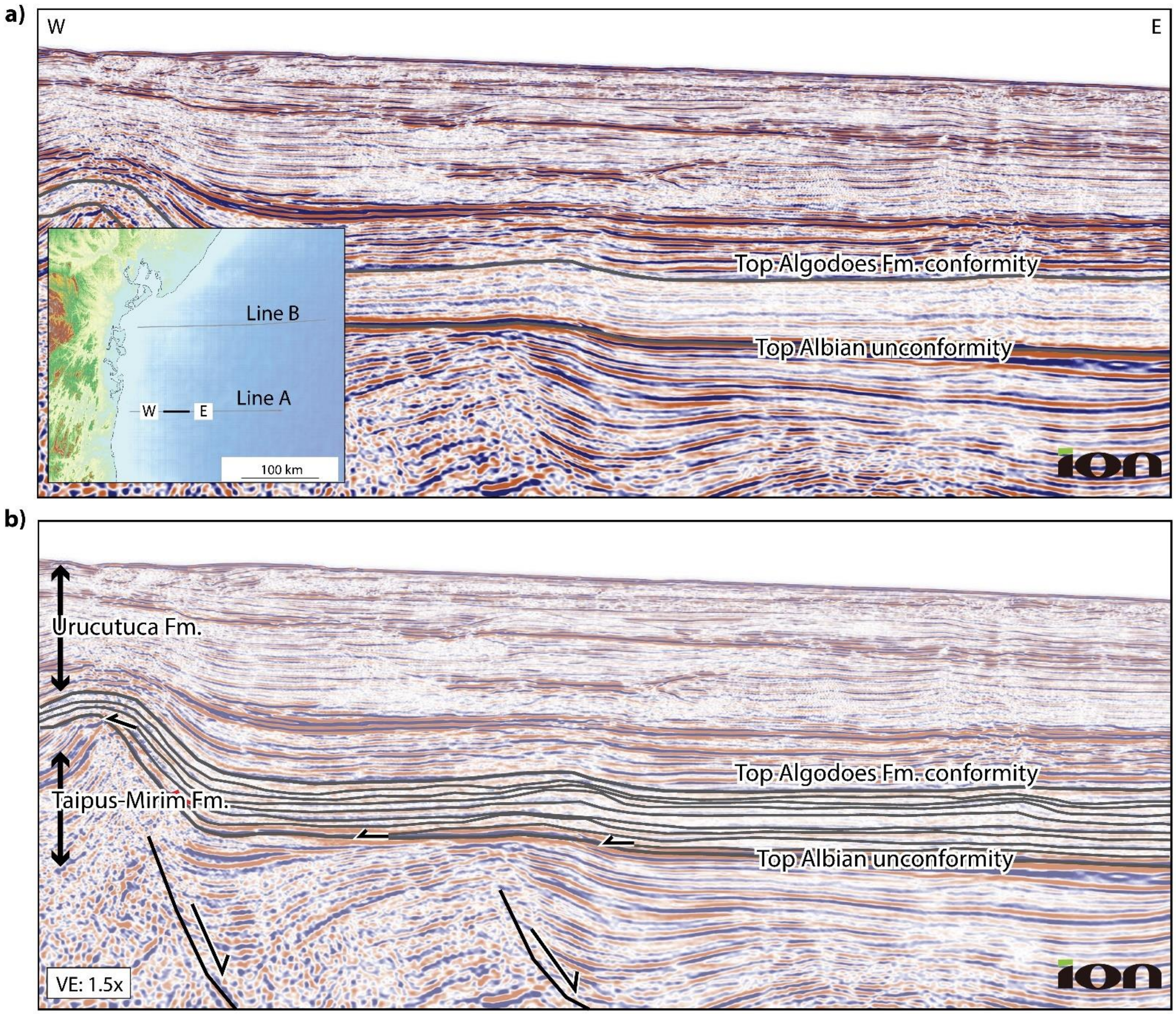

a)
W
E
Top Algodoes Fm. conformity
Line B
Top Albian unconformity
Line A
W
E
100 km
b)
Urucutuca Fm.
Top Algodoes Fm. conformity
Taipus-Mirim Fm.
Top Albian unconformity
VE: 1.5x

4.3.7 Comparisons based on 1D modeling

1D subsidence histories allow simple, but useful, comparisons – especially when trying to compare subsidence rates between different geographical locations. I applied the new results from the 2D structural restorations to 1D subsidence models using Petromod software. Two pseudowell locations along both models were selected: one located above the salt-withdrawal mini-basins and the other located within the deepwater regime over the most distal, potential Morro do Barro source rock (Milani et al., 2007) (Figure 4.15). Inspection of these subsidence plots helped subdivide the geohistory into five uplift/erosive phases: 1) Lower Cretaceous, 2) Upper Cretaceous, 3) Paleocene, 4) Eocene, and 5) Miocene to Present.

4.3.7.1 Results from pseudowells 1 and 2 in the Camamu sub-basin

Pseudowell 1 (PW1) in the Camamu sub-basin (Figure 4.15b) is located nearer to the shore and suggested a complex subsidence pattern marked by large uplift events. All five of the uplift/erosive phases were resolved for a grand total of 5300 m of cumulative erosion, with the largest events in the Lower Eocene responsible for 2200 m of erosion. Water depths increased from zero at the end of salt deposition to 1475 m at the present-day. Three quiescent periods could be resolved in the Lower Cretaceous, Upper Cretaceous, and from the Oligocene to the later Miocene. Each of these phases were resolved in the PW2 model, albeit with less frequency, except for event 5 (Figure 4.15c). This was likely caused by the rapid increase in paleowater depths after the Upper Cretaceous from near zero to present-day depths of 2450 m.

Figure 4.15 a) Location of pseudowell 1 (PW1) and pseudowell 2 (PW2) on the 230 km-long Line B crossing the Camamu sub-basin. PW1 is located on the slope above the marginal rift and its overlying sag basin filled with Aptian salt and PW2 is located in the deep basin where the Morro de Barro source rock was inferred to most distal. Color key for formations on the plot is given in Figure 5.3. **b)** Burial plot of PW1 based on the periods of subsidence and erosion inferred from the restored Camamu cross-section shown in Figure 15a. Water depths increased from 0 at the end of salt deposition to 1475 m at the present day. As PW1 is closer to the land area, it recorded all five of the major uplift and erosion phases that occurred in the: 1) Early Cretaceous, 2) Late Cretaceous, 3) Eocene, 4) Paleocene, and 5) Miocene to Recent. Three quiescent periods of no significant uplift and erosion included the Lower Cretaceous, Upper Cretaceous, and from the Oligocene to the later Miocene. **c)** PW2 is located over deepwater, hyperextended crust and recorded all major uplift events except for the Miocene, likely due to the increase in water depths from near zero to 2450 m in the present-day. **d)** Location of pseudowell 3 (PW3) and pseudowell 4 (PW4) on the 200 km-long line A crossing the Almada sub-basin. PW3 is located on the slope above the marginal rift and its overlying sag basin filled with Aptian salt and PW4 is located in the deep basin where the most distal Morro de Barro source rock was inferred. **e)** As PW3 is located nearer to the shore, all five uplift phases were recorded for a total erosion of 2300 m. Paleowater depth increased from 0 during salt deposition to 1525 m at present day. **f)** PW4 is located over deepwater, hyperextended continental crust and recorded a history of no resolvable erosion, reflecting that for most of the depositional history this location was under water depths greater than 1 km before subsiding to a final depth of 2625 m.

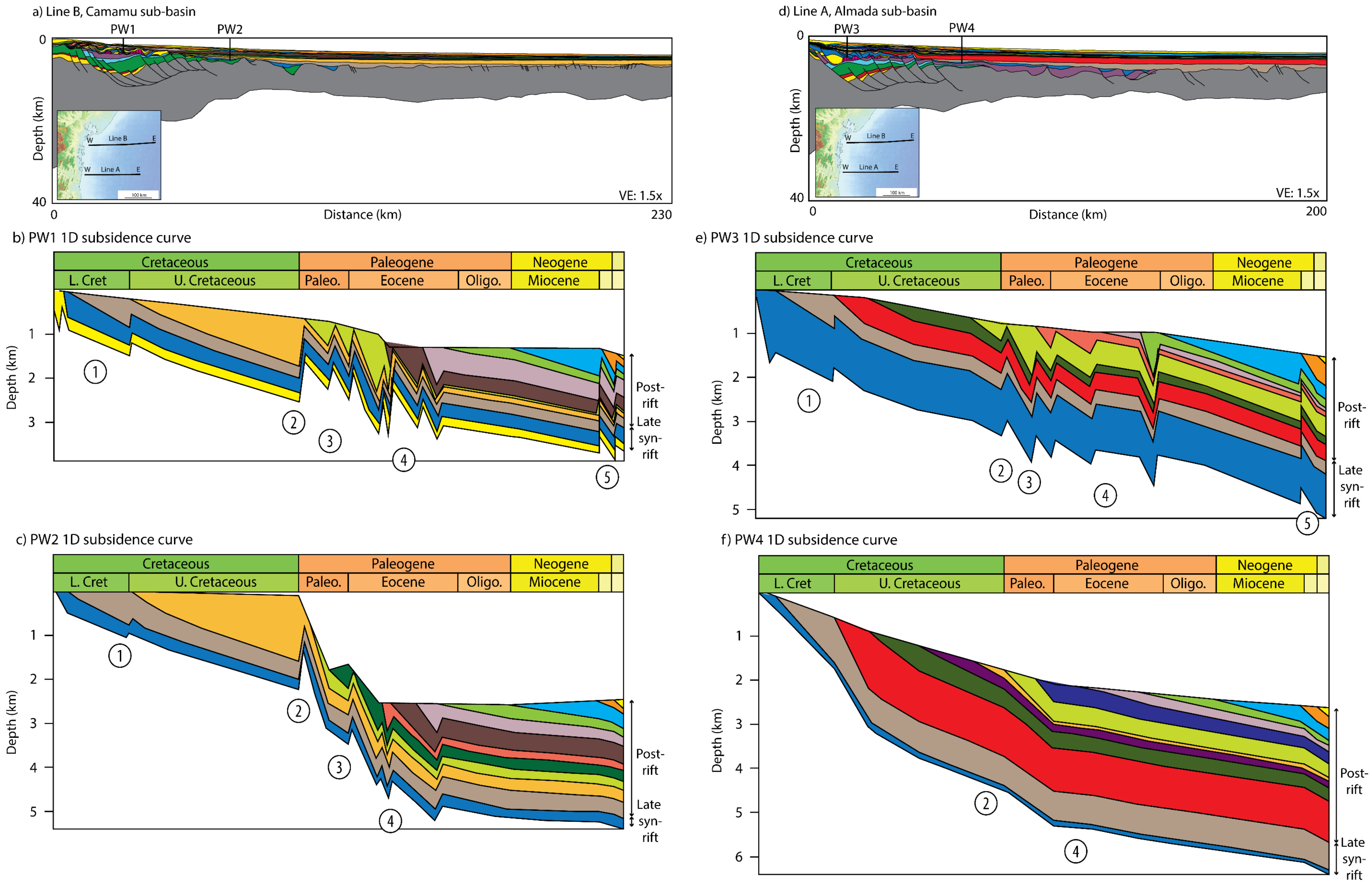

a) Line B, Camamu sub-basin
PW1
PW2
Depth (km)
0
40
Distance (km)
0
230
VE: 1.5x
Line B
Line A
W
E
d) Line A, Almada sub-basin
PW3
PW4
Depth (km)
0
40
Distance (km)
0
200
VE: 1.5x
b) PW1 1D subsidence curve
c) PW2 1D subsidence curve
e) PW3 1D subsidence curve
f) PW4 1D subsidence curve
Cretaceous
Paleogene
Neogene
L. Cret
U. Cretaceous
Paleo.
Eocene
Oligo.
Miocene
Depth (km)
Post-rift
Late syn-rift

4.3.7.2 Results from pseudowells 3 and 4 in the Almada sub-basin

Within the Almada model, all five phases were resolvable within the nearshore model PW3 (Figure 4.15e) for a total erosion of 2300 m. These events occurred from the Lower Cretaceous to Present, with the largest single event in the Upper Eocene. Paleowater depth increased from 0 during salt deposition to 1525 m at present day.

PW4 (Figure 4.15f) displayed a history that lacked erosion, likely reflective of the water depths greater than 1 km for most of its depositional history, before the area subsided to a final and present-day depth of 2625 m. Correlations in this location could be made between events 2 and 4 with periods of slowed subsidence, but no obvious unconformities were identified.

4.4 Discussion

4.4.1 Prediction of a more extensive and thicker section of Aptian salt in the Camamu-Almada basin

Through successive restorations of bedding geometries within the post-rift, the areal size and thickness of Aptian salt were reconstructed immediately following deposition in the shallow water, sag basin. Initial thicknesses and cross-sectional area reached 1.75 km and 39.9 km^2 in the Camamu basin and 3.5 km and 60.3 km^2 in the Almada basin. These salt estimates are the minimum required to accommodate the overlying post-rift sedimentation, indicating that the salt body was likely larger and extended close to the present-day coastline, described in more detail Chapter 5. Using my results and previous studies (Davison 1999; Brandão et al. 2020), the present-day salt extent was mapped (Figure 4.16).

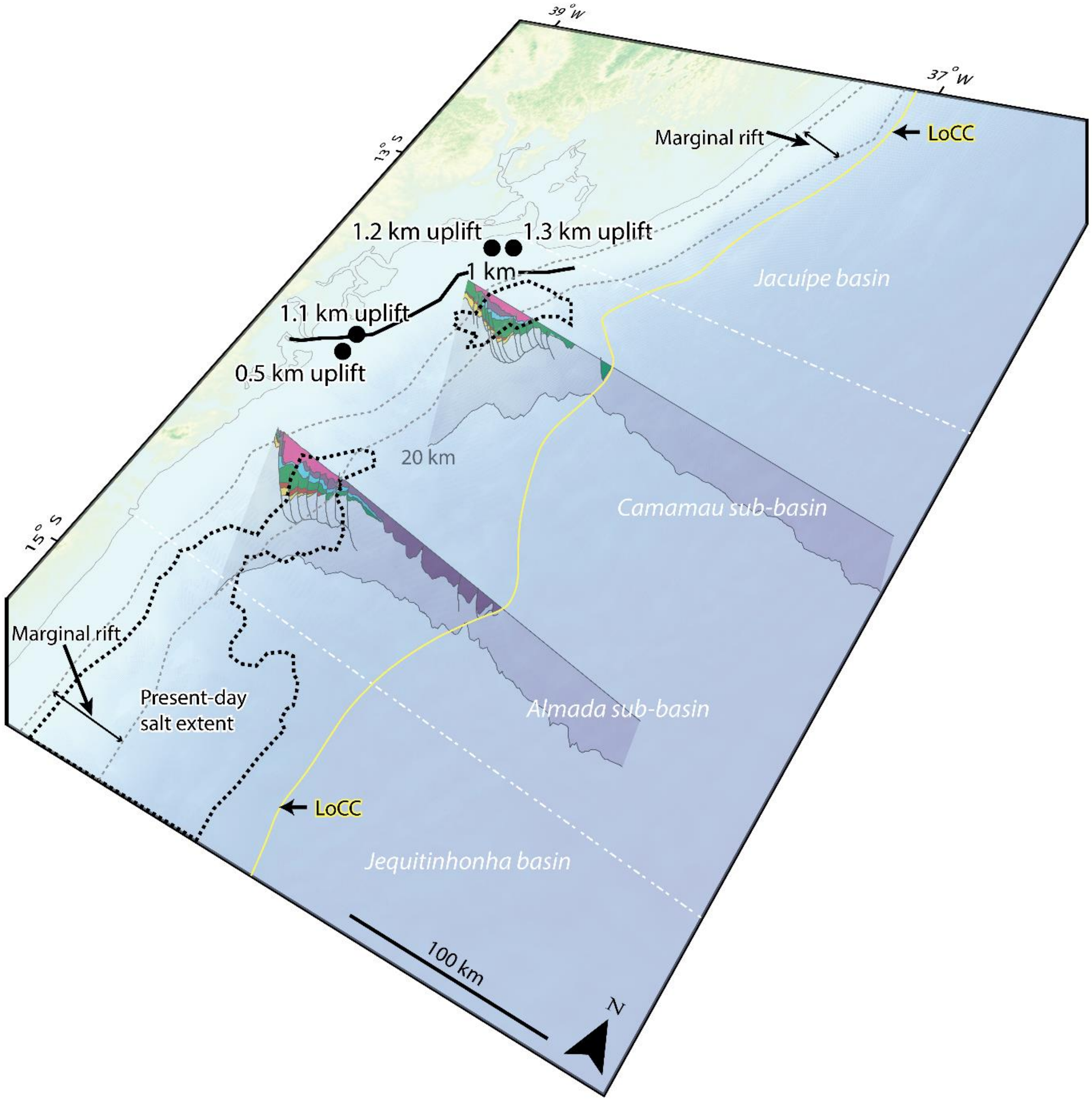

Figure 4.16 Oblique view looking to the northwest across the restored Almada sub-basin, as seen on Line A, and the restored Camamu sub-basin, as seen on Line B, in the period of Aptian salt deposition within the sag basin overlying the Berriasian-Aptian marginal rift, shown by the gray dotted line. The limit of continental crust (LoCC) is shown by the yellow line and is based on the results of Chapter 3. Aptian evaporites that were deposited within the sag basin have since deflated and flowed offshore and to the southeast, as shown in the present-day salt extent (heavier, black dashed line). Uplift estimates in km from onland studies by Scotchman and Chiossi (2009) suggested higher magnitude of uplift in the Camamu, which likely resulted in greater salt evacuation.

Evaporites originally spanned the area from immediately offshore until the edge of the salt basin that I identified in Figure 4.7. The Aptian salt basin thinned to the north as the margin narrowed; today, most of this salt has evacuated (Figure 4.4 and 4.5). However, salt tectonism in the Camamu was active until the Upper Eocene (Figure 4.11) and in the Almada until the Miocene (Figure 4.12).

Comparing salt deflation through time suggests that the periods of fastest change in the extent and volume of the salt occurred during major uplift phases in the Early Cretaceous and the Late Cretaceous to Eocene (Figure 4.17). This movement resulted in large salt-withdrawal mini-basins that deformed the overlying sediments and created laterally extensive welds as the salt bodies were either exposed and dissolved or pushed further offshore (Figure 4.16). Though salt dissolution is generally considered to have minimal impact in deepwater environments because of sedimentary cover (Rowan 2020), multiple uplift phases in the Camamu-Almada had the potential to erode the caprock and expose the salt to dissolution. This may be why salt deflation occurred most rapidly in the Early Cretaceous within the Almada sub-basin and from the Late Cretaceous to the mid-Eocene in the Camamu sub-basin; these were both periods of intense uplift, erosion, and potential salt exposure (Figure 4.15 and 4.17). A less controversial explanation is that Aptian evaporites flowed to the southeast through time as proposed by Brandão et al. (2020) and as suggested by the present-day limits of the Brazilian salt basin (Figure 4.16).

Evaporites were a first-order influence on much of the overlying post-salt sedimentation, and this history of halokinesis has been preserved in the reflector geometries used to constrain the structural modeling.

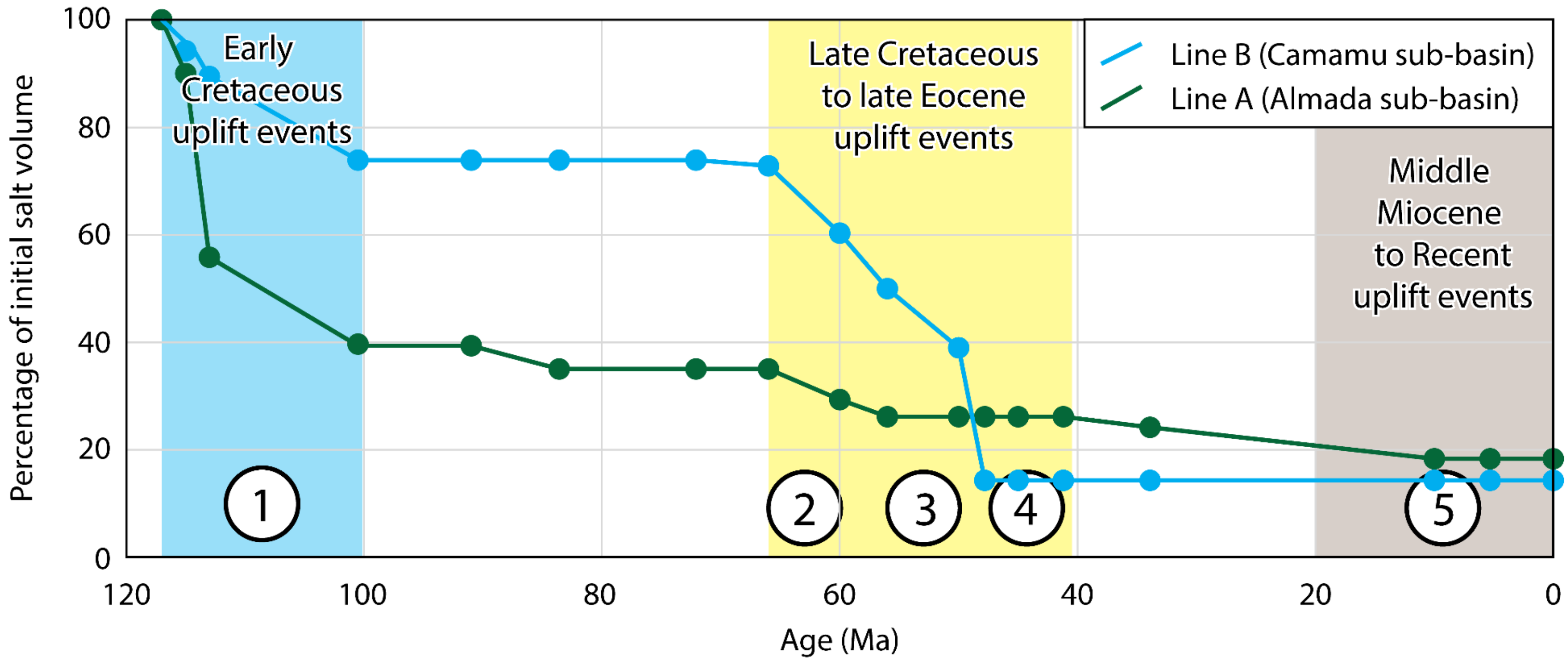

Figure 4.17 Graphical plot of salt deflation shown as percentages from Early Cretaceous to Recent based on the restorations of Lines A and B through the Almada and Camamu sub-basins. The most rapid period of salt deflation occurred during uplift events in the Early Cretaceous (Phase 1), and in the events between the Late Cretaceous to Eocene (Phase 2–4). Both the Almada and the Camamu sub-basin experienced rapid salt deflation in the Early Cretaceous in the period immediately following salt deposition. Salt also evacuated rapidly during the Paleocene and Eocene within the Camamu sub-basin, which coincided with the large Eocene unconformity shown on the seismic line in Figure 13. Salt within the entire basin stabilized and was unaffected by the Miocene to Recent uplift events (Phase 5).

4.4.2 Comparison of the distribution and magnitude of the uplift and erosion events affecting the Camamu and Almada sub-basins

Distinct differences between the uplift and erosion events in the northern Camamu and in the southern Almada events were observed (Table 1). Most erosive intervals prior to the Upper Miocene in the Camamu sub-basin were larger, almost by a factor of two, than similar events in the Almada sub-basin. This contrast in the magnitude of erosion may have reflected one of two things: 1) water depths increased across the Almada model much faster than across the Camamu model, potentially shielding the Almada sub-basin from a larger amount of westward-derived, terrigenous erosion; or 2) differences in the structure between the two basins, with the Almada sub-basin's roughly south-north fault orientation and the Camamu sub-basin's roughly southwest-northeast faults (Ferreira, 2018), caused each region to respond differently to the same uplift event.

Evaporite thickness and influence were another distinction between the two sub-basins, with the thicker and more extensive salt deposition in the southern Almada sub-basin reflecting the northward narrowing of the continental margin and the presence of the larger and thicker area of the Brazilian salt basins to the south (Figure 4.16). This difference in evaporite prominence also affected the timing and impact of salt tectonism within the Camamu-Almada sub-basins. The structural restorations suggested that salt tectonism in the Almada sub-basin, with a last pulse in the Miocene, lasted longer than in the Camamu sub-basin, where salt-related deformation ended in the Lower Eocene. It is still important to recognize that the present-day Camamu basin is not devoid of salt; most evaporites have evacuated the sub-basin, but trapped salt structures still exist as isolated salt pillows and diapirs (Figure 4.5).

4.4.3 Summary of post-rift uplift and erosion events affecting the Camamu-Almada rifted-passive margin

This study resolves a complex history of major erosive events in the Early/Late Cretaceous, Paleocene, Eocene, and Miocene/Recent (Figure 4.18). I compared my restoration results with results from previous workers using different methods including: 1) onshore uplift estimates (Japsen et al., 2012); 2) South American apatite fission-track (AFT) frequency (Zavala, 2018); 3) Atlantic mid-ocean ridge spreading velocities (Colli et al., 2014); and 4) activity of the Andean orogeny (Colli et al., 2014).

Like Japsen et al. (2012), I find broad correlation between the interpreted uplift phases and either Andean mountain-building or varying South Atlantic oceanic spreading rates. However, in addition to far field effects another possible mechanism for this uplift could be mantle-derived (Figure 4.18). Evidence for massive, post-rift magmatic activity is found within the Abrolhos Magmatic Province, active from 69 to 32 Ma (Cordani, 1970; Sobreira and Szatmari, 2003; Mohriak, 2005; França et al., 2007) (Figure 4.1), the Poxoreu Igneous Province (~84 Ma), and the Trindade volcanic chain (50–10 Ma), all linked geochemically together by Fodor and Hanan (2000) (Figure 4.1).

These results suggest that localized uplift, isostatic rebound, or dynamic topography are all unlikely mechanisms for these uplift events. The correlatability of the uplift events, that include the offshore areas of the Camamu and Almada sub-basins and onland Brazil, argue against localized uplift causes, as a large area of northwestern Brazil was being uplifted.

Isostatic rebound is generally related to higher latitude areas affected by glaciation, and not tropical areas like Brazil. Dynamic topography acts at rates from 1 m/Ma (Flament et al. 2013) to over 100 m/Ma (Rowley et al. 2013; Austermann et al. 2017); while it is possible for the >1 km of uplift to be caused by an event on the upper end of that range in tens of millions of years, both far field and mantle plume effects offer more plausible solutions and can be tied temporally.

Significant erosion has been interpreted onshore, and this work has shown similar events in the offshore. These uplift events have led to the denudation of hundreds of meters, sometimes kilometers, of rock across wide areas from the Cretaceous to Recent. This widespread denudation resulted in enhanced deepwater deposition of clastic sediment along with nearshore sediment bypass/erosion as observed on the seismic data (Figs. 4.4–4.5, and 4.13c–4.13d).

Table 4.1 Estimated erosion at mapped intervals along both lines

	Camamu		Almada	
Surface	Max erosion	Erosion footprint	Max erosion	Erosion footprint
Recent	0.64	37.2	0.53	12.5
Miocene	0.55	95	0.45	53.7
Upper Eocene	0.52	48.2	0.65	80
Middle Eocene II	0.6	67	0.55	5.5
Middle Eocene I	0.5	48	N/A	N/A
Lower Eocene II	0.92	95	0.58	48.5
Lower Eocene I	1.1	67	N/A	N/A
Paleocene II	1	130	0.72	17.2
Paleocene I	0.46	50	0.65	40.5
Cretaceous	1.3	109	0.24	27.2
Santonian	N/A	N/A	0.77	39.7
Albian	1	78.5	0.45	37.5
Alagoas I	0.82	64.8	0.33	40

4.4.3.1 Phases 1 and 2: Cretaceous uplift and erosion events

Two smaller events in the Early Cretaceous (Phase 1; Figure 4.18) broadly correlate with the initial Andean mountain building phase that occurred as early as the Aptian in northern Peru (Mégard, 1984), though these events may be linked to Aptian continental rifting (Figure 4.3).

Uplift events in the Late Cretaceous (Phase 2; Figure 4.17) correlate with the first significant Andean phase, the Peruvian, that was active from 90 to 75 Ma; however, these events also coincided with the creation around 84 Ma of the Poxoreu Igneous Province, onshore Brazil (Figure 4.1 and 4.17).

4.4.3.2 Phase 3: Paleocene uplift and erosion events

Uplift events resolved during the Paleocene (Phase 3; Figure 4.18) stand out as occurring during a time of general Andean quiescence and decreasing spreading rates. In fact, previous researchers had interpreted the Oligocene-Miocene period to be one of widespread subsidence (Japsen et al., 2012). The cause for these events may ultimately lie in the mantle; it has been shown that during the latest Cretaceous and earliest Paleocene, the Abrolhos Magmatic Province was active and may have impacted the Camamu-Almada sub-basins (Figure 4.1 and 4.17).

4.4.3.3 Phase 4: Eocene uplift and erosion events

I recognized five separate Eocene uplift events (Phase 4; Figure 4.18) affecting the Camamu-Almada sub-basins. These events correspond neatly with both increasing Mid-Atlantic spreading rates and the Andean Incaic period between 50 and 33 Ma (Japsen et al., 2012; Pfiffner and Gonzalez, 2013). The Abrolhos Magmatic Province also continued to develop during this time, with final emplacement in the latest Eocene and earliest Oligocene, along with the potential effects of the Trindade volcanic chain starting in the early Eocene (Figure 4.1 and 4.17).

4.4.3.4 Phase 5: Miocene to present-day uplift and erosion events

Activity in the Miocene and Recent (Phase 5; Figure 4.18) corresponded to a time of either steady or decreasing seafloor spreading rates, the Andean Pliocene Quecha phase of major east-west shortening (Soulas, 1977; Megard, 1984), and the continued offshore emplacement of the Trindade volcanic chain (Figure 4.1 and 4.17).

There remains a possibility that uplift is ongoing. Japsen et al. (2012) recognized minor uplift events in the Quaternary (Japsen et al., 2012), and the seismic profiles imaged a major unconformity along the present-day seafloor across the Camamu and Almada sub-basins (Figure 4.4 and 4.5) although the exact timing remains inconclusive. Likely the best way to resolve potential ongoing uplift would be a multi-year, onshore, GPS survey, which may help determine the true cause of these uplift events.

Figure 4.18 a) Compilation of previously proposed tectonic mechanisms that deformed, uplifted, and eroded the Camamu-Almada passive margin and adjacent Brazilian craton. Apatite fission track frequency compiled by Zavala (2018) was compared with the Andean orogenic phases from Japsen et al. (2012) and the South Atlantic spreading rate velocity from (Colli et al. (2014). **b)** Large-scale magmatic events that may have impacted the passive margin evolution of the Camamu-Almada margin and the northeastern Brazilian craton include: 1) Paraná flood basalts (132 Ma); 2) the Poxoreu igneous province (~84 Ma); 3) the Abrolhos magmatic province (69-32 Ma); and 4) the Trindade volcanic chain (50-10 Ma) (Fodor and Hanan, 2000). **c)** 1D burial history of the offshore Camamu and Almada sub-basins compared to the onland geomorphic and thermochronologic study by Japsen et al. (2012). PW1–4 denote the pseudowell subsidence curves generated along the structural restorations in this chapter, as summarized on Figure 4.13. Numbers 1–5 indicate the major uplift and erosional event identified in this study: 1) Lower Cretaceous, 2) Upper Cretaceous, 3) Paleocene, 4) Eocene, and 5) Miocene/Recent. Previous work had identified events that occurred in the Cretaceous, Eocene, and Miocene; this study identifies a new major period of uplift that affected northeastern Brazil in the Paleocene.

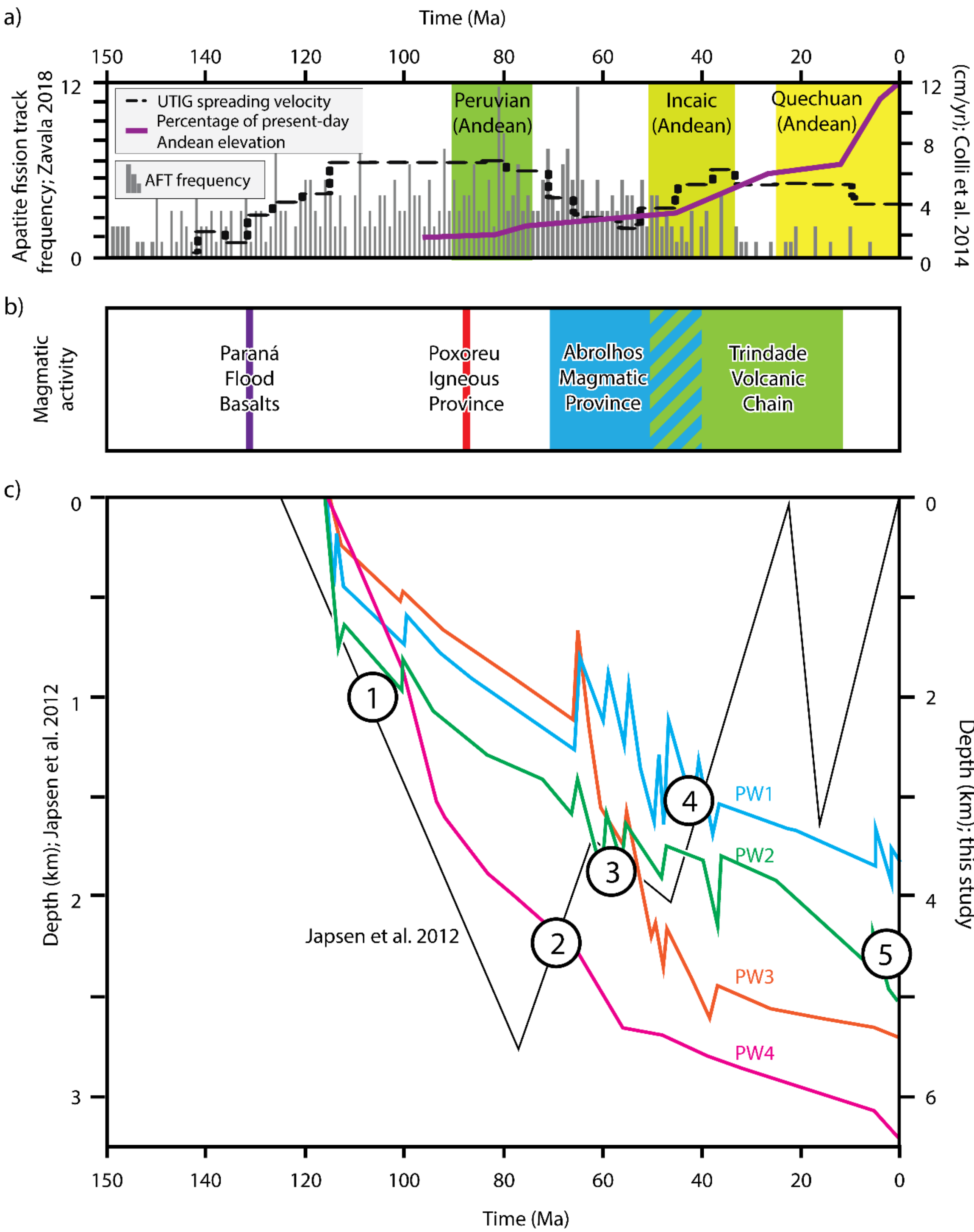

a)
Time (Ma)
150
140
120
100
80
60
40
20
0
Apatite fission track frequency; Zavala 2018
12
0
UTIG spreading velocity
Percentage of present-day Andean elevation
AFT frequency
Peruvian (Andean)
Incaic (Andean)
Quechuan (Andean)
Spreading velocity (cm/yr); Colli et al. 2014
12
8
4
0
b)
Magmatic activity
Paraná Flood Basalts
Poxoreu Igneous Province
Abrolhos Magmatic Province
Trindade Volcanic Chain
c)
Depth (km); Japsen et al. 2012
0
1
2
3
Depth (km); this study
0
2
4
6
Japsen et al. 2012
PW1
PW2
PW3
PW4
1
2
3
4
5
150
140
120
100
80
60
40
20
0
Time (Ma)

4.4.4 Comparison of the results of this study to previous models for uplift and erosion events

The resolution that exists in the offshore realm enabled me to better understand the erosive events impacting the northeastern rifted-passive margin of Brazil. This resolution was possible because in deeper water, the entire rock column can be preserved, and I was able to interpret both the shallow water unconformities and their correlative deeper conformities.

While my work suggests similar timing to uplift events proposed by previous workers, several key differences exist. First, a new uplift event was recognized in the Paleocene that does not fit the proposed far field model. Second, the seismic interpretation has resolved multiple erosive events within each uplift phase, indicating a stepwise uplift history rather than a continuous one. While it had been recognized that many of these uplift events coincided with far field influence of major Andean orogenic activity or increased seafloor spreading, a potential link between uplift and the Poxoreu Igneous Province, Abrolhos Magmatic Province, and Trindade volcanic chain is proposed for the first time.

4.4.5 Implications of revised history of uplift and erosion events on basin modeling for the prediction of hydrocarbons

I modeled hydrocarbon evolution in the Camamu-Almada at two locations: one in the Camamu sub-basin and the other within the Almada sub-basin (see Figure 4.19 for the thermal calibration). The Camamu-Almada is considered a frontier basin (Scotchman and Chiossi, 2009) with most exploration success limited to the onshore and shelf (Gonçalves et al., 2000). According to Beglinger et al. (2012), nearshore hydrocarbon accumulations sourced from the Camamu-Almada syn-rift Morro do Barro (!) are mainly gas, in contrast to the oils generally found in Gabon. The authors hypothesized that this could be due to a higher thermal gradient, uplift and erosion events, gas-prone source rock, or even the differences in thermal conductivity of sediments, such as salt.

To generate more constraints, I created two 1D basin models at the PW2 and PW4 locations within the deepwater area (Figure 4.16 and 4.20). As my restorations have shown, the numerous erosive intervals had little impact in the deepwater areas. Basin modeling results suggest that if source-rock quality Morro do Barro is preserved in the modern-day deepwater, it is thermally mature enough to generate oil, creating the potential for migration into deepwater, post-rift turbidite or chert reservoirs (Beglinger et al., 2012) (Figure 4.20).

Figure 4.19 Thermal calibration for 1D modeling based on vitrinite reflectance data compiled from deep-water well 1-BP-10-BAS. **a)** Map locating seismic and well log. **b)** Seismic section across deepwater well tie. The well penetrated to the top of the Cenomanian, and seismic interpretation suggested syn-rift ages for this section along with the presence of the Morro do Barro syn-rift source rock. **c)** Calibration plot with red line as the calculated vitrinite reflection with depth and the black crosses showing observed values from well 1-BP-10-BAS. There is a good fit between modeled and observed vitrinite reflectance, validating the model.

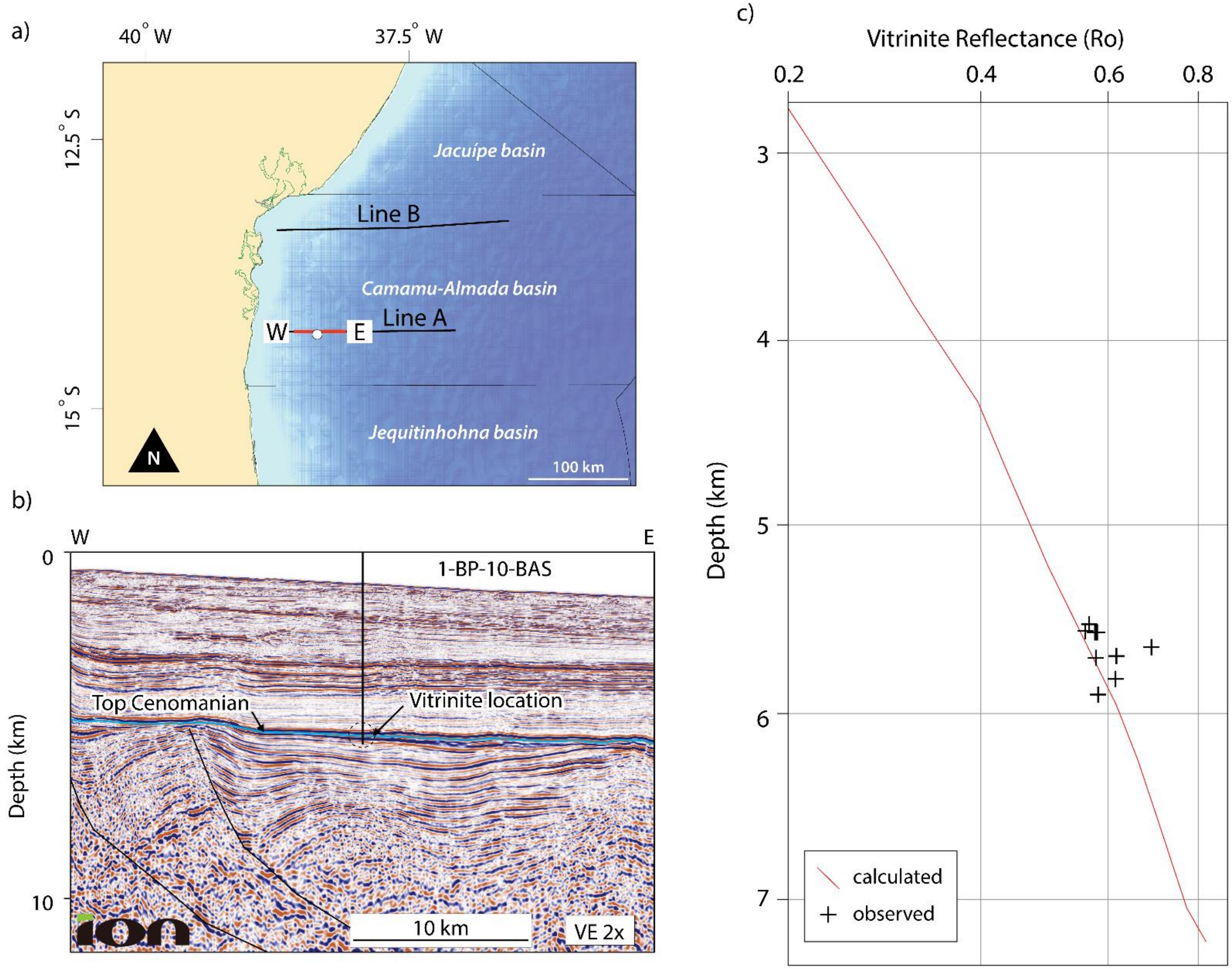
a)
40° W
37.5° W
12.5° S
15° S
Jacuípe basin
Line B
Camamu-Almada basin
Line A
W
E
Jequitinhohna basin
N
100 km
b)
W
E
0
1-BP-10-BAS
Top Cenomanian
Vitrinite location
Depth (km)
10
10 km
VE 2x
c)
Vitrinite Reflectance (Ro)
0.2
0.4
0.6
0.8
3
4
5
6
7
Depth (km)
calculated
observed

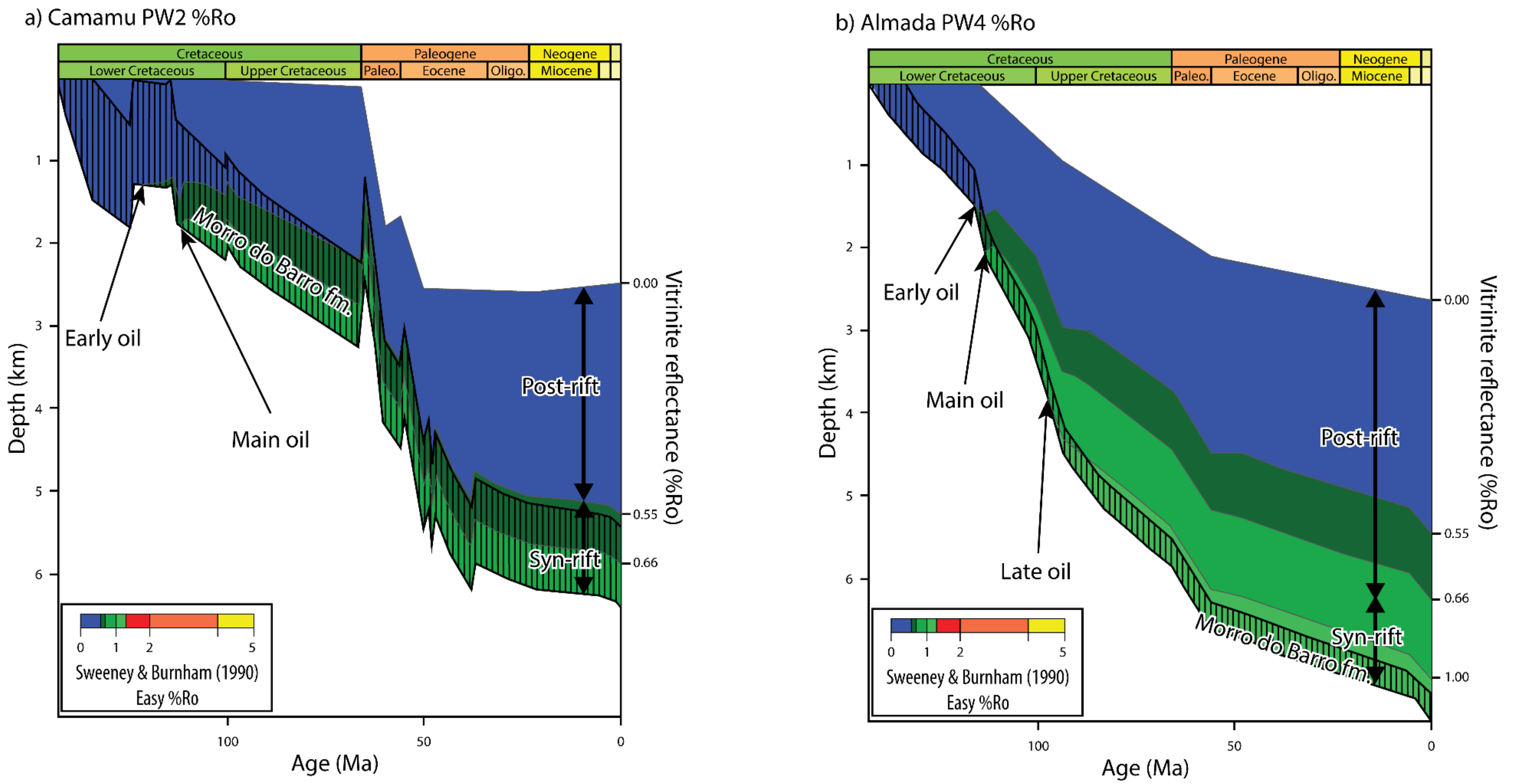

Figure 4.20 1D basin models for PW2 in the Camamu sub-basin and PW4 in the Almada sub-basin based on the Sweeney and Burnham (1990) method. **a)** PW2 in the deepwater Camamu sub-basin located on Figure 4.15 expelled hydrocarbons as early as the mid-Cretaceous, and the proven Morro do Barro source rock has remained in the oil window. Large erosive events occurred in the Late Cretaceous with up to 700 m of erosion but had little impact on maturity. **b)** PW4 in the deepwater Almada sub-basin, located on Figure 4.15 expelled hydrocarbons as early as the mid-Cretaceous, and the proven Morro do Barro source rock has remained in the late oil window. Erosive events were not observed at PW4 as the basin deepened rapidly following the main Berriasian-Albian rifting event.

4.5 Conclusion of this chapter

I utilized a 2D structural restoration workflow based on established methodologies and visualized these restoration results within four 1D basin models, two in the Camamu sub-basin and two in the Almada sub-basin, to better understand salt movement, uplift, and deep-water hydrocarbon potential.

At the end of evaporitic deposition, the restorations suggest that initial salt was much thicker than had been reported, with deposits up to 1750 m in the Camamu sub-basin and 3500 m in the Almada sub-basin. Although most salt has evacuated through sedimentary loading, salt tectonism in the Camamu sub-basin remained active until the Lower Eocene and in the Almada until the Miocene, creating large salt-withdrawal mini-basins and laterally extensive salt welds. Evaporites exerted a first-order control on much of the overlying sedimentation, and recognition of these controls could prove important for future exploration efforts.

I interpreted fourteen discrete erosive events within the post-rift history of the Camamu-Almada rifted-passive margin and temporally tied them to different uplift mechanisms: 1) Far field effects related to the Andean orogeny, spreading rate accelerations along the Atlantic mid-ocean ridge, or a combination of these effects; and 2) mantle-induced effects related to the emplacement of the Poxoreu Igneous Province, the Abrolhos Magmatic Province, and the Trindade volcanic chain.

Major differences exist between previous interpretations and the results from this chapter. First, a new uplift phase was resolved during the Paleocene. Second, multiple small erosive events appear to have occurred at each uplift phase rather than one large episode, indicating a stepwise uplift history rather than a linear one. These conclusions were made possible through the study of regional 2D seismic lines that imaged both the nearshore unconformities and the correlative conformities in deeper water areas.

This complex history of uplift and subsidence likely increases uncertainty on petroleum system timing and hydrocarbon phase. Exploration onshore and along the shelf has discovered more gas than oil, likely influenced by the proposed one to three kilometers of net coastal uplift. My modeling of two deep-water pseudowell locations in the Camamu-Almada sub-basins suggests potential for Morro do Barro (!) maturation, oil generation, and accumulation in overlying post-rift reservoir strata.

CHAPTER 5: AI-ASSISTED STRUCTURAL INTERPRETATION OF COMPLEX FAULTING AND SALT ON THE SHELF AND SLOPE OF THE CAMAMU BASIN, NORTHEASTERN BRAZIL

5.1 Introduction and significance

Evaporites in the South Atlantic passive margins deposited during the Aptian (Davison, 2007) and were thickest on the conjugate margins of western Africa and within the southern basins of offshore eastern Brazil (Davison, 1999). Within the Camamu sub-basin, deposition occurred in a narrow sag basin with limited accommodation (Gordon et al. 2013) (Figure 5.1). Thick salt has been shown to have an outsized effect on later sediment deformation because salt is relatively incompressible, mechanically weak, and flows like a fluid over geologic time intervals (Hudec and Jackson, 2007).

The Camamu sub-basin has been traditionally interpreted as the northern limit of Aptian evaporites, and for that reason salt tectonics have not been commonly discussed. Though most workers mention small amounts of salt, they do not explore salt tectonics to a large extent (Davison, 1999; Blaich et al., 2010). In fact, some researchers even discount the development of salt-related mini-basins within the Camamu (Scotchman and Chiossi, 2009).

Figure 5.1 Tectonic and geologic setting of the study area of the Camamu sub-basin located north of the Almada-sub-basin. The inset map in the top left shows the location of this segment of the Cretaceous-Cenozoic rifted-passive margin of northeastern Brazil. The dashed white lines outline the Camamu sub-basin, adjacent to the Almada sub-basin to the south. The limit of continental crust (LoCC) is shown as the yellow line and the Aptian-Albian marginal rift is shown in the black, dashed line. Aptian salt deposits are shown in pink, were compiled from Davison (2007), and were deposited in an elongate sag basin overlying the Berriasian-Aptian marginal rift. Areas of igneous activity in the area that have affected the Brazilian rifted-passive margin and are shown in purple include (Coffin and Eldhom, 1994): 1) Paraná large igneous province of Early Cretaceous (Valangian age ~132 Ma) that was related to pre-rift activity of the Tristan hotspot. This Brazilian hotspot track is continuous with the Walvis ridge and Etendeka large igneous province on the conjugate margin of southwest Africa; 2) the adjacent Poxoreu igneous province emplaced in the passive margin phase during the Late Cretaceous (~84 Ma); 3) the Rio Grande Rise and the early Cenozoic Abrolhos magmatic province (69-32 Ma), also erupted during the passive margin phase; and 4) the Trindade volcanic chain, a semi-continuous hotspot trail related to the proposed Trindade hotspot that extended eastward across the Brazilian rifted margin during the Cenozoic passive margin phase (50-10 Ma). Black dashed lines in normal oceanic crust of the South Atlantic Ocean are the mapped seafloor spreading anomalies Q2 (108 Ma) and Q1 (92 Ma) from Granot and Dyment (2015). Boxed areas show the location of the more detailed map of the study area shown in Figure 5.2.

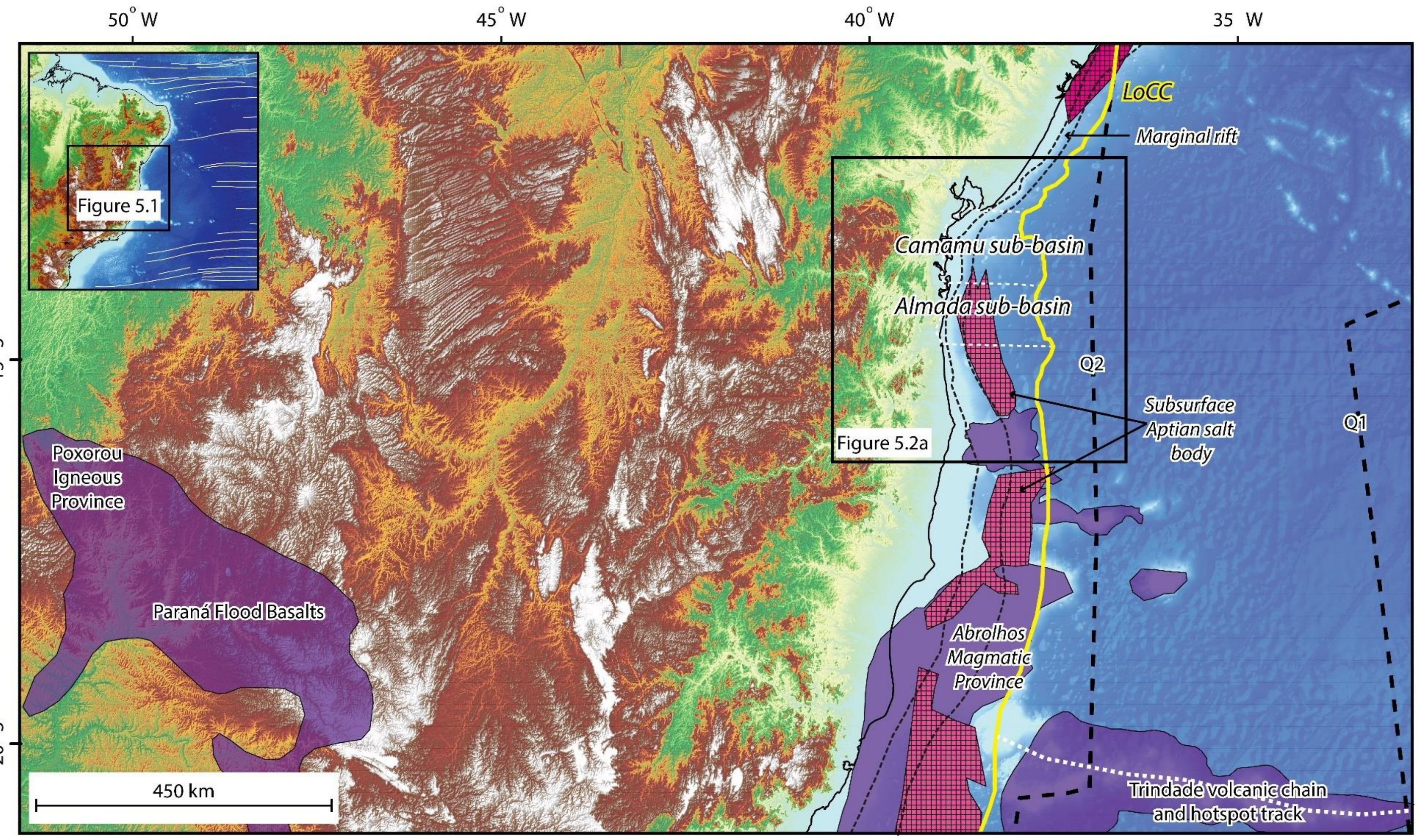
50° W
45° W
40° W
35 W
15° S
20° S
Figure 5.1
LoCC
Marginal rift
Camamu sub-basin
Almada sub-basin
Q2
Q1
Subsurface
Aptian salt
body
Figure 5.2a
Poxorou
Igneous
Province
Paraná Flood Basalts
Abrolhos
Magmatic
Province
450 km
Trindade volcanic chain
and hotspot track

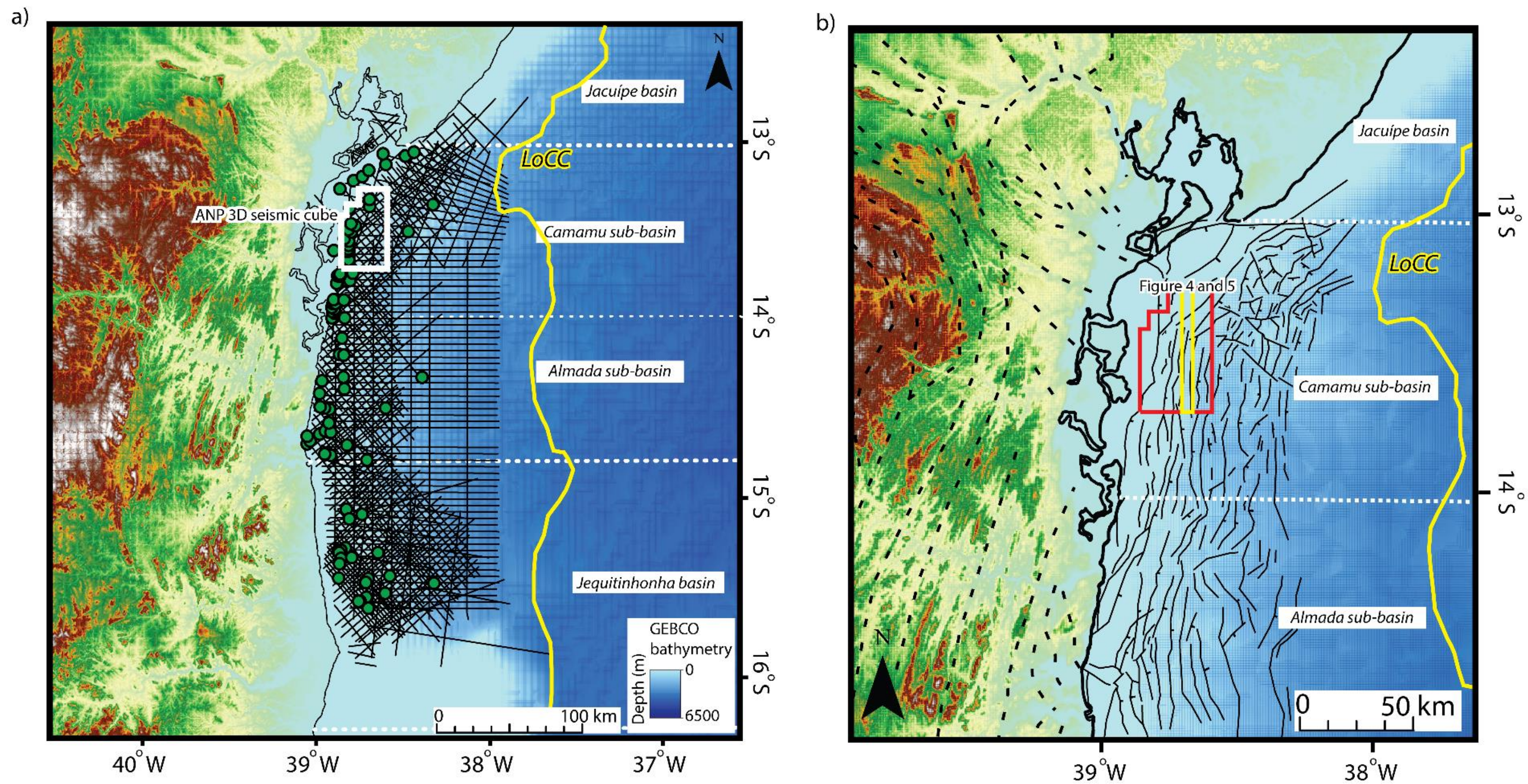

Figure 5.2 a) Map showing the distribution of subsurface data used for this chapter. 3D seismic survey (BCAM-40-BM-CAL-4) was provided by ANP and is shown in the white box that is located over the shelf and upper slope of the Camamu sub-basin. Additional 2D seismic reflection data from ANP is shown as the black lines and was tied to the ANP well logs shown by white circles. The topographic and bathymetric grids are from GEBCO (2021). **b)** Map showing the location of the strike seismic profiles from the 3D seismic cube (red box) that are interpreted in Figures 5.4 and 5.5. The strike lines cross an area of northwest-southeast striking orogenic grains and basement faults as described in Chapter 3.

If the margin had appreciable amounts of salt deposition, it would have affected overlying sedimentary structures of which there should be a geologic record recognizable in seismic reflection data. The only previous study on this topic was by Brandão et al. (2020) that focused on the Almada sub-basin, directly south of the Camamu. In their study, they recognized salt cushions, rollers, and walls, and interpreted zones of salt inflation and deflation.

Understanding salt tectonism and possible remnant salt bodies is also significant for oil and gas exploration, because small subsalt gas accumulations have been discovered in the coastal area (Gonçalves et al., 2000). Determination of salt movement and abundance is timely and necessary for future hydrocarbon exploration efforts, and in-depth study is required to successfully characterize these structures.

I used AI-assisted interpretation methodologies to quickly interpret a 3D survey on the shelf and upper slope areas of the Camamu sub-basin. I interpreted both fault planes and salt bodies and proposed a post-rift history that began with a thick, Aptian evaporitic body that deflated and left behind multiple salt detachments and salt-withdrawal mini-basins.

5.2 Dataset and methods used in this study

I interpreted a 1,400 km^2 3D post-stack time-migrated survey shot by Petrobras in 2013 and made public in 2018 (Figure 5.2) that consisted of a grid of 1150 inlines and 1975 crosslines. This dataset was kindly made available by the Agência Nacional do Petróleo, Gás Natural e Biocombustíveis (ANP). Supporting data included three different 2D surveys and 105 well logs, 23 of which are within the 3D survey area.

Figure 5.3 Summary of the iterative, artificial intelligence (AI)-based methodology used in this chapter (seismic line shown is line 1743 from the ANP survey BCAM-40-BM-CAL-4 3D that is located on Figure 5.2). The four, repeated steps included: **a)** Initial inspection of the seismic to select and label lines that were representative of the structural diversity of the dataset used to train the AI model; **b)** Fault planes and salt bodies interpreted and labeled within InteractivAI software; **c)** AI neural network initiated and run until the model could approximate the user-interpreted labels. **d)** User-interpreted labels compared to the AI interpretations to see if there were any additional geologic features that needed to be labeled and updated. These four steps were repeated until the neural network was capable of successfully interpreting both the user-labeled lines and uninterpreted, random lines from the survey.

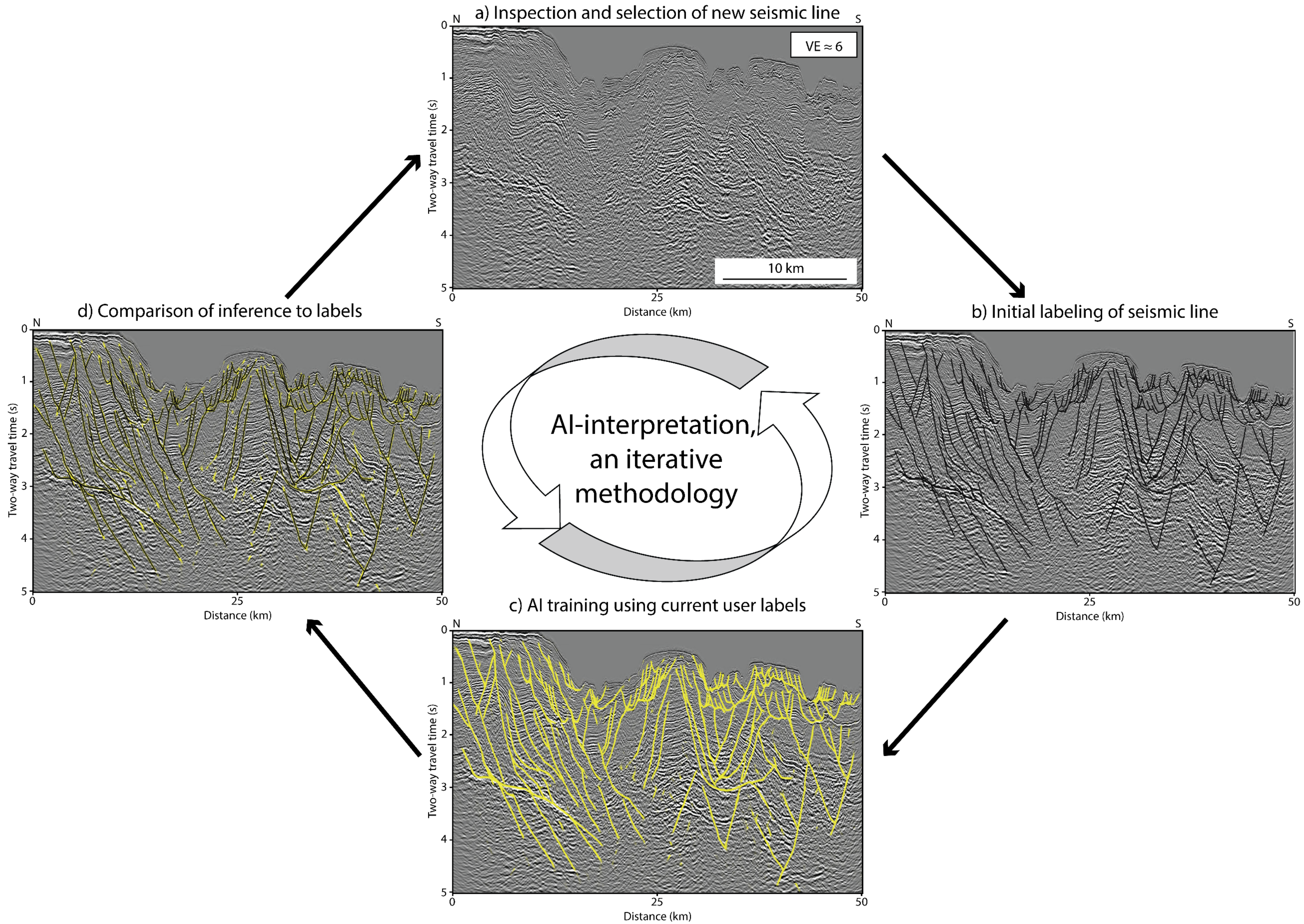
a) Inspection and selection of new seismic line
N
S
VE ≈ 6
10 km
Two-way travel time (s)
Distance (km)
b) Initial labeling of seismic line
c) AI training using current user labels
d) Comparison of inference to labels
AI-interpretation, an iterative methodology

Artificial intelligence can be defined as “the ability to make computers do things that would require intelligence if done by humans” (Boden, 1977). Machine learning algorithms are characterized by their ability to learn without being explicitly programmed. For this chapter, I used Bluware’s InteractivAI software that was created to learn from a user’s interpretation of geologic features such as salt bodies or fault planes. Before work began, I converted the original .segy seismic survey to BluWare’s .vds format within their proprietary Headwave software, permitting faster data access within a smaller file size. This .vds was then imported within InteractivAI for interpretation.

My generalized AI workflow in the interpretation of both fault planes and salt bodies was as follows (Figure 5.3):

1) Initial inspection and selection of a representative seismic line
2) Interpretation and labeling of resolvable features
3) Initialization of network training using Bluware algorithms to generate AI inferences
4) Comparison of inferences to user labeling to improve interpretation
5) Training model reset; new line chosen

The entire seismic volume was inspected to determine the best inlines and crosslines to label; lines that were chosen had to display a representative variety of either fault orientations or salt structures. Faults within the survey were initially labeled across four inlines and crosslines.

As I started the neutral network and inspected the output fault plane inferences, it became clear that more labels were needed to fully capture the heterogeneity and complexity found within the survey. The final model included labels across eight inlines and seven crosslines and ran for a total of six hours until reaching an accuracy match of 95.2%. The resulting probability cube and surfaces were exported from InteractivAI and imported within Petrel for visualization.

A similar workflow was used to interpret evaporites within the survey area. I began with six inlines and five crosslines before initiating the neural network; however, the data quality severely affected the accuracy of the algorithm. I iteratively improved the model, labeling twenty-three inlines and seven crosslines, and ran the model a final time for eight hours until an accuracy match of 99.5% was reached. The resulting probability cube and surfaces were exported from InteractivAI and imported into Petrel for visualization.

5.3 Main results of this study

I labeled a total of 15 seismic reflection lines to train the AI-assisted fault detection model, along with labeling 30 seismic reflection lines to train the AI-assisted salt interpretation model. The locations of select crosslines are shown in Figure 5.2b and the corresponding lines are shown in Figure 5.4–5.5.

This workflow has shown that AI-assisted interpretation methodologies can be used successfully to interpret older, vintage 3D seismic across structurally challenging environments. Fault plane interpretation was relatively straightforward and simple; salt body interpretation seemed to be the most sensitive to lower data quality. This intuitively makes sense, as the interpretation of an evaporite geobody was based on both top and base reflection strength/polarity and internal seismic character; either of these may resemble noise in the data. Increasing the number of lines interpreted directly influenced the model by providing better control; in this way, incorrect AI-picks in the final model were significantly reduced.

Figure 5.4 a) Uninterpreted 2D seismic reflection line is inline 1743 of the ANP 3D survey (BCAM-40-BM-CAL-4 3D), located on the map in Figure 5.2b, and is 50 km-long. **b)** User-interpreted seismic inline 1743 showing listric normal faults within the pre-salt section that sole out across a mid-crustal detachment, as seen in Chapter 3. Listric normal faults also occur within the overlying, post-salt section and sole out across two detachment surfaces. A flower structure formed by strike-slip faulting is imaged and correlates with a strike-slip fault in the same areas as previously interpreted by Cobbold et al. (2010). **c)** Uninterpreted 2D seismic reflection line is inline 1812 of the ANP 3D survey (BCAM-40-BM-CAL-4 3D), located on the map in Figure 5.2b, and is 50 km-long. **d)** AI-interpreted line 1812; note similarities between user and AI interpretation in pre- and post-salt fault dip angles and the two low-angle detachments within the post-salt interval.

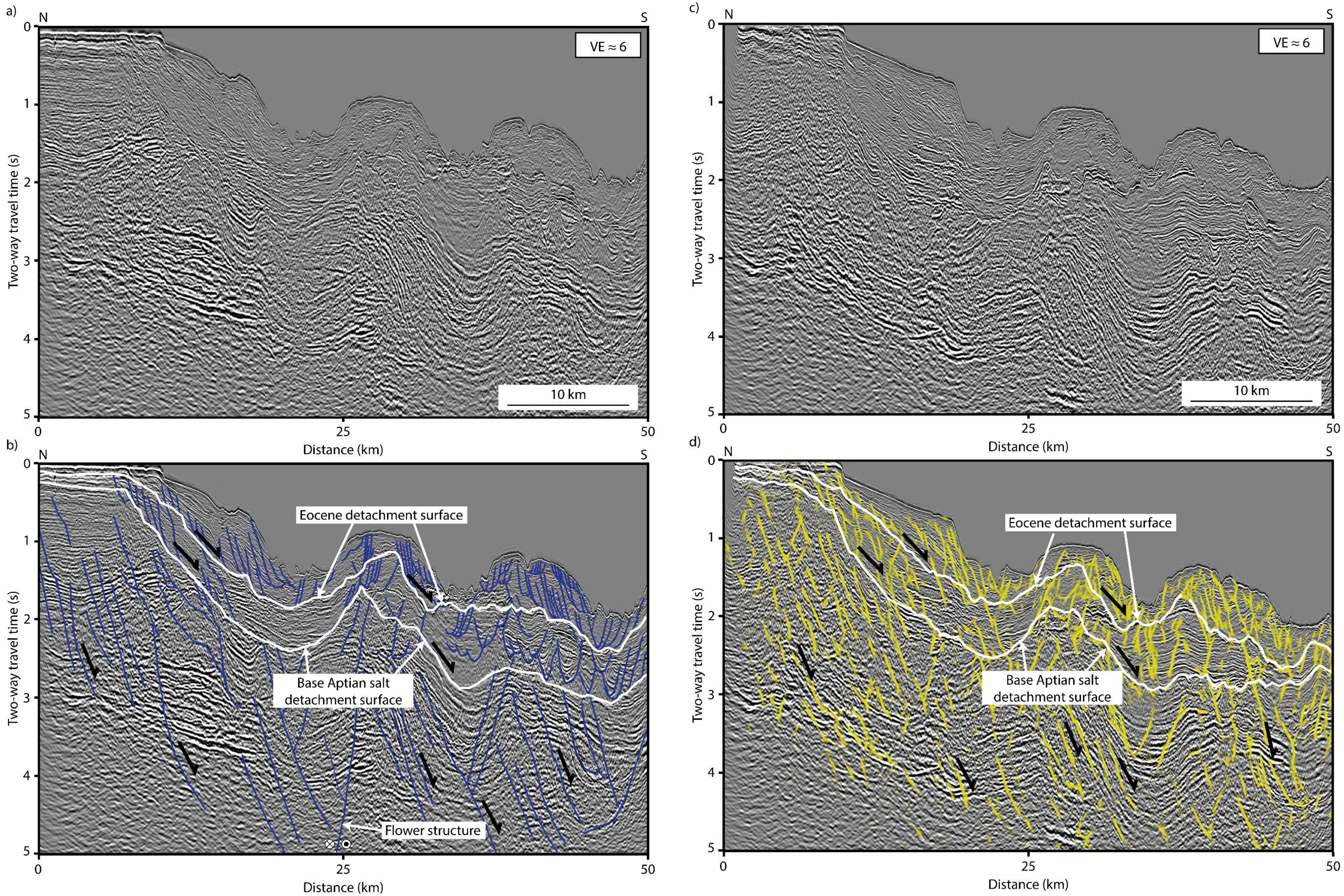
a)
N
S
VE ≈ 6
10 km
Two-way travel time (s)
Distance (km)
b)
Eocene detachment surface
Base Aptian salt detachment surface
Flower structure
c)
d)

Figure 5.5 a) Uninterpreted 2D seismic reflection line is inline 1622 of the ANP 3D survey (BCAM-40-BM-CAL-4 3D), located on the map in Figure 5.2b, and is 50 km-long. **b)** User-interpreted seismic inline 1743 showing remnant salt immediately above the detachment surface at the base of the Aptian salt interval. **c)** Uninterpreted 2D seismic reflection line is inline 1672 of the ANP 3D survey (BCAM-40-BM-CAL-4 3D), located on the map in Figure 5.2b, and is 50 km-long. **d)** AI-interpreted seismic line showing small and isolated salt bodies localized along the base Aptian salt detachment surface and along an overlying Eocene detachment surface. This Eocene surface was determined to be the updip projection of the large, early Eocene unconformity described in Chapter 4.

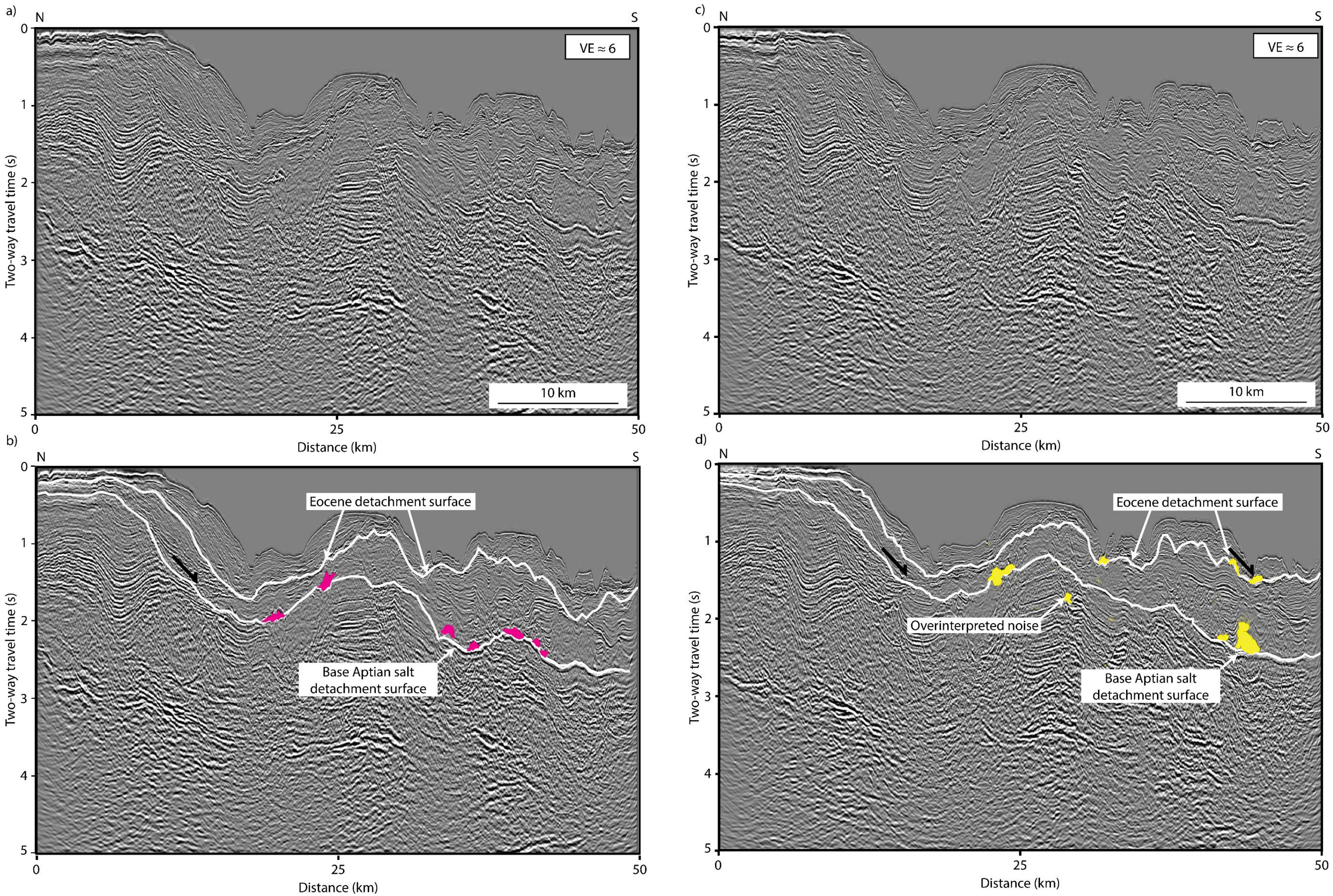

a)
N
S
VE ≈ 6
10 km
Two-way travel time (s)
Distance (km)
b)
Eocene detachment surface
Base Aptian salt detachment surface
c)
d)
Overinterpreted noise

5.3.1 Fault plane interpretations from 3D seismic reflection data

I iteratively interpreted fault planes across eight inlines and seven crosslines from the 3D cube. Interpretation of the selected lines and the 3D fault model created through the machine learning algorithms helped to characterize the fault architecture (Figure 5.4). Fault planes within the pre- and syn-rift are steeply dipping listric faults that sole out across a mid-crustal detachment at depth, as seen in Chapter 3. Deeper fault movement essentially ceased at salt deposition; younger, shallower faults in the post-salt tend to be shorter, shallower-dipping, and sole out across one of two shallow detachments (Figure 5.4–5.5).

Most faults in the survey are simple, listric normal faults, except for one large flower structure seen at the shelf break (Figure 5.5b). This structure was first described by Cobbold et al. (2010) and may be related to the anomalous post-rift uplift events that the Camamu sub-basin underwent from the Late Cretaceous to Quaternary that resulted in net uplift of 1 to 3 km across the shelf and coastal area (Scotchman and Chiossi, 2009).

5.3.2 Salt body interpretations from 3D seismic reflection data

I iteratively interpreted salt structures across twenty-three inlines and seven crosslines within the 3D cube. Although most salt within the Camamu basin evacuated, remnant and isolated salt bodies – including pillows and diapirs – were resolvable on these seismic data. Both allochthonous and autochthonous evaporites were interpreted along one of two detachment surfaces, suggesting that both detachments occurred across salt welds (Figure 5.4–5.5).

Figure 5.6 Depositional model for the Camamu basin. **a)** Aptian evaporites formed in restricted marine conditions in an elongate sag basin developed above the marginal rift shown in map view on Figure 5.1. **b)** Salt withdrawal in areas of sediment loading produced salt-withdrawal mini-basins. **c)** Sedimentation from coastal sources continued to load the evaporite sag basin and evacuated the salt into deepwater areas. **d)** Continued loading and salt deflation caused development of allochthonous diapirs and canopies. **e)** Creation of stable salt welds/detachments at the level of the Aptian salt and at the level of the Eocene unconformity led to the isolated salt remnants along both surfaces observed on the seismic reflection data.

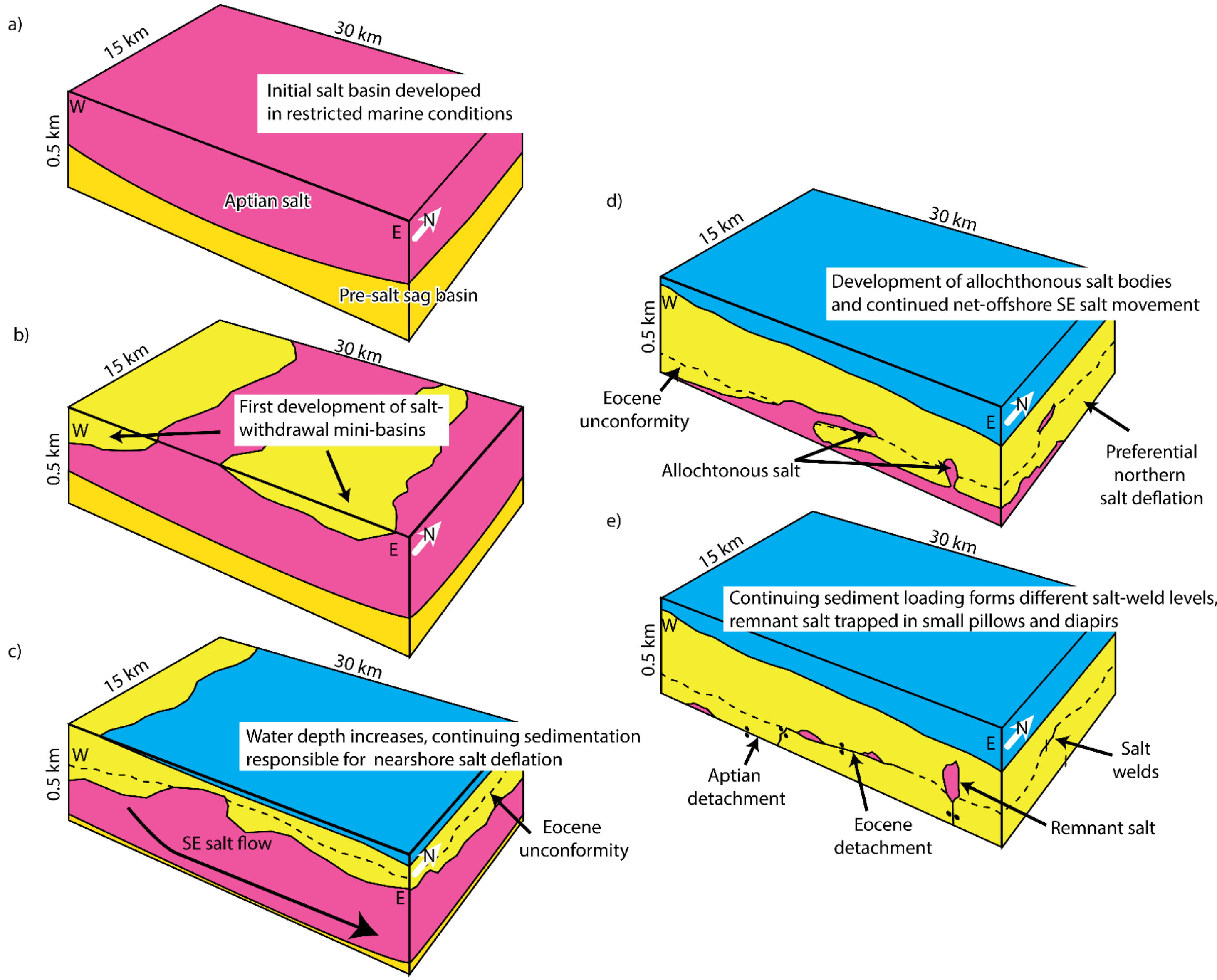
a)
15 km
30 km
Initial salt basin developed
in restricted marine conditions
W
0.5 km
Aptian salt
E
N
Pre-salt sag basin
b)
15 km
30 km
First development of salt-
withdrawal mini-basins
W
0.5 km
E
N
c)
15 km
30 km
Water depth increases, continuing sedimentation
responsible for nearshore salt deflation
W
0.5 km
SE salt flow
Eocene
unconformity
N
E
d)
15 km
30 km
Development of allochthonous salt bodies
and continued net-offshore SE salt movement
W
0.5 km
Eocene
unconformity
E
N
Allochtonous salt
Preferential
northern
salt deflation
e)
15 km
30 km
Continuing sediment loading forms different salt-weld levels,
remnant salt trapped in small pillows and diapirs
W
0.5 km
E
N
Salt
welds
Aptian
detachment
Eocene
detachment
Remnant salt

These interpretations suggest that a few, small, salt bodies remain below the shelf, but most of the larger accumulations are found in the slope region (Figure 5.4–5.5). This observation is supported by work in the Almada sub-basin, where Brandão et al. (2020) recognized a similar pattern of nearshore deflation and net-offshore, southeastern movement of salt through sediment loading.

5.3.3 Model of the post-rift evolution of the Camamu-Almada rifted-passive margin

Complex post-salt evolution was approximated by a simple, five-step model (Figure 5.6). Initially, Aptian evaporites developed in restricted marine conditions over a late-rift sag basin (Figure 5.6a). Loading of clastic sediments from the coastal zone led to the formation of small, separated minibasins (Figure 5.6b). Continued sediment loading caused the underlying evaporites to evacuate and move downslope (Figure 5.6c). Extreme loading resulted in the development of allochthonous diapirs and canopies (Figure 5.6d) that would eventually lead to the formation of geologically-stable salt welds, remnant salt pillows, and diapirs (Figure 5.6e), similar to the present day Camamu sub-basin.

Most wells that drilled through the thinned Taipus-Mirim formation in the shelf area have found it to be devoid of salt (Figure 5.7); only two wells, 1-BAS-21-BA and 1-BAS-75-BA, in the very south of the survey, encountered remnant evaporites in beds of about 50 m in thickness that were intercalated with dolomite, limestone, and shale. The presence of minor salt corroborates the interpretation that most of the salt below the shelf has been evacuated as a result of the overlying sedimentary loading of the post-rift deposition (Figure 5.6–5.7).

Figure 5.7 a) Uninterpreted, east–west-striking, 2D seismic reflection line is crossline 2592 of the ANP 3D survey (BCAM-40-BM-CAL-4 3D), located on the inset map, is 28 km-long and is intersected by three well logs (4-ELPS-12-BAS, 3-ELPS-11-BAS, and 4-ELPS-13-BAS) that penetrated to the pre-salt level. **b)** AI-interpreted fault planes and salt bodies along the seismic dip line with well-control. Green denotes pre-salt section, as determined from the well logs and seismic interpretation. The deepest base Aptian salt detachment marks the top of the pre-salt section. Remnant salt pillows and salt-withdrawal minibasins are marked in pink and yellow, respectively. The shallower, Eocene detachment formed along the major early Eocene unconformity interpreted in Chapter 4. Listric fault planes within the pre-salt are steeply dipping and terminate along the HAR interpreted in Chapter 3. Listric fault planes within the post-salt are more gently sloped and detach along the Aptian and Eocene detachments.

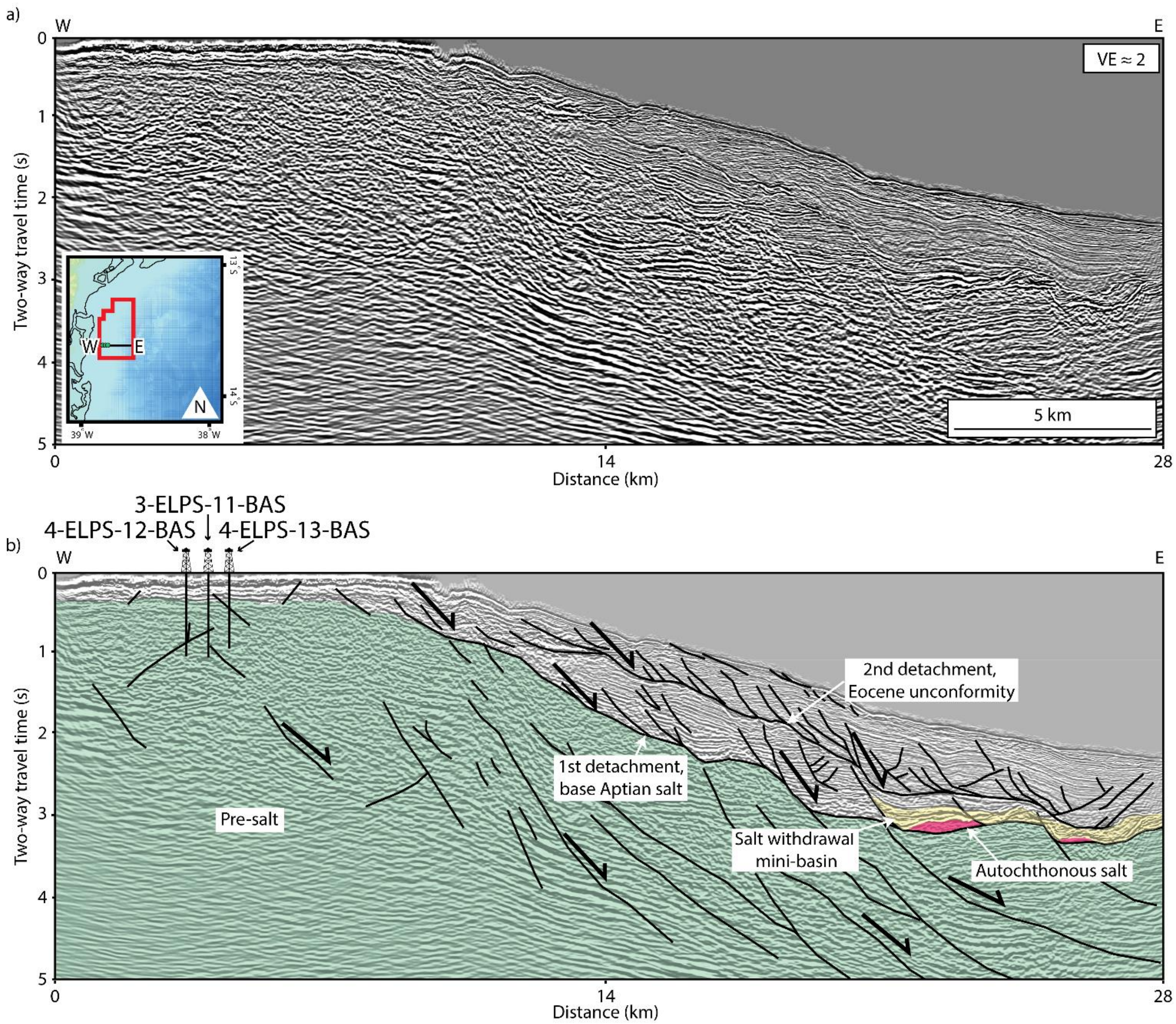
a)
W
E
VE ≈ 2
5 km
W
E
N
13°S
14°S
39°W
38°W
Two-way travel time (s)
Distance (km)
b)
3-ELPS-11-BAS
4-ELPS-12-BAS
4-ELPS-13-BAS
2nd detachment, Eocene unconformity
1st detachment, base Aptian salt
Pre-salt
Salt withdrawal mini-basin
Autochthonous salt

Accumulations of evaporites are present in small volumes under the shelf or as larger pillows and diapirs in the slope region. However, evidence for thicker initial salt that once existed throughout the Camamu basin exists. While this 3D survey is in time and a horizontal scale was difficult to estimate, thicker salt is suggested by the occurrence of the Aptian and Eocene detachments and the seismic evidence for thick salt-withdrawal mini-basins (Figure 5.7). This greater salt influence is also supported by data presented in Chapter 4 of this dissertation, where structural restorations suggest that thicker salt previously existed across the northeastern Brazilian margin.

Both detachments appear to be salt-related and underlie the majority of the interpreted salt bodies (Figure 5.7). The deeper detachment marks the base of the Aptian salt, while stratigraphic control from deepwater well 1-BRSA-28-BAS suggests an Eocene age for the shallower detachment surface (Figure 5.7). Comparing subsidence and deflation rates calculated in Chapter 4 of this work reveals a link between the detachment age, the major lower Eocene unconformity in the Camamu, and a period of rapid salt deflation (Figure 5.8). I infer that this uplift may result from far field orogenic forces (Figure 5.8a) or mantle-induced forces (Figure 5.8b). Lower slope and deepwater salt tectonics responded strongly to major Late Cretaceous to late Eocene uplift, and this was reflected in the Eocene timing for the second, shallow detachment within the shelf and upper slope of the Camamu (Figure 5.8c–d).

5.3.4 Advantages of AI-assisted modeling of complex fault arrays and remobilized salt

A key advantage of this AI-assisted methodology is the ability to collect a large amount of detail on the 3D orientations of fault planes and salt bodies (Figure 5.9). Dense 3D meshes of faults interpreted under the shelfal areas are steeply-dipping in both onshore and offshore directions (Figure 5.9a). Below the slope, most faults are listric normal faults that dip seaward as the post-rift sag and passive margin thickened and remobilized the underlying salt by loading (Figure 5.9b).

Salt bodies in the Camamu sub-basin are thin to absent under the shelf (Figure 5.9c), while beneath the slope region isolated salt bodies increase in both frequency and size (Figure 5.9d). These salt bodies thicken and become more numerous in a southwestwardly direction, which is consistent with the overall movement of salt as it evacuated from the shelf area and was displaced down the slope in a southwestwardly direction (Brandão et al., 2020; Chapter 4). The concentrations of faults and salt are sub-parallel to the shelf break and follow a curvilinear pattern that suggests linked deformation (Figure 5.9a, 5.9c).

Figure 5.8 a) Compilation of previously proposed tectonic mechanisms that deformed, uplifted, and eroded the Camamu-Almada passive margin and adjacent Brazilian craton. Apatite fission track frequency compiled by Zavala (2018) was compared with the Andean orogenic phases from Japsen et al. (2012) and the South Atlantic spreading rate velocity from Colli et al. (2014). **b)** Large-scale magmatic events that may have impacted the passive margin evolution of the Camamu-Almada margin and the northeastern Brazilian craton include: 1) the Poxoreu igneous province (~84 Ma); 2) the Abrolhos magmatic province (69-32 Ma); and 3) the Trindade volcanic chain (50-10 Ma) (Fodor and Hanan, 2000). **c)** 1D burial history of the offshore Camamu and Almada sub-basins compared to the onland geomorphic and thermochronologic study by Japsen et al. (2012). PW1–4 denote the pseudowell subsidence curves generated along the structural restorations in Chapter 4. Numbers 1–5 indicate the major uplift and erosional event identified in this study: 1) Lower Cretaceous, 2) Upper Cretaceous, 3) Paleocene, 4) Eocene, 5) Miocene to Recent. **d)** Graphical plot of salt deflation through time, shown as percentages, compared to the shallower, Eocene detachment age. Note rapid deflation during uplift events in the Early Cretaceous (Event 1), and between the Late Cretaceous to late Eocene (Event 2–4). Salt within the Camamu sub-basin stabilized before the latest uplift post mid-Miocene (Event 5).

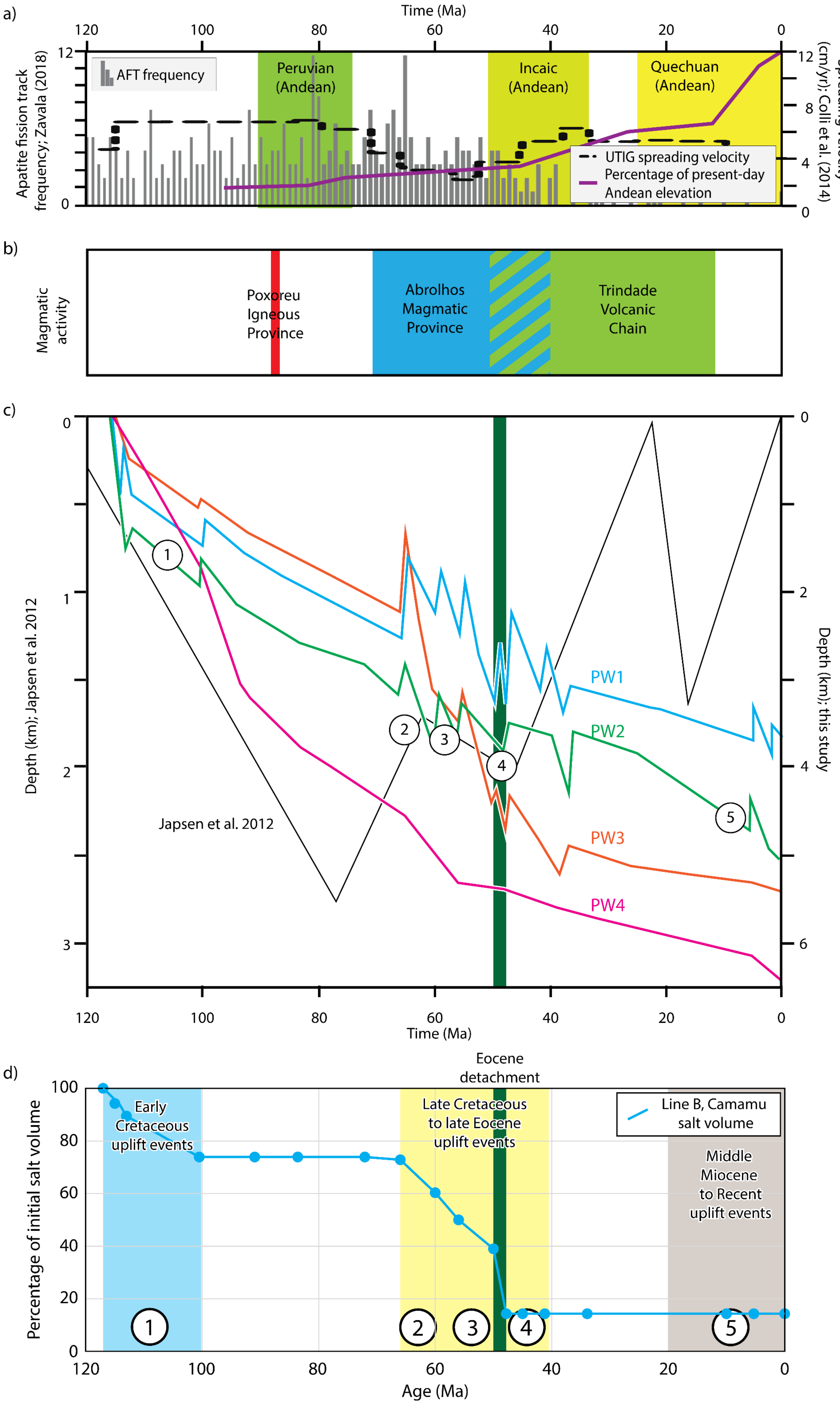
a)
Time (Ma)
120
100
80
60
40
20
0
12
0
Apatite fission track frequency; Zavala (2018)
AFT frequency
Peruvian (Andean)
Incaic (Andean)
Quechuan (Andean)
UTIG spreading velocity
Percentage of present-day Andean elevation
12
8
4
0
Spreading velocity (cm/yr); Colli et al. (2014)
b)
Magmatic activity
Poxoreu Igneous Province
Abrolhos Magmatic Province
Trindade Volcanic Chain
c)
0
1
2
3
Depth (km); Japsen et al. 2012
0
2
4
6
Depth (km); this study
PW1
PW2
PW3
PW4
Japsen et al. 2012
1
2
3
4
5
120
100
80
60
40
20
0
Time (Ma)
d)
Eocene detachment
100
80
60
40
20
0
Percentage of initial salt volume
Early Cretaceous uplift events
Late Cretaceous to late Eocene uplift events
Line B, Camamu salt volume
Middle Miocene to Recent uplift events
1
2
3
4
5
120
100
80
60
40
20
0
Age (Ma)

Figure 5.9 a) Map of all fault planes interpreted using the AI-based interpretation. Curvilinear trends in the light, yellow lines are concentrations of AI-mapped faults that are associated with the isolated salt bodies. The shelf edge is marked by the black line and the inferred edges of the Berriasian-Aptian marginal rift interpreted in Chapter 3 are shown by the black dashed line. **b)** Block diagram based on the 3D seismic cube showing the same map area as shown in 5.9a; the curvilinear trends shown by the light, yellow lines are concentrations of AI-mapped faults that are associated with the isolated salt bodies. **c)** Map view of isolated salt bodies, in green, interpreted by the AI- based methodologies with the yellow lines marking concentrations of AI-mapped faults associated with those salt bodies, and the dotted lines showing the extent of the original salt basin concentrated in the sag above the marginal rift. The combined map patterns indicate that most of the salt has evacuated from beneath the shelf area in a southeastern direction and now underlies the upper slope. **d)** Block diagram based on the 3D seismic cube showing the dip on the base Aptian salt detachment, the isolated salt remnants in red, and the concentrations of AI-mapped faults shown as the yellow lines. The interpretation is that the salt has been evacuated from beneath the shelf and has now moved downslope and to the southwest along both the lower base Aptian salt detachment and a shallower Eocene detachment.

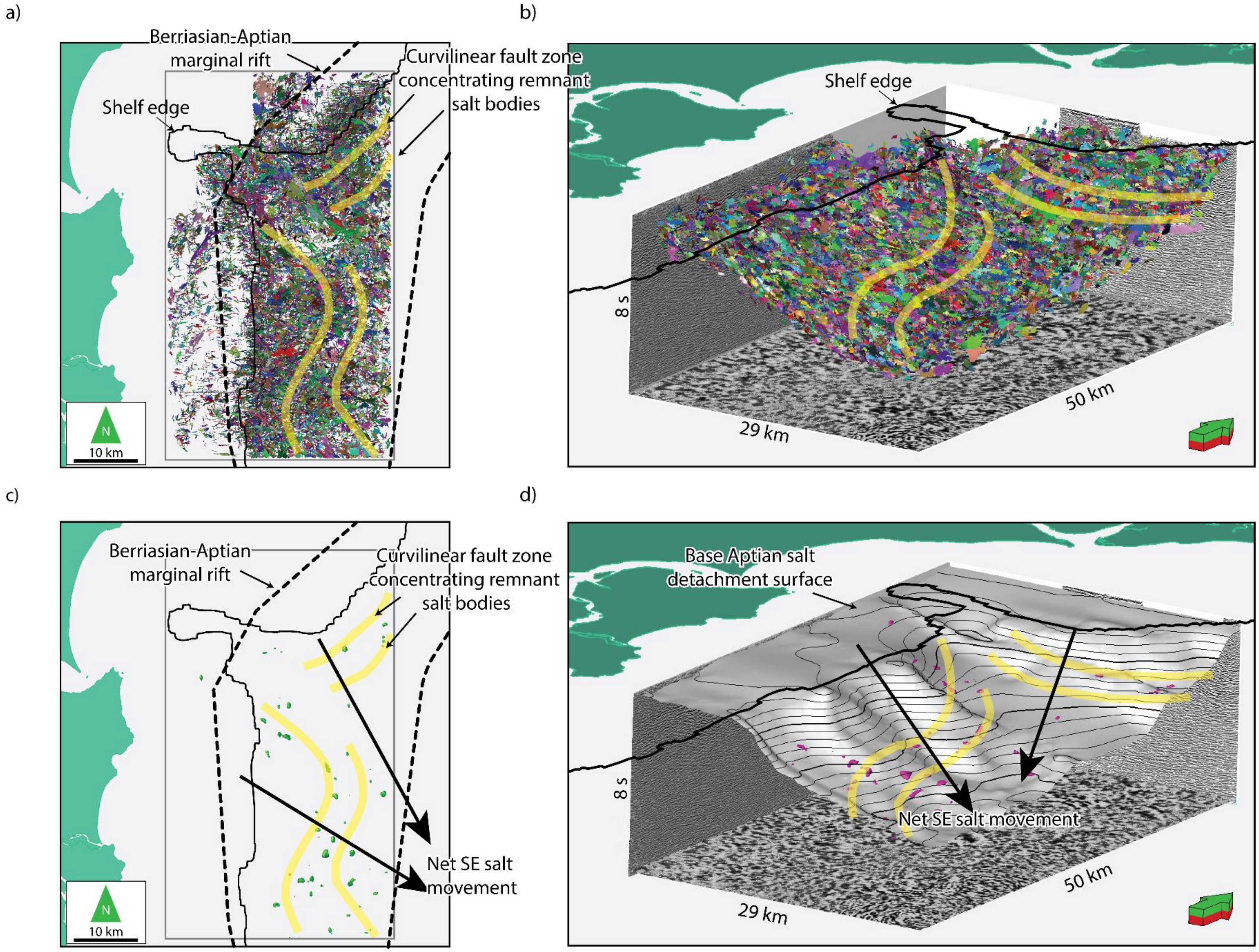
a)
Berriasian-Aptian marginal rift
Curvilinear fault zone concentrating remnant salt bodies
Shelf edge
N
10 km
b)
Shelf edge
8 s
29 km
50 km
c)
Berriasian-Aptian marginal rift
Curvilinear fault zone concentrating remnant salt bodies
Net SE salt movement
N
10 km
d)
Base Aptian salt detachment surface
Net SE salt movement
8 s
29 km
50 km

5.4 Conclusions of this chapter

The main results of this study include:

1) It is possible to use AI-assisted interpretation tools to interpret older, vintage 3D seismic from structurally complex environments, such as the deformed rifted-passive margin of northeastern Brazil. The high level of detail for the AI-assisted interpretation of salt and faults, which took several weeks, would not have been possible to manually map over a period of several months.
2) These workflows and AI-assisted seismic interpretations revealed that the near-shore Camamu basin once contained a much thicker and more extensive Aptian salt body than previously recognized. Progressive loading of the salt body by coastal-derived clastic sediments led to the seaward and downslope evacuation of the salt in several pulses during the Cretaceous and Cenozoic. AI-assisted seismic interpretations showed small and isolated salt bodies along two basinward-dipping, salt related detachments, one at the base of the Aptian salt and the other along a major Eocene unconformity.
3) These results change the present understanding of the distribution and original thickness of the Brazilian salt basin. Previously considered salt-poor and the northern limit of Aptian salt offshore Brazil, the Camamu salt basin was once considerably thicker and more extensive – but today has been largely evacuated.

BIBLIOGRAPHY

Abdelmalak, M. M., T. B. Andersen, S. Planke, J. I. Faleide, F. Corfu, C. Tegner, G. E. Shephard, D. Zastrozhnov, and R. Myklebust, 2015, The ocean-continent transition in the mid-Norwegian margin: Insight from seismic data and an onshore Caledonian field analogue: Geology, v. 43, p. 1011–1014.

Aitken, T., 2005, Stratigraphic and tectonic history of the Grenada and Tobago basins as determined from marine seismic data, wells, and onland geology: MSc thesis, University of Texas at Austin, Austin, TX, 89 p.

Aitken, T., P. Mann, A. Escalona, and G. L. Christeson, 2011, Evolution of the Grenada and Tobago basins and implications for arc migration: Marine and Petroleum Geology, v. 28, p. 235–258.

Alkmim, F. F., and M. A. Martins-Neto, 2012, Proterozoic first-order sedimentary sequences of the São Francisco craton, eastern Brazil: Marine and Petroleum Geology, v. 33, p. 127–139.

Alldredge, L. R., and G. D. Van Voorhis, 1961, Depth to sources of magnetic anomalies: Journal of Geophysical Research, v. 66, p. 3793–3800.

Allen, R. W., J. S. Collier, A. G. Stewart, T. Henstock, S. Goes, A. Rietbrock, and the V. Team, 2019, The role of arc migration in the development of the Lesser Antilles: A new tectonic model for the Cenozoic evolution of the eastern Caribbean: Geology, v. 47, p. 891–895.

Almeida, F. F. M., Y. Hasui, B. B. de Brito Neves, and R. A. Fuck, 1981, Brazilian structural provinces: An introduction: Earth-Science Reviews, v. 17, p. 1–29.

Amante, C. and B. W. Eakins, 2009, ETOPO1 global relief model converted to PanMap layer format: NOAA National Geophysical Data Center, PANGAEA.

Andjić, G., J. Escuder-Viruete, C. Baumgartner-Mora, P. O. Baumgartner, S. F. Mitchell, M. Caron, and E. Caus, 2019b, Sedimentary record of arc-continent collision along Mesozoic SW North America (Siuna Belt, Nicaragua): Tectonics, v. 38, p. 4399–4425.

Andjić, G., P. O. Baumgartner, and C. Baumgartner-Mora, 2019a, Collision of the Caribbean large igneous province with the Americas: earliest evidence from the forearc of Costa Rica: GSA Bulletin, v. 131, p. 1555–1580.

Arden Jr., D. D., 1975, Geology of Jamaica and the Nicaraguan Rise, in A. E. M. Nairn, and F. H. Stehli, eds., *The Ocean Basins and Margins*: Plenum, New York, NY, p. 617–661.

Armitage, J. J., J. S. Collier, T. A. Minshull, and T. J. Henstock, 2011, Thin oceanic crust and flood basalts: India-Seychelles breakup: Geochemistry, Geophysics, Geosystems, v. 12, Article Q0AB07.

Assumpção, M., M. Bianchi, J. Julià, F. L. Dias, G. Sand França, R. Nascimento, S. Drouet, C. G. Pavão, D. F. Albuquerque, and A. E. V. Lopes, 2013, Crustal thickness map of Brazil: Data compilation and main features: Journal of South American Earth Sciences, v. 43, p. 74–85.

Austermann, J., J. X. Mitrovica, P. Huybers, and A. Rovere, 2017, Detection of a dynamic topography signal in last interglacial sea-level records: Science Advances, v. 3, Article e1700457.

Bader, Richard G, 1970, Initial Reports of the deep-sea drilling project, Volume IV: U.S. Government Printing Office, Washington, D.C., 753 p.

Bangs, N. L., G. L. Christeson, and T. H. Shipley, 2003, Structure of the Lesser Antilles subduction zone backstop and its role in a large accretionary system: Journal of Geophysical Research, Solid Earth, v. 108, Article 2358.

Bankey, V., A. Cuevas, et al., 2002, Digital data grids for the magnetic anomaly map of North America: U.S. Geological Survey Open-File Report 02-414, U.S. Geological Survey, Denver, Colorado, USA.

Baranov, V., and H. Naudy, 1964, Numerical calculation of the formula of reduction to the magnetic pole: Geophysics, v. 29, p. 67–79.

Barnard, A., W. W. Sager, J. E. Snow, and M. D. Max, 2015, Subsea gas emissions from the Barbados Accretionary Complex: Marine and Petroleum Geology, v. 64, p. 31–42.

Baumgartner, P. O., K. Flores, A. N. Bandini, F. Girault, and D. Cruz, 2008, Upper Triassic to Cretaceous radiolaria from Nicaragua and Northern Costa Rica - The Mesquito Composite Oceanic Terrane: Ofioliti, v. 33, p. 1–19.

Baumgartner, P., G. Andjić, D. Buchs, A. Bandini-Maeder, and K. Flores, 2018, Synthesis of terrane stratigraphy and assembly of Southern Central America: AAPG Hedberg conference abstracts, Sigüenza, Spain.

Beauchamp, W., R. W. Allmendinger, M. Barazangi, A. Demnati, M. El Alji, and M. Dahmani, 1999, Inversion tectonics and the evolution of the High Atlas Mountains, Morocco, based on a geological-geophysical transect: Tectonics, v. 18, p. 163–184.

Bécel, A., J. K. Davis, B. D. Shuck, H. J. A. Van Avendonk, and J. C. Gibson, 2020, Evidence for a prolonged continental breakup resulting from slow extension rates at the eastern North American volcanic rifted margin: Journal of Geophysical Research, Solid Earth, v. 125, Article e2020JB020093.

Becker, K., D. Franke, R. Trumbull, M. Schnabel, I. Heyde, B. Schreckenberger, H. Koopmann, K. Bauer, W. Jokat, and C. M. Krawczyk, 2014, Asymmetry of high-velocity lower crust on the South Atlantic rifted margins and implications for the interplay of magmatism and tectonics in continental breakup: Solid Earth, v. 5, p. 1011–1026.

Beglinger, S. E., M. P. Corver, H. Doust, S. Cloetingh, and A. K. Thurmond, 2012, A new approach of relating petroleum system and play development to Basin evolution: An application to the conjugate margin Gabon coastal and Almada-Camamu Basins: AAPG Bulletin, v. 96, p. 953–982.

Belgarde, C., G. Manatschal, N. Kusznir, S. Scarselli, and M. Ruder, 2015, Rift processes in the Westralian Superbasin, North West Shelf, Australia: Insights from 2D deep reflection seismic interpretation and potential fields modeling: APPEA Conference abstracts, Melbourne, Australia.

Bernardo, L. M., and C. Bartolini, 2015, Petroleum source rock analysis in the western Caribbean region: an overview, in C. Bartolini, and P. Mann, eds., *Petroleum Geology and Potential of the Colombian Caribbean Margin*: AAPG, Tulsa, OK, p. 587–614.

Bird, D. E., S. A. Hall, J. F. Casey, and P. S. Millegan, 1993, Interpretation of magnetic anomalies over the Grenada Basin: Tectonics, v. 12, p. 1267–1279.

Bird, D. E., S. A. Hall, J. F. Casey, P. S. Millegan, and K. J. Hsu, 1999, Tectonic evolution of the Grenada Basin, in P. Mann, ed., *Caribbean Basins*: Elsevier Science, Amsterdam, The Netherlands, p. 389–416.

Blaich, O. A., J. I. Faleide, F. Tsikalas, D. Franke, and E. León, 2009, Crustal-scale architecture and segmentation of the Argentine margin and its conjugate off South Africa: Geophysical Journal International, v. 178, p. 85–105.

Blaich, O. A., J. I. Faleide, F. Tsikalas, R. Lilletveit, D. Chiossi, P. Brockbank, and P. Cobbold, 2010, Structural architecture and nature of the continent-ocean transitional domain at the Camamu and Almada Basins (NE Brazil) within a conjugate margin setting, in B. A. Vining, and S. C. Pickering, eds., *Petroleum Geology Conference Proceedings*: Geological Society, Special Publications, London, UK, v. 7, p. 867–883.

Blakely, R. J., 1995, Potential theory in gravity and magnetic applications: Cambridge University Press, Cambridge, UK, 468 p.

Blanco, J. M., P. Mann, and L. Nguyen, 2015, Location of the suture zone separating the great arc of the Caribbean from continental crust of northwestern South America inferred from regional gravity and magnetic data, in C. Bartolini, and P. Mann, eds., *Petroleum Geology and Potential of the Colombian Caribbean Margin*: AAPG, Tulsa, OK, p. 161–178.

Boden, M. A., 1977, Artificial intelligence and natural man: Basic Books, New York, NY, 590 p.

Bodur, Ö. F., O. H. Göğüş, R. N. Pysklywec, and A. I. Okay, 2018, Mantle lithosphere rheology, vertical tectonics, and the exhumation of UHP rocks: Journal of Geophysical Research, Solid Earth, v. 123, p. 1824–1839.

Bodvarsson, G. and G. P. L. Walker, 1964, Crustal drift in Iceland: Geophysical Journal International, v. 8, p. 285–300.

Boillot, G., D. Mougenot, J. Girardeau, and E. L. Winterer, 1989. Rifting processes on the West Galicia margin, Spain, in A.J. Tankard and H.R. Balkwill, eds., *Extensional Tectonics and Stratigraphy of the North Atlantic Margins*: AAPG Memoir, v. 46, p. 363–377.

Boillot, G., S. Grimaud, A. Mauffret, D. Mougenot, J. Kornprobst, J. Mergoil-Daniel, and G. Torrent, 1980, Ocean-continent boundary off the Iberian margin: A serpentinite diapir west of the Galicia Bank: Earth and Planetary Science Letters, v. 48, p. 23–34.

Boschman, L. M., E. Van der Wiel, K. E. Flores, C. G. Langereis, and D. J. J. Van Hinsbergen, 2019, The Caribbean and Farallon plates connected: Constraints from stratigraphy and paleomagnetism of the Nicoya peninsula, Costa Rica: Journal of Geophysical Research, Solid Earth, v. 127, p. 6243–6266.

Boutilier, R. R., and C. E. Keen, 1999, Small-scale convection and divergent plate boundaries: Journal of Geophysical Research, Solid Earth, v. 104, p. 7389–7403.

Bouysse, P., 1988, Opening of the Grenada back-arc basin and evolution of the Caribbean plate during the Mesozoic and early Paleogene: Tectonophysics, v. 149, p. 121–143.

Bouysse, P., P. Andreieff, M. Richard, J. C. Baubron, A. Mascle, R. C. Maury, and D. Westercamp, 1985, Aves swell and northern Lesser Antilles ridge: Rock-dredging results from Arcante 3 cruise, in A. Mascle, ed., *Symposium Geodynamique des Caraibes*: Editions Technip, Paris, France, p. 65–76.

Bowland, C. L., 1984, Seismic stratigraphy and structure of the Colombian Basin, Caribbean Sea: MSc thesis, University of Texas at Austin, Austin, Texas, 248 p.

Bowland, C. L., 1993, Depositional history of the western Colombian Basin, Caribbean Sea, revealed by seismic stratigraphy: GSA Bulletin, v. 105, p. 1321–1345.

Bowland, C. L., and E. Rosencrantz, 1988, Upper crustal structure of the western Colombian basin, Caribbean Sea: GSA Bulletin, v. 100, p. 534–546.

Boynton, C. H., G. K. Westbrook, M. H. P. Bott, and R. E. Long, 1979, A seismic refraction investigation of crustal structure beneath the Lesser Antilles island arc: Geophysical Journal International, v. 58, p. 371–393.

Bradley, D. C., 2008, Passive margins through Earth history: Earth-Science Reviews, v. 91, p. 1–26.

Brandão, A., P. Vidigal-Souza, and M. Holz, 2020, Evaporite occurrence and salt tectonics in the Cretaceous Camamu-Almada Basin, northeastern Brazil: Journal of South American Earth Sciences, v. 97, p. 1–12.

Bronner, A., D. Sauter, G. Manatschal, G. Péron-Pinvidic, and M. Munschy, 2011, Magmatic breakup as an explanation for magnetic anomalies at magma-poor rifted margins: Nature Geoscience, v. 4, p. 549–553.

Bronner, A., D. Sauter, M. Munschy, J. Carlut, R. Searle, M. Cannat, and G. Manatschal, 2014, Magnetic signature of large, exhumed mantle domains of the Southwest Indian Ridge – results from a deep-tow geophysical survey over 0 to 11 Ma old seafloor: Journal of Geophysical Research, Solid Earth, v. 5, p. 339–354.

Brown, K. M., and G. K. Westbrook, 1987, The tectonic fabric of the Barbados Ridge accretionary complex: Marine and Petroleum Geology, v. 4, p. 71–90.

Buchs, D. M., A. C. Kerr, J. C. Brims, J. P. Zapata-Villada, T. Correa-Restrepo, and G. Rodríguez, 2018, Evidence for subaerial development of the Caribbean oceanic plateau in the Late Cretaceous and palaeo-environmental implications: Earth and Planetary Science Letters, v. 499, p. 62–73.

Buchs, D. M., R. J. Arculus, P. O. Baumgartner, C. Baumgartner-Mora, and A. Ulianov, 2010, Late Cretaceous arc development on the SW margin of the Caribbean Plate: Insights from the Golfito, Costa Rica, and Azuero, Panama, complexes: Geochemistry, Geophysics, Geosystems, v. 11, p. 1–35.

Buck, W. R., 2017, The role of magmatic loads and rift jumps in generating seaward-dipping reflectors on volcanic rifted margins: Earth and Planetary Science Letters, v. 466, p. 62–69.

Burke, K., 1988, Tectonic Evolution of the Caribbean: Annual Reviews of Earth and Planetary Sciences, v. 16, p. 201–230.

Burov, E. B., and M. Diament, 1995, The effective elastic thickness (Te) of continental lithosphere: What does it really mean?: Journal of Geophysical Research, Solid Earth, v. 100, p. 3905–3927.

Caixeta, J. M., T. S. Ferreira, D. L. M. Jr, J. L. Teixeira, and M. A. T. Romeiro, 2014, Albian rift systems in the northeastern Brazilian margin: An example of rifting in hyper-extended continental crust: AAPG ICE extended abstracts, Istanbul, Turkey, p. 13.

Caixeta, J.M., O. S. Milhomem, R. E. Witzke, I. S. S. Dupuy, and G. A. Gontijo, 2007, Bacia de Camamu: Boletim de Geociências da Petrobrás, v. 15, p. 455–461.

Cann, J. R. Langseth, M.G. et al., 1983, Volume 69 Covering Leg 68 (Site 501), Leg 69, and Leg 70 (Site 504) of the Cruises of the Drilling Vessel Glomar Challenger, Puntarenas, Costa Rica to Balboa, Panama, July–December 1979, in *Initial Reports of the Deep Sea Drilling Project*: US Government Printing Office, Washington, DC, 29 p.

Carlson, R. L., and G. S. Raskin, 1984, Density of the ocean crust: Nature, v. 311, p. 555–558.

Carvajal-Arenas L.C., 2017, Hydrocarbon prospectivity of the Nicaraguan Rise and Colombia Basin, western Caribbean Sea: PhD dissertation, University of Houston, Houston, TX, 359 p.

Carvajal-Arenas, L. C., and P. Mann, 2018, Western Caribbean intraplate deformation: Defining and continuous and active microplate boundary along the San Andres rift and Hess Escarpment fault zone, Colombian Caribbean Sea: AAPG Bulletin, v. 102, p. 1523–1563.

Carvajal-Arenas, L. C., L. Torrado, and P. Mann, 2015, Early and late Eocene/Oligo-Miocene (!) petroleum system on the Nicaraguan Rise: Insights from basin and three-dimensional petroleum system modeling, in C. Bartolini, and P. Mann, eds., *Petroleum Geology and Potential of the Colombian Caribbean Margin*: AAPG, Tulsa, OK, p. 615–646.

Case, J. E., W. D. MacDonald, and P. J. Fox, 1990, Caribbean crustal provinces; seismic and gravity evidence, in G. Dengo, and J. E. Case, eds., *The Geology of North America Vol H: The Caribbean Region*: GSA, Boulder, CO, p. 15–36.

Castillo, K. and P. Mann, 2021, Structure, stratigraphy, and hydrocarbon potential of the easternmost part of the Eastern Venezuelan foreland basin, in C. Bartolini, ed., *South America-Caribbean-Central Atlantic Boundary: Tectonic Evolution, Basin Architecture and Petroleum Systems*: AAPG Memoir, Tulsa, OK, v. 123, p. 591-620.

Castillo, V., Benkovics, L., Cobos, C., Demuro, D. and Franco, A, 2017, Perla field: the largest discovery ever in Latin America, in R. K. Merrill, and C. A. Sternbach, eds., *Giant Fields of the Decade 2000–2010*: AAPG Memoir, Tulsa, OK, v. 113, p. 141–152.

Chamberlin, R. T., 1910, The Appalachian folds of central Pennsylvania: The Journal of Geology, v. 18, p. 228–251.

Chang, H. K., R. O. Kowsmann, A. M. F. Figueiredo and A. Bender, 1992, Tectonics and stratigraphy of the East Brazil Rift system: An overview: Tectonophysics, v. 213, p. 97–138.

Christeson, G. L., P. Mann, A. Escalona, and T. J. Aitken, 2008, Crustal structure of the Caribbean-northeastern South America arc-continent collision zone: Journal of Geophysical Research, v. 113, p. 1–19.

Clerc, C., L. Jolivet, and J. C. Ringenbach, 2015, Ductile extensional shear zones in the lower crust of a passive margin: Earth and Planetary Science Letters, v. 431, p. 1–7.

Cobbold, P. R., G. Gilchrist, I. Scotchman, D. Chiossi, F. G. D. Souza, and F. F. Lilletveit, R. Chaves, 2010, Large submarine slides on a steep continental margin (Camamu Basin, NE Brazil): Journal of the Geological Society, v. 167, p. 583–592.

Coelho, A. C., S. Fontes, E. La Terra, M. Tupinambá, V. Maurya, G. Bueno, and J. Pereira, 2019, Integrated modeling of seismic, gravity and magnetic data of Camamu Basin, Brazilian Eastern Margin – Tectonostratigraphic framework, structural aspects, petroleum system, volcanic activity and crustal domains: 16th International Congress of the Brazilian Geophysical Society conference abstracts volume, Rio de Janeiro, Brazil.

Coffin, M. F., 1992a, Subsidence of the Kerguelen Plateau: the Atlantis concept, in Wise, S.W., R. Schlich and A. A. P. Julson, eds., *Proceedings of the Ocean Drilling Program, Scientific Results, Vol. 120*: US Government Printing Office, Washington, DC, p. 945–949.

Coffin, M. F., 1992b, Emplacement and subsidence of Indian Ocean Plateaus and submarine ridges, in R. A. Duncan, D. K. Rea, R. B. Kidd, et al., eds., *Synthesis of Results from Scientific Drilling in the Indian Ocean*: Geophysical Monograph Series, AGU, Washington, DC, v. 70, p. 115–125.

Coffin, M. F., and O. Eldholm, 1994, Large igneous provinces: Crustal structure, dimensions, and external consequences: Reviews of Geophysics, v. 32, p. 1–36.

Colli, L., I. Stotz, H. P. Bunge, M. Smethurst, S. Clark, G. Iaffaldano, A. Tassara, F. Guillocheau, and M. C. Bianchi, 2014, Rapid South Atlantic spreading changes and coeval vertical motion in surrounding continents: Evidence for temporal changes of pressure-driven upper mantle flow: Tectonics, v. 33, p. 1304–1321.

Cooper, G. R. J., and D. R. Cowan, 2008, Edge enhancement of potential-field data using normalized statistics: Geophysics, v. 73, p. H1-H4.

Corbeau, J., F. Rolandone, S. Leroy, K. Guerrier, D. Keird, G. Stuart, V. Clouard, R. Gallacher, S. Ulysse, D. Boisson, R. Bien-aimé Momplaisir, F. Saint Preux, C. Prépetit, J. M. Saurel, B. Mercier de Lépinay, and B. Meyera, 2017, Crustal structure of western Hispaniola (Haiti) from a teleseismic receiver function study: Tectonophysics, v. 709, p. 9–19.

Cordani, U. G., 1970, Idade do vulcanismo no oceano Atlântico sul: Boletim IGA, v. 1, p. 9–75.

Cordell, L., and V. J. S. Grauch, 1985, Mapping basement magnetization zones from aeromagnetic data in the San Juan basin, New Mexico, in W. J. Hinze, ed., *The Utility of Regional Gravity and Magnetic Anomaly Maps*: SEG, Tulsa, OK, p. 181–197.

Cordell, L., 1979, Gravimetric expression of graben faulting in Santa Fe Country and the Espanola Basin, New Mexico, in R.V. Ingersoll, ed., *Guidebook to Santa Fe Country*: New Mexico Geological Society, Socorro, NM, p. 59–64.

Courtillot, V., 1982, Propagating rifts and continental breakup: Tectonics, v. 1, p. 239–250.

Crough, S. T., 1983, The correction for sediment loading on the seafloor: Journal of Geophysical Research, Solid Earth, v. 88, p. 6449–6454.

Curet, E, 1992, Stratigraphy and evolution of the Tertiary Aruba basin: Journal of Petroleum Geology, v. 15, p. 283–304.

Davis, J. K., A. Bécel, and W. R. Buck, 2018, Estimating emplacement rates for seaward-dipping reflectors associated with the U.S. East Coast Magnetic Anomaly: Geophysical Journal International, v. 215, p. 1594–1603.

Davison, I., 1999, Tectonics and hydrocarbon distribution along the Brazilian South Atlantic margin, in N. R. Cameron, R. H. Bate, and V. S. Clure, eds., *The Oil and Gas Habitats of the South Atlantic*: Geological Society, Special Publications, London, UK, v. 153, p. 133–151.

Davison, I., 2007, Geology and tectonics of the South Atlantic Brazilian salt basins, in A. C. Ries, R. W. H. Butler, and R. H. Graham, eds., *Deformation of the Continental Crust: The Legacy of Mike Coward*: Geological Society, Special Publications, London, UK, v. 272, p. 345–359.

De Voogd, B., R. Nicolich, J. L. Olivet, F. Fanucci, J. Burrus, A. Mauffret, G. Pascal, A. Argnani, J. M. Auzende, M. Bernabini, C. Bois, L. Carmignani, A. Fabbri, I. Finetti, A. Galdeano, C. Y. Gorini, P. Labaume, D. Lajat, P. Patriat, B. Pinet, J. Ravat, F. Ricci Lucchi, and S. Vernassa, 1991, First deep seismic reflection transect from the Gulf of Lions to Sardinia (Ecors-Crop profiles in Western Mediterranean): Geodynamics Series, v. 22, p. 265–274.

Deng, H., J. Ren, X. Pang, P. F. Rey, K. R. McClay, I. M. Watkinson, J. Zheng, and P. Luo, 2020, South China Sea documents the transition from wide continental rift to continental break up: Nature Communications, v. 11, Article 4583.

Desmurs, L., G. Manatschal, and D. Bernoulli, 2001, The Steinmann Trinity revisited: Mantle exhumation and magmatism along an ocean-continent transition: the Platta nappe, eastern Switzerland, in R. C. L. Wilson, R. B. Whitmarsh, B. Taylor, and N. Froitzheim, eds., *Non-Volcanic Rifting of Continental Margins: A Comparison of Evidence from Land and Sea*: Geological Society, Special Publications, London, UK, v. 187, p. 235–266.

Desmurs, L., O. Müntener, and G. Manatschal, 2002, Onset of magmatic accretion within a magma-poor rifted margin: a case study from the Platta ocean-continent transition, eastern Switzerland: Contributions to Mineralogy and Petrology, v. 144, p. 365–382.

Detrick, R. S., J. G. Sclater, and J. Thiede, 1977, The subsidence of aseismic ridges: Earth and Planetary Science Letters, v. 34, p. 185–196.

Dewey, J. F., and J. L. Pindell, 1986, Reply to 'Comments on "Neogene block tectonics of eastern Turkey and northern South America: continental applications of the finite difference method"': Tectonics, v. 5, p. 703–705.

Diebold, J. B., P. L. Stoffa, P. Buhl, and M. Truchan, 1981, Venezuelan Basin crustal structure: Journal of Geophysical Research, v. 86, p. 7901–7923.

Diebold, J., N. Driscoll, EW-9501-Science Team, 1999, New insights on the formation of the Caribbean basalt province revealed by multichannel seismic images of volcanic structures in the Venezuelan Basin, in P. Mann, ed., *Caribbean Basins*: Elsevier Science, Amsterdam, The Netherlands, p. 561–589.

Donnelly, T. W., G. S. Horne, R. C. Finch, and E. Lopez-Ramos, 1990, Northern Central America; The Maya and Chortis blocks, in G. Dengo, and J. E. Case, eds., *The Geology of North America Vol H: The Caribbean Region*: GSA, Boulder, CO, p. 371–396.

Donnelly, T. W., W. Melson, R. Kay, and J. W. Rogers, 1973, Basalts and dolerites of late Cretaceous age from the central Caribbean, in *Initial Reports of the Deep Sea Drilling Project*: U.S. Government Printing Office, Washington, DC, p. 989–1011.

Doré, T., and E. Lundin, 2015, Research Focus: Hyperextended continental margins—Knowns and unknowns: Geology, v. 43, p. 95–96.

Draper, G., T. A. Jackson, and S. K. Donovan, 1994, Geologic provinces of the Caribbean region, in S. K. Donovan, and T. A. Jackson, eds., *Caribbean Geology: An Introduction*: UWIPA, Kingston, Jamaica, p. 3–12.

Driscoll, N. W., and J. B. Diebold, 1998, Deformation of the Caribbean region: One plate or two?: Geology, v. 26, p. 1043–1046.

Driscoll, N. W., and J. B. Diebold, 1999, Tectonic and stratigraphic development of the eastern Caribbean: New constraints from multichannel seismic data, in P. Mann, ed., *Caribbean Basins*: Elsevier Science, Amsterdam, The Netherlands, p. 591–626.

Droxler, A., J. W. Morse, K. S. Glaser, G. A. Haddad, and P. A. Baker, 1991, Surface sediment carbonate mineralogy and water column chemistry: Nicaragua Rise versus the Bahamas: Marine Geology, v. 100, p. 277–289.

Druet, M., A. Muñoz-Martín, J. L. Granja-Bruña, A. Carbó-Gorosabel, J. Acosta, P. Llanes, and G. Ercilla, 2018, Crustal structure and continent-ocean boundary along the Galicia continental margin (NW Iberia): Insights from combined gravity and seismic interpretation: Tectonics, v. 37, p. 1576–1604.

Dürkefälden, A., K. Hoernle, F. Hauff, J. A. Wartho, P. van den Bogaard, and R. Werner, 2019a, Age and geochemistry of the Beata Ridge: Primary formation during the main phase (~89 Ma) of the Caribbean Large Igneous Province: Lithos, v. 328–329, p. 69–87.

Dürkefälden, A., K. Hoernle, F. Hauff, R. Werner, and D. Garbe-Schönberg, 2019b, Second-stage Caribbean Large Igneous Province volcanism: The depleted icing on the enriched cake: Chemical Geology, v. 509, p. 45–63.

Edgar, N. T., J. I. Ewing, and J. Hennion, 1971, Seismic refraction and reflection in Caribbean Sea: AAPG Bulletin, v. 55, p. 833–870.

Edgar, T., J. Saunders, H. Bolli, R. Boyce, W. Broecker, T. Donnelly, J. Gieskes, W. Hay, R. Horowitz, F. Maurrasse, H. Pérez Nieto, W. Prell, and I. Premoli Silva, 1973, Initial reports of the Deep Sea Drilling Project, covering Leg 15 of the cruises of the drilling vessel Glomar Challenger, San Juan, Puerto Rico to Cristobal, Panama; December 1970-February 1971: US Government Printing Office, Washington, DC, 20 p.

Ehlers, B. M., and W. Jokat, 2009, Subsidence and crustal roughness of ultra-slow spreading ridges in the northern North Atlantic and the Arctic Ocean: Geophysical Journal International, v. 177, p. 451–462.

Eldholm, O., T. P. Gladczenko, J. Skogseid, and S. Planke, 2000, Atlantic volcanic margins: A comparative study, in A. Nøttvedt, ed., *Dynamics of the Norwegian Margin*: Geological Society, Special Publications, London, UK, v. 167, p. 411–428.

Eldholm, O., J. Thiede, and E. Taylor, 1989, Evolution of the Vøring volcanic margin, in O. Eldholm, J. Thiede, E. Taylor, et al., eds., *Proceedings of the Ocean Drilling Program, Scientific Results*: US Government Printing Office, Washington, DC, v. 104, p. 1033–1065.

Epin, M.-E., G. Manatschal, F. Sapin, and M. G. Rowan, 2021, The tectono-magmatic and subsidence evolution during lithospheric breakup in a salt-rich rifted margin: Insights from a 3D seismic survey from southern Gabon: Marine and Petroleum Geology, v. 128, Article 105005.

Erlich, R.N., T. Villamil, and J. Keens-Dumas, 2003, Controls on the depositional of Upper Cretaceous organic carbon-rich rocks from Coast Rica to Suriname, in C. Bartolini, R. T. Buffler, and J. F. Blickwede, eds., *The Circum-Gulf of Mexico and the Caribbean: Hydrocarbon Habitats, Basin Formation and Plate Tectonics*: AAPG Memoir, v. 79, p. 1–45.

Escalona, A., and P. Mann, 2011, Tectonics, basin subsidence mechanisms, and paleogeography of the Caribbean-South American plate boundary zone: Marine and Petroleum Geology, v. 28, p. 8–39.

Escuder-Viruete, J., A. Pérez-Estaún, F. Contreras, M. Joubert, D. Weis, T. D. Ullrich, and P. Spadea, 2007, Plume mantle source heterogeneity through time: Insights from the Duarte Complex, Hispaniola, northeastern Caribbean: Journal of Geophysical Research, Solid Earth, v. 112, p. 1–19.

Escuder-Viruete, J., M. Joubert, M. Abad, F. Pérez-Valera, and J. Gabites, 2016, The basaltic volcanism of the Dumisseau Formation in the Sierra de Bahoruco, SW Dominican Republic: A record of the mantle plume-related magmatism of the Caribbean Large Igneous Province: Lithos, v. 254–255, p. 67–83.

Escuder-Viruete, J., P. Valverde-Vaquero, Y. Rojas-Agramonte, J. Gabites, M. Castillo-Carrión, and A. Pérez-Estaún, 2013, Timing of deformational events in the Río San Juan complex: Implications for the tectonic controls on the exhumation of high-P rocks in the northern Caribbean subduction–accretionary prism: Lithos, v. 177, p. 416–435.

Evain, M., A. Alfilhado, C. Rigoti, A. Loureiro, D. Alves, F. Klingelhoefer, P. Schnurle, A. Feld, R. Fuck, J. Soares, M.V. de Lima, C. Corela, L. Matias, M. Benabdellouahed, A. Baltzer, M. Rabineau, A. Viana, M. Moulin, and D. Aslanian, 2015, Deep structure of the Santos Basin-São Paulo Plateau System, SE Brazil: Journal of Geophysical Research, Solid Earth, v. 120, p. 5401–5431.

Ewing, J. I., C. B. Officer, H. R. Johnson, and R. S. Edwards, 1957, Geophysical investigations in the eastern Caribbean: Trinidad Shelf, Tobago Trough, Barbados Ridge, Atlantic Ocean: GSA Bulletin, v. 68, p. 897–912.

Ewing, J. I., J. Antoine, and M. Ewing, 1960, Geophysical measurements in the western Caribbean and Gulf of Mexico: Journal of Geophysical Research, Solid Earth, v. 65, p. 4087–4126.

Ewing, M., and J. L. Worzel, 1954, Gravity anomalies and the structure of the West Indies, Part I: GSA Bulletin, v. 65, p. 165–174.

Fernandez, O., A. Olaiz, L. Cascone, P. Hernandez, A. de F. Pereira, J. Tritlla, M. Ingles, B. Aida, I. Pinto, R. Rocca, C. Sanders, A. Herrá, and N. Tur, 2020, Geophysical evidence for breakup volcanism in the Angola and Gabon passive margins: Marine and Petroleum Geology, v. 116, Article 104330.

Ferreira, T. S., 2009, Controle do embasamento no rifteamento das bacias de Camamu e Almada: Boletim de Geociências da Petrobrás, v. 17, p. 69–88.

Ferreira, T. S., 2018, The Jequitinhonha-Almada-Camamu rift system: An approach to the rifting evolution on the northeast Brazilian margin: Boletim de Geociências da Petrobras, v. 23, p. 1–31.

Ferreira, T. S., J. M. Caixeta, and C. A. Rigoti, 2011, The diachronous Aptian-Cenomanian rifting controlled by basement inheritance along the Brazilian northeastern margin: Gondwana 14 conference abstracts volume, Búzios, Brazil, p. 216.

Flament, N., M. Gurnis, R. D. Müller, 2013, A review of observations and models of dynamic topography: Lithosphere, v. 5, p. 189–210.

Flores, K. E., S. Skora, C. Martin, G. E. Harlow, D. Rodríguez, and P. O. Baumgartner, 2015, Metamorphic history of riebeckite- and aegirine-augite-bearing high-pressure-low-temperature blocks within the Siuna Serpentinite Mélange, northeastern Nicaragua: International Geology Review, v. 57, p. 943–977.

Fodor, R. V., and B. B. Hanan, 2000, Geochemical evidence for the Trindade hotspot trace: Columbia seamount ankaramite: Lithos, v. 51, p. 293–304.

Fox, P. J., and B. C. Heezen, 1985, Geology of the Caribbean crust, in A. E. M. Nairn, and F. G. Stehli, eds., *The Gulf of Mexico and Caribbean*: Plenum, New York, NY, p. 421–466.

Fox, P. J., E. S. Schreiber, and B. C. Heezen, 1971, The geology of the Caribbean crust: Tertiary sediments, granitic and basic rocks from the Aves Ridge: Tectonophysics, v. 12, p. 89–109.

Fox, P. J., W. F. Ruddiman, W. B. F. Bryan, and B. C. Heezen, 1970, The geology of the Caribbean crust, I: Beata Ridge: Tectonophysics, v. 10, p. 495–513.

França, R. L., A. C. Del Rey, C. V. Tagliari, J. R. Brandão, P. D. R. Fontanelli, 2007, Bacia do Espírito Santo: Boletim de Geociências da Petrobrás, v. 15, p. 501-509.

Frizon de Lamottea, D., P. Leturmy, Y. Missenarda, S. Khomsi, G. Ruiz, O. Saddiqi, F. Guillocheau, and A. Michard, 2009, Mesozoic and Cenozoic vertical movements in the Atlas system (Algeria, Morocco, Tunisia): An overview: Tectonophysics, v. 475, p. 9–28.

Frost, B. R., 2018, Reconstructing the early depositional history of a failed ocean basin from a large 3-d dataset acquired in the Colombia Basin, Western Caribbean Sea, Offshore Colombia: AAPG ACE abstracts, Salt Lake City, UT.

Gailler, A., F. Klingelhoefer, J.-L. Olivet, and D. Aslanian, 2009, Crustal structure of a young margin pair: New results across the Liguro–Provencal Basin from wide-angle seismic tomography: Earth and Planetary Science Letters, v. 286, p. 333–345.

GEBCO, GEBCO Compilation Group, 2021, GEBCO 2021 Grid, https://www.gebco.net/

Geoffroy, L., 2005, Volcanic passive margins: Comptes Rendus Geoscience, v. 337, p. 1395–1408.

Gernigon, L., A. Blischke, A. Nasuti, and M. Sand, 2015, Conjugate volcanic rifted margins, seafloor spreading, and microcontinent: Insights from new high-resolution aeromagnetic surveys in the Norway Basin: Tectonics, v. 34, p. 907–933.

Ghosh, N., 1990, Magnetic anomaly studies of the Colombian basin area and gravity field study of the southeastern Caribbean plate boundary zone: PhD dissertation, University of Houston, Houston, TX, 375 p.

Gillard, M., J. Autin, G. Manatschal, D. Sauter, M. Munschy, and M. Schaming, 2015, Tectonomagmatic evolution of the final stages of rifting along the deep conjugate Australian-Antarctic magma-poor rifted margins: Constraints from seismic observations: Tectonics, v. 34, p. 753–783.

Goff, J. A., 1991, A global and regional stochastic analysis of near-ridge abyssal hill morphology: Journal of Geophysical Research, Solid Earth, v. 96, p. 21713–21737.

Goff, J. A., 1992, Quantitative characterization of abyssal hill morphology along flow lines in the Atlantic Ocean: Journal of Geophysical Research, Solid Earth, v. 97, p. 9183–9202.

Goff, J. A., B. E. Tucholke, J. Lin, G. E. Jaroslow, and M. C. Kleinrock, 1995, Quantitative analysis of abyssal hills in the Atlantic Ocean: A correlation between inferred crustal thickness and extensional faulting: Journal of Geophysical Research, Solid Earth, v. 100, p. 22509–22522.

Gomez, S., 2018, Tectonostratigraphic evolution of the Barbados accretionary prism and surrounding sedimentary basins within the southeastern Caribbean-South America plate boundary zone: PhD dissertation, University of Houston, Houston, TX, 233 p.

Gomez, S., D. Bird, and P. Mann, 2018, Deep crustal structure and tectonic origin of the Tobago-Barbados Ridge: Interpretation, v. 6, p. 1–49.

Gómez-García, Á.M., C. Meeßen, M. Scheck-Wenderoth, J. Monsalve, G. Bott, A. Bernhardt, and G. Bernal, 2019, 3-D modeling of vertical gravity gradients and the delimitation of tectonic boundaries: the Caribbean oceanic domain as a case study: Geochemistry, Geophysics, Geosystems, v. 20, p. 5371–5393.

Gonçalves, F. T. T., R. P. Bedregal, L. F. C. Coutinho, and M. R. Mello, 2000, Petroleum system of the Camamu–Almada Basin: a quantitative modeling approach, in M. R. Mello and B. J. Katz, eds., *Petroleum systems of South Atlantic margins*: AAPG, Tulsa, OK, v. 73, p. 257–271.

Gontijo, G. A., P. S. Milhomem, J. M. Caixeta, I. S. S. Dupuy, and P. E. L. Menezes, 2007, Bacia de Almada: Boletim de Geociências da Petrobrás, v. 15, p. 463–473.

Gordon, A. C., 2011. Arquitetura crustal da Bacia de Almada no contexto das bacias da margem leste da América do Sul: PhD dissertation, Universidade do Estado de Rio de Janeiro, Rio de Janeiro, Brazil, 335 p.

Gordon, A. C., W. U. Mohriak, and V. C. F. Barbosa, 2013, Crustal architecture of the Almada basin, northeastern Brazil: An example of a non-volcanic rift segment of the South Atlantic passive margin, in W. U. Mohriak, A. Danforth, P. J. Post, et al., eds., *Conjugate Divergent Margins*: Geological Society, Special Publications, London, UK, v. 369, p. 215–234.

Gordon, M. B., and W. R. Muehlberger, 1994, Rotation of the Chortís block causes dextral slip on the Guayape fault: Tectonics, v. 13, p. 858–872.

Gose, W. A., 1983, Late Cretaceous-Early Tertiary tectonic history of southern Central America: Journal of Geophysical Research: Solid Earth, v. 88, p. 10585–10592.

Granot, R., and J. Dyment, 2015, The Cretaceous opening of the South Atlantic Ocean: Earth and Planetary Science Letters, v. 414, p 156–163.

Gray, D. R., D. A. Foster, J. G. Meert, B. D. Goscombe, R. Armstrong, R. A. J. Trouw, and C. W. Passchier, 2008, A Damara orogen perspective on the assembly of southwestern Gondwana, in R. J. Pankhurst, R. A. J. Trouw, B. B. de Brito Neves, and M. J. de Wit, eds., *West Gondwana: Pre-Cenozoic Correlations Across the South Atlantic Region*: Geological Society, Special Publications, London, UK, v. 294, p. 257–278.

Gueguen, E., C. Doglioni, and M. Fernandez, 1998, On the post-25 Ma geodynamic evolution of the western Mediterranean: Tectonophysics, v. 298, p. 259–269.

Hastie, A. R., A. C. Kerr, S. F. Mitchell, and I. L. Millar, 2008, Geochemistry and petrogenesis of Cretaceous oceanic plateau lavas in eastern Jamaica: Lithos, v. 101, p. 323–343.

Hastie, A. R., A. C. Kerr, S. F. Mitchell, and I. L. Millar, 2009, Geochemistry and tectonomagmatic significance of Lower Cretaceous island arc lavas from the Devils Racecourse Formation, eastern Jamaica, in K. H. James, M. A. Lorente, and J. L. Pindell, eds., *The Origin and Evolution of the Caribbean Plate*: Geological Society, London, Special Publication, v. 328, p. 339–360.

Hastie, A. R., and A. C. Kerr, 2010, Mantle plume or slab window? Physical and geochemical constraints on the origin of the Caribbean oceanic plateau: Earth-Science Reviews, v. 98, p. 283–293.

Hauff, F., K. Hoernle, P. van den Bogaard, G. Alvarado, and D. Garbe-Schönberg, 2000, Age and geochemistry of basaltic complexes in western Costa Rica: Contributions to the geotectonic evolution of Central America: Geochemistry, Geophysics, Geosystems, v. 1, Article 1009.

Hill, R., and C. Schenk, 2005, Petroleum geochemistry of oil and gas from Barbados: implications for distribution of Cretaceous source rocks and regional petroleum prospectivity: Marine and Petroleum Geology, v. 22, p. 917–943.

Hinz, K., 1981, A hypothesis on terrestrial catastrophies wedges of very thick oceanward dipping layers beneath passive continental margins: Their origin and paleoenvironmental significance: Geologisches Jahrbuch. Reihe E, Geophysik, v. 22, p. 3-28.

Hoggard, M. J., J. Winterbourne, K. Czarnota, and N. White, 2017, Oceanic residual depth measurements, the plate cooling model, and global dynamic topography: Journal of Geophysical Research, Solid Earth, v. 122, p. 2328–2372.

Holcombe, T. L., J. W. Ladd, G. Westbrook, N. T. Edgar, and C. L. Bowland, 1990, Caribbean marine geology: Ridges and basins of the plate interior, in G. Dengo, and J. E. Case, eds., *The Geology of North America Vol H: The Caribbean Region*: GSA, Boulder, CO, p. 231–260.

Hopper, J. R., T. Funck, B. E. Tucholke, H. C. Larsen, W. S. Holbrook, K. E. Louden, D. Shillington, and H. Lau, 2004, Continental breakup and the onset of ultraslow seafloor spreading off Flemish Cap on the Newfoundland rifted margin: Geology, v. 32, p. 93–96.

Houtz, R. E., and W. J. Ludwig, 1977, Structure of Colombia Basin, Caribbean Sea, from profiler-sonobuoy measurements: Journal of Geophysical Research, v. 82, p. 4861–4867.

Howell, D. G., 1985, Terranes: Scientific American, v. 253, p. 116–125.

Hudec, M. R., and M. P. Jackson, 2007, Terra infirma: Understanding salt tectonics: Earth-Science Reviews, v. 82, p. 1–28.

Huismans, R. S., and C. Beaumont, 2014, Rifted continental margins: The case for depth-dependent extension: Earth and Planetary Science Letters, v. 407, p. 148–162.

Ito, G., and P. D. Clift, 1998, Subsidence and growth of Pacific Cretaceous plateaus: Earth and Planetary Science Letters, v. 161, p. 85–100.

Jagoutz, O., O. Müntener, G. Manatschal, D. Rubatto, G. Péron-Pinvidic, B. D. Turrin, and I. M. Villa, 2007, The rift-to-drift transition in the North Atlantic: A stuttering start of the MORB machine?: Geology, v. 35, p. 1087–1090.

Japsen, P., and J. A. Chalmers, 2000, Neogene uplift and tectonics around the North Atlantic: Overview: Global and Planetary Change, v. 24, p. 165–173.

Japsen, P., J. M. Bonow, P. F. Green, P. R. Cobbold, D. Chiossi, R. Lilletveit, L. P. Magnavita, and A. Pedreira, 2012, Episodic burial and exhumation in NE Brazil after opening of the South Atlantic: GSA Bulletin, v. 124, p. 800–816.

Jha, S., D. L. Harry, and D. L. Schutt, 2017, Toolbox for Analysis of Flexural Isostasy (TAFI)—A MATLAB toolbox for modeling flexural deformation of the lithosphere: Geosphere, v. 13, p. 1555–1565.

Jolivet, L., C. Gorini, J. Smit, and S. Leroy, 2015, Continental breakup and the dynamics of rifting in back-arc basins: The Gulf of Lion margin: Tectonics, v. 34, p. 662–679.

Katz, B., and K. Williams, 2003, Biogenic gas potential offshore Guajira peninsula, Colombia, in C. Bartolini, R. T. Buffler, and J. F. Blickwede, eds., *The Circum-Gulf of Mexico and the Caribbean: Hydrocarbon Habitats, Basin Formation and Plate Tectonics*: AAPG Memoir, v. 79, p. 961–968.

Kearey, P., 1974, Gravity and seismic reflection investigations into the crustal structure of the Aves Ridge, eastern Caribbean: Geophysical Journal of the Royal Astronomical Society, v. 38, p. 435–448.

Kelemen, P. B., and W. S. Holbrook, 1995, Origin of thick, high-velocity igneous crust along the U.S. East Coast Margin: Journal of Geophysical Research, Solid Earth, v. 100, p. 10077–10094.

Kerr, A. C., J. Tarney, A. Nivia, G. F. Marriner, and A. D. Saunders, 1998, The internal structure of oceanic plateaus: Inferences from obducted Cretaceous terranes in western Colombia and the Caribbean: Tectonophysics, v. 292, p. 173–188.

Kerr, A. C., M. A. Iturralde-Vinent, A. D. Saunders, T. L. Babbs, and J. Tarney, 1999, A new plate tectonic model of the Caribbean: Implications from a geochemical reconnaissance of Cuban Mesozoic volcanic rocks: GSA Bulletin, v. 111, p. 1581–1599.

Kerr, A. C., J. Tarney, G. F. Marriner, A. Nivia, and A. D. Saunders, 1997, The Caribbean-Colombian Cretaceous Igneous Province: the internal anatomy of an oceanic plateau, in J. J. Mahoney, and M. F. Coffin, eds., *Large Igneous Provinces: Continental, Oceanic, and Planetary Flood Volcanism*: Geophysical Monograph Series, AGU, Washington, DC, v. 100, p. 123–144.

Kerr, A.C., R. V. White, P. M. E. Thompson, J. Tarney, and A. D. Saunders, 2003, No oceanic plateau-no Caribbean Plate? The seminal role of an oceanic plateau in Caribbean Plate Evolution, in C. Bartolini, R. T. Buffler, and J. F. Blickwede, eds., *The Circum-Gulf of*

Mexico and the Caribbean: Hydrocarbon Habitats, Basin Formation and Plate Tectonics: AAPG Memoir, v. 79, p. 126–168.

Klingelhoefer, F., M. Evain, A. Afilhado, C. Rigoti, A. Loureiro, D. Alves, A. Leprêtre, M. Moulin, P. Schnurle, M. Benabdellouahed, A. Baltzer, M. Rabineau, A. Feld, A. Viana, and D. Aslanian, 2015, Imaging proto-oceanic crust off the Brazilian continental margin: Geophysical Journal International, v. 200, p. 471–488.

Klingelhöfer, F., L. Géli, L. Matias, N. Steinsland, and J. Mohr, 2000, Crustal structure of a super-slow spreading centre: a seismic refraction study of Mohns Ridge, 72° N: Geophysical Journal International, v. 141, p. 509–526.

Korenaga, J., W. S. Holbrook, G. M. Kent, P. B. Kelemen, R. S. Detrick, H.-C. Larsen, J. R. Hopper, and T. Dahl-Jensen, 2000, Crustal structure of the southeast Greenland margin from joint refraction and reflection seismic tomography: Journal of Geophysical Research, Solid Earth, v. 105, p. 21591–21614.

Kroehler, M. E., P. Mann, A. Escalona, and G. L. Christeson, 2011, Late Cretaceous-Miocene diachronous onset of back thrusting along the South Caribbean deformed belt and its importance for understanding processes of arc collision and crustal growth: Tectonics, v. 30, Article TC6003.

Kumar, N., A. Danforth, P. Nuttall, J. Helwig, D. E. Bird, and S. Venkatraman, 2012, From oceanic crust to exhumed mantle: a 40-year (1970–2010) perspective on the nature of crust under the Santos Basin, SE Brazil, in W. U. Mohriak, A. Danforth, P. J. Post, et al., eds., *Conjugate Divergent Margins*: Geological Society, Special Publications, London, UK, v. 369, p. 147–165.

Kusznir, N. J., and G. D. Karner, 2007, Continental lithospheric thinning and breakup in response to upwelling divergent mantle flow: application to the Woodlark, Newfoundland and Iberia margins, in M. Reolid, L. V. Duarte, E. Mattioli, and W. Ruebsam, eds., *Carbon Cycle and Ecosystem Response to the Jenkyns Event in the Early Toarcian (Jurassic)*: Geological Society, Special Publications, London, UK, v. 282, p. 389–419.

Ladd, J. W., J. L. Worzel, and J. S. Watkins, 1977, Multi-fold seismic reflection records from the Northern Venezuelan Basin and the north slope of the Muertos Trench, in M. Talwani, and W. C. Pittman III, eds., *Island Arcs, Deep Sea Trenches and Back-Arc Basins, Volume 1: Maurice Ewing Series*: AGU, Washington, DC, p. 41–56.

Ladd, J. W., T. C. Shih, and C. J. Tsai, 1981, Cenozoic tectonics of central Hispaniola and adjacent Caribbean Sea: AAPG Bulletin, v. 65, no. 3, p. 466–489.

Lapierre, H. et al., 2000, Multiple plume events in the genesis of the peri-Caribbean Cretaceous oceanic plateau province: Journal of Geophysical Research, Solid Earth, v. 105, p. 8403–8421.

Larue, D. K., and A. J. Warner, 1991, Sedimentary basins of the NE Caribbean plate boundary zone and their petroleum potential: Journal of Petroleum Geology, v. 14, p. 275–290.

Laske, G., G. Masters., Z. Ma, and M. Pasyanos, 2013, Update on CRUST1.0 - A 1-degree global model of Earth's crust, EGU General Assembly, Geophysical Research Abstracts, Article EGU2013-2658.

Le Douaran, S., J. Burrus, and F. Avedik, 1984, Deep structure of the north-western Mediterranean Basin: Results of a two-ship seismic survey: Marine Geology, v. 55, p. 325–345.

Leprêtre, R., J. Barbarand, Y. Missenard, F. Leparmentier, and D. Frizon De Lamotte, 2014, Vertical movements along the northern border of the West African Craton: The Reguibat Shield and adjacent basins: Geological Magazine, v. 151, p. 885–898.

Leroy, S., A. Mauffret, P. Patriat, and B. M. de Lepinay, 2000, An alternative interpretation of the Cayman trough evolution from a reidentification of magnetic anomalies: Geophysical Journal International, v. 141, p. 539–557.

Leroy, S., B. M. Delepinay, A. Mauffret, and M. Pubellier, 1996, Structural and tectonic evolution of the eastern Cayman Trough (Caribbean Sea) from seismic reflection data: AAPG Bulletin, v. 80, p. 222–247.

Lewis, J. F., G. Kysar Mattietti, M. Perfit, and G. Kamenov, 2011, Geochemistry and petrology of three granitoid rock cores from the Nicaraguan rise, Caribbean Sea: Implications for its composition, structure and tectonic evolution: Geologica Acta, v. 9, p. 467–479.

Lidiak, E. G., and T. H. Anderson, 2015, Evolution of the Caribbean plate and origin of the Gulf of Mexico in light of plate motions accommodated by strike-slip faulting, in T. H. Anderson, A. N. Didenko, C. L. Johnson, et al., eds., *Late Jurassic Margin of Laurasia–A Record of Faulting Accommodating Plate Rotation*: GSA Special Papers, Boulder, CO, v. 513, p. 1–88.

Loureiro, A., P. Schnürle, F. Klingelhöfer, A. Afilhadoac, J. Pinheiro, M. Evain, F. Gallais, N. A. Dias, M. Rabineau, A. Baltzere, M. Benabdellouahed, J. Soares, R. Fuck, J. A. Cupertino, A. Viana, L. Matias M. Moulin, and D. Aslanian, 2018, Imaging exhumed lower continental crust in the distal Jequitinhonha basin, Brazil: Journal of South American Earth Sciences, v. 84, p. 351–372.

Lu, R. S., and K. J. McMillen, 1982, Multichannel seismic survey of the Colombia Basin and adjacent margins in J. S. Watkins, and C. L. Drake, eds., *Studies in Continental Margin Geology Vol 34*: AAPG, Tulsa, OK, p. 395–410.

Lucazeau, F., 2019, Analysis and mapping of an updated terrestrial heat flow data set: Geochemistry, Geophysics, Geosystems, v. 20, p. 4001–4024.

Ludwig, W., R. Houtz, and J. Ewing, 1975, Profile-sonobuoy measurements in the Colombian and Venezuelan Basins, Caribbean Sea: AAPG Bulletin, v. 59, p. 115–123.

Lundin, E. R., and A. G. Doré, 2011, Hyperextension, serpentinization, and weakening: A new paradigm for rifted margin compressional deformation: Geology, v. 39, p. 347–350.

Magnavita, L. P., I. Davison, and N. J. Kusznir, 1994, Rifting, erosion, and uplift history of the Recôncavo-Tucano-Jatobá Rift, northeast Brazil: Tectonics, v. 13, p. 367–388.

Malinverno, A., 1991, Inverse square-root dependence of mid-ocean-ridge flank roughness on spreading rate: Nature, v. 352, p. 58–60.

Manatschal, G., D. Sauter, A. M. Karpoff, E. Masini, G. Mohn, and Y. Lagabrielle, 2011, The Chenaillet Ophiolite in the French/Italian Alps: An ancient analogue for an oceanic core complex?: Lithos, v. 124, p. 169–184.

Mann, P., R. Rogers, and L. Gahagan, 2006, Overview of plate tectonic history and its unresolved tectonic problems, in J. Bundschuh, and G. E. Alvarado, eds., *Central America: Geology, Resources and Hazards*: Taylor and Francis, Leiden, The Netherlands, p. 201–237.

Mann, P., Taylor, F. W., Lawrence, R. and Ku, T., P., 1995, Actively evolving microplate formation by oblique collision and sideways motion along strike-slip faults: An example from the northeastern Caribbean plate margin: Tectonophysics, v. 246, p. 1–69.

Marotta, A. M., and F. Mongelli, 1998, Flexure of subducted slabs: Geophysical Journal International, v. 132, p. 701–711.

Matos, R. D. D., 2000, Tectonic evolution of the Equatorial South Atlantic, in W. U. Mohriak and M. Talwani, eds., *Atlantic Rifts and Continental Margins*: Geophysical Monograph Series, AGU, Washington, DC, v. 115, p. 331–354.

Mauffret, A. and S. Leroy, 1997, Seismic stratigraphy and structure of the Caribbean igneous province: Tectonophysics, v. 283, p. 61–104.

McCarthy, A., T. J. Falloon, I. Sauermilch, J. M. Whittaker, K. Niida, and D. H. Green, 2020, Revisiting the Australian-Antarctic ocean-continent transition zone using petrological and geophysical characterization of exhumed subcontinental mantle: Geochemistry, Geophysics, Geosystems, v. 21, Article e2020GC009040.

McDermott, C., L. Lonergan, J. S. Collier, K. G. McDermott, and P. Bellingham, 2018, Characterization of seaward-dipping reflectors along the South American Atlantic margin and implications for continental breakup: Tectonics, v. 37, p. 3303–3327.

McKenzie, D., 1978, Some remarks on the development of sedimentary basins: Earth and Planetary Science Letters, v. 40, p. 25–32.

Mégard, F., 1984, The Andean orogenic period and its major structures in central and northern Peru: Journal of the Geological Society, v. 141, p. 893.

Merrill, R. K., and C. A. Sternbach, 2017, Concepts, Technology, Price, and Access Drive Giant Field Discoveries, R. K. Merrill, and C. A. Sternbach, eds., *Giant Fields of the Decade 2000–2010*: AAPG Memoir, AAPG, Tulsa, OK, v. 113, p. 1.

Meyer, B., A. Chulliat, and R. Saltus, 2017, Derivation and error analysis of the Earth magnetic anomaly grid at 2 arc min resolution version 3 (EMAG2v3): Geochemistry, Geophysics, Geosystems, v. 18, p. 4522–4537.

Milani, E. J., and I. Davison, 1988, Basement control and transfer tectonics in the Recôncavo-Tucano-Jatobá rift, Northeast Brazil: Tectonophysics, v. 154, p. 41–70.

Milani, E. J., H. D. Rangel, G. V. Bueno, J. M. Stica, W. R. Winter, J. M. Caixeta, and O. D. C. P. Neto, 2007, Bacias sedimentares brasileiras - Cartas estratigráficas: Boletim de Geociências da Petrobrás, v. 15, p. 183–205.

Minshull, T. A., 1999, On the roughness of Mesozoic oceanic crust in the western North Atlantic: Geophysical Journal International, v. 136, p. 286–290.

Mitchell, S. F., 2003, Sedimentology and tectonic evolution of the cretaceous rocks of central Jamaica: relationships to the plate tectonic evolution of the Caribbean, in C. Bartolini, R. T. Buffler, and J. F. Blickwede, eds., *The Circum-Gulf of Mexico and the Caribbean: Hydrocarbon Habitats, Basin Formation and Plate Tectonics*: AAPG Memoir, v. 79, p. 605–623.

Mohn, G., G. Manatschal, O. Müntener, M. Beltrando, and E. Masini, 2010, Unravelling the interaction between tectonic and sedimentary processes during lithospheric thinning in the Alpine Tethys margins: International Journal of Earth Sciences, v. 99, p. 75–101.

Mohriak, W. U., 2005, Interpretação geológica e geofísica da Bacia do Espírito Santo e da região de Abrolhos: petrografia, datação radiométrica e visualização sísmica das rochas vulcânicas: Boletim de Geociências da Petrobrás, v. 14, p. 133–142.

Mohriak, W. U., M. Bassetto, and I. S. Vieira, 1998, Crustal architecture and tectonic evolution of the Sergipe-Alagoas and Jacuípe basins, offshore northeastern Brazil: Tectonophysics, v. 288, p. 199–220.

Mohriak, W., M. Nemčok, and G. Enciso, 2008, South Atlantic divergent margin evolution: Rift-border uplift and salt tectonics in the basins of SE Brazil, in R. J. Pankhurst, R. A. J. Trouw, B. B. de Brito Neves, and M. J. de Wit, eds., *West Gondwana: Pre-Cenozoic*

Correlations Across the South Atlantic Region: Geological Society Special Publication, v. 294, p. 365–398.

Molina-Garza, R. S., D. J. J. van Hinsbergen, L. M. Boschman, R. D. Rogers, and M. Ganerød, 2019, Large-scale rotations of the Chortis Block (Honduras) at the southern termination of the Laramide flat slab: Tectonophysics, v. 760, p. 36–57.

Moonan, X., M. Ramadhar, and T. Needham, 2018, Structural restoration of the Jasmine Complex and implications for Pleistocene depositional environment within the Paria sub-basin: Search and Discovery Article, v. 11088, p. 1–33.

Mooney, W. D., G. Laske, and T. G. Masters, 1998, CRUST 5.1: A global crustal model at 5× 5: Journal of Geophysical Research, Solid Earth, v. 103, p. 727–747.

Mortimer, E. J., M. Gouiza, D. A. Paton, R. Stanca, K. Rodriguez, N. Hodgson, and A. A. Hussein, 2020, Architecture of a magma poor passive margin – Insights from the Somali margin: Marine Geology, v. 428, Article 106269.

Muller, M. R., C. J. Robinson, T. A. Minshull, R. S. White, and M. J. Bickle, 1997, Thin crust beneath ocean drilling program borehole 735B at the Southwest Indian Ridge?: Earth and Planetary Science Letters, v. 148, p. 93–107.

Müller, R.D., M. Seton, S. Zahirovic, S. E. Williams, K. J. Matthews, N. M. Wright, G. E. Shephard, K. T. Maloney, N. Barnett-Moore, M. Hosseinpour, D. J. Bower, and J. Cannon, 2016, Ocean basin evolution and global-scale plate reorganization events since Pangea breakup: Annual Review of Earth and Planetary Sciences, v. 44, p. 107-138.

Müntener, O., and J. Hermann, 1996, The Val Malenco lower crust–upper mantle complex and its field relations (Italian Alps): Schweizerische Mineralogische und Petrographische Mitteilungen, v. 76, p. 475–500.

Mutter, J. C., M. Talwani, and P. L. Stoffa, 1982, Origin of seaward-dipping reflectors in oceanic crust off the Norwegian margin by “subaerial sea-floor spreading”: Geology, v. 10, p. 353–357.

Mutter, J. C., W. R. Buck, and C. M. Zehnder, 1988, Convective partial melting: 1. A model for the formation of thick basaltic sequences during the initiation of spreading: Journal of Geophysical Research, Solid Earth, v. 93, p. 1031–1048.

Nagle, F., J. J. Stipp, and D. E. Fisher, 1976, K–Ar geochronology of the Limestone Caribbees and Martinique, Lesser Antilles, West Indies: Earth and Planetary Science Letters, v. 29, p. 401–412.

Neill, I., A. C. Kerr, A. R. Hastie, J. L. Pindell, and I. L. Millar, 2013, The Albian-Turonian island arc rocks of Tobago, West Indies: Geochemistry, petrogenesis, and Caribbean plate tectonics: Journal of Petrology, v. 54, p. 1607–1639.

Neill, I., A. C. Kerr, A. R. Hastie, K. P. Stanek, and I. L. Millar, 2011, Origin of the Aves Ridge and Dutch–Venezuelan Antilles: interaction of the Cretaceous 'Great Arc' and Caribbean–Colombian Oceanic Plateau?: Journal of the Geological Society, v. 168, p. 333–348.

Nemčok, M., S. T. Sinha, C. J. Stuart, C. Welker, M. Choudhuri, S. P. Sharma, A. A. Misra, N. Sinha, and S. Venkatraman, 2012, East Indian margin evolution and crustal architecture: Integration of deep reflection seismic interpretation and gravity modeling, in W. U. Mohriak, A. Danforth, P. J. Post, et al., eds., *Conjugate Divergent Margins*: Geological Society, Special Publications, London, UK, v. 369, p. 477–496.

Netto, A. S. T., 1978, A implantação da fase rift na Bacia do Recôncavo: Congresso Brasileiro de Geologia extended abstracts, São Paulo, Brazil, p. 506–517.

Netto, A. S. T., and J. J. O. Oliveira, 1985, Preenchimento do rift-valley na Bacia do Recôncavo: Revista Brasileira de Geociências, v. 15, p. 97–102.

Netto, A. S. T., J. R. Wanderley, and F. J. Feijó, 1994, Bacias de Jacuípe, Camamu e Almada: Boletim de Geociências da Petrobrás, v. 8, p. 173–184.

Neumann, G. A., and D. W. Forsyth, 1995, High resolution statistical estimation of seafloor morphology: Oblique and orthogonal fabric on the flanks of the Mid-Atlantic Ridge, 34°–35.5° S: Marine Geophysical Researches, v. 17, p. 221–250.

Nunes, O., and M. Holz, 2019, Tectonic and stratigraphic evolution of southern Jacuípe Basin (Brazil) based on seismic sequence stratigraphy: Journal of South American Earth Sciences, v. 96, Article 102370.

Odegard, M. E., W. G. Dickson, B. R. Rosendahl, R. E. Weger, 2002, Proto-oceanic crust in the North and South Atlantic: Types, characteristics, emplacement mechanisms, and its influence on deep and ultra-deep water exploration: AAPG Hedberg conference abstracts volume, Stavanger, Norway.

Officer, C. B., M. Ewing, and P. C. Wuenschel, 1952, Seismic refraction measurements in the Atlantic Ocean. Part IV: Bermuda, Bermuda Rise, and Nares Basin: GSA Bulletin, v. 63, p. 777–808.

Officer, C., J. Ewing, J. Hennion, D. Harkinder, and D. Miller, 1959, Geophysical investigations in the eastern Caribbean - summary of the 1955 and 1956 cruises: Physics and Chemistry of the Earth, v. 3, p. 17–26.

Ott, B. M., 2015, Cretaceous-Cenozoic tectonostratigraphic evolution of the Nicaraguan Rise based on seismic reflection, wells, and potential fields data: PhD dissertation, University of Houston, Houston, TX, 245 p.

Palumbo, F., I. G. Main, and G. Zito, 1999, The thermal evolution of sedimentary basins and its effect on the maturation of hydrocarbons: Geophysical Journal International, v. 139, p. 248–260.

Parker, R. L., 1973, The rapid calculation of potential anomalies: Geophysical Journal of the Royal Astronomical Society, v. 31, p. 447–455.

Parsons, B., and J. G. Sclater, 1977, An analysis of the variation of ocean floor bathymetry and heat flow with age: Journal of Geophysical Research, v. 82, p. 803–827.

Paton, D. A., J. Pindell, K. McDermott, P. Bellingham, and B. Horn, 2017, Evolution of seaward-dipping reflectors at the onset of oceanic crust formation at volcanic passive margins: Insights from the South Atlantic: Geology, v. 45, p. 439–442.1

Perfit, M. R., 1977, Petrology and geochemistry of mafic rocks from the Cayman Trench: Evidence for spreading: Geology, v. 5, p. 105-110.

Perfit, M. R., B. C. Heezen, M. Rawson, and T. W. Donnelly, 1980, Chemistry, origin and tectonic significance of metamorphic rocks from the Puerto Rico Trench: Marine Geology, v. 34, p. 125-156.

Perfit, M., 2018, Earth's oceanic crust, in W. M. White, ed., *Encyclopedia of Geochemistry: A Comprehensive Reference Source on the Chemistry of the Earth*: Springer International Publishing, Berlin, Germany, p. 430–439.

Péron-Pinvidic, G., and G. Manatschal, 2010, From microcontinents to extensional allochthons: Witnesses of how continents rift and break apart?: Petroleum Geoscience, v. 16, p. 189–197.

Péron-Pinvidic, G., G. Manatschal, and P. T. Osmundsen, 2013, Structural comparison of archetypal Atlantic rifted margins: A review of observations and concepts: Marine and Petroleum Geology, v. 43, p. 21–47.

Péron-Pinvidic, G., G. Manatschal, and the "IMAGinING RIFTING" Workshop Participants, 2019, Rifted margins: state of the art and future challenges: Frontiers in Earth Science, v. 7, p. 1–8.

Péron-Pinvidic, G., G. Manatschal, E. Masini, E. Sutra, J. M. Flament, I. Haupert, and P. Unternehr, 2017, Unravelling the along-strike variability of the Angola-Gabon rifted margin: A mapping approach, in T. S. Ceraldi, R. A. Hodgkinson, and G. Backe, eds., *Petroleum*

Geoscience of the West Africa Margin: Geological Society, Special Publications, London, UK, v. 438, p. 49–76.

Pfiffner, O. A., and L. Gonzalez, 2013, Mesozoic–Cenozoic evolution of the western margin of South America: Case study of the Peruvian Andes, in D. A. Foster, ed., *Continental Accretion and Evolution*: Geosciences, Basel, Switzerland, v. 3, p. 262–310.

Piccardo, G. B., E. Rampone, and R. Vannucci, 1990, Upper mantle evolution during continental rifting and ocean formation: Evidences from peridotite bodies of the western Alpine-northern Apennine system: Mémoires de la Société Géologique de France, v. 156, p. 323–333.

Pindell, J. and J. F. Dewey, 1982, Permo-Triassic reconstruction of western Pangea and the evolution of the Gulf of Mexico/Caribbean region: Tectonics, v. 1, p. 179–211.

Pindell, J. L., 1990, Geological arguments suggesting a Pacific origin for the Caribbean Plate, in Larue, D.K. and Draper, G., eds, *Transactions of the 12th Caribbean Geologic Conference St Croix*, *7–11 August 1989*: Miami Geological Society, Miami, FL, p. 1–4.

Pindell, J. L., and L. Kennan, 2009, Tectonic evolution of the Gulf of Mexico, Caribbean and northern South America in the mantle reference frame: An update, in K. H. James, M. A. Lorente, and J. L. Pindell, eds., *The Origin and Evolution of the Caribbean Plate*: Geological Society, Special Publications, London, UK, v. 328, p. 1–55.

Pindell, J., L. Kennan, K. P. Stanek, W. V. Maresch, and G. Draper, 2006, Foundations of Gulf of Mexico and Caribbean evolution: eight controversies resolved: Geologica Acta, v. 4, p. 303–341.

Pindell, J.L., S. C. Cande, W. C. Pitman, D. B. Rowley, J. F. Dewey, J. Labrecque, and W. Haxby, 1988, A plate-kinematic framework for models of Caribbean evolution: Tectonophysics, v. 155, p. 121–138.

Pinet, B., D. Lajat, P. LeQuellec, and P. Bouysse, 1985, Structure of Aves Ridge and Grenada Basin from multichannel seismic data, in A. Mascle, ed., *Symposium Geodynamique des Caraibes*: Technip, Paris, France, p. 53–64.

Pressling, N., A. Morris, B. E. John, and C. J. MacLeod, 2012, The internal structure of an oceanic core complex: An integrated analysis of oriented borehole imagery from IODP Hole U1309D (Atlantis Massif): Geochemistry, Geophysics, Geosystems, v. 13, Article Q04G10.

Punnette, S. and P. Mann, 2021, Subsurface structure of the Hinge Line fault zone and its control on the distribution of gas fields of the North Coast Marine Area (NCMA) of offshore, northern Trinidad: AAPG Memoir, v. 123, p. 357-386.

Quirk, D. G., A. Shakerley, and M. J. Howe, 2014, A mechanism for construction of volcanic rifted margins during continental breakup: Geology, v. 42, p. 1079–1082.

Rabinowitz, P. D., and J. LaBrecque, 1979, The Mesozoic South Atlantic Ocean and evolution of its continental margins: Journal of Geophysical Research, Solid Earth, v. 84, p. 5973–6002.

Ramos, E. L., 1975, Geological summary of the Yucatan Peninsula, in A. E. M. Nairn, and F. G. Stehli, eds., *The Gulf of Mexico and the Caribbean*: Springer, Boston, MA, p. 257–282.

Rampone, E., A. W. Hofmann, G. B. Piccardo, R. Vannucci, P. Bottazzi, and L. Ottolini, 1995, Petrology, mineral and isotope geochemistry of the external Liguride peridotites (Northern Apennines, Italy): Journal of Petrology, v. 36, p. 81–105.

Ramsay, A.T.S., J.W. Finch, 1973, Fluctuations in the past rates of carbonate solution in site 149: a comparison with other ocean basins and an interpretation of their significance, in *Initial Reports of the Deep Sea Drilling Project Leg 15*: U.S. Government Printing Office, Washington, D.C., p. 805–811.

Rao, Y. and H. Yang, 2019, Plays prospectivity and exploration direction of pre-salt section in South Gabon basin, West Africa: AAPG ACE abstracts, San Antonio, Texas.

Rehault, J.-P., G. Boillot, and A. Mauffret, 1984, The Western Mediterranean Basin geological evolution: Marine Geology, v. 55, p. 447–477.

Reston, T. J., 2009, The structure, evolution and symmetry of the magma-poor rifted margins of the North and Central Atlantic: A synthesis: Tectonophysics, v. 468, p. 6–27.

Reuber, K., and P. Mann, 2019, Control of Precambrian-to-Paleozoic orogenic trends by along-strike variations in Early Cretaceous continental rifts of the South Atlantic Ocean: Interpretation, v. 7, p. SH45–SH69.

Reuber, K., P. Mann, and J. Pindell, 2019, Hotspot origin for asymmetrical conjugate volcanic margins of the austral South Atlantic Ocean as imaged on deeply penetrating seismic reflection lines: Interpretation, v. 7, p. SH71–SH97.

Révillon, S., E. Hallot, N. T. Arndt, C. Chauvel, and R. A. Duncan, 2000, A complex history for the Caribbean plateau: petrology, geochemistry, and geochronology of the Beata Ridge, South Hispaniola: The Journal of Geology, v. 108, p. 641–661.

Rivadeneyra-Vera, C., M. Bianchi, M. Assumpção, V. Cedraz, J. Julià, M. Rodríguez, L. Sánchez, G. Sánchez, L. Lopez-Murua, G. Fernandez, R. Fugarazzo, and the “3-Basins” Project Team, 2019, An updated crustal thickness map of central South America based on receiver function measurements in the region of the Chaco, Pantanal, and Paraná Basins, Southwestern Brazil: Journal of Geophysical Research, Solid Earth, v. 124, p. 8491–8505.

Roberts, A. M., N. J. Kusznir, G. Yielding, and P. Styles, 1998, 2D flexural backstripping of extensional basins: the need for a sideways glance: Petroleum Geoscience, v. 4, p. 327–338.

Roden-Tice, M. K., D. P. West Jr., J. K. Potter, S. M. Raymond, and J. L. Winch, 2009, Presence of a long-term lithospheric thermal anomaly: Evidence from apatite fission-track analysis in northern New England: The Journal of Geology, v. 117, p. 627–641.

Roden-Tice, M. K., S. J. Tice, and I. S. Schofield, 2000, Evidence for differential unroofing in the Adirondack Mountains, New York State, determined by apatite fission-track thermochronology: The Journal of Geology, v. 108, p. 155–169.

Rogers, R. D., P. Mann, and P. A. Emmet, 2007a, Tectonic terranes of the Chortis block based on integration of regional aeromagnetic and geologic data, in P. Mann, ed., *Geologic and Tectonic Development of the Caribbean Plate Boundary in Northern Central America*: GSA Special Papers, Boulder, CO, v. 428, p. 65–88.

Rogers, R. D., P. Mann, P. A. Emmet, and M. E. Venable, 2007b, Colon fold belt of Honduras: Evidence for late Cretaceous collision between the continental Chortis block and intra-oceanic Caribbean arc, in P. Mann, ed., *Geologic and Tectonic Development of the Caribbean Plate Boundary in Northern Central America*: GSA Special Papers, Boulder, CO, v. 428, p. 129–149.

Rosencrantz, E., 1990, Structure and tectonics of the Yucatan Basin, Caribbean Sea, as determined from seismic reflection studies: Tectonics, v. 9, p. 1037–1059.

Rosencrantz, E., and J. G. Sclater, 1986, Depth and age in the Cayman Trough: Earth and Planetary Science Letters, v. 79, p. 133–144.

Rosencrantz, E., M. I. Ross, and J. G. Sclater, 1988, Age and spreading history of the Cayman Trough as determined from depth, heat flow, and magnetic anomalies: Journal of Geophysical Research, v. 93, p. 2141–2157.

Rowan, M. G., 2020, Salt- and shale-detached gravity-driven failure of continental margins, in N. Scarselli, J. Adam, D. Chiarella, D. G. Roberts, A. W. Bally, eds., *Regional Geology and Tectonics*: Elsevier, Amsterdam, Netherlands, p. 205–234.

Rowley, D. B., A. M. Forte, R. Moucha, J. X. Mitrovica, N. A. Simmons, and S. P. Grand, 2013, Dynamic topography change of the eastern United States since 3 million years ago: Science, v. 340, p. 1560–1563.

Royden, L., and C. E. Keen, 1980, Rifting process and thermal evolution of the continental margin of Eastern Canada determined from subsidence curves: Earth and Planetary Science Letters, v. 51, p. 343–361.

Sánchez, C., and A. Permanyer, 2006, Origin and alteration of oils and oil seeps from the Sinú-San Jacinto Basin, Colombia: Organic Geochemistry, v. 37, p. 1831–1845.

Sanchez, C.J., P. Mann, and P. Emmet, 2016, Late Cretaceous-Cenozoic tectonic transition from collision to transtension, Honduran Borderlands and Nicaraguan Rise, NW Caribbean plate boundary, in M. Nemčok, S. Rybár, S. T. Sinha, S. A. Hermeston, and L. Ledvényiová, eds., *Transform Margins: Development, Controls and Petroleum Systems*: Geological Society, Special Publications, London, UK, v. 431, p. 273–297.

Sanchez, J., P. Mann, L. C. Carvajal-Arenas, and R. Bernal-Olaya, 2019, Regional transect across the western Caribbean Sea based on integration of geologic, seismic reflection, gravity, and magnetic data: AAPG Bulletin, v. 103, p. 303–343.

Sandoval, M. I., P. O. Baumgartner, J. Escuder-Viruete, J. Gabites, and B. Mercier de Lépinay, 2015, Late Cretaceous radiolarian biochronology of the Pedro Brand section, Tireo Group, eastern Central Cordillera, Dominican Republic: A contribution to the stratigraphy of the Caribbean Large Igneous Province: Revue de Micropaléontologie, v. 58, p. 85–106.

Sandwell, D. T., R. D. Müller, W. H. F. Smith, E. Garcia, and R. Francis, 2014, New global marine gravity model from CryoSat-2 and Jason-1 reveals buried tectonic structure: Science, v. 346, p. 65–67.

Sauter, D., H. Sloan, M. Cannat, J. Goff, P. Patriat, M. Schaming, and W. R. Roest, 2011, From slow to ultra-slow: How does spreading rate affect seafloor roughness and crustal thickness?: Geology, v. 39, p. 911–914.

Sauter, D., J. Tugend, M. Gillard, M. Nirrengarten, J. Autin, G. Manatschal, M. Cannat, S. Leroy, and M. Schaming, 2018, Oceanic basement roughness alongside magma-poor rifted margins: Insight into initial seafloor spreading: Geophysical Journal International, v. 212, p. 900–915.

Sauter, D., P. Unternehr, G. Manatschal, J. Tugend, M. Cannat, P. Le Quellec, N. Kusznir, M. Munschy, S. Leroy, J. M. de Lepinay, J. W. Granath, and B. W. Horn, 2016, Evidence for magma entrapment below oceanic crust from deep seismic reflections in the Western Somali Basin: Geology, v. 44, p. 407–410.

Schaff, P., D. Moran-Zenteño, M. Hernandez-Bernal, G. Solis-Pichardo, G. Tolson, and H. Kohler, 1995, Paleogene continental margin truncation in southwestern Mexico: Geochronological evidence: Tectonics, v. 14, p. 1339–1350.

Schnabel, M., D. Franke, M. Engels, K. Hinz, S. Neben, V. Damm, S. Grassmann, H. Pelliza, and P. R. Dos Santos, 2008, The structure of the lower crust at the Argentine continental margin, South Atlantic at 44°S: Tectonophysics, v. 454, p. 14–22.

Sclater, J. G., and P. A. F. Christie, 1980, Continental stretching: An explanation of the Post-Mid-Cretaceous subsidence of the central North Sea Basin: Journal of Geophysical Research, Solid Earth, v. 85, p. 3711–3739.

Scotchman, I. and D. Chiossi, 2009, Kilometre-scale uplift of the Early Cretaceous rift section, Camamu Basin, offshore North-East Brazil: AAPG ICE abstracts, Cape Town, South Africa.

Scott, D. T., 2015, Characterization of the South Gabon Basin passive-margin fold and thrust belt from 2D seismic interpretation: Unpublished BSc thesis, University of Houston, Houston, TX, 37 p.

Sen, G., R. Hickey-Vargas, D. G. Waggoner, and F. Maurrasse, 1988, Geochemistry of basalts from the Dumisseau Formation, southern Haiti: Implications for the origin of the Caribbean Sea crust: Earth and Planetary Science Letters, v. 87, p. 423–437.

Seton, M., R. D. Müller, S. Zahirovic, S. Williams, N. M. Wright, J. Cannon, J. M. Whittaker, K. J. Matthews, and R. McGirr, 2020, A global data set of present-day oceanic crustal age and seafloor spreading parameters: Geochemistry, Geophysics, Geosystems, v. 21, Article e2020GC009214.

Shipboard Scientific Party, 1998, Site 1070, in R. B. Whitmarsh, M. O. Beslier, P. J. Wallace, et al., eds., in *Initial Reports of the Deep Sea Drilling Project*: U.S. Government Printing Office, Washington, DC, v. 173, p. 265–294.

Shipboard Scientific Party, 2004, Site 1276, in B.E. Tucholke, J. C. Sibuet, A. Klaus, et al., eds., in *Initial Reports of the Deep Sea Drilling Project*: U.S. Government Printing Office, Washington, DC, v. 210, p. 1–358.

Sigurdsson, Haraldur, R. M. Leckie, G. D. Acton, et al., 1997, Caribbean ocean history and the Cretaceous/Tertiary boundary event; Covering leg 165 of the cruises of the drilling vessel JOIDES Resolution, Miami, Florida, to San Juan, Puerto Rico, Sites 998-1002, in *Initial Reports of the Ocean Drilling Program*: US Government Printing Office, Washington, DC, USA., 66 p.

Sinton, C. W., H. Sigurdsson, and R. A. Duncan, 2000, Geochronology and petrology of the igneous basement at the Lower Nicaraguan Rise, Site 1001, in R. M. Leckie, H. Sigurdsson, G. D. Acton, et al., eds., *Proceedings of the Ocean Drilling Program*: US Government Printing Office, Washington, DC, p. 233–236.

Sinton, C. W., R. A. Duncan, M. Storey, J. Lewis, and J. J. Estrada, 1998, An oceanic flood basalt province within the Caribbean plate: Earth and Planetary Science Letters, v. 155, p. 221–235.

Skarstein, G. L. S., 2018, Geochemical characterisation of oils and sediments from Cuba and Jamaica; Implications for the northern Caribbean petroleum system: MSc thesis, University of Stavanger, Norway, 129 p.

Smith, W. H. F., and D. T. Sandwell, 1997, Global seafloor topography from satellite altimetry and ship depth soundings, Science, v. 277, p. 1957-1962.

Snoke, A. W., and P. J. Noble, 2001, Ammonite-radiolarian assemblage, Tobago Volcanic Group, Tobago, West Indies—Implications for the evolution of the Great Arc of the Caribbean: GSA Bulletin, v. 113, p. 256–264.

Sobreira, J. F. F., and P. Szatmari, 2003, Idades Ar–Ar para as rochas ıgneas do Arquipélago de Abrolhos, margem sul da Bahia: IX Simpósio Nacional de Estudos Tectônicos abstract volume, Buzios, Brazil, p. 382–383.

Soulas, J. P., 1977, Les phases tectoniques andines du Tertiaire superieur, resultats d'une transversale de Pisco-Ayacucho (Perou central): Académie des Sciences Paris, v. 284, p. 2207–2210.

Speed, R. C., and G. K. Westbrook, 1984, Lesser Antilles arc and adjacent terranes: Marine Science International, Regional Atlas Series, Ocean Margin Drilling Program, Woods Hole, MA, Atlas 10, 27 p.

Spotila, J. A., G. C. Bank, P. W. Reiners, C. W. Naeser, N. D. Naeser, and B. S. Henika, 2003, Origin of the Blue Ridge escarpment along the passive margin of Eastern North America: Basin Research, v. 16, p. 41–62.

Stoffa, P. L., A. Mauffret, M. Truchan, and P. Buhl, 1981, Sub-B″ layering in the southern Caribbean: The Aruba Gap and Venezuela Basin: Earth and Planetary Science Letters, v. 53, p. 131–146.

Stoker, M. S., D. Praeg, B. O. Hjelstuen, J. S. Laberg, T. Nielsen, and P. M. Shannon, 2005, Neogene stratigraphy and the sedimentary and oceanographic development of the NW European Atlantic margin: Marine and Petroleum Geology, v. 22, p. 977–1005.

Stüwe, K., 2007, Geodynamics of the lithosphere: Springer International Publishing, Berlin, Germany, 497 p.

Sutra, E., G. Manatschal, G. Mohn, and P. Unternehr, 2013, Quantification and restoration of extensional deformation along the Western Iberia and Newfoundland rifted margins: Geochemistry, Geophysics, Geosystems, v. 14, p. 2575–2597.

Sweeney, J. J., and A. K. Burnham, 1990, Evaluation of a simple model of vitrinite reflectance based on chemical kinetics: AAPG Bulletin, v. 74, p. 1559–1570.

Talwani, M., C. C. Windisch, P. L. Stoffa, P. Buhl, and R. E. Houtz, 1976, Multi-channel seismic study in the Venezuelan Basin and the Curacao Ridge: AGU Transactions, v. 57, p. 266.

Teisserenc, P., and J. Villemin, 1989, Sedimentary basin of Gabon – Geology and oil systems, in J.D. Edwards, and P. A. Santogrossi, eds., *Divergent/Passive Margin Basins*: AAPG, Tulsa, OK, v. 48, p. 117–119.

Torrado, L., 2018, Tectono-stratigraphic controls on petroleum system elements in passive margin settings: studies of the western Nicaraguan Rise and the deep-water, Foz do Amazonas basin, Brazil: PhD dissertation, University of Houston, Houston, TX, 277 p.

Torrado, L., L. C. Carvajal-Arenas, J. Sanchez, P. Mann, and J. C. Silva-Tamayo, 2019, Late Cretaceous-Cenozoic sequence stratigraphic and paleogeographic controls on petroleum system elements of the Nicaraguan platform, western Caribbean Sea: AAPG Bulletin, v. 103, p. 1925–1962.

Triezenberg, P. J., Hart, P. E., and Childs, J. R., 2016, National Archive of Marine Seismic Surveys (NAMSS): A USGS data website of marine seismic reflection data within the U.S. Exclusive Economic Zone (EEZ): U.S. Geological Survey Data Release.

Trommsdorff, V., G. B. Piccardo, and A. Montrasio, 1993, From magmatism through metamorphism to sea floor emplacement of subcontinental Adria lithosphere during pre-Alpine rifting (Malenco, Italy): Schweizerische Mineralogische und Petrographische Mitteilungen, v. 73, p. 191–203.

Tucholke, B.E., and Sibuet, J. C., 2007. Leg 210 synthesis: Tectonic, magmatic, and sedimentary evolution of the Newfoundland-Iberia rift, in B.E. Tucholke, J. C. Sibuet, and A. Klaus, eds., *Proceedings of the Ocean Drilling Program*: US Government Printing Office, Washington, DC, v. 201, p. 1–56.

Tucker, P. M., and H. J. Yorston, 1973, Pitfalls in seismic interpretation: SEG, Tulsa, OK, 57 p.

Tugend, J., G. Manatschal, and N. J. Kusznir, 2015, Spatial and temporal evolution of hyperextended rift systems: Implication for the nature, kinematics, and timing of the Iberian-European plate boundary: Geology, v. 43, p. 15–18.

Tugend, J., M. Gillard, G. Manatschal, M. Nirrengarten, C. Harkin, M.-E. Epin, D. Sauter, J. Autin, N. Kusznir, and K. McDermott, 2018, Reappraisal of the magma-rich versus magma-poor rifted margin archetypes, in K. R. McClay, and J. A. Hammerstein, eds., *Passive Margins: Tectonics, Sedimentation and Magmatism*: Geological Society, Special Publications, London, UK, v. 476, p. 23–47.

Turcotte, D. L., and G. Schubert, 1982, Geodynamics: Cambridge University Press, Cambridge, UK, 636 p.

Uchupi, E., 1975, The physiography of the Gulf of Mexico and the Caribbean Sea, in A. E. M. Nairn, and F. G. Stehli, eds., *The Gulf of Mexico and the Caribbean*: New York, NY, Plenum Press, p. 1–64.

Unternehr, P., G. Péron-Pinvidic, G. Manatschal, and E. Sutra, 2010, Hyper-extended crust in the South Atlantic: In search of a model: Petroleum Geoscience, v. 16, p. 207–215.

Venable, M., 1994, A geological tectonic, and metallogenetic evaluation of the Siuna terrane (Nicaragua): PhD dissertation, University of Arizona, Tucson, AZ, 154 p.

Viana, C. F., Junior, E. G. da G., Simoes, I. E. de A., Moura, J. A., Fonseca, J. dos R., and Alves, R. J., 1971, Revisão histórica da estratigrafia das bacias de Recôncavo e Tucano: Boletim Tecnico da Petrobrás, v. 14, p. 157–192.

Vigliotti, L., and D. V Kent, 1990, Paleomagnetic results of Tertiary sediments from Corsica: Evidence of post-Eocene rotation: Physics of the Earth and Planetary Interiors, v. 62, p. 97–108.

Warren, J. K., 2006, *Evaporites: Sediments, resources and hydrocarbons*: Springer International Publishing, Berlin, Germany, 1042 p.

Watkins, J. S., J. L. Worzel, M. H. Houston, M. Ewing, and J. B. Sinton, 1975, Deep seismic reflection results from the Gulf of Mexico: Part I: Science, v. 187, p. 834–836.

Weatherall, P., K. M. Marks, M. Jakobsson, T. Schmitt, S. Tani, J. E. Arndt, M. Rovere, D. Chayes, V. Ferrini, and R. Wigley, 2015, A new digital bathymetric model of the world's oceans: Earth and Space Science, v. 2, p. 331–345.

Weigelt, E., and W. Jokat, 2001, Peculiarities of roughness and thickness of oceanic crust in the Eurasian Basin, Arctic Ocean: Geophysical Journal International, v. 145, p. 505–516.

Westbrook, G. K., 1975, The structure of the crust and upper mantle in the region of Barbados and the Lesser-Antilles: Geophysical Journal of the Royal Astronomical Society, v. 43, p. 201–242.

Westbrook, G., J. Ladd, P. Buhl, N. Bangs, and G. Tiley, 1988, Cross section of an accretionary wedge: Barbados Ridge complex: Geology, v. 16, p. 631–635.

Westphal, M., J. Orsini, and P. Vellutini, 1976, Le microcontinent Corso-Sarde, sa position initiale: Donnees paleomagnetiques et raccords geologiques: Tectonophysics, v. 30, p. 141–157.

White, R. S., D. N. Mckenzie, and K. O. Nions, 1992, Oceanic crustal thickness from seismic measurements and rare earth element inversions: Journal of Geophysical Research, v. 97, p. 19683–19715.

White, R. S., L.K. Smith, A.W. Roberts, P.A.F. Christie, N.J. Kusznir, A.M. Roberts, D. Healy, R. Spitzer, A. Chappell, J.D. Eccles, R. Fletcher, N. Hurst, Z. Lunnon, C.J. Parkin, and V.J. Tymms, 2008, Lower-crustal intrusion on the North Atlantic continental margin: Nature, v. 452, p. 460–464.

White, R., and D. McKenzie, 1989, Magmatism at rift zones: The generation of volcanic continental margins and flood basalts: Journal of Geophysical Research, Solid Earth, v. 94, p. 7685–7729.

Whitmarsh, R. B., G. Manatschal, and T. A. Minshull, 2001, Evolution of magma-poor continental margins from rifting to seafloor spreading: Nature, v. 413, p. 150–154.

Wilson, J. T., 1966, Did the Atlantic close and then re-open? Nature, v. 211, p. 676–681.

Withjack, M. O., P. E. Olsen, and R. W. Schlische, 1995, Tectonic evolution of the Fundy rift basin, Canada: Evidence of extension and shortening during passive margin development: Tectonics, v. 14, p. 390–405.

Yang, W., and A. Escalona, 2011, Tectonostratigraphic evolution of the Guyana Basin: AAPG Bulletin, v. 95, p. 1339–1368.

Zalán, P. V., 2015, Similarities and differences between magma-poor and volcanic passive margins? Applications to the Brazilian marginal basins: 14th International Congress of the Brazilian Geophysical Society & EXPOGEF abstracts, Rio de Janeiro, Brazil, p. 37–42.

Zalán, P. V., M. d. C. G. Severino, C. A. Rigoti, L. P. Magnavita, J. A. B. De Oliveira, and A. R. Vianna, 2011, An entirely new 3D-view of the crustal and mantle structure of a South Atlantic Passive Margin—Santos, Campos and Espírito Santo Basins, Brazil: AAPG ACE abstracts, Houston, Texas.

Zavala, O., 2018, Comparison of spreading rate variations in the South Atlantic Ocean with subsidence histories of offshore wells and apatite fission track cooling ages from the South American and African conjugate margins: Unpublished BSc thesis, University of Houston, Houston, TX, 23 p.

Zhang, J., W. W. Sager, and J. Korenaga, 2015, The Shatsky Rise oceanic plateau structure from two-dimensional multichannel seismic reflection profiles and implications for oceanic plateau formation, in C. R. Neal, W. W. Sager, T. Sano, E. and Erba, eds., *The Origin, Evolution, and Environmental Impact of Oceanic Large Igneous Provinces*: GSA Special Paper, Boulder, CO, v. 511, p. 103–126.